The Design of an Imager to Safeguard Spent Fuel Using Passive Fast Neutron Emission Tomography

A Dissertation Presented for the
Doctor of Philosophy
Degree
The University of Tennessee, Knoxville

Anagha Srikanth Iyengar
May 2019

Copyright © 2019 by Anagha Srikanth Iyengar
All rights reserved.

ACKNOWLEDGEMENTS

I would like to thank my dissertation committee, which includes Dr. Jason Hayward, Dr. Paul Hausladen, Dr. Howard Hall, and Dr. Lawrence Heilbronn for the support they have provided me during my dissertation research and journey through graduate school.

I am so grateful and indebted to my research advisor, Dr. Paul Hausladen, for his consistent support, expertise, valuable guidance, humor, and patience. I especially appreciate his time and effort to make my Ph.D. experience productive and stimulating. His willingness to listen and create a welcoming environment has made him a thoughtful and irreplaceable mentor.

I would also like to express my immense gratitude to Dr. Jason Hayward for serving as my academic advisor for both my M.S. and Ph.D. degrees, and for being so patient, responsive, and so supportive throughout the process.

I would like to thank Dr. Jinan Yang for her guidance and help in using MCNP to model the complicated detector geometries, and for all her assistance in debugging and running my simulations when I did not have access to a cluster. I would also like to thank Dr. Jianwei Hu for his help in generating the fuel assembly source terms and for his guidance and technical expertise. Special thanks to Dr. Lorenzo Fabris for all his assistance and brilliance in fixing the detector electronics, help in running the experiments, and for being patient with me while I asked him countless questions. Thank you also to the staff at the Radiation Standards and Calibration Laboratory (RaSCaL) for helping with the experiments.

I am extremely grateful for my ORNL family in Building 3500 for supporting me through the hardest parts of this journey. Thank you for making me laugh, listening to me when things were hard, and for your advice and support that gave me a sense of home when I needed it. I am forever indebted to you.

Thank you to Dr. Lee Riedinger for providing me the opportunity to pursue a Ph.D. that offered a healthy interdisciplinary mix of science and policy that would be difficult to find anywhere else.

I would like to dedicate my Ph.D. to my grandfather, Mr. Belakavadi Gopalachar Narayana Iyengar. I am forever grateful that I was able to complete and defend my research in time for him to know I passed. He was my biggest cheerleader, and I will miss him every day, but he will forever inspire me to *"be bold"* in the face of fear. To my parents Srikanth and Mrudula, I owe everything I have achieved and how far I have come to you. Thank you both for supporting me and for working so hard for decades to make sure I had all the opportunities available to me. Thank you also to all of my friends, who in the absence of siblings, took the place of family in my life. I am so lucky to have you all.

I would like to thank the Department of Energy National Nuclear Security Administration's (DOE/NNSA) Office of International Nuclear Safeguards (NA-241) for supporting me as a Nuclear Nonproliferation International Safeguards Fellow. I would also like to thank DOE/NNSA's Office of Defense Nuclear Nonproliferation Research and Development (NA-22) for supporting the project that enabled my Ph.D. research.

ABSTRACT

Safeguarding spent fuel in spent fuel pools, during transportation, and at dry cask storage sites has been a continuing priority for the International Atomic Energy Agency (IAEA.) The IAEA implements partial defect testing on all easily dismountable fuel before transfer to difficult-to-access storage. This project is focused on developing a new imaging capability using fast neutron emission tomography in support of the IAEA's mission. The capability is intended to address the buildup of spent fuel inventories around the world from decommissioning activities by creating an efficient and effective tool for verification of a variety of fuel types for long-term disposition.

While the sensitivity of gamma emission tomography is limited by self-attenuation, neutron measurements may have better sensitivity for resolving individual pins toward the center of larger fuel assemblies. Because the neutron signal originates primarily from ^{244}Cm, which is sensitive to exposure, this method could also be sensitive to assemblies containing fuel pins replaced after a single cycle in the reactor and subsequently irradiated in the core. This work describes a set of simulation and measurement work completed in order to investigate and converge on the final design of a fast neutron emission tomography system for imaging a spent nuclear fuel assembly. To conduct a constrained optimization for the design, a range of imager design parameters were identified to be varied, and MCNP was used to build hundreds of geometries to investigate. The analysis was split in two components for gamma or neutron analysis. Simulations and proof-of-concept measurements presented here suggest that it is viable to build a compact equivalent to a parallel slit collimator imager that has sufficient spatial resolution to image spent fuel pins. Furthermore, it is expected to be able to withstand the high photon rates present in the relevant environment. Recommended future work is also discussed.

TABLE OF CONTENTS

1. Introduction 1
   1.1. Safeguards Context 1
   1.2. Spent Fuel 3
      1.2.1. Spent Fuel Signatures 4
      1.2.2. Pu vs. Cm 12
      1.2.3. Fuel Assembly Parameters 13
   1.3. Tomography Overview 14
      1.3.1. Conventional emission tomography methods 17
      1.3.2. Application challenges 19
   1.4. Overview of Dissertation 20
2. Literature Review 21
   2.1. Verification Methods 21
   2.2. Gross Measurement Techniques 21
      2.2.1. Fork Detector Irradiated Fuel Measuring System (FDET) 22
      2.2.2. Safeguards MOX python (SMOPY) 25
      2.2.3. Neutron Gamma Attribute Tester (NGAT) 25
      2.2.4. Spent Fuel Attribute Tester (SFAT) 26
      2.2.5. Irradiated Fuel Attribute Tester (IRAT) 26
      2.2.6. CANDU Bundle Verifier (CBVB) 26
      2.2.7. Cask Radiation Profiling System (CRPS) 26
      2.2.8. Optical Fiber Radiation Probe System (OFPS) 27
      2.2.9. Neutron Coincidence Techniques 27
      2.2.10. Cherenkov Viewing Devices 29
      2.2.11. Passive Neutron Albedo Reactivity (PNAR) 30
   2.3. Imaging 33
      2.3.1. Passive Gamma Emission Tomography 33
      2.3.2. Neutron Emission Tomography 37
   2.4. Gaps in Technology 40
   2.5. Novel Contributions 41
3. System Design 43
   3.1. Lines of Response and Collimation 43
   3.2. Imaging System Requirements 46
   3.3. Parallel-Slit Ring Collimator Design Concept 47
   3.4. Baseline Design 50
   3.5. Imager Geometries Considered 53
      3.5.1. Procedure 55
   3.6. Neutron Detectors 57
      3.6.1. Boron Coated Straw Detector Configuration 59
   3.7. Simulated Geometry 62
4. Gamma Exposure Sensitivity 64
   4.1. Experiments 64
      4.1.1. Measurement Campaign #1 67
      4.1.2. Measurement Campaign #2 70

4.1.3. Measurement Campaign #3 72
5. Simulation Design Study: Gamma Exposure 79
5.1. Gamma Source Term 79
5.2. Exposure Simulation Results 81
5.3. Constant Exposure Contour 88
6. Simulation Design Study: Neutron Response 101
6.1. Neutron Response 101
6.2. Point Spread Function 104
6.3. Inter-Detector Scatter 110
6.4. "Direct" and "Edge" Effects on Neutron Counts 114
6.5. Collimator Penetration 121
6.5.1. Predicting Collimator Penetration 126
6.6. Parametric Study and Signal-to-Noise Ratio Results 142
7. Final Imager Design 151
7.1. Final Geometry 151
7.2. Edge Effects in the Final Geometry 156
7.3. Correction Factor for Direction of Slit 160
7.4. Predicting Collimator Penetration 170
7.5. Expected Signal-to-Noise of Final System 178
7.6. Tomography Simulations 183
7.7. Testing of Detector Prototype 189
8. Conclusions and Future Work 200
References 204
Appendix 210
Vita 214

LIST OF TABLES

Table 1. Major isotopes and their measurable gamma rays in a typical spent fuel assembly [17]. 7
Table 2. Spontaneous fission and (α,n) yields for the major neutron emitting isotopes in spent fuel [20]..... 10
Table 3. List of sixteen combinations of stainless-steel and borated polyethylene thicknesses making up the imager collimator that were used as the basis for evaluating different imager geometries [57] [58] 54
Table 4. Neutron and gamma-ray interaction probability for common neutron detectors [59]. 58
Table 5. Main components of a boron carbide straw and respective dimensions and material parameters [60]..... 61
Table 6. Gamma source information for Cs-137 irradiator facility (RaSCaL) at ORNL. The exposure at three different source-detector distances is shown along with the attenuation factors. 66
Table 7. MCNP calculated closed fractions and mean exposures for all 45 of the parallel slit cases with total collimator thickness of 45 cm. 91
Table 8. Calculated m values using Equation 13 for a starting thickness of 5 cm stainless steel and increasing. 96
Table 9. MCNP predicted and calculated total areal densities for various stainless steel and borated polyethylene combinations to maintain a given exposure. 96
Table 10. MCNP predicted and calculated total areal densities using all corrections for various stainless steel and borated polyethylene combinations to maintain a given exposure. 99
Table 11. Calculated Wp values for the different distances and slit widths simulated .. 118
Table 12. List of the total collimator thicknesses and outer borated polyethylene thicknesses. 124
Table 13. To extract the stainless-steel correction factor, the slope of each line from the previous figure was extracted. The slopes of the lines with the same steel thicknesses are similar and are listed here. 132
Table 14. Dimensions of the final collimator design. 152
Table 15. Values for the three constants ($\mu 0$, $\Delta\mu$, and $Cslit$) in Equation (33) that result in the calculated effective thickness in mfp plotted against the MCNP calculated effective thickness in mfp lying along a slope of approximately 1. 174
Table 16. List of slit widths and corresponding scaling factors. 181
Table 17. Source information for the six ^{252}Cf pellets used in the experiment along with the initial activity and date created. 194
Table 18. Coefficients for the double Gaussian fit..... 211

LIST OF FIGURES

Figure 1. Fission product distribution for thermal fission of ^{235}U and ^{239}Pu [15]. 6
Figure 2. ^{137}Cs fission product concentration (weight % of initial U concentration) as a function of exposure or burnup (GWd/tU) [15]. 8
Figure 3. The main neutron sources from a PWR fuel assembly and their emission rates as a function of cooling time [15]. 10
Figure 4. Neutron rate per fuel rod due to Cm-244 as a function of burnup or exposure within an average commercial PWR (shown for 4% initial enrichment and 2-year cooling time) [21]. 11
Figure 5. ^{239}Pu content as a function of fuel assembly burnup or exposure [21]. 12
Figure 6. Neutron count rate [neutrons per second per meter] by pin for a typical 17 x 17 fuel assembly with initial enrichment of 4%, 40 GWd/tU burnup, and a 1 year cooling time. 14
Figure 7. General CT measurement set up where a radiation source is collimated and the beam interrogates the sample of interest. The sample is then rotated so the detector array can acquire data from all projections [30]. 15
Figure 8. The image on the left shows the scanning of a slice where traditional tomography is performed (attenuation based) where the lines of response are formed by the transmitted intensity [29]. The image on the right shows the method of performing emission tomography where the inspection object is the source and a collimator is used to isolate lines of response along which the activity is measured [33]. 17
Figure 9. Diagram of sample conventional imager designs adapted for use to measure spent fuel using emission tomography [34]. See text for details. 18
Figure 10. Exposures at 1 meter perpendicular to the center of a PWR or CANDU fuel assembly as a function of cooling time [35]. 20
Figure 11. Fork detector irradiated fuel measuring system (FDET) [10]. 23
Figure 12. (Left) View from the top of the fork detector with detector arms around a 17x17 fuel assembly being inspected. (Right) the vertical cross-sectional view of the fork detectors showing where the fission chambers and ion chamber sit [38]. 24
Figure 13. Results of the $Nc/(Gc)^4$ ratio, normalized to the ratio of a full configuration, for several configurations of spent fuel with 50% of the fuel pins missing [38]. 24
Figure 14. Configuration 69 (left) and 70 (right), where 50% of the fuel pins has been removed in a homogeneous way [38]. 25
Figure 15. Cross section view of the AEFC device. The ^{3}He detectors are placed in two rows and are housed in an HDPE matrix. The measurement is done under water where a fuel assembly is inserted through the annulus shown in blue [39]. 27
Figure 16. Cross sectional view of SFCC. The 20 ^{3}He tubes are shown in yellow, and the ion chamber is shown in red [41]. 28
Figure 17. Horizontal cross-sectional view of the PNAR system optimized for BWR fuel [43]. 31
Figure 18. the BWR PNAR Ratio, simulated with fresh water, is illustrated as a function of burnup for 12 assemblies with three different initial enrichments [43]. 32

Figure 19. PNAR Ratio for BWR assemblies as a function of net multiplication [43]. ... 32
Figure 20. PGET prototype arrangement [50]. ... 34
Figure 21. The final design of the PGET consists of 174 CdZnTe gamma detectors split between two heads, two ^{10}B neutron detectors, a data acquisition system, safety sensors, and a motor assembly [51]. ... 36
Figure 22. Tomography data from PGET measurements of various fuel assemblies [51]. ... 36
Figure 23. (Left) Schematic diagram of the imager. (Right) Prototype of the slit-collimator imager [55]. ... 37
Figure 24. (Left) Experimental setup of ^{252}Cf sources (yellow) and machining grit (black). (Right) Tomographic reconstruction of the sample on the left showing location of the five sources [55]. ... 38
Figure 25. (Left) Picture of the soup can containing 31 Pu MOX fuel rodlets and one DU rodlet marked by the 'X'. (Right) Tomographic reconstruction of the neutron source strength as a function of source position. The blue region corresponds to the location of the DU rodlet [55] [56]. ... 39
Figure 26. Shows the point spread functions for various thicknesses of stainless steel evaluated. The curves are normalized to the 10cm borated polyethylene / 30cm steel data. There is not much difference in the 'noise' between the 25cm borated poly case and 40 cm borated poly case. ... 44
Figure 27. Example lines of response for a detector counting neutrons that exit a single 3 mm wide collimator slit, shown (a) as a schematic diagram. The results of a ^{244}Cm point source simulated at each assumed fuel pin location are shown (b) for a 15 cm thick collimator and (c) for a 30 cm thick collimator [34]. ... 45
Figure 28. The parallel-slit ring collimator (e) is equivalent to the parallel slit collimator in (a). As shown in (b)-(d), each slit is rotated from the dashed red to the solid red line so that after rotation, the resulting slits are (e) spaced equally around the circle. Each slit still inspects the same chord of the inspection volume [57]. ... 49
Figure 29. Close up of the borated polyethylene component of the collimator with slits pointing to detectors. The two cadmium (Cd) layers are shown in addition to the outer borated polyethylene layer to prevent in-scatter. The high-density polyethylene matrix that the straws are embedded in is shown in red. ... 50
Figure 30. Plan view of the entire imager with a 17 × 17 fuel assembly in the center. ... 52
Figure 31. Three-dimensional configuration of the collimator and neutron detectors around a typical fuel assembly (green). The imager is shown (left) without and (right) with stainless steel (pink) and borated polyethylene shielding (yellow) at the top and bottom of the imager to shield from fuel assembly shine [34]. ... 53
Figure 32. (left) A commercially available transport cask by GNS. (right) A 3-D rendering of imager concept in a cask-like container that would fit in a fuel encapsulation facility [59] [34]. ... 55
Figure 33. Cross sectional image of a single boron carbide straw [62]. ... 60
Figure 34. Illustration of three different detector straw geometries simulated by PTI [34]. ... 60
Figure 35. Detector efficiency as a function of boron carbide thickness for the three different pitch sizes simulated [34]. ... 61

Figure 36. MCNP model of a single straw and its various components located in a high density polyethylene matrix. 62
Figure 37. (Left) The detector box with a repeated hexagonal lattice filled with 23 straws in an 8-7-8 pattern. (Right) A close-up of what the 100 repeated detector cells look like when the box on the left is translated. 63
Figure 38. The prototype detector during irradiation experiments at the RaSCaL facility. The gamma radiation from the ^{137}Cs source was centered on the crosshairs of the red laser, ... 64
Figure 39. View from end of detector showing all 23 straws. 65
Figure 40. Experimental setup for the final measurement campaign conducted at the RaSCaL facility. 67
Figure 41. Setup with ^{252}Cf source for the first measurement campaign on October 4, 2017. 68
Figure 42. Count rate measured as a function of threshold setting using the first bipolar circuit design for the three different exposures as well as a 0R/hr measurement. This data set was collected without cable termination. 69
Figure 43. Count rate measured as a function of threshold for different exposures with 50Ω termination on the signal cable. 69
Figure 44. Count rate as a function of threshold for different exposures using the circuit provided by PTI with the ^{252}Cf source present. 71
Figure 45. Circuit diagram of PTI's configuration. 71
Figure 46. Count rate as a function of threshold for different exposurees using the circuit with resistor replaced. 72
Figure 47. Count rate as a function of threshold for different exposurees using the circuit with resistor replaced. The two additional curves shown are the count rates for 430 R/hr divided by 4 and 105.1 R/hr divided by 4.77. 73
Figure 48. Unipolar pulses with 50 ns peaking time where the signal goes down to 0 between each pulse. 74
Figure 49. Example of overlapping unipolar pulses in a high-count rate situation where the pulse cannot die down to 0. 74
Figure 50. Scope traces from the detector exposed to different gamma exposures [63]. . 76
Figure 51. Pulse height spectrum vs. energy (MeV) from a MCNP simulation of a (a) beam of 662-keV photons incident on a single detector and (b) pulse height spectrum for neutrons [63]. 76
Figure 52. Measured (solid) and simulated (dashed) counts per second in a single detector module as a function of detector threshold for different exposures [63]. 78
Figure 53. Plan view of the imager with 3 mm parallel slits in the collimator with 10 cm steel and 30 cm borated polyethylene. 82
Figure 54. Side view of the MCNP geometry of the fuel assembly, imager, and container. 83
Figure 55. Map of gamma exposures [R/hr] seen at all the detector straws for a collimator with 10 cm stainless steel, 30 cm borated polyethylene, and 3 mm parallel slits with a 40 GWd/MTU burnup fuel with 1-year cooling time as the source term [34]. 84
Figure 56. Exposure rate [R/hr] at each detector for an imager with 10 cm stainless steel, 30 cm of borated polyethylene, and 3 mm parallel slits [34]. 85

Figure 57. The exposure [R/hr] at Detector #20 which had the maximum exposure as a function of slit width for 10 cm stainless steel and 30 cm borated polyethylene [34]. 86
Figure 58. Maximum exposure rates for all 512 geometries modeled as a function of the stainless-steel open fraction. The red line shows the geometries that fall above and below the 500 R/hr limit for maximum exposure tolerable by the detectors. 87
Figure 59. Maximum exposure rate for all 512 geometries being considered plotted as a function of the open fractions of the collimator components. The data in the red is the maximum exposure plotted as a function of the borated polyethylene open fraction, and in blue against the stainless-steel open fraction. 88
Figure 60. The mean gamma-ray exposure per centimeter as a function of the total collimator areal density [63]. 90
Figure 61. Total areal densities for various stainless-steel thicknesses as a function of slit width while maintaining a total collimator thickness of 45 cm. 96
Figure 62. Total collimator areal density as a function of steel thickness to maintain the same exposure. The red curve shows what the MCNP calculated areal density values should be, and the blue curve shows the areal density values calculated using the equation derived and the m value. 97
Figure 63. Diagram showing the radius values used to correct for the change in open fraction as the stainless steel (grey) and borated polyethylene (blue) radii change. . 97
Figure 64. The total collimator areal density calculated using all correction factors as a function of steel thickness to maintain the exposure at 257.31 R/hr. The MCNP areal density values are in red, and the blue curve shows the areal density values calculated using all correction factors. 100
Figure 65. Calculated m values for the various steel thicknesses that maintain the exposure at 257.311 R/hr. The m is reflective of the required collimator slit width at a given steel thickness. 100
Figure 66. Total neutron cross section and the absorption cross section for neutrons in boron carbide [64]. 102
Figure 67. Simulation set up showing location of the 244Cm line source aligned to the centerline of the slit opening to detector number 50. The detectors are numbered 1 to 100 starting at the bottom tangent slit (#1) going around clockwise to detector 100 [34].. 105
Figure 68. Diagram showing the areas overlapped by the fields of view of slits corresponding to detectors 50 and 51. The two source positions along slit 51's centerline used to generate the PSFs are also shown here relative to the origin (0,0), which is the center of the fuel cavity. The ^{244}Cm was first placed in the position marked by the red dot to generate PSFs for background quantification and was placed in the position marked by the blue dot outside of the overlap region of the two slits for a second set of simulations to accurately quantify the signal [65]..... 106
Figure 69. Point spread functions for a ^{244}Cm line source at two different distances from the slit 51 opening using a collimator with 10 cm stainless steel and 30 cm borated poly and 3 mm wide parallel slits [65]. 107
Figure 70. Ratio of counts seen at detector 51 to all the other detectors for a line source moving down the centerline of slit 51 across the field of view. 108

Figure 71. Detector 51 response to a ^{244}Cm line source placed in the non-overlap region (source position 2). 109
Figure 72. Signal at detector 51 for all 512 cases as a function of the borated polyethylene open fraction. 110
Figure 73. All interactions (collision and absorption) of neutrons in the imaging system originating from a beam of ^{244}Cm neutrons shot at the central detector. The red points show where the maximum probability of interaction is, and the blue shows areas with lower interaction probabilities [34]. 111
Figure 74. Visual representation of neutron absorption reactions seen in each straw (in the boron carbide layer) when a beam of ^{244}Cm neutrons is shot to the center detector only. The bottom plot shows the average relative counts of boron captures (per 10^6 source particles) [34] [63]. 112
Figure 75. Detector 50 response in counts per source particle to each point in inspection area for an imager with 3 mm slits [65]. 113
Figure 76. Single slit geometry pointing at Detector 51 (highlighted in pink) used to simulate a line source at 3 different distances moving perpendicular to the slit 51 centerline [65]. 115
Figure 77. Detector 51 response for various source positions along the 10.08 cm away chord for the different slit widths investigated. 117
Figure 78. Plot of the peak counts registered at Detector 51 with the single slit geometry when the source is located on the slit 51 centerline 10.08 cm away for various parallel slit widths. 117
Figure 79. Collimator penetration components of the detector response for the 3 distances as a function of the source position relative to the slit centerline. 119
Figure 80. Projected width (Wp) in the single slit geometry [65]. 119
Figure 81. Scaled intensity calculated for all source positions at the three distances and plotted as a function of the source distance from the slit edge in terms of Wp [63] [65]. 120
Figure 82. Normalized point spread functions for the seven different detector radii with no collimator in place. 122
Figure 83. Normalized Detector 51 F4 response per source particle for each of the 7 collimator radii (corresponding to different collimator thicknesses). The black dots are calculated $1/r$ and the red dots show the actual drop-off seen with the MCNP simulations. 123
Figure 84. Diagram of imager geometry without collimator used to conduct the backscatter and 1/r simulations. 124
Figure 85. Ratio of the neutrons backscattered into the detector to the ones leaving the detector as a function of the thickness of the outer borated polyethylene. 125
Figure 86. Plot of the normalized particle flux on the surface showing the fraction of particles backscattered into the detectors for each of the seven different radii. 126
Figure 87. Dimensions of the collimator components labeled. Steel is shown in grey and borated polyethylene is shown in green. 127
Figure 88. The error or the difference in mean free paths between the calculated transmission and the actual tranmission plotted against the actual transmission for all 512 geometries. 130

Figure 89. Error, or difference between the calculated and actual transmission plotted as a function of the borated polyethylene open fraction. 131
Figure 90. To understand how the stainless-steel affects the neutron transmission through the collimator, the slope values of the lines for each of the 16 cases was extracted and are plotted against the steel thickness. 134
Figure 91. Error, or difference between the calculated and actual transmission corrected for the stainless steel component plotted as a function of the borated polyethylene open fraction 135
Figure 92. Error values (difference between the calculated and actual transmission) after corrected for steel and streaming paths as a function of the borated polyethylene open fraction. 137
Figure 93. The log(noise) as a function of the effective thickness for each of the different cases simulated. 138
Figure 94. Extracted Y intercept values from the open fraction correction applied plot as a function of the borated polyethylene thickness. 140
Figure 95. Error between the calculated and actual transmission as a function of the borated polyethylene open fraction. The calculated transmission here accounts for all the correction factors. 140
Figure 96. Calculated thickness using all three correction factors in mean free paths versus the simulated actual thickness in mean free paths for all 512 cases. 141
Figure 97. Image of a 17 × 17 fuel assembly with the two components making up the signal highlighted. In the left image, a single pin is shown, and on the right, the area around the pin, the “halo” is highlighted [63]. 143
Figure 98. Pictorial of the SNR equation used to evaluate all the geometries with sinograms [65]. 144
Figure 99. SNR values for all 512 cases plotted against the geometric mean (cm) of the slit widths. 145
Figure 100. SNR for all 512 cases plotted against the geometric mean (cm) of the slits. The case with the least amount of borated polyethylene (10cm steel and 30 cm borated polyethylene) and the most amount of borated polyethylene (5 cm steel and 50 cm borated polyethylene) are highlighted. 147
Figure 101. The SNRs for all 512 geometries plotted against the maximum gamma exposures for each configuration. The line defining the 500 R/hr operational limit for the detectors is shown on the plot as well. 148
Figure 102. SNR values for the four cases with the thickest (55cm) and thinnest (40cm) collimator configurations as a function of the maximum exposure. 150
Figure 103. SNR values for the 10 cm steel and 30 cm borated polyethylene case broken up by parallel slits, tapered slits with inner slit widths of 1 mm, 2 mm, 2.5 mm, and 3 mm. A line of fit (yellow) shows what the SNR would scale as if the inner slit width remained at 3 mm and the outer slit width were increased beyond 5 mm. 150
Figure 104. Photos of the final detector module with 24 rows of straws. (Top) the view of the detector circuitry with the top open. (Bottom) The outer view of the detector module aluminum casing and the 6 readout ports [57]. 152

Figure 105. MCNP model of a single detector module in the final geometry. A single module contains 24 rows of 8 straws, and the imager contains 12 modules, or 288 rows of straws [57]. 153
Figure 106. Close-up of two detector modules showing the Al walls (purple), air gap (pink), and the Cd layer (green). 154
Figure 107. Close-up of the final imager geometry in MCNP. The slits corresponding to the first (1) detector and last (96) are labeled in the picture, as are the first and last rows as constructed in MCNP. 155
Figure 108. Diagram showing how the projected width for a tapered slit is calculated for a source at a specific perpendicular distance from the slit. 157
Figure 109. Scaled intensity at Detector 49 for a source moved perpendicular to a single slit at three different distances (5.08, 10.08, and 20.16 cm). 157
Figure 110. Scaled intensity calculated using the MCNP results plotted against the calculated average path length for a ^{244}Cm line source moved perpendicular to a single slit 5.04 cm away from the slit opening. 158
Figure 111. Scaled intensity calculated using the MCNP results plotted against the calculated average path length for a ^{244}Cm line source moved perpendicular to a single slit 10.08 cm away from the slit opening. 159
Figure 112. Scaled intensity calculated using the MCNP results plotted against the calculated average path length for a ^{244}Cm line source moved perpendicular to a single slit 20.16 cm away from the slit opening. 159
Figure 113. Response of all detector rows for 96 simulations where a ^{244}Cm source was shot down each of the 96 slits in turn. The row numbers were adjusted so that for a given slit the source was being shot down, the row was renumbered as 0 to make it easier to visualize the detectors at which the signals peak and show that not all slits point directly perpendicular into the row of interest so the signal peaks at the neighboring row. 161
Figure 114. Plot of the FWHM (in unites of detector rows) of the two Gaussian curves against one another for each of the 96 curves. 163
Figure 115. Centroid values for the first and second Gaussian terms calculated for all 96 slits. 164
Figure 116. FWHM values of the first and second Gaussian curves making up the data that has centroid values $b1$and $b2$ between +1 and -1. 165
Figure 117. Calculated FWHM using the custom double Gaussian equation for all 96 simulations. 167
Figure 118. Data for source pointing down slit 5 (black points) along with the custom double Gaussian fit (blue). 168
Figure 119. Centroid values for curves generated for source pointing down each of the 96 slits. The centroid values increase from -1 to +1 as the slit numbers increase. 169
Figure 120. Point spread function for a ^{244}Cm line source placed close to the origin (17.5cm from the slit 49 opening). 172
Figure 121. The MCNP effective thickness in mean free paths plotted against the calculated effective thickness using Equation (33) for 10 cm steel and 30 cm borated polyethylene. Each of the 32 points corresponds to a different slit width case simulated. 173

Figure 122. Closed fraction of the collimator seen by each of the 288 detector rows as calculated using Equation (33), the constants from Table 15, and the borated polyethylene thickness of 29.523 cm. 175
Figure 123. Calculated effective thickness and the MCNP effective thickness in mean free paths seen for each of the detector rows. 177
Figure 124. Detector response per source particle from the MCNP simulation (blue), and the calculated collimator penetration (red)..... 178
Figure 125. (Left) diagram of the collimator with 96 slits with a slit width of 1.1 cm. This shows how extending the slit width to larger sizes requires that more of the collimator be removed. (Right) Diagram showing what the collimator with 96 tapered slits looks like with 3 mm inner slit width and 8 mm outer slit width. 179
Figure 126. Detector response registered at the detector (row 158) pointing at slit 49 for a ^{244}Cm source on the centerline 5 cm away for a variety of parallel slit widths ranging from 0.1 cm to 1.1 cm. 180
Figure 127. SNR for all 11 parallel slit cases and the final tapered slit design with 3mm inner slit width and 8mm outer slit width. 182
Figure 128. The red points are overlaid on a 17 ×17 fuel assembly lattice to show where the ^{244}Cm line sources were placed for the tomography simulations [57].. 184
Figure 129. Sinograms from a tomography simulation of five-line sources. The fact that we are able to isolate 5 threads in the sinogram proves that imaging with this geometry could be feasible [57]. 184
Figure 130. Reconstructed image using the sinogram data from the simulations of five line sources. 185
Figure 131. Diagram of a standard 17 ×17 fuel assembly used in the tomography simulations. The grey points correspond to fuel pins, the pink ones are empty guide tubes filled with air, and the yellow points are the positions where fuel pins were removed in the tomography simulations. 187
Figure 132. Sinograms from a tomography simulation of a standard 17 ×17 fuel assembly with five pins missing. 187
Figure 133. Plan view of the final imager geometry with 96 slits and a fuel assembly in the center with five pins removed. 188
Figure 134. (Top) Final detector module top view without the high voltage board. Here the 24 rows of straws with their corresponding preamplifiers are shown. (Middle) Readout board showing the 6 ethernet cable ports that are used to readout the signals from each straw. (Bottom) Top layer of the detector with various readouts and ports labeled. 190
Figure 135. Interface box that takes in the 24 LVDS signals from the 6 ethernet cables reading the 24 rows and sends the signals out in 2 ribbon cables that feed into a CAEN TDC. 191
Figure 136. Ribbon cables from the interface box feeding into the CAEN boards. (Not Shown) a 20KHz pulser was used for timing synchronization because of the way the post processing software was written. 192
Figure 137. Block diagram of the readout electronics from a single detector. 192
Figure 138. Measurement setup for the single slit experiment showing the single module, borated polyethylene collimator, the polyethylene shielding blocks, and the borated

aluminum sheets. The six ^{252}Cf pellets are present and aligned to the slit but are hidden in this setup. 194
Figure 139. The tubing with six 252Cf pellets taped to the center of the slit opening, and aligned to the middle of the collimator length-wise. The tubing was surrounded by polyethylene blocks to shield from neutrons escaping the source. 195
Figure 140. The three source positions used to acquire data for the single slit measurements. 195
Figure 141. Count rates with corresponding error bars for the background measurement. Count rates for each of the 24 rows are presented. 196
Figure 142. Count rate data for the source placed at the three different positions after subtracting the background contribution. 198
Figure 143. Normalized count rates for the source centered on the single slit corrected for background and collimator penetration from the measurements (blue), and the simulation data showing the spread of inter-detector scatter (red). 199

1. INTRODUCTION

In the field of international safeguards, there are many tools that the International Atomic Energy Agency (IAEA) uses to provide credible assurances that States are honoring their legal obligations to ensure that nuclear material is being used only for peaceful purposes [1]. Within the nuclear fuel cycle, safeguarding spent fuel is a high priority for the IAEA and the project presented in this dissertation aims to address an identified gap in the IAEA's current toolset. This chapter will set the stage by providing some safeguards context as it relates to spent fuel safeguards, the characteristics and signatures from spent fuel that are used for attribute testing, an overview of tomography and the advantages it can provide in spent fuel measurement, and an outline of the remainder of the document.

1.1. Safeguards Context

The IAEA's safeguards mission is to prevent the spread of nuclear weapons via early detection of the misuse or diversion of nuclear material and related technology. The international safeguards system is built to act as a confidence-building measure and an early warning mechanism to set in motion other responses by the international community if the need arises [2]. Spent fuel from nuclear reactors is an important aspect in a country's fuel cycle that needs to be safeguarded. A spent fuel assembly that has been discharged from a commercial power reactor (~40GWd/MTU burnup) contains about 1% plutonium (Pu). For a typical pressurized water reactor (PWR) assembly, this corresponds to approximately 5 kg of total elemental Pu, or slightly less than one-half of a significant quantity (SQ) of irradiated, direct use material [3]. Due to the sensitivity associated with the material contained in spent fuel, safeguarding the fuel assemblies at the spent fuel pools at facilities, during transportation, and at dry cask storage sites has been a continuing priority for the IAEA. Of the thousands of SQs that are under IAEA safeguards, the majority has originated from light water reactor (LWR) operation over the last 50 years [4]. The IAEA Safeguards Research and Development (R&D) Plan that was released in January 2018 states that a top priority R&D need for them is to "develop safeguards equipment to establish and maintain knowledge of spent fuel in shielding / storage / transport containers at all points in their life

cycle." [5] Ultimate disposition plans vary from country to country and, due to some countries lacking a final disposition pathway, there is an ever-increasing amount that accumulates at facilities. Due to the thousands of metric tons of heavy metal being discharged from nuclear reactors globally, countries like Finland and Sweden are taking the lead to develop underground repositories to store their used nuclear fuel [6] [7]. The three main aspects that influence how the IAEA safeguards LWRs are [4]:

- LWR fuel assemblies are considered items;
- LWR cores are periodically opened and emptied; and
- Spent fuel assemblies are stored in open pools.

The IAEA considers spent fuel storage facilities as an item facility, meaning that all nuclear material is contained in identifiable items (e.g. fuel assemblies, sealed canisters, spent fuel casks). In the case of spent fuel in pools, an individual spent fuel assembly is considered an item and IAEA safeguards are based on item accounting procedures which include item counting, identification, nondestructive assay (NDA), and containment and surveillance methods [8]. The normal core loading at a LWR occurs in 12 to 18 month intervals, during which spent fuel is transferred from the core to the storage ponds, where it is then verified by the IAEA inspector [8]. Starting in the 1980's, LWR operators were replacing leaking fuel rods during outages. Although most of the fuel elements remain untouched throughout the irradiation cycle, a small subset of pins is replaced or stripped out from fuel assemblies [4]. This complicates and calls into question the item-specific measurements performed because item accountancy is only satisfactory as long as the fuel assembly integrity can be assured [9]. One way to address the uncertainty associated with the item-specific approach is to measure and quantify the amount of nuclear material within each assembly, however this technique would be too difficult for the IAEA to reconcile differences between measurements and simulations. The primary reason for the difficulty in quantifying material is that determining the composition of the spent fuel is the limited accuracy of burnup codes that have uncertainties of a few percent. More sophisticated methods that do a better job of reducing the uncertainties in the material unaccounted for, or discrepancies between measurements and operator declarations, rely on destructive analysis techniques, which are

not possible on intact spent fuel assemblies destined for long term storage. As a result, the IAEA has to rely primarily on NDA techniques.

The main purpose of performing nuclear material accountancy using NDA and resolving inspector findings with operator records is to detect missing items or gross defects [10]. In 2010, the IAEA recognized that gross defects sampling plans alone are not sufficient and, to strengthen safeguards, it should rely more on partial defect testing to assure the inspectors that at least half (50%) of the fuel pins are present in the fuel assembly being inspected [11]. The stated IAEA policy is to perform verification on the spent fuel assembly or item prior to transfer to difficult to access storage [12]. The partial defect test as implemented by the IAEA currently only covers the diversion scenario where irradiated pins are extracted from the fuel completely or the pins are replaced with unirradiated material. A more complicated scenario where the pins are replaced and undergo subsequent irradiation is not within the detection scope of the current suite of partial defect safeguards tools. As a result, more advanced partial defect tools based on imaging techniques are being investigated and these will be discussed in Chapter 2. Since all fuel consolidation systems most likely have some mechanism for handling single pins that are either damaged or unacceptable for consolidation, a "trickle diversion" removing single pins over time could be possible and a successful safeguards tool should be able to detect single pin diversion [9]. The fast neutron emission tomography system presented in this dissertation aims to address this diversion scenario.

1.2. Spent Fuel

A typical spent fuel assembly is irradiated in high neutron fluxes within a reactor for 3 to 6 years and this changes the original isotopic content of the fuel (^{238}U, ^{235}U, and ^{16}O), and 4-7% of the initial mass is converted to other actinides or fission products [13]. The ability to calculate the spent fuel compositions when the design and operating conditions are well known is established, but if this information is unavailable, the amount of uncertainty is fairly large. This is often the case since reactor operators can vary the isotopic content in spent fuel by changing parameters such as [13]:

- Power level over time,
- Length of refueling outages,

- Location of fuel assemblies within the reactor core, which changes the burnup,
- Boron concentration circulating through the reactor as a function of time,
- Removal of an assembly for some cycles of operation, or
- When control blades are inserted.

Because of the high amount of variation an inspector could encounter in inspecting fuel assemblies, imaging techniques have the ability to provide insight into the completeness and irradiation history of fuel assemblies at the pin level that other existing methods do not. This section will cover the signatures and attributes from spent fuel that are normally used and the spent fuel assembly parameters that are used in this project to perform simulations detailed later in this dissertation.

1.2.1. Spent Fuel Signatures

In applying nuclear material accountancy, IAEA safeguards inspectors measure attributes or observables of spent fuel assemblies using non-destructive assay techniques. The attribute test, according to the IAEA Safeguards Glossary is a statistical test of a characteristic of an item to which the response is either a 'yes' or 'no' [14]. For spent fuel, this means that a 'yes' indicates the presence of radiation in a specified range, and a 'no' is indicative of a possible defect [4]. Typical attributes of spent fuel are gammas, spontaneous fission neutrons, and Cherenkov light emission. The gamma-rays from fission products and the neutrons from the transuranic nuclides mask the gamma-rays and neutrons from the U and Pu isotopes in the fuel; thus, instruments have to rely on indirect measurement techniques to perform material accountancy, and these are described below.

1.2.1.1. Cherenkov Light

The gamma rays from fission and activation products produce high speed electrons, and when they travel faster than the phase velocity of light in the spent fuel pond water, Cherenkov light is created. The most significant production of Cherenkov light is from high-energy fission product gamma-rays interacting with the fuel cladding or water [15]. The gamma-rays produce electrons and positrons by Compton scattering, pair production, and beta-plus decay. The light is a soft blue glow that can be used for safeguards monitoring when photographed using a tool such as the Digital Cherenkov Viewing Device (DCVD). A

more comprehensive discussion of the DCVD and its capabilities and limitations will be presented in Chapter 2. The absolute Cherenkov light intensity and its decay over time are correlated to the burnup of the pins in the fuel assembly [15].

1.2.1.2. Gamma-rays

Since the direct gammas from the U and Pu in the spent fuel are masked by the ones that originate from the fission products, for this reason the buildup of specific fission products can be used as a quantitative measure of the burnup of a fuel assembly [15]. For gamma spectroscopy, the gamma signature can be used to estimate burnup if certain criteria are met [16]:

- The gamma emitting fission product should have similar fission yields for the major U and Pu fissioning nuclides;
- The fission product itself must have a low neutron capture cross section;
- The fission product must have a relatively long half-life compared to the irradiation time; or
- The gammas being emitted must have high enough energy so that they can escape the fuel assembly without significant attenuation.

^{137}Cs is one of about 10 dominant gamma emitting fission products in spent fuel and is the most commonly used indicator of fuel burnup because its neutron absorption cross section and also its yields from ^{235}U and ^{239}Pu are about equal, as shown in Figure 1, which means the gamma ray emissions from this can be used to determine the total number of fissions [15]. The major isotopes that are gamma emitters a typical spent fuel assembly that can be measured are shown in Table 1.

In addition to the fission product yields of ^{137}Cs being about the same for both U and Pu, its long half-life and the fact that its concentration grows linearly with exposure makes it the best candidate for monitoring burnup as shown in Figure 2. The ^{137}Cs activity can be used to determine burnup with an accuracy of 1-4% for individual fuel pins [15]. The production of ^{137}Cs as a function of burnup is insensitive to irradiation history and initial enrichment, and, due to its long half-life, it can be used as a signature to measure fuels with longer cooling times [17]. In addition to ^{137}Cs, both ^{134}Cs and ^{154}Eu emit gamma rays that can be observed in the gamma spectrum from a typical spent fuel assembly [18].

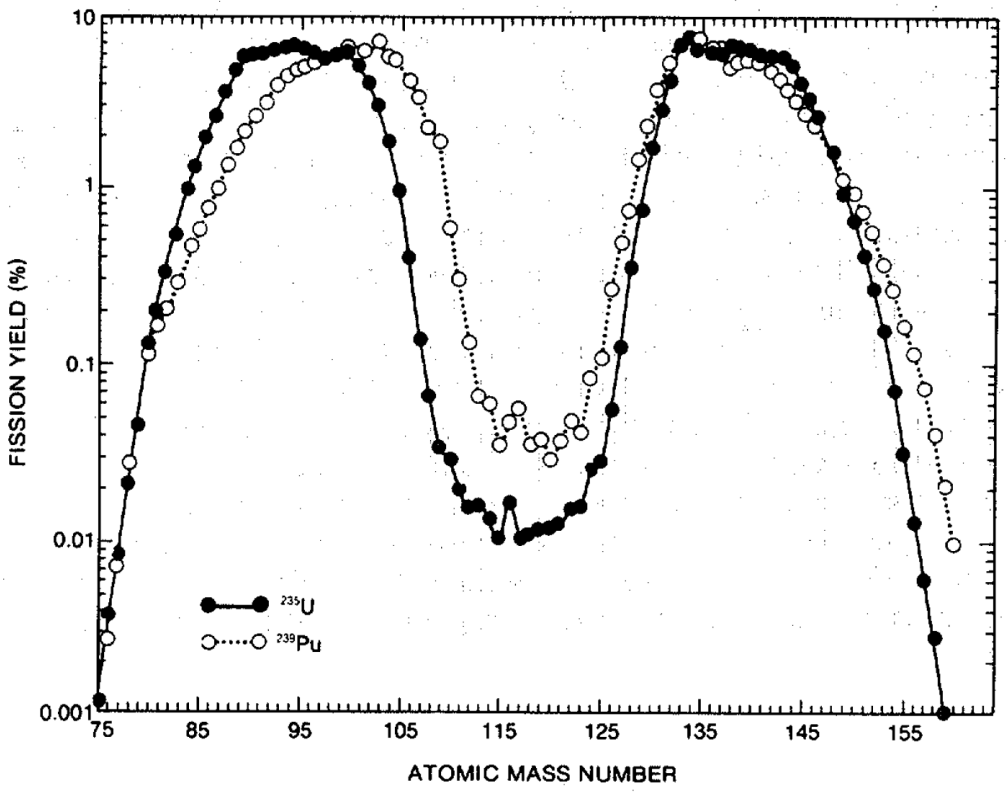


Figure 1. Fission product distribution for thermal fission of ^{235}U and ^{239}Pu [15].

Table 1. Major isotopes and their measurable gamma rays in a typical spent fuel assembly [17].

Fission Product Isotope	**Half-life**	**Fission Yield in ^{235}U (%)**	**Fission Yield in ^{239}Pu (%)**	**Gamma Energy (keV)**	**Branching Ratio (%)**
^{95}Zr	64 days	6.5	4.89	724.2 756.7	43.1 54.6
^{95}Nb	35 days	6.5	4.89	765.8	99.8
^{103}Ru	39.4 days	3.04	6.95	497.1 610.3	86.4 5.4
^{106}Ru-Rh	366.4 days	0.40	4.28	622.2 1050.5	9.8 1.6
^{134}Cs	2.06 years	1.27×10^{-5}	9.89×10^{-4}	604.7 795.8 801.1 1167.9 1365.1	97.6 85.4 8.7 1.8 3.0
^{137}Cs	30.17 years	6.22	6.69	661.6	85.1
^{144}Ce-Pr	284.5 days	5.48	3.74	696.5 1489.2 2185.6	1.3 0.3 0.7
^{154}Eu	8.5 years	2.69×10^{-6}	9.22×10^{-5}	996.3 1004.8 1274.4	10.3 17.4 35.5

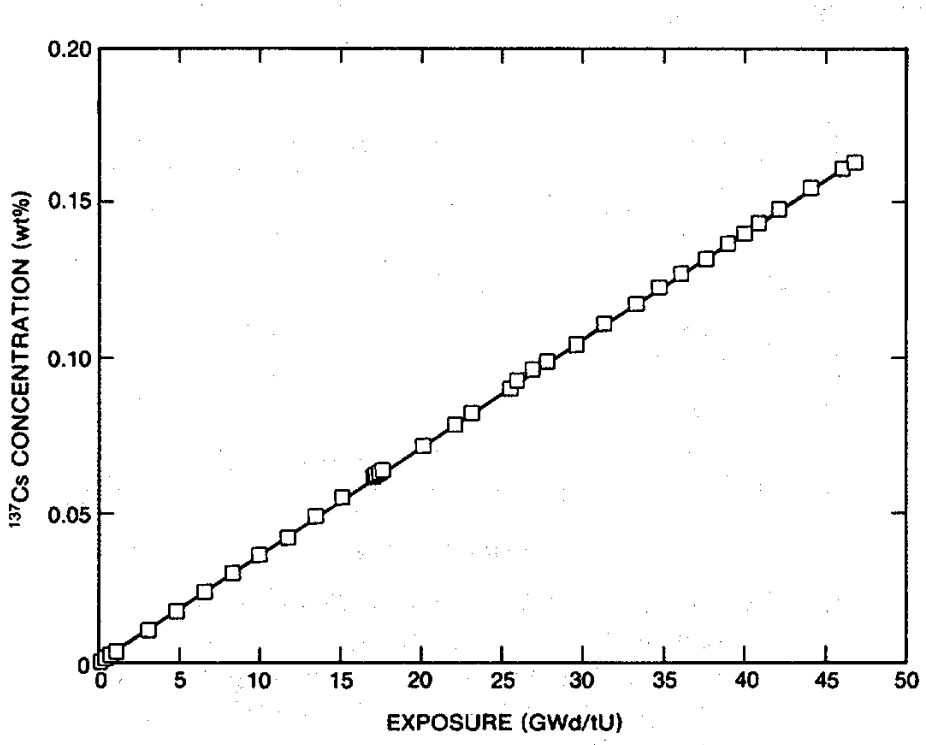


Figure 2. ^{137}Cs fission product concentration (weight % of initial U concentration) as a function of exposure or burnup (GWd/tU) [15].

The ^{137}Cs is produced via neutron capture in ^{136}Xe and from beta decay of ^{137}I to ^{137}Xe, which decays to ^{137}Cs. Another method to estimate the burnup of spent fuel is by using the ratios of ^{134}Cs /^{137}Cs and ^{154}Eu/^{137}Cs. The ^{134}Cs is produced primarily from resonance absorption of neutrons by ^{133}Cs and has a quadratic relationship to burnup. At higher fuel enrichments, there is a smaller amount of ^{134}Cs produced because a fewer number of neutrons are needed at high enrichments, so fewer neutrons exist to be captured by ^{133}Cs and contribute to production of ^{134}Cs. The production of ^{154}Eu is more complicated and can be produced by 20 different reaction chains, including (n,γ) reaction with ^{153}Eu [16] [17].

1.2.1.3. Neutrons

The neutron signature from spent fuel offers an advantage over the gamma signatures in that the fast neutrons emitted are more penetrating and do not scatter or get absorbed as much within the fuel assembly as they travel out. Spent fuel normally has a relatively high neutron

emission rate (on the order of 10^7 to 10^8 n/s per assembly) [16]. The uranium in the fuel captures neutrons, and, as a result, neutron emitting transuranics build up in spent fuel. The main sources of neutrons in fuel assemblies are ^{244}Cm, ^{242}Cm, ^{240}Pu, ^{238}Pu, and ^{242}Pu. The emission rate of ^{242}Cm falls as a function of cooling time due to its short half-life, thus not making it very useful for monitoring purposes. Figure 3 shows the emission rates for the five primary neutron emitters in spent fuel as a function of the assembly cooling time for a typical PWR fuel assembly with a burnup of 31.5 GWd/tU [15]. From the image, it can be seen that at longer cooling times the total neutron rate is mostly dominated by the ^{244}Cm emission rate and has a half-life of about 18.2 years. Many of these neutron emitters produce neutrons via spontaneous fission reactions or (α,n) reactions. The neutrons from photofission and photoneutron reactions can be excluded since their intensity is insignificant in comparison [19]. In heavy nuclides, the probability that the nucleus will spontaneously fission due to repulsive forces being strong is high. For U and Pu, the spontaneous fission rate is fairly low (except for the isotopes ^{238}Pu, ^{240}Pu, and ^{242}Pu), but the spontaneous fission yields for ^{242}Cm and ^{244}Cm are several orders of magnitude higher, as seen in Table 2.

Overall, the neutron emission from spent nuclear fuel is dominated by the spontaneous fission of ^{244}Cm. A single fuel pin from an assembly that has been exposed to 40 GWd/tU has a total neutron emission rate of 2.55 x 10^5 neutrons s^{-1} m^{-1}. The contribution from ^{244}Cm makes up most of that and can be seen in Figure 4. The ^{244}Cm emission rate per second per meter per pin is shown for a range of burnups for fuel with 4% initial enrichment, and the rate increases as a function of burnup. The total neutron emission rate for a single pin (^{244}Cm and other fission products) is shown in red and is not much higher than the ^{244}Cm emission rate fit curve, indicating that most of the neutrons emitted from spent fuel can be attributed to emissions from ^{244}Cm. The goal of this project is to use the fast neutron emission from ^{244}Cm as the chosen attribute to perform tomography and verify the completeness of a fuel assembly on a pin-by-pin basis. The following sections will detail why the ^{244}Cm signature is a better safeguards approach to verify completeness than using neutron emissions to quantify Pu in the spent fuel.

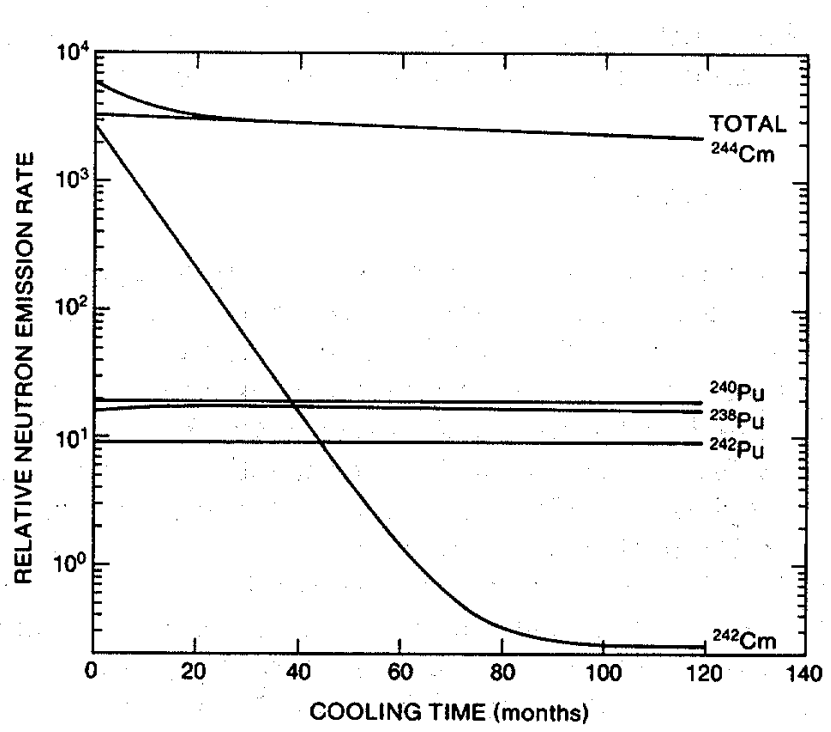


Figure 3. The main neutron sources from a PWR fuel assembly and their emission rates as a function of cooling time [15].

Table 2. Spontaneous fission and (α,n) yields for the major neutron emitting isotopes in spent fuel [20].

Isotope	***Spontaneous Fission Yield [n(SF)/s-tU]***	***(α,n) Yield [n(α,n)/s-tU]***
^{238}Pu	3.67 x 10^5	2.48 x 10^6
^{240}Pu	2.02 x 10^6	4.66 x 10^5
^{242}Pu	8.16 x 10^5	
^{242}Cm	5.44 x 10^7	1.15 x 10^7
^{244}Cm	2.07 x 10^8	1.88 x 10^6

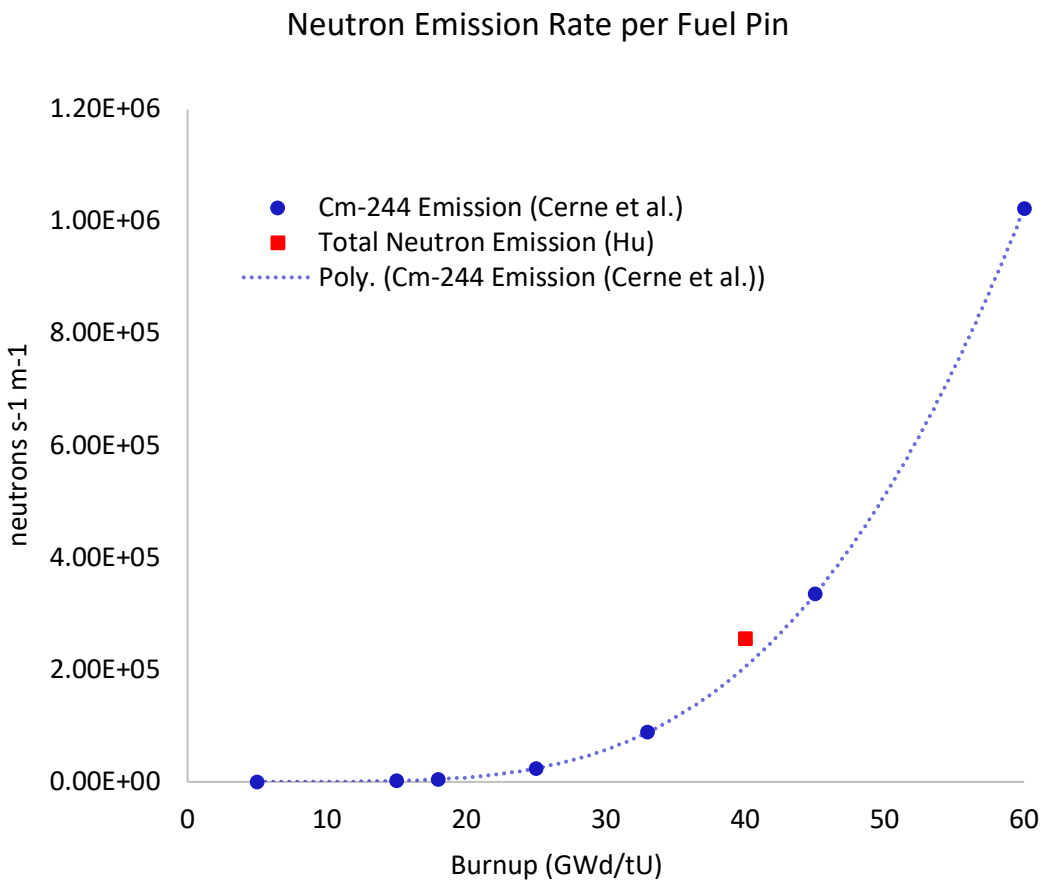


Figure 4. Neutron rate per fuel rod due to Cm-244 as a function of burnup or exposure within an average commercial PWR (shown for 4% initial enrichment and 2-year cooling time) [21].

1.2.2. Pu vs. Cm

Traditional methods of measuring neutrons from spent fuel result in the measurement of ^{239}Pu content. However, Pu content is only known to a few percent in burnup codes, and the effort to resolve any discrepancies in the operator declaration would be too difficult. Figure 5 shows that the Pu content saturates with increased burnup or exposure. This means that instruments that use this technique for spent fuel accountancy would be minimally sensitive to rod replacements made after the first cycle in a reactor. Unlike the Pu content, the ^{244}Cm does not saturate as a function of burnup as shown in Figure 4, so using this as the signature of choice would enable an imager to be sensitive to rod replacements made after the first cycle. For the initial simulations of the neutron response and the point spread functions presented in this dissertation, a line source of ^{244}Cm was used.

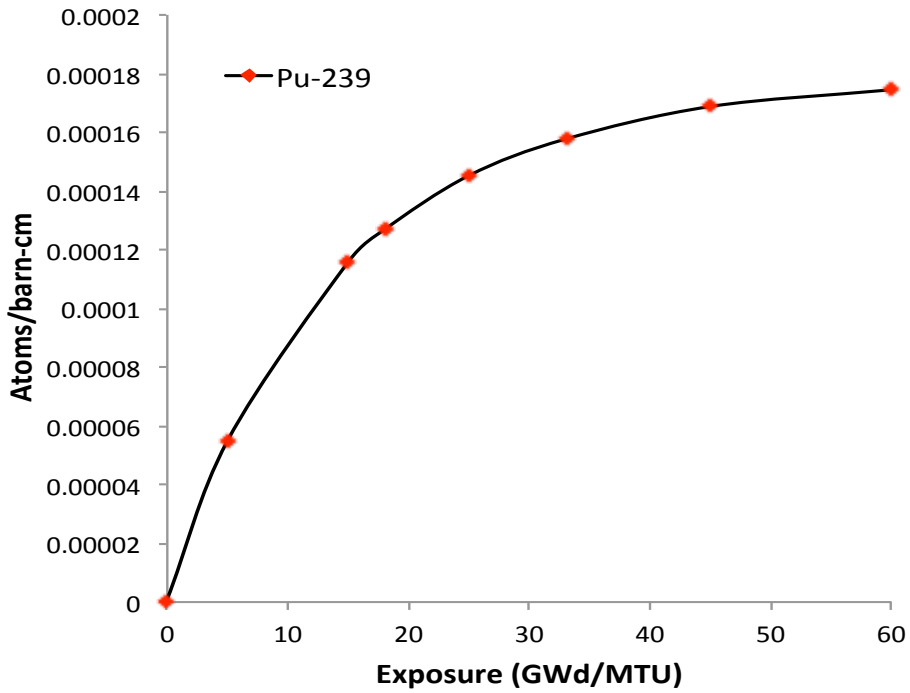


Figure 5. ^{239}Pu content as a function of fuel assembly burnup or exposure [21].

1.2.3. Fuel Assembly Parameters

A typical LWR fuel pin is made up of a stack of UO_2 pellets in a zircalloy cladding, which is a long cylindrical tube that is about 4 m tall and ~1 cm in diameter. The dimensions of the assembly itself, the pitch, and the cladding thickness depend on the type of fuel [22]. There are currently over 440 nuclear reactors operating worldwide, and, as a result, over 10,000 tons of heavy metal are unloaded from these reactors each year. The majority of countries that generate electricity using nuclear power do not possess reprocessing capabilities or any spent fuel disposition pathway. As a result, they have adopted a "wait and see" position, making spent fuel storage and repositories a likely solution [23]. Typical pressurized water reactor (PWR) lattices are 17×17 in dimension with 264 fuel pins, and boiling water reactor (BWR) lattices are 8×8 in dimension with 63 fuel pins. To maintain efficient reactor performance, about a third of the spent fuel is removed every year or 18 months, to be replaced with fresh fuel. The length of the fuel cycle is correlated with the use of burnable absorbers in the fuel, which also allows for higher burn-ups [24]. Westinghouse-type fuel assemblies can be 14×14, 15×15, or 17×17 arrays, depending on the plant design. The 14×14 and 15×15 arrays each contain 20 guide tubes and a central instrument tube. The 17×17 array contains 24 guide tubes and a central instrument tube [25]. Typical fresh fuel enrichments range from 3-5%, and for calculations in this work involving simulated spent fuel, an initial enrichment of 4% was assumed in a 17×17 PWR lattice. Figure 6 shows the neutron emission rate [neutron s^{-1} m^{-1}] on a pin by pin basis for the fuel assembly used for simulations in this study. The initial enrichment is 4%, exposed to 40 GWd/tU burnup, and 1-year cooling time.

The empty pin slots correspond to locations where the control rods go, and the gray pins correspond to the gadolinium (Gd) rods used as burnable poisons. These rods are inserted into the fuel lattice since they have a higher absorption cross section for neutrons than ^{235}U, compensating for excess reactivity during the early stages of core lifetime. The absorbers are meant to burn out or transmute faster than the fuel burns, so that later in the core life they can contribute negligible negative reactivity. Burnable poisons allow for larger initial fuel inventories, so the core lifetime is increased without any decrease in control safety [26].

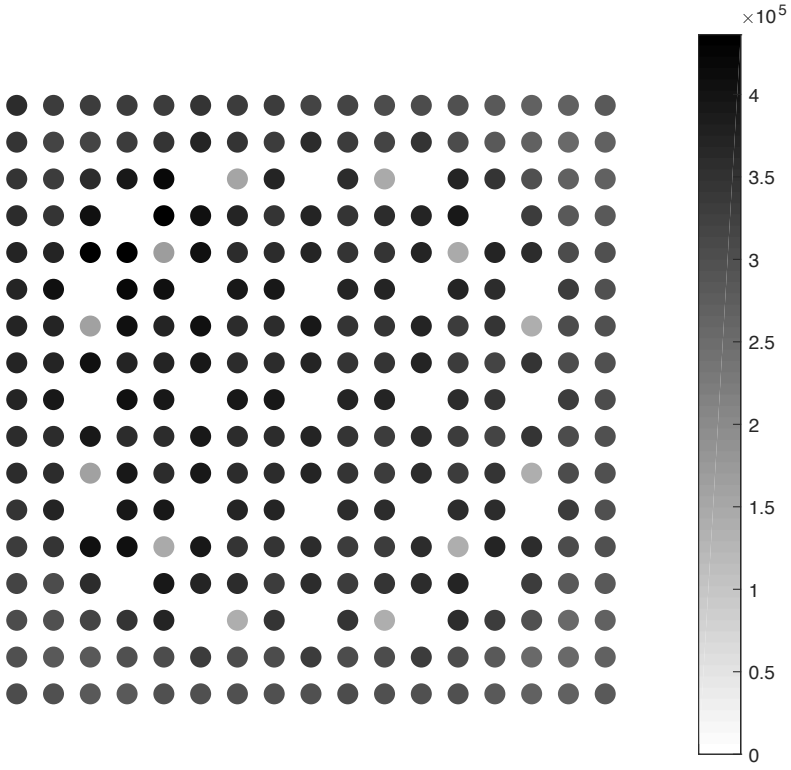


Figure 6. Neutron count rate [neutrons per second per meter] by pin for a typical 17 x 17 fuel assembly with initial enrichment of 4%, 40 GWd/tU burnup, and a 1 year cooling time.

1.3. Tomography Overview

Computed tomography (CT) is a common technique used in medical physics. Tomography is the mechanism by which cross-sectional imaging (in a 2D case) of an object is conducted by either transmission or emission data collected by illuminating the object from many different directions [27]. X-ray CT has been commonplace for decades and emission tomography such as positron emission tomography (PET) and single photon emission computed tomography (SPECT) are the primary techniques used in the medical field. The conventional active or transmission CT scanners measure the attenuating effects of an object using an incident interrogating beam that travels in a straight path. In traditional tomography

methods, a source interrogates the object to be imaged, and the quantity that is reconstructed is the line integral of the attenuation paths of the particles, as described by the Beer-Lambert law [28]

$$g[S(E),L] = \int_L f[S(E),x]du = ln\left[\frac{I_0[S(E),L]}{I[S(E),L]}\right] \quad (1)$$

where *du* is the incremental distance along *L* (the ray path) [28]. Conventional tomography, therefore, is attenuation-based and relies on lines of response or paths through the object. The traditional method involves having an external source of particles that is collimated by slits, apertures, or collimator systems to interrogate the object [29]. A diagram of a general CT is shown in Figure 7 [30]. A radiation source (photons, neutrons, etc.) is collimated such that a beam with intensity I_0 interrogates the sample. The particles that are transmitted through the sample have an intensity *I*, which is then recorded in the detector array on the other side of the sample. The sample is scanned in a large number of positions and is rotated and translated so that the attenuation of the source particles is measured for each projection by the detectors. This data is then reconstructed into an image where the different attenuation coefficients in the materials in the sample correspond to different intensities.

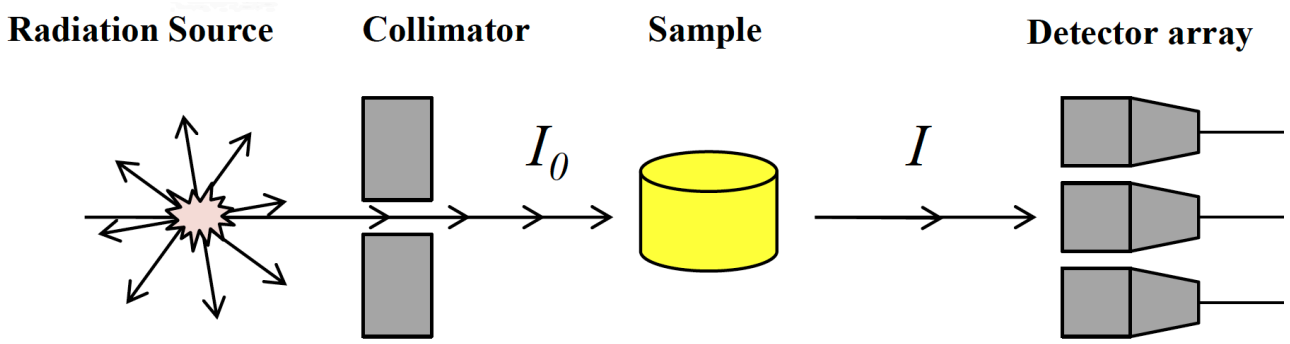


Figure 7. General CT measurement set up where a radiation source is collimated and the beam interrogates the sample of interest. The sample is then rotated so the detector array can acquire data from all projections [30].

Neutrons and photons interact differently in matter and as a result, they can provide complimentary information about the structure of the material under investigation. Depending on the energy and the atomic number Z of the elements in the material, photons will interact by means of the photoelectric effect, Compton scattering, or pair production. When neutrons interact, they may undertake a variety of nuclear processes including elastic scattering, inelastic scattering, radiative neutron capture, induced fission, and other types of nuclear reactions such as (n, p), (n, d), (n, α), etc. For some elements with low Z, the interaction cross section for elastic scattering is relatively high [32]. Due to the varying attenuation coefficients, neutron and gamma-ray tomography can yield different results when imaging the same objects [31]. Traditional external sources used in neutron tomography include nuclear reactors, accelerators or spallation sources, neutron generators, and radioactive sources like AmBe or ^{252}Cf [30]. Neutron tomography systems typically consist of a source of neutrons, a collimator, a means for gathering a variety of projections of a given sample (using a rotating platform), and a detector system [32]. This work aims to use passive emission tomography – the passive emissions from spent fuel instead of an external source to reconstruct an image. The identification of nuclear material is often based on the detection of the radiation they emit, and this can be done in a passive method depending on the signature or attribute [31]. Emission tomography does not require an external source to image the object since the object being inspected emits the radiation necessary. In this method, a collimator is used to isolate the lines of response through the object similar to the attenuation-based method. In the case of passive fast neutron emission tomography, a line of response refers to a path through the inspected object along which an observable (such as neutron emission activity) can be integrated, rather than the traditional way of measuring the intensity of the attenuated beam. The neutron counts in the detectors at the end of each collimator slit correspond to an integral of neutron activity along the corresponding path. The end result after reconstructing this data is an image that shows the amount of activity at each position within the fuel assembly, instead of an image showing the contrast in attenuation. Figure 8 shows the concept is essentially the same since in the image on the left the level of attenuation is measured over the lines of response, and in the image on the right the neutron activity is integrated over the lines of response [29] [33].

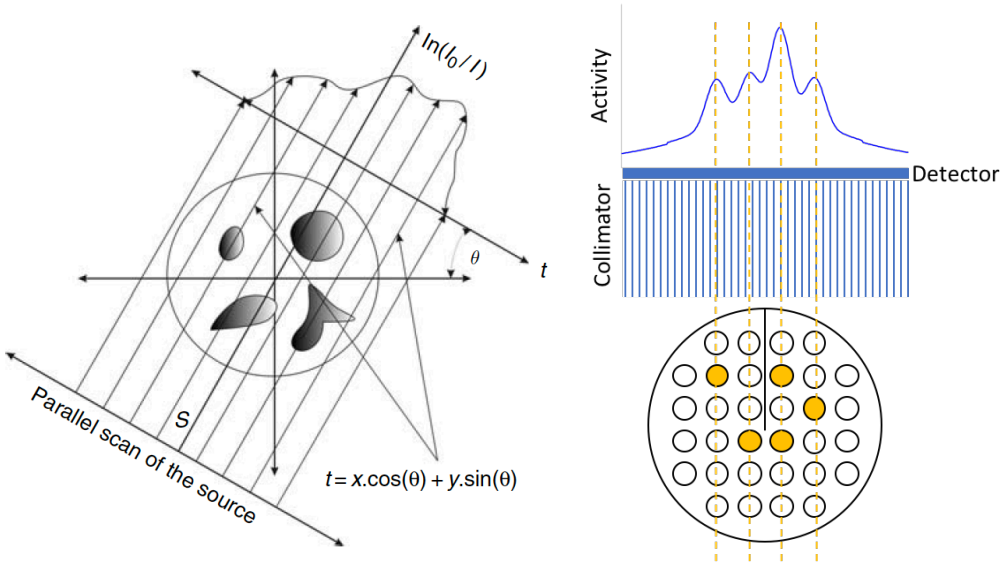


Figure 8. The image on the left shows the scanning of a slice where traditional tomography is performed (attenuation based) where the lines of response are formed by the transmitted intensity [29]. The image on the right shows the method of performing emission tomography where the inspection object is the source and a collimator is used to isolate lines of response along which the activity is measured [33].

1.3.1. Conventional emission tomography methods

In neutron imaging, due to neutron scattering, large detectors are required to isolate neutrons along a path (especially if moderation is required). There are currently two design that allow for the use of large detectors, a parallel slit design and a radial collimator system. Figure 9 shows a concept diagram of the two designs adapted for spent fuel measurement applications. On the left is the parallel slit design where the sample is rotated, and at each projection requires fine scanning with the detectors to gather projections at all 360°. The benefit of this is that it is a practical size, but the downside of this design is the measurement time would be too long to be of practical use in the field. The second option, shown on the right, is the radial collimator option where there are many large detectors. The neutrons from the fuel assembly are collimated through a slit, and the radial collimator points to several detectors. Here the sample would need to be rotated to gather projections at all angles, but due to the larger number of detectors, it would take less time to conduct a single measurement in comparison with the parallel slit option. The downside to this design is that it would be too

large of a physical footprint to be practical to implement. Ultimately the imager must be practical for safeguards use, it is important to understand the various challenges that need to be addressed.

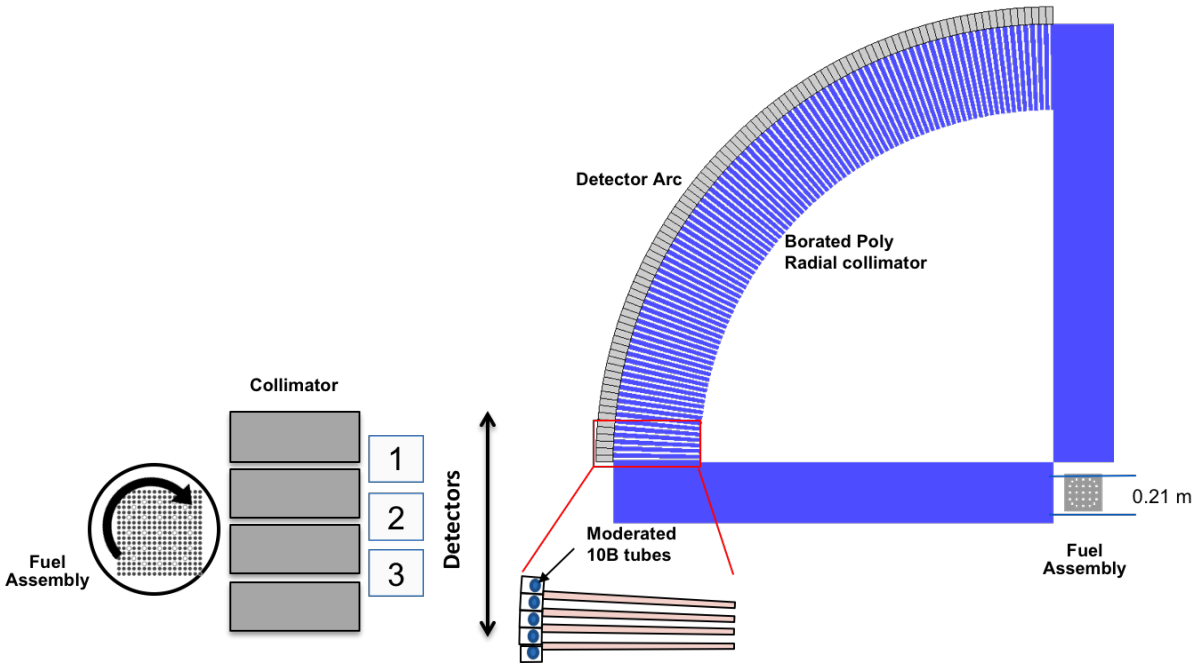


Figure 9. Diagram of sample conventional imager designs adapted for use to measure spent fuel using emission tomography [34]. See text for details.

1.3.2. Application challenges

Several challenges need to be considered when developing the physics design for a practical and feasible imaging system with which one may measure spent fuel. These challenges include maintaining detection efficiency, reconstructing an image with sufficient resolution, minimizing the gamma exposures at the detector, and limiting the design to a practical size. The neutron source strength from the fuel assembly is fairly modest relative to the gamma strength, which necessitates the efficient use of the neutrons that are emitted from the spent fuel. The efficiency can be optimized by placing larger detectors closer to the fuel assembly, and by increasing the collimator slit widths. Using larger slit widths with a traditional parallel slit design would be unfeasible since the open fraction would detract from the collimation effectiveness of the other slits. Spatial resolution in the case of imaging spent fuel pertains to the ability to resolve individual fuel pins. In order to resolve individual pins, assuming a Westinghouse 17 x 17 lattice fuel assembly in which pins have a diameter of about a centimeter and pitch of 1.27 cm, the collimator slits need to be small enough to resolve the gaps between the fuel pins, and the collimator needs to be thick enough so that a line of response can be created. The other factor to keep in mind is mitigating the gamma exposures at the detector. In order to do so, a collimator that moderates or absorbs neutrons is not sufficient. A high-Z shielding component needs to be incorporated in order to reduce the high gamma exposures from spent fuel. Figure 10 shows the gamma exposures 1 m from PWR and CANDU fuel assemblies over a range of cooling times [35]. At cooling times less than 5 years, the exposure is around 100 Sv/hr, which corresponds to 10,000 Rad/hr. This rate is too high for detectors to operate in reasonably; hence, shielding with lead, tungsten, or stainless steel is required in addition to the low-Z neutron moderation material.

Finally, to be accepted into a facility for measurements, the imager needs to be a compact size so it doesn't disrupt operations. The most compact geometry is a ring geometry, which is what the imager design presented in this work is based on. It is possible to achieve fast neutron tomography having the desired resolution provided each line of response sufficiently isolates a path through the object, the object is sampled with a sufficient number of lines of response, and there are a sufficient number of views through the object to invert measured data to form an image.

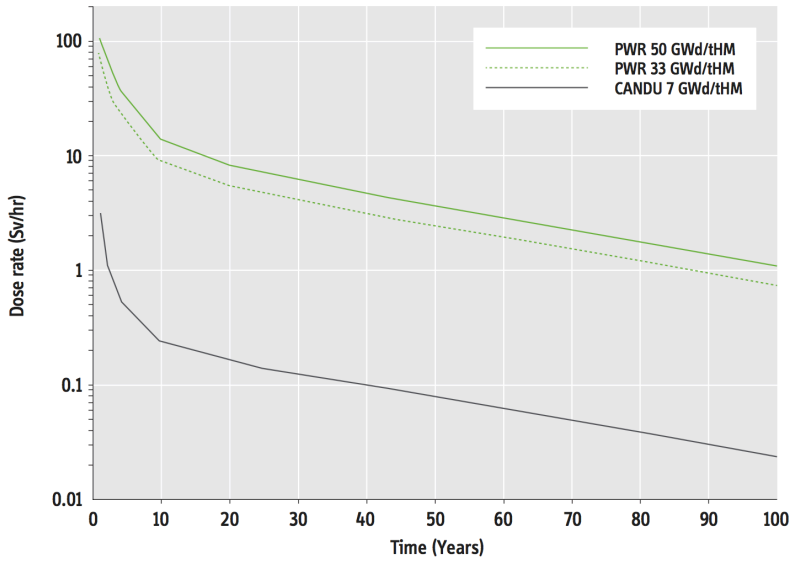


Figure 10. Exposures at 1 meter perpendicular to the center of a PWR or CANDU fuel assembly as a function of cooling time [35].

1.4. Overview of Dissertation

The work presented in this dissertation includes an overview of the imager design concept, parameters considered, simulations conducted, and gamma and neutron experiments conducted at Oak Ridge National Laboratory (ORNL) to characterize the neutron detectors used. Chapter 2 will include a literature review on prior research and work that has gone into developing the tools currently used by the IAEA and in producing viable tomography systems for spent fuel accountancy for safeguards. Chapter 3 will present the Monte Carlo simulation results of the gamma exposures from the various imager designs considered with a full up fuel assembly. Chapter 4 will cover the Monte Carlo simulation results of the neutron response of the various imager designs considered using a line source. An overview of the measurements conducted with the prototype detector at ORNL in gamma radiation fields will be provided in Chapter 5. This chapter will also include measurements of inter-detector scatter with a prototype detector. Chapter 6 will cover simulated reconstruction results with the final imager design selected to be built and include the neutron response to a full fuel assembly. Chapter 7 will discuss the conclusions and future work.

2. LITERATURE REVIEW

Since safeguarding spent fuel is a high priority for the IAEA, tools have been developed to assay spent fuel and there are tools that are being investigated currently to address the partial defect challenge. This chapter will focus on the tools that are currently used by the IAEA in spent fuel safeguards verification and the efforts underway to develop technologies to address the partial defect problem presented in Chapter 1. Additionally, this chapter will cover the existing gaps in technology, and the novel contributions of the project presented in this dissertation.

2.1. Verification Methods

There are two types of detection levels that the IAEA implements when inspecting spent fuel: gross and partial defect tests. A gross defect is detected when an entire fuel assembly is missing or has been substituted with a dummy or fake assembly. A partial defect test confirms whether or not more than 50% of the pins are missing from a single fuel assembly [36]. The IAEA is interested in safeguarding the fissile material in spent fuel since it can be a primary source of ^{239}Pu and ^{235}U (^{233}U for thorium fuel cycles). NDA methods can be applied in verification of spent fuel in cases where continuity of knowledge is lost or interrupted, to verify records with depletion calculations made with burnup codes, and as a deterrence to possible diversion [37]. As mentioned in Chapter 1, the stated IAEA policy is to perform verification on the spent fuel assembly or item prior to transfer to a difficult-to-access storage [12]. The following sections will describe the technologies used to perform gross and partial defect testing, as well as their associated limitations.

2.2. Gross Measurement Techniques

Gross defect refers to an item or a batch that has been falsified to the largest extent possible so that all or most of the declared material is missing [14]. The IAEA has approved the use of several instruments to perform gross defect testing of spent fuel based on gross gamma and neutron counting. These are described below:

2.2.1. Fork Detector Irradiated Fuel Measuring System (FDET)

The FDET system is one of the most commonly used tools in spent fuel measurements by the IAEA. It is a U-shaped device that measures spent fuel assemblies individually under water. The components include a detector head and gamma/ neutron detector electronics. There are two different types of detector heads that can be used based on the type of fuel being measured (boiling water reactor or pressurized water reactor fuel). The detectors in the detector head consist of four gas-filled fission chamber proportional counters as neutron detectors and two gas filled ionization chambers as the gamma-ray detectors. Figure 11 shows an image of the system performing a measurement of a spent fuel assembly under water [10]. Figure 12 shows the location of the gamma and neutron detectors in each of the detection arms.

The ratio of the gross neutron (from ^{244}Cm) and gamma-ray count rates (from ^{137}Cs) to the fourth power are used to verify the spent fuel assemblies. The FDET works by evaluating the consistency of signatures within a population of items. The benefit of the device is that it is fairly easy to use and can be installed in facilities, but it is limited in its ability to detect diversion of pins since the ratio of the neutron to gamma counts is not sensitive enough if the fuel pins are carefully rearranged. Figure 13 shows the neutron-to-gamma ratio results from a fork detector measurement for various configurations. The data on the Y-axis is the ratio value normalized to the ratio of a complete fuel assembly. The assemblies shown here have 50% of the fuel pins removed. A ratio of a 100% indicates that the signal from the configuration is similar to that of a full configuration [38]. Configurations 69 and 70 have signals similar to a complete fuel assembly even with half the rods removed. A diagram of the two configurations is shown in Figure 14 where the fuel pins have been removed in a homogeneous way. The results show that an inspector would not be able to easily tell the difference between a full assembly and one with half the pins removed [38].

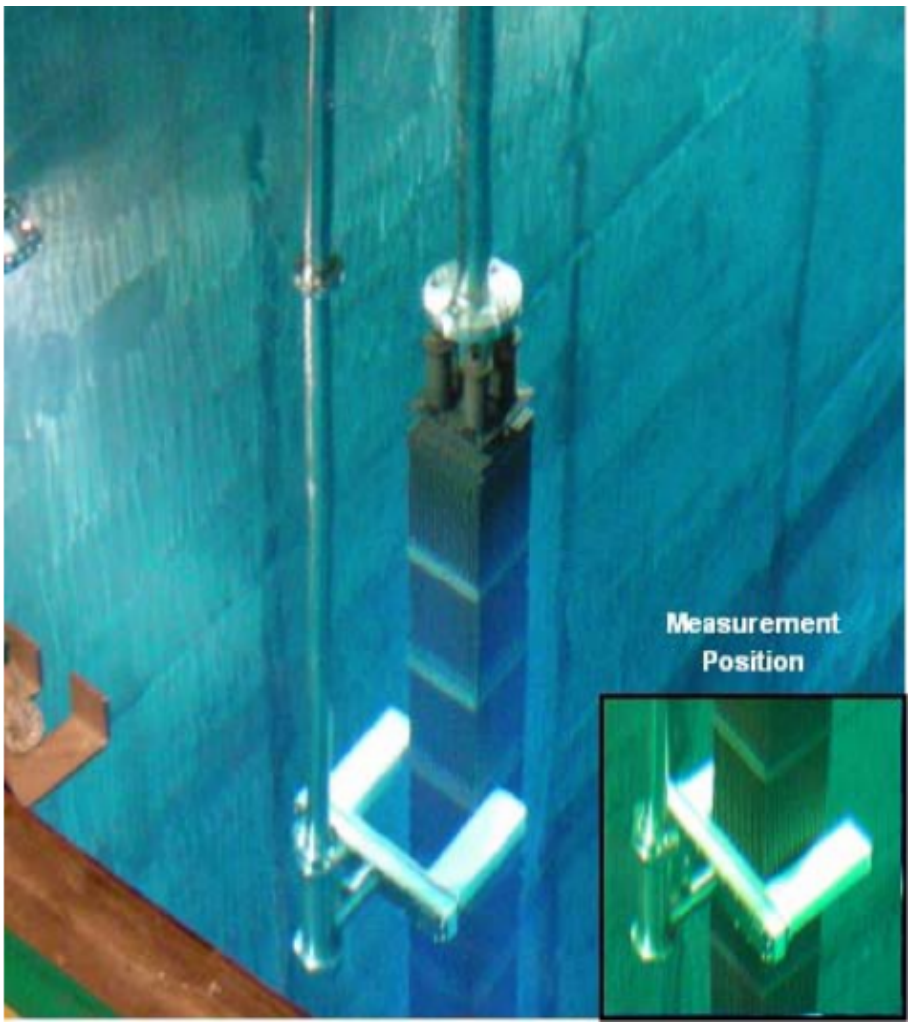


Figure 11. Fork detector irradiated fuel measuring system (FDET) [10].

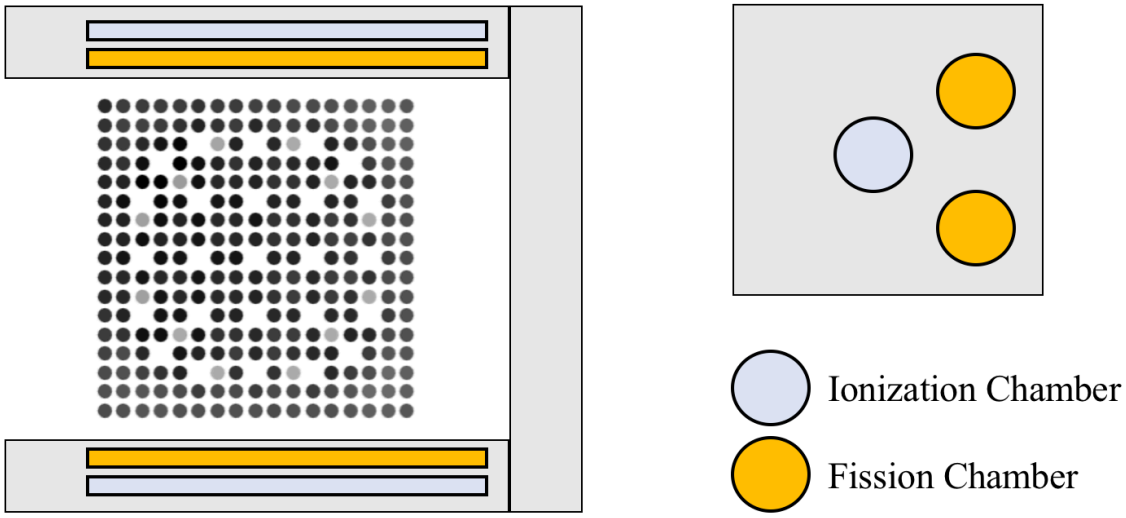


Figure 12. (Left) View from the top of the fork detector with detector arms around a 17x17 fuel assembly being inspected. (Right) the vertical cross-sectional view of the fork detectors showing where the fission chambers and ion chamber sit [38].

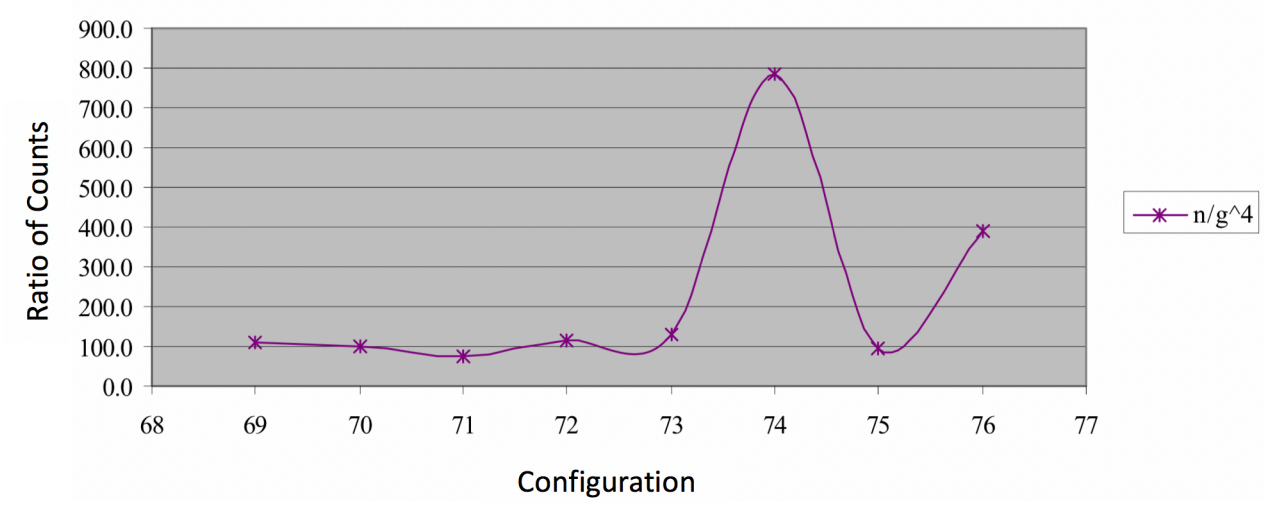


Figure 13. Results of the $Nc/(Gc)^4$ ratio, normalized to the ratio of a full configuration, for several configurations of spent fuel with 50% of the fuel pins missing [38].

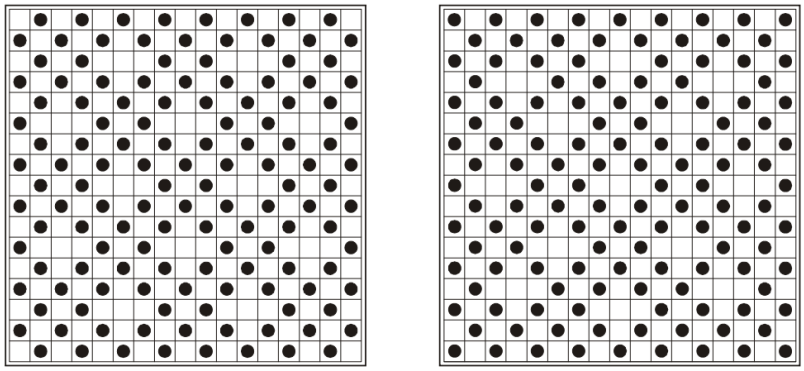


Figure 14. Configuration 69 (left) and 70 (right), where 50% of the fuel pins has been removed in a homogeneous way [38].

2.2.2. Safeguards MOX python (SMOPY)

The SMOPY device uses gross neutron counts from a fission chamber and low-resolution gamma spectroscopy from a lead-shielded CZT (cadmium-zinc-telluride) detector to characterize spent fuel. The way the device is used is to lift a spent fuel assembly through a measurement cavity, and during the course of a measurement the device will verify the burnup of a spent fuel assembly and can distinguish between mixed-oxide (MOX) and low-enriched uranium (LEU) fuel [37]. A two-step approach is used to confirm item integrity. First, the burnup is confirmed using the gamma spectrometry, and then, the detection of missing elements is done by comparing the measured and simulated neutron count rates. The device can detect if ~25% of rods are missing. The SMOPY device does provide inspectors with a slightly more accurate tool than the FDET or DCVD, but it cannot detect at lower defect levels [4].

2.2.3. Neutron Gamma Attribute Tester (NGAT)

The NGAT is a gross defect measurement device that is used underwater to verify fission product presence in an irradiated fuel assembly. It can also be used to verify fresh MOX fuel assemblies as well as open or closed containers with irradiated and non-irradiated materials including non-fuel items [10].

2.2.4. Spent Fuel Attribute Tester (SFAT)

The SFAT device is a gross measurement system that only verifies the presence of fission or activation products at the top of spent fuel assemblies [4]. The SFAT is used by inspectors when Cherenkov radiation from the fuel is too weak to use the DCVD like in the case of lower burnups, longer cooling times, or unclear water. This is not a quantitative measurement and only provides a qualitative check that spent fuel is present via the gross detection of ^{137}Cs or ^{95}Zr/^{95}Nb gamma-rays [10].

2.2.5. Irradiated Fuel Attribute Tester (IRAT)

The IRAT is a gross measurement device that uses CZT detectors and can be suspended from a spent fuel bridge. This device only differentiates between irradiated non-fuel items and irradiated fuel items in fuel ponds using the gamma-ray emissions from fission products. This does not get down to the single pin level. The presence of fission product isotopes like ^{137}Cs, ^{134}Cs, ^{144}Pr, and ^{154}Eu, is used to confirm the irradiated fuel characteristics. In the case of a structural item, the presence of certain isotopes like ^{60}Co indicates prior exposure to a significant neutron flux [10].

2.2.6. CANDU Bundle Verifier (CBVB)

The CANDU Bundle Verifier consists of a highly collimated and shielded CdTe detector, which uses the 662 keV line to verify the presence of spent fuel cooled for longer than two years, and uses the ratio of 757/766 keV lines corresponding to the ratio ^{95}Zr/^{95}Nb for shorter cooling times [10]. This instrument uses the intensity to detect the presence of CANDU bundles that are stored in spent fuel pools [37].

2.2.7. Cask Radiation Profiling System (CRPS)

The CRPS consists of a CZT detector in a verification tube that is inside of a dry storage cask and is placed parallel to the spent fuel contents. The scan is used for re-verification purposes where an acquired fingerprint is compared to a baseline fingerprint. Consistency between fingerprints indicates that the spent fuel has not been disturbed [10].

2.2.8. Optical Fiber Radiation Probe System (OFPS)

The OFPS is a gross gamma measurement system that uses an optical fiber scintillator to re-verify the presence of CANDU spent fuel assemblies. The benefit of the OFPS is that it is not obstructed by the funnel structure like the CRPS is [10].

2.2.9. Neutron Coincidence Techniques

2.2.9.1. Advanced Experimental Fuel Counter (AEFC)

The AEFC is a neutron coincidence counter that measures research reactor fuel under water. It can be used in a passive or active mode where an AmLi source is either removed or inserted to induce fission in the fuel. In the passive mode, the device measures ^{240}Pu content, and in active mode the residual ^{235}U mass is measured [39].The device consists of six ^{3}He detectors that are embedded in a high density polyethylene (HDPE) matrix and arranged in two rows as shown in Figure 15. The four detectors in the inner row measure neutron coincidences to distinguish fission neutrons from background radiation [40]. The two detectors in the outer row are placed farther back within the polyethylene moderator, and the signal seen by them is approximately proportional to the fission rate in the fuel item.

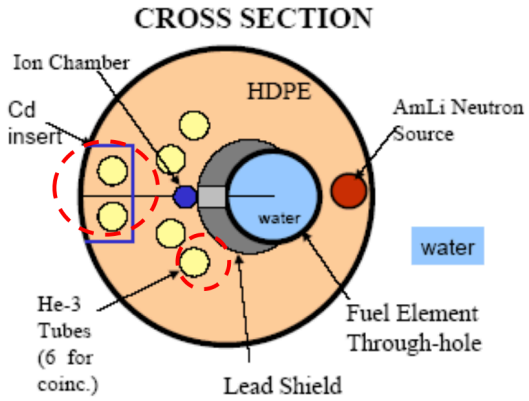


Figure 15. Cross section view of the AEFC device. The ^{3}He detectors are placed in two rows and are housed in an HDPE matrix. The measurement is done under water where a fuel assembly is inserted through the annulus shown in blue [39].

2.2.9.2. Spent Fuel Coincidence Counter (SFCC)

The SFCC is a neutron counter that can be used underwater to verify operator declarations of Pu content in breeder reactor spent fuel by looking for partial defects [10]. The counter has an ion chamber that measures the gamma exposure to identify the optimal high voltage to operate at to minimize pileup in the neutron detectors. The SFCC consists of a ring of 20 neutron detectors (^{3}He tubes) embedded in polyethylene. A cross-sectional view in shown in Figure 16 [41].

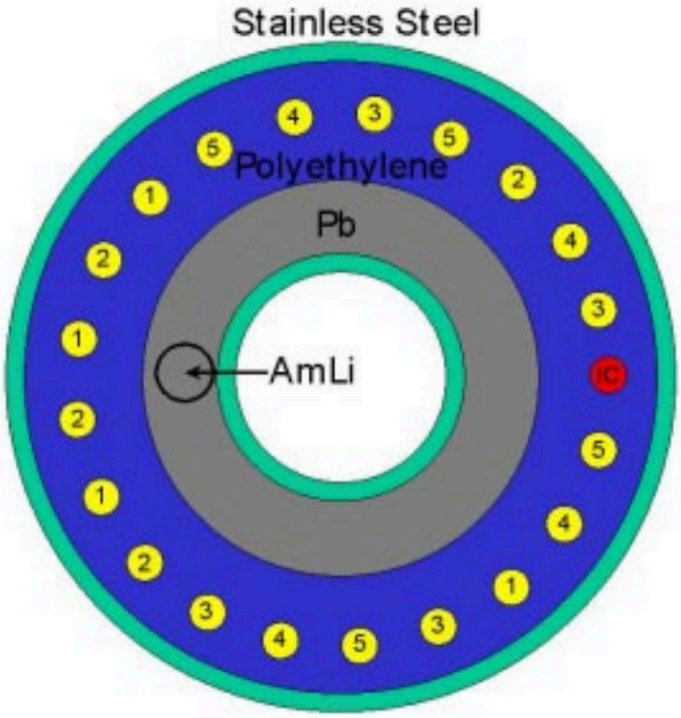


Figure 16**.** Cross sectional view of SFCC. The 20 ^{3}He tubes are shown in yellow, and the ion chamber is shown in red [41].

2.2.10. Cherenkov Viewing Devices

The Improved Cherenkov Viewing Device (ICVD) and the Digital Cherenkov Viewing Device (DCVD) are image intensifier viewing devices that are sensitive to ultraviolet radiation. The ICVD and DCVD work by performing gross measurements that detect the Cherenkov radiation emitted from the spent fuel as described in Section 1.2.1. The Cherenkov light emitted from spent fuel in the pools is from high-energy fission product gamma-rays interacting with the fuel cladding or water [15]. The DCVD and ICVD only give a qualitative check of the assembly integrity but the advantage is that they are non-intrusive, and the spent fuel assembly being inspected does not have to be moved from its place for the inspector to verify the presence or look for partial defects. The DCVD is mounted on the railing above the fuel pool, while the ICVD can be used as a hand-held device. There are several factors that influence the Cherenkov intensity from spent fuel that can affect the inspector's ability to draw an accurate conclusion. These factors include:

- The fuel type: the fuel geometry influences the intensity of the light emitted because varying spacer grid and top plate geometries can change the amount of light generated or escaping.
- Rod reflectivity: The probability of a Cherenkov photon to scatter off a surface or get absorbed.
- Water quality: The quality of the spent fuel pool water is not very clear and may contain particles that may disperse the light, diverting it from the camera. The circulation pumps also cause turbulence in the water that alters the measured intensity of light.
- Fuel Materials: The gamma transmission changes depending on the fuel material.
- Light from environment: Background from the pool or facility lights can interfere with measurements.
- Near neighbor effect: The light from other fuel assemblies in other parts of the spent fuel pool or the neighboring assemblies can interfere with the assembly being inspected.

The DCVD, although approved for partial defect verification, does not work as well for fuel that has been cooled for a long time or in murky spent fuel pool conditions. It also does not tell the inspector anything about the items beyond the presence of irradiated material.

2.2.11. Passive Neutron Albedo Reactivity (PNAR)

The PNAR NDA method involves comparing the neutron count rate of the fuel assembly in two different configurations – one where the sample is surrounded by a material to enhance neutron multiplication and the second where the multiplication is decreased by surrounding it with a different material [42]. Multiplication is increased by measuring the fuel in water, whereas for the second configuration, to lower multiplication, a Cd liner is moved into position to surround the fuel cavity [43]. The ratio of the singles or doubles count rates from both configurations are used to calculate a PNAR ratio. The PNAR ratio scales with the assembly multiplication and fissile content. A calibration measurement to determine the expected multiplication from operator declared burnups needs to be performed first. Most assemblies of the same fuel type will be expected to have the same multiplication, so PNAR could be used to detect partial defect if the measured multiplication of one assembly is inconsistent with other measured signatures or with what is expected using operator declaration [42].

The PNAR system design consists of four neutron detectors (either fission chambers or ^{3}He tubes) that are housed in polyethylene to thermalize the neutrons and lead to shield from the intense gamma radiation. The instrument needs to be adapted to the dimensions of each fuel type, so there is no one universal PNAR instrument – currently BWR and VVER specific PNAR systems have been designed. Figure 17 shows the horizontal cross-sectional view of a BWR specific PNAR instrument. The instrument was designed to be similar to the FDET system. ^{3}He detectors can be used instead of fission chambers to reduce the count time to less than 5 minutes, but for low burnup and long cooling times, the measurement time could take up to 20 minutes. The PNAR instrument can easily detect a significant removal of fissile material from the assembly.

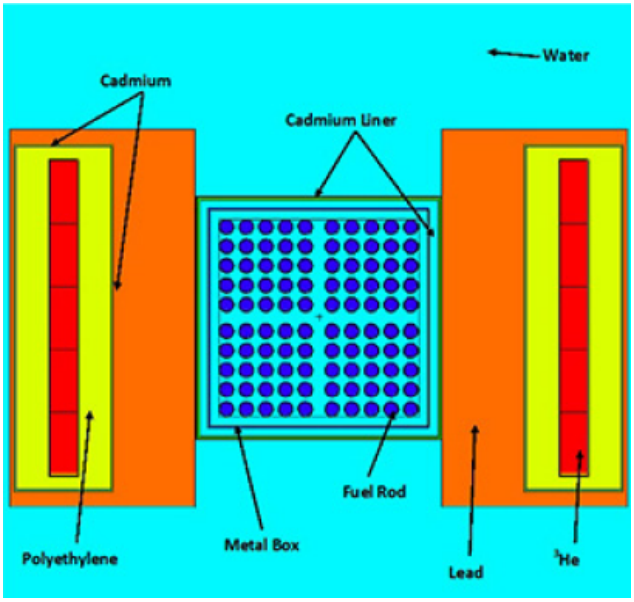


Figure 17. Horizontal cross-sectional view of the PNAR system optimized for BWR fuel [43].

Figure 18 shows the calculated PNAR ratio as a function of assembly burnup for 12 different assemblies of three different initial enrichments in water with a cooling time of 20 years. The PNAR Ratio decreases as a function of burnup for a given initial enrichment. Figure 19 shows the PNAR ratio as a function of the net multiplication (ratio of the number of neutrons that started in the fuel to the number of neutrons during the course of the simulation). The cluster of points at the bottom left that indicate the fully irradiated assemblies with different initial enrichments and cooling times. Regardless of the initial enrichment and cooling time, for fully irradiated assemblies, the PNAR ratio remains around 1.14 and the multiplication value is around 1.4 [43]. The instrument is sensitive to large changes or removal of fissile material in the assembly. So, if a fully irradiated assembly were replaced with a non-multiplying assembly, then the PNAR ratio would change from 1.14 to 1.002, alerting the inspector of a mismatch between assembly declarations and measurements. PNAR's role is to verify that fissile material is present, and simulations with SCALE and MCNP6 have the role of verifying that the total neutron count rates, gross gamma intensity and multiplication are all consistent with the declaration [44]. In order to detect a single missing pin, PNAR needs to be used with a more sensitive imaging technique.

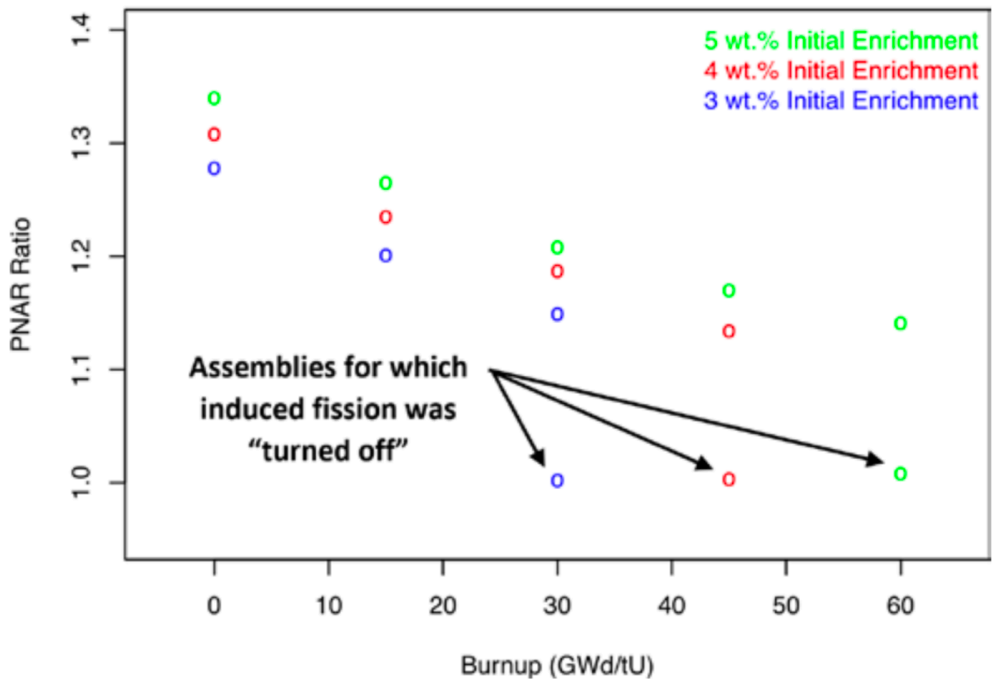


Figure 18. the BWR PNAR Ratio, simulated with fresh water, is illustrated as a function of burnup for 12 assemblies with three different initial enrichments [43].

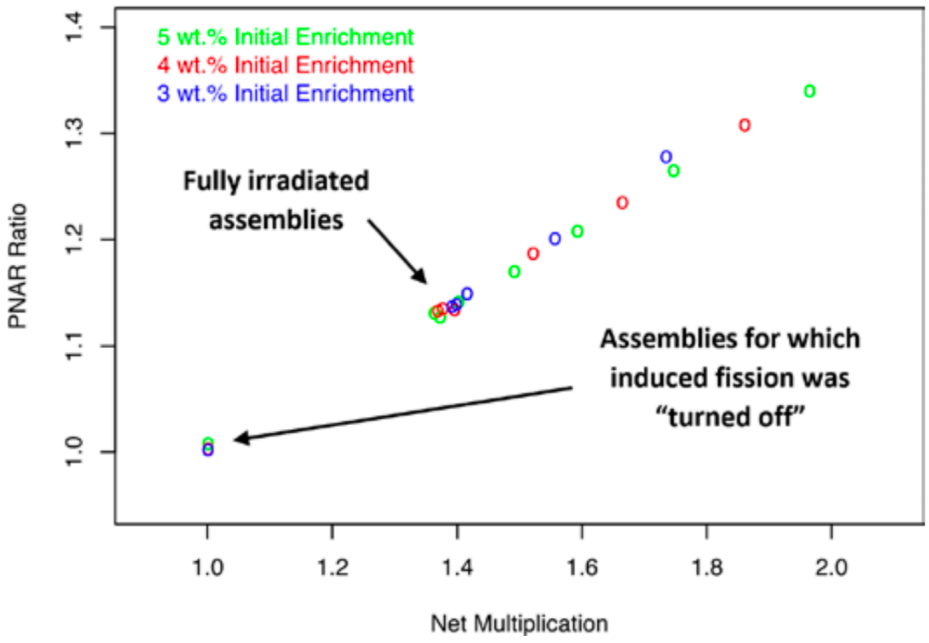


Figure 19. PNAR Ratio for BWR assemblies as a function of net multiplication [43].

2.3. Imaging

The gross techniques discussed up until this point all measure the fuel assembly as a single item; thus, the ability to detect a partial defect at the pin level is limited in most cases. When dealing with complex geometries such as fuel assemblies, imaging can prove to be a better tool to acquire information from each fuel pin. Imaging is the visual representation of the spatial distribution of an observable. Methods based on tomographic verification are being investigated in order to image fuel assemblies. In order to gather information from all rods in the fuel assembly, high energy gamma-rays or neutrons need to be used as the signature of interest. As mentioned in Section 1.3, imaging techniques involve reconstructing an image from measured radiation intensity profiles of an object. Measurements of the objects are made by scanning, and a measurement at a certain angle is called a projection [45]. Since 1993, the use of gamma-rays emitted from spent fuel to detect partial defect via imaging has been investigated [45]. Initial efforts were based on an Algebraic Reconstruction Technique, and the results were presented in graphical form (normalized relative intensity as a function of fuel rod number) [46]. In 2000, gamma tomography methods were used to generate a three dimensional map of deviations from average activity from each pin location in a mock assembly for two scenarios: the removal of rods and the replacement of rods with fresh fuel or dummy material [47]. An imaging method based on the detection of gamma-rays emitted from spent fuel called the passive gamma emission tomography system discussed in this section is the only tomography system to date that has been accepted by the IAEA as a tool for verification of partial defects in 2017 [48].

2.3.1. Passive Gamma Emission Tomography

The passive gamma emission tomography system (PGET) is a result of research that began in the 1980s. Research on this topic was conducted and implemented in a series of member state support program (MSSP) tasks and is still continuing today. The original method development and the evaluation of feasibility was conducted by the Finnish Support program more than a decade ago [49]. The goal of this system is to conduct NDA partial defect verification of spent LWR fuel without a priori information of the operator-declared-data and generate a radiation intensity map using gamma emissions. The PGET system consists

of two collimated detector arrays that rotate around the spent fuel assembly similar to single photon emission computed tomography (SPECT). The detectors rotate step-by-step around the assembly, and each array measures a complete 360˚ with 4 mm sampling. The detector arrays are made of CdZnTe and the collimator is made of tungsten [50]. The final design of the PGET system consists of 174 detectors split between the two detector heads [51]. The prototype arrangement is shown in Figure 20 [50]. Each detector array is in a sealed chamber and the device is designed in order to conduct measurements underwater. The outer appearance of the system housing is a torus with a central annulus where the fuel assembly will be inserted during measurement. The cavity diameter is 32.5 cm so as to accommodate a standard 17 x 17 PWR fuel assembly. The outer diameter of the system is about a meter [50]. The final design of the PGET and its components are shown in Figure 21.

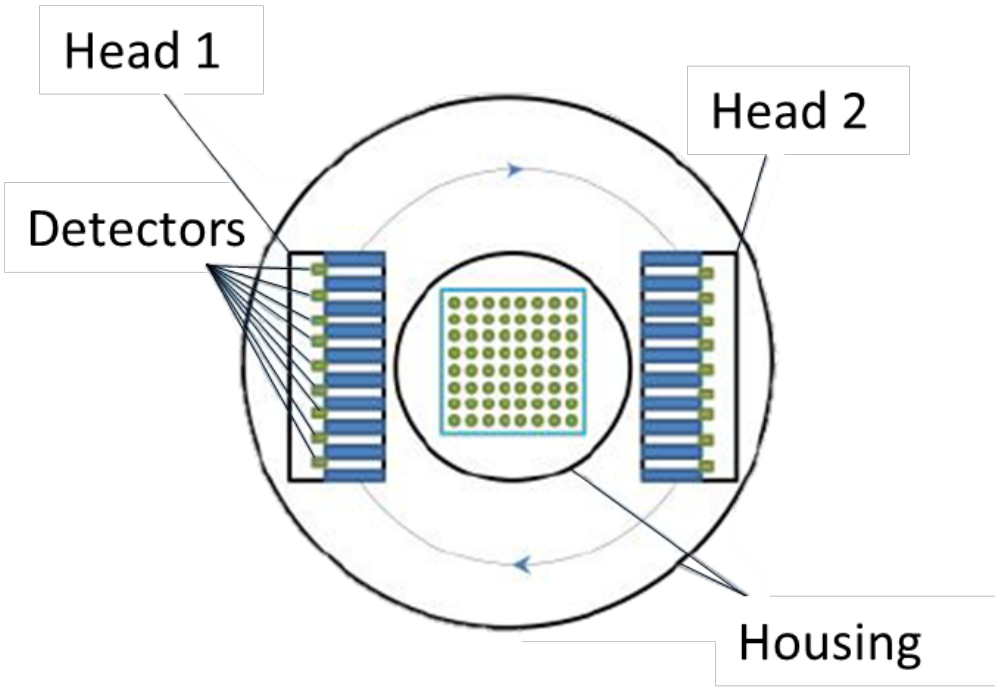


Figure 20. PGET prototype arrangement [50].

The gamma-ray emitting isotopes of interest that are measured by PGET are ^{137}Cs (661.65 keV) and ^{154}Eu (1274.43 keV) due to their longer half-lives of 30.1 years and 8.6 years, respectively, and high energies, which means the probability of escaping the fuel assembly is larger [52]. The two neutron detectors included in the PGET device only measure the total neutron count rate (counts per second) to verify the declared burnup. The PGET device has been demonstrated on VVER, BWR, PWR, and random pin geometries, as shown in Figure 22 [51]. The reconstructed image is clear for smaller fuel assemblies and is a bit blurrier for larger assemblies due to the increased number of mean free paths that the gammas need to traverse to get through the fuel assembly. PGET has been field tested at Ringhals, Sweden in 2009; Ispra, Italy in 2012; Olkiluoto, Finland in 2013; and Loviisa, Finland in 2014 [50]. Although PGET has now demonstrated the ability to resolve assemblies down to the pin level, for spent fuel with longer cooling times (~80 years), the imager relies on the ^{137}Cs line due to its long half-life of 30.17 years. Compared to the shorter lived isotopes, ^{137}Cs has a lower energy of 661.7 keV, resulting in a decreased ability to resolve the innermost pins of large PWR assemblies [53]. The mean free path of a 661.7 keV photon in UO_2 is 0.75 cm, while the mean free path of the most probable ^{244}Cm energy neutron (~1.5 MeV) in UO_2 is 3.98 cm [54]. Since fast neutrons are more penetrating, this is where neutron emission tomography can help complement measurements made by passive gamma emission tomography methods.

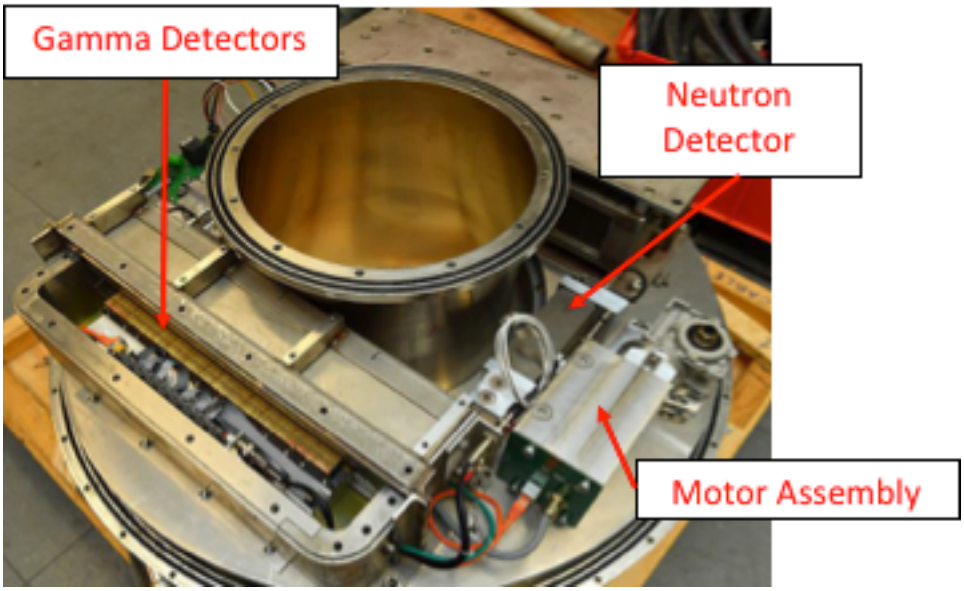


Figure 21. The final design of the PGET consists of 174 CdZnTe gamma detectors split between two heads, two ^{10}B neutron detectors, a data acquisition system, safety sensors, and a motor assembly [51].

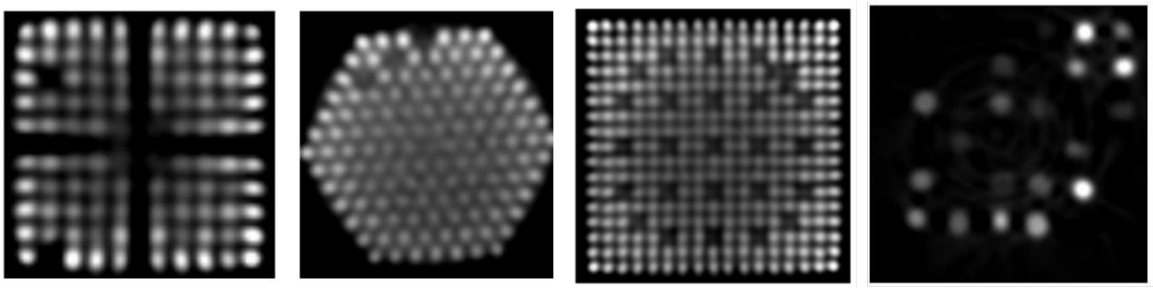


Figure 22. Tomography data from PGET measurements of various fuel assemblies [51].

2.3.2. Neutron Emission Tomography

Prior work at ORNL has successfully demonstrated that tomographic imaging of fuel pins can be performed using neutron emanations to distinguish pins containing Pu from those not containing Pu. An imager was designed, constructed, and tested at Idaho National Laboratory's Zero Power Physics Reactor (ZPPR) to measure fast neutrons from MOX fuel rodlets [55]. Fast-neutron imaging is difficult to perform for the very reason that it is desirable – fast neutrons penetrate a good deal of shielding allowing them to escape highly attenuating material unlike gamma-rays. Imaging depends on the modulation of the incident flux by some sort of an aperture, the simplest of which is a pinhole. The imager used in this proof of concept utilized a pinhole and radial slits as shown in Figure 23 [55].

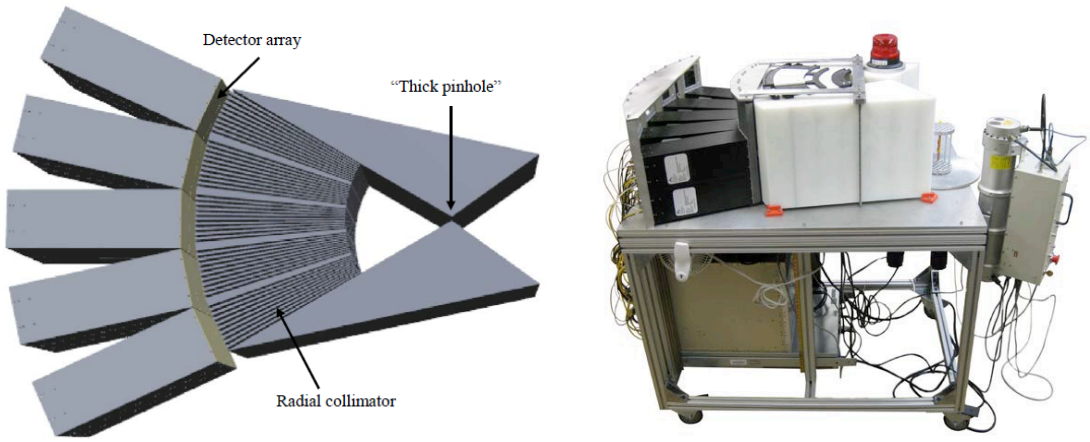


Figure 23. (Left) Schematic diagram of the imager. (Right) Prototype of the slit-collimator imager [55].

The two-component collimator is made of high-density polyethylene (HDPE). The 'thick pinhole' part of the collimator is closest to the source and serves to shield the detectors from neutrons that would reduce the resolution. The radial component of the collimator consists of slits that all center on the opening of the pinhole such that the collimated neutrons originate primarily from the source itself. The detector array consists of pixelated liquid scintillator imaging detectors arranged in five columns of three detectors each positioned along an arc that placed the detector front faces 52.5 cm from the slit position [55]. For initial proof-of-concept tomographic measurements at ORNL, a set of five identical ^{252}Cf sources was used whose emission rates were each approximately 42,000 neutrons/second as of February 2011. The arrangement and results from tomographic reconstruction of data from the slit imager measuring ^{252}Cf sources is shown in Figure 24. The samples with black stoppers contain machining grit, and the containers with yellow stoppers contain ^{252}Cf. The reconstructed image on the right clearly shows the position of each neutron source, and this experiment proved that neutron emission tomography can resolve sources that are placed as close as 1.5cm apart (comparable to a fuel pin pitch).

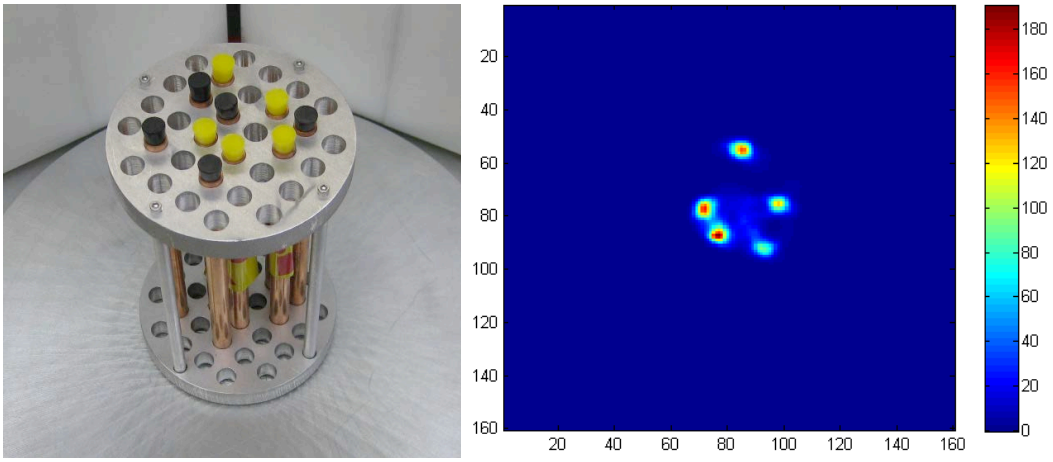


Figure 24. (Left) Experimental setup of ^{252}Cf sources (yellow) and machining grit (black). (Right) Tomographic reconstruction of the sample on the left showing location of the five sources [55].

The imager was then used to image a soup can containing MOX fuel rodlets at the ZPPR facility at INL. The imager needed to be modified to shield the detectors from gamma-rays. The measurement sample was a soup can containing 32 positions for fuel pins. 31 of the 32 positions contained 6-inch-long Pu MOX fuel rodlets that each contained 3.66g of ^{240}Pu that produced about 3700 neutrons per second from spontaneous fission. The remaining position marked by the 'X' in Figure 25 was filled with a depleted uranium (DU) rod. The tomographic reconstruction of the sample shown on the right side of in Figure 25 shows a visual representation of neutron sources as a function of position, and the location of the DU rodlet is clearly visible [55], [56]. The experiments performed at INL and ORNL successfully demonstrated the capability of neutron emission tomography using fresh MOX and ^{252}Cf sources. The imager design and components would need to be modified in order to be used on spent fuel since the gamma-ray fields would be too high for the segmented scintillator detectors.

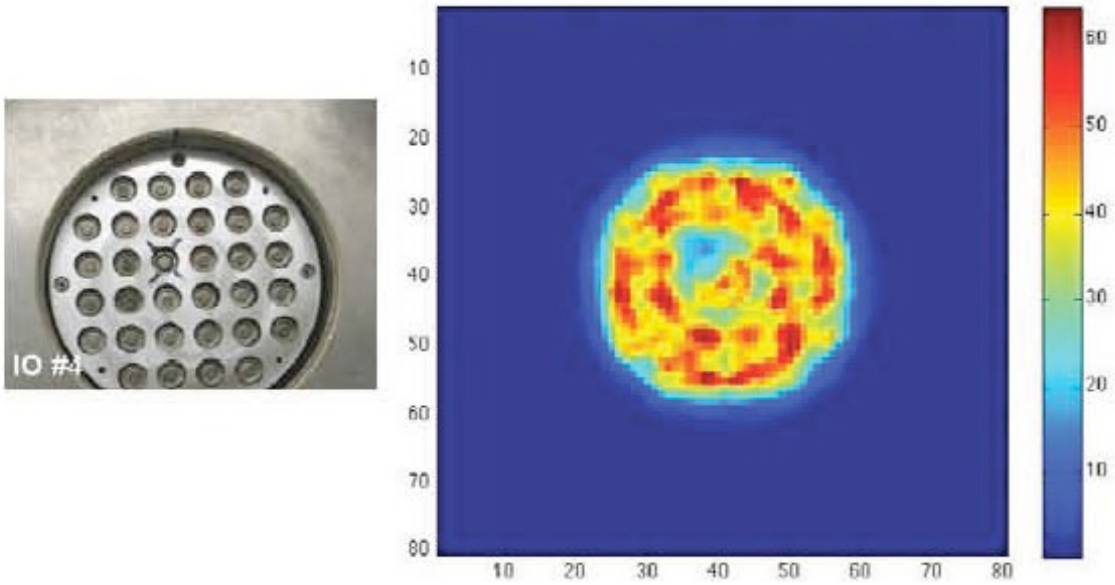


Figure 25. (Left) Picture of the soup can containing 31 Pu MOX fuel rodlets and one DU rodlet marked by the 'X'. (Right) Tomographic reconstruction of the neutron source strength as a function of source position. The blue region corresponds to the location of the DU rodlet [55] [56].

2.4. Gaps in Technology

Currently, a tool based on passive neutron emission tomography to measure and image spent fuel down to the pin level does not exist. To date, various techniques based on gross counting of neutrons and gamma-rays from spent fuel have been developed and utilized by the IAEA to verify operator declarations to draw safeguards conclusions. Although they can detect partial defects in spent fuel assemblies, the gross measurement systems are not sensitive enough to detect the diversion of a single pin. As a result, the IAEA recognized the need for a more sensitive imaging-based approach to spent fuel accountancy. The only imaging technique to date that has been approved by the IAEA for use in spent fuel tomography is the PGET system that is based on looking at the passive gamma emissions. The gamma-rays from spent fuel cannot easily escape the center of the fuel assembly due to the high atomic number materials present in spent fuel. As a result, PGET may not be able to resolve down to the single pin level in larger assemblies at longer cooling times. This is where fast neutron emission tomography could potentially have an advantage since fast neutrons are more highly penetrating than gamma rays. To date, passive neutron emission tomography has not been successfully demonstrated as a spent fuel imaging tool. Another issue is that is that the only diversion scenarios addressed by the tools are: (1) fuel pins have been removed, and (2) fuel pins have been replaced with dummy rods or fresh fuel. The tools that are in use have not been designed to work to detect rods that have been replaced with fresh fuel pins that have then been subsequently irradiated.

The imaging capability presented in this project is intended to verify the integrity of spent fuel assemblies, and not to quantify the presence of Pu. The Pu content saturates with burnup, as discussed in Section 0. This means that traditional techniques that use the presence of Pu in spent fuel to confirm burnup are not as sensitive to rod placements made after the first irradiation cycle in a reactor. The neutron emission from spent nuclear fuel is dominated by the spontaneous fission of ^{244}Cm. Due to ^{244}Cm's unique relationship with respect to burnup, using the fast neutrons emitted by ^{244}Cm, a neutron emission-based imager can be sensitive to rod replacements at higher burnups. Expected advantages of a neutron-based tomography measurement system include:

- Neutron measurements rely chiefly on the ingrowth of ^{244}Cm, which occurs mostly at the end of the exposure cycle, so the technique should be sensitive to assemblies containing fuel pins that were replaced after a single cycle in the reactor and subsequently irradiated in the core.
- Because fast neutrons can penetrate the entire fuel assembly, fast neutron emission tomography may be the only method with the potential to detect single-pin diversion in larger fuel assemblies where the attenuation of gamma radiation is significant.
- Fissile loading of each pin can possibly be determined in addition to ^{244}Cm content.
- This technique could be used to verify the burnup profile of a spent fuel assembly.

2.5. Novel Contributions

This dissertation makes novel contributions to the areas of spent fuel NDA by developing a physics design for a new passive capability for detecting the diversion of single fuel pins (rods) from nuclear spent fuel assemblies using fast neutron emission tomography. To date, a viable spent fuel imaging system using passive fast neutron emission tomography has not been demonstrated. The work presented in this dissertation will serve as a benchmark for developing a neutron emission tomography-based tool for spent fuel safeguards.

First, an approach to converge on the ideal physics design for an imager was developed as part of this project. The two parts that fed into the design considerations were surveying the parameter space and component optimization. With regards to the parameter space survey, size constraints were identified to reasonably deploy an imager with facility considerations. Three parameter sets were identified to be varied for this project – total collimator thickness, different steel and borated polyethylene thicknesses, and slit widths of the collimator. Based on this, a range of total collimator thicknesses was identified while keeping in mind the maximum imager radius. In addition, the slit widths in the collimator were varied – both parallel and tapered. MCNP models of the imager were developed for each of the different parameter variation combinations. The surface definitions for the collimator geometry were generated with help from the Reactor and Nuclear Systems Division (RNSD) at ORNL[1].

[1] Courtesy of Dr. Jinan Yang.

The second novel contribution of this project was a new way to estimate the neutron response for this complicated geometry and all parameter variations using fewer simulations. Neutron response of the imager for a source's signal, collimator penetration, and edge effects were all calculated in addition to simulations of the inter-detector scatter to feed into a signal-to-noise ratio (SNR) calculation that was then used to evaluate the various geometries. Such a comprehensive survey across the imager design space has not been conducted before. Additionally, for this new design concept, simulations of gamma exposures for the various parameter combinations were conducted for the first time, and a constant exposure contour method was developed. This method can be used for future applications of this imager to identify the ideal imager parameters that would optimize neutron response for a given cooling time and gamma exposure.

In conjunction with gamma exposure simulations, this project involved conducting proof-of-concept experiments with a single detector module to evaluate the gamma rejection ability of the boron straw detectors at extremely high exposures. The proof-of-concept measurements provided new insight into how these neutron detectors could be used for this application and what their limitations are. The experiments with the ^{137}Cs irradiator were conducted at the Radiation Standards and Calibration Laboratory (RAScal) facility at ORNL and provided information on the gamma sensitivity for the unique detector configuration and provided information on how to optimize the circuit. Gamma sensitivity measurements at high exposure rates (430 R/hr) for this detector configuration have never been conducted before. These measurements were used to find the operational limit of the detector configuration, which was used in conjunction with the simulation results to converge on an optimal design.

Finally, using an ORNL-developed SNR code, each of the different geometry configurations was evaluated for its neutron response. The most optimal configuration was found, and a laboratory proof-of-concept experiment was designed based on the simulation recommendations for the optimal design. The proof-of-concept measurements based on the simulations showed for the first time that an imager based on passive neutron emission tomography with the required spatial resolution to identify individual fuel pins is feasible.

3. SYSTEM DESIGN

This chapter will provide an overview of the imaging system design concept and simulations conducted that fed into selecting the optimal imager design. Both gamma exposure and neutron simulations were conducted, but the data for those will be presented in the following chapters. This chapter opens by describing the isolation of lines of response based on collimation. Then, the concept of the parallel-slit ring collimator is introduced. Last of all, the baseline imager design is presented as a basis for comparison of a suite of imager designs having different dimensions.

3.1. Lines of Response and Collimation

As covered in Chapter 1, a crucial element of computed tomography and image reconstruction is to be able to divide the object being inspected into lines of response. Lines of response refer to the paths through the object along which an observable, which in this case is the neutron emission rate, is summed or integrated over several projections. In passive neutron imaging, collimation is used to isolate paths, or lines of response through a fuel assembly, and neutron counts registered by detectors at the end of each collimator slit correspond to the summed activity along a particular path. It is possible to perform fast neutron emission tomography with the desired resolution as long as each line of response sufficiently isolates a path through the object, the object is sampled with sufficient number of lines of response, and there are an adequate number of views through the object to generate an image.

In order to illustrate the concept of a line of response, a series of simulations were performed using a collimator consisting of an annulus of 5% enriched (^{10}B) borated polyethylene with a single 3 mm wide slit cut in it. MCNP6 simulations were performed with a ^{244}Cm point source placed at the 17^2 locations corresponding to a grid separated by the pin pitch of a 17×17 PWR fuel assembly. (However, note that a full fuel assembly with structural components was not simulated.) For each simulation, the neutron counts were tallied at the exit of the slit via the FMESH card with the F4 tally for calculating neutron flux through a cell.

Figure 26 shows the point spread functions for a set of different thicknesses of stainless steel and borated polyethylene in the collimator. The ideal point spread function is one that looks like a delta function, so the most desirable collimator is one that maximizes the signal (component that traverses down the slit) and minimizes the collimator penetration or *noise*. The curves in the figure are normalized with respect to the 10 cm borated polyethylene and 30 cm stainless-steel data. It can be seen that beyond 25 cm of borated polyethylene there is not much of a difference in the noise suppression.

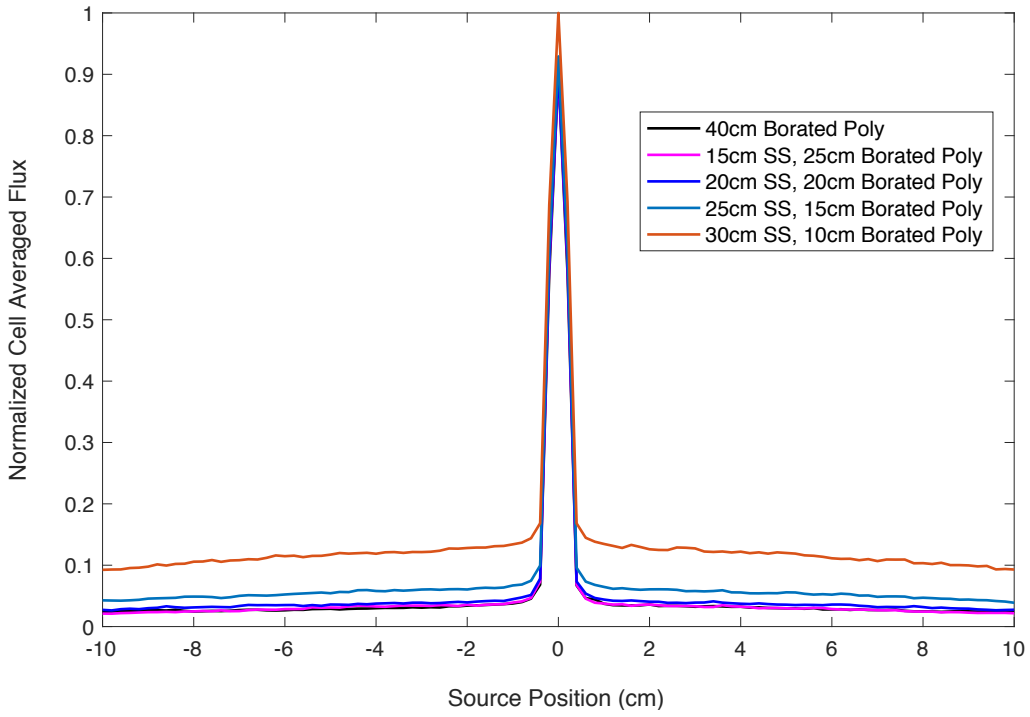


Figure 26. Shows the point spread functions for various thicknesses of stainless steel evaluated. The curves are normalized to the 10cm borated polyethylene / 30cm steel data. There is not much difference in the 'noise' between the 25cm borated poly case and 40 cm borated poly case.

A schematic diagram of the geometry for simulations done with a cylindrical collimator is shown in Figure 27 (a). The resulting image in Figure 27 (b) shows the neutron counts associated with each source location for a collimator thickness of 15 cm. In this image, there is an identifiable path through the inspection volume that is strongest along a path seen by the collimator slit, but significant contributions remain from all the neighboring source positions. Similarly, Figure 27 (c) shows the counts associated with each source location for a collimator thickness of 30 cm. Here, almost all response is limited to a particular path across the inspection volume, but the larger collimator thickness reduces the total intensity. Based on the initial single slit line of response simulation results, a minimum amount of borated polyethylene consisting of 30 cm was chosen as the limiting criteria for evaluating several designs options. Although the initial point spread function simulation showed little difference in noise suppression beyond 25 cm borated polyethylene, since the final collimator will have numerous slits cut into it, the effective density of the collimator is reduced, thus reducing the modulation effectiveness of the collimator.

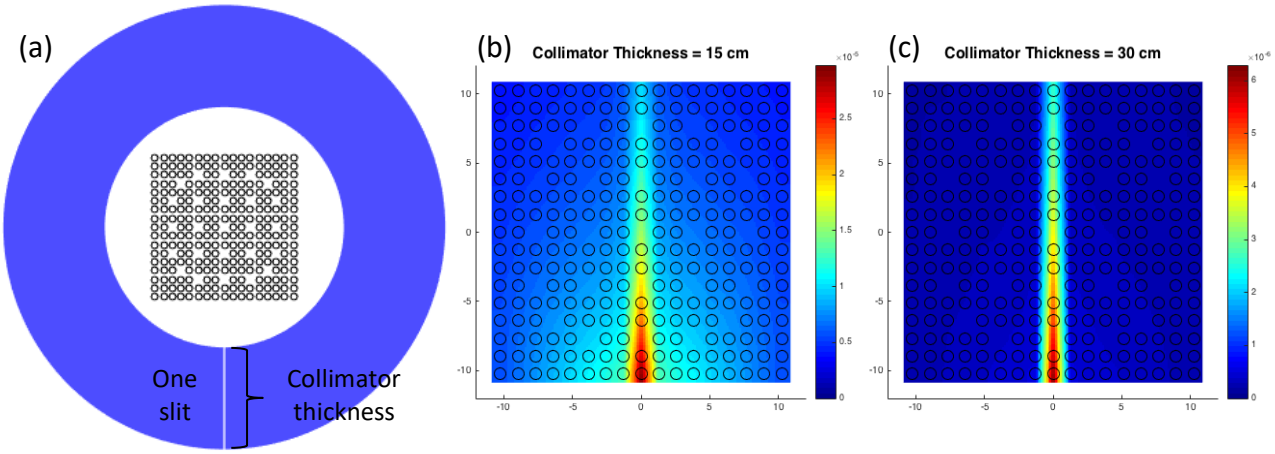


Figure 27. Example lines of response for a detector counting neutrons that exit a single 3 mm wide collimator slit, shown (a) as a schematic diagram. The results of a ^{244}Cm point source simulated at each assumed fuel pin location are shown (b) for a 15 cm thick collimator and (c) for a 30 cm thick collimator [34].

As a result, increasing the borated polyethylene thickness to 30 cm may compensate for the reduced density. For the various simulations presented and discussed in this dissertation, a minimum borated polyethylene thickness of 30 cm was used.

3.2. Imaging System Requirements

As mentioned in Chapter 1, measuring fast neutrons for material accountancy is desirable because neutrons penetrate a good deal of shielding and can escape from high density materials within the fuel assembly. Unfortunately, their ability to penetrate shielding is also what makes fast neutrons difficult to collimate and measure with fine spatial resolution. The challenges posed by using fast neutrons for safeguards verification make it such that attributes of an ideal detector or collimator conflict with one another when trying to optimize several facets like resolution and detection efficiency. The intent of the work discussed here is to develop a functional equivalent to a parallel slit collimator. The ideal imager has to have the following characteristics:

1. High efficiency: The neutron emissions from spent fuel is not as strong as the gamma ray emissions. High efficiency is a requirement for practical measurement times, and in order to satisfy this the detectors need to be placed closer to the spent fuel. Another way to increase the efficiency is to increase the slit width, but this would result in a reduction of shielding material. Large detectors are a requirement when it comes to neutron measurements since neutrons have a tendency to scatter. Using a traditional parallel slit collimator with large detectors would mean that fine scanning and rotation would be required, making the measurement time impractically long.
2. High resolution: In order to be able to identify individual pins, the resolution needs to be such that it is possible to differentiate and identify the gap between fuel pins. The fuel pin pitch (from pin center to neighboring pin center) in a standard 17 × 17 fuel assembly is 1.26 cm, and the pin outer diameter including the cladding is around 0.914 cm. Thus, slits on the order of a few millimeters are required to resolve the gaps between the pins and generate a good enough line of response through the assembly. Another way to increase resolution is to increase the amount of moderating material used in the collimator, but although using only borated polyethylene would

create a better response, the high gamma exposure would still be a problem for the detectors.

3. Gamma exposure minimization: The gamma exposure from spent fuel is too overwhelming for the neutron detectors to operate without any shielding since for fuel with short cooling times (less than 5 years) the exposures are on the order of 10,000 R/hr. Most neutron detectors are sensitive to some degree to gamma-rays in addition to neutrons. In any detector, gamma-rays can transfer energy to electrons in the detector materials via Compton scattering interactions. If this were to take place in the detector fill gas, the resulting high energy electron would ionize the fill gas and other material within the detector. When the electronic pulses from gamma-rays are similar in size to the neutron pulses false counts can be registered in the detectors. If the induced gamma-ray pulses are smaller, they can pile up in a short amount of time, also resulting in false neutron counts. As a result, gamma shielding needs to be incorporated into the imager design even when using relatively gamma-blind detectors. The most gamma-blind detectors with a high fast-neutron interaction probability are moderated neutron detectors, where the neutrons lose energy in the moderating material that the detectors are embedded in.
4. Compact size: A compact detector size is desirable so that it may be practically field tested and used in a facility without disrupting facility operations. The most compact geometry for an imager is in the shape of a ring.

3.3. Parallel-Slit Ring Collimator Design Concept

A more compact version of a parallel-slit collimator in the form of a ring can be constructed to address the challenges and requirements detailed in the previous section. If 100 detectors were to be used in a parallel slit design, it would not be possible to build it in a compact enough size and maintain enough material between slits to modulate neutrons effectively or shield the detectors from gamma-rays. In addition to not having enough material to shield or modulate the radiation, the detectors would have to be on the order of a few millimeters, which is not feasible for neutron detection. The modified parallel-slit ring collimator is based on the traditional parallel slit collimator, but since it would be impossible to build a compact

parallel slit collimator with 100 neutron detectors in a compact form, the slits are moved by rotated each by a known angle so the slits and detectors at the end of each slit located on the outer ring are equally spaced from one another. By doing so, the modified parallel-slit ring collimator maintains correspondence to the traditional parallel slit collimator. This way, the same lines of response that would have been isolated through the sample with parallel slits can be isolated along the sample using this modified ring collimator. By moving the slits further apart around the ring, the detector size can be increased. Figure 28 illustrates how the collimator starting from the traditional parallel slit form (a) can be modified to a parallel-slit ring equivalent (e). In this diagram only 20 slits are shown for ease of viewing, but for the remainder of the simulations 100 slits and 100 detectors will be used. In (a) there is not sufficient collimator material between the slits to modulate the neutrons effectively to generate a good line of response. Also, the detectors would have to be incredibly small to fit. The detectors can be moved apart by taking each slit and rotating them to equiangular points around the circle as shown in (e). The modified parallel-slit ring collimator would have a neutron detector on the outside at the end of each slit. To gather data from all projection angles, the collimator would rotate around the object, while the object and detectors can stay stationary. This is an added advantage to this imaging system since the object and detector positioning doesn't have to be too precise as long as there is no relative motion during the measurement.

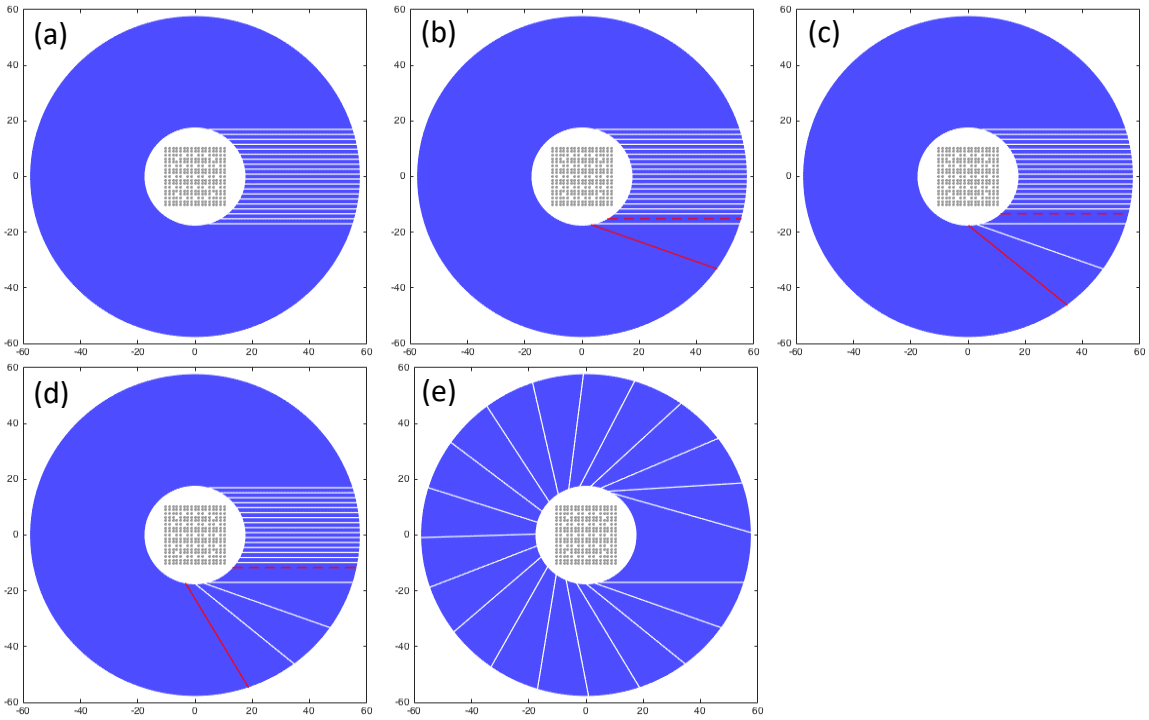


Figure 28. The parallel-slit ring collimator (e) is equivalent to the parallel slit collimator in (a). As shown in (b)-(d), each slit is rotated from the dashed red to the solid red line so that after rotation, the resulting slits are (e) spaced equally around the circle. Each slit still inspects the same chord of the inspection volume [57].

3.4. Baseline Design

The imager is made up of an annular collimator surrounded by a ring of detectors, where each detector is positioned at the outer end of each slit. Between the detectors and the collimator is a thin layer of cadmium to eliminate the lower energy neutrons and ensure the detectors are most sensitive to fast neutrons that make it through. There is another cadmium layer on the outer radius of the detectors as well. The next section will describe the detectors in more detail. On the outside of the outer layer of cadmium is a layer of borated polyethylene in order to limit the number of neutrons that would be reflected back into the detectors and also to shield the detectors from other neighboring neutron sources that may be in the vicinity. Figure 29 shows a closeup of the collimator with slits pointing to the detectors that have cadmium on the inner and outer radii.

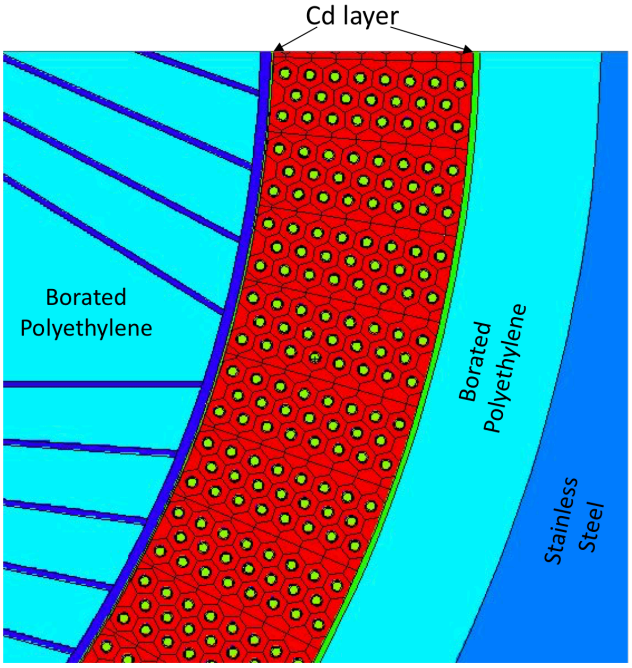


Figure 29. Close up of the borated polyethylene component of the collimator with slits pointing to detectors. The two cadmium (Cd) layers are shown in addition to the outer borated polyethylene layer to prevent in-scatter. The high-density polyethylene matrix that the straws are embedded in is shown in red.

The inner radius of the imager annulus is 17.667 cm, which was calculated to accommodate an assembly 1cm greater than the half diagonal of a standard 17 × 17 fuel assembly (24 cm). The total outer radius limit of the imager (including the outer layer of borated polyethylene) was selected so that it can be reasonably handled by a facility based on the envisioned concept of operations of the imager. This means that the imager can fit in a spent fuel cask or cask-like container that operators at spent fuel encapsulation facilities would typically handle. A concept considered here in this project is to house the imager in a fuel cask-type of container in order to shield the surroundings from the intense gamma radiation from the spent fuel assembly being measured. For the baseline imager, two commercial casks with different internal diameters were used to evaluate different collimator thicknesses. For eleven of the sixteen collimator geometries, an imager outer diameter was chosen so the device would fit within the internal cavity of the GNS Castor series of transport casks (internal cavity diameter of 148 cm), as this cask type is commonly used for international fuel shipments. For the remaining five geometries, the Fuel Solutions TS125 cask with an internal cavity diameter of 170 cm was used to constrain the imager outer diameter. Figure 30 shows the plan view of the baseline design of the imager along with a 17 × 17 fuel assembly in the center of the cavity. As can be seen, the collimator is made up of two materials – the inner 10 cm is made of stainless steel (green) and the outer 30 cm is made of borated polyethylene (yellow).

The collimator as described above briefly consists of two materials – the borated polyethylene and a stainless-steel component. The stainless-steel component is towards the center of the collimator and has two roles: acts as high-density material shielding for the detectors to lower the gamma exposures from the spent fuel, and also for structural integrity since the slits cut in pretty closely, and since the envisioned imager is about a meter in length, there may be warping along the length if the borated polyethylene were to be placed towards the center. The borated polyethylene is meant to act as the neutron moderating material that effectively modulates the neutrons so that the fast neutrons are the ones that primarily get down the slits. The collimator active length (height) was chosen to be ~1 m in order to maximize the measurement efficiency. However, the length is also constrained because spent fuel assemblies may warp along the entire 4 m length by as much as 1cm. If the imager active

length was longer than 1m, the image reconstruction may not be as accurate. This way, the maximum amount of uncertainty as seen by the imager would be 0.25cm along the fuel length, which is comparable to the space between each pin. A three-dimensional view of the imager that shows its length compared to that of a fuel assembly is shown in Figure 31. There is shielding made up of borated polyethylene and stainless steel on the top and bottom of the imager to protect the detectors from the fuel assembly shine resulting from the fuel assembly extending out on either side of the imager.

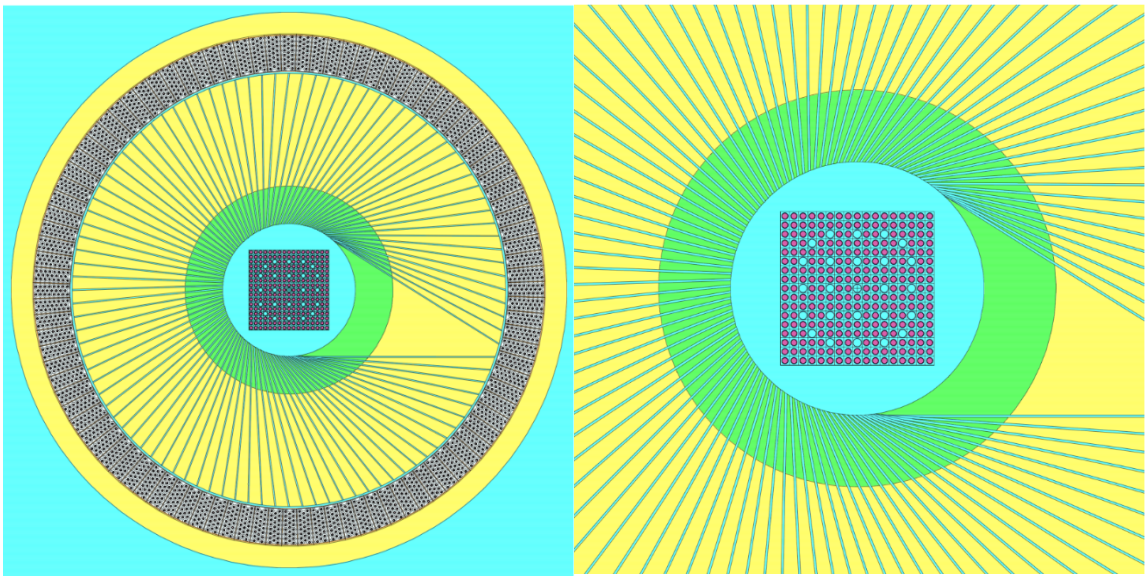


Figure 30. Plan view of the entire imager with a 17 × 17 fuel assembly in the center.

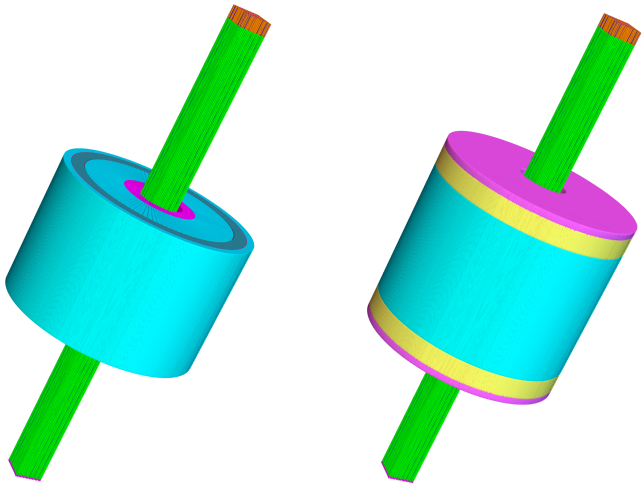


Figure 31. Three-dimensional configuration of the collimator and neutron detectors around a typical fuel assembly (green). The imager is shown (left) without and (right) with stainless steel (pink) and borated polyethylene shielding (yellow) at the top and bottom of the imager to shield from fuel assembly shine [34].

3.5. Imager Geometries Considered

In order to converge on the optimal imager design, a survey of the design space was conducted. First, the parameters to be varied in the imager design were identified, then the various permutations of imager geometries were simulated in MCNP to calculate a neutron response and expected gamma exposures. The parameters of the imager that were identified to be varied while constraining the design by practicality considerations for deployment are: stainless steel thickness, borated polyethylene thickness, and slit width. The size constraint to fit the imager into one of the two identified commercial transportation casks in combination with the point spread function simulation results presented in Section 3.1 that showed the minimum amount of borated polyethylene required (30cm) was used to come up with sixteen different combinations of stainless steel and borated polyethylene thicknesses in the collimator, resulting in seven different total thicknesses. The 16 thickness combinations that were simulated are shown in Table 3. In addition to varying the stainless-steel and borated polyethylene thicknesses, 32 different slit widths were simulated. These included 9 parallel slit dimensions (1 mm to 5 mm in 0.5mm intervals), 23 tapered slit combinations with inner dimensions of 1 mm, 2 mm, 2.5 mm, and 3 mm going to an outer

dimension of 5 mm in 0.5 mm intervals, resulting in 512 different geometries. Figure 32 shows a 3-dimensional SolidWorks rendering of the proposed imager housed in a GNS container. On the outside of the imager detectors, to limit the amount of backscatter of neutrons, a layer of borated polyethylene was simulated between the detector outer radius and the stainless-steel portion of the container. The dimensions of the borated polyethylene and stainless-steel components of the collimator and the container are shown in the table below.

Table 3. List of sixteen combinations of stainless-steel and borated polyethylene thicknesses making up the imager collimator that were used as the basis for evaluating different imager geometries [58] [59] .

Transport Cask Name	***Collimator Components***			***Outside Detector***	
	Steel Thickness (cm)	***Borated Polyethylene (cm)***	***Total Thickness (cm)***	***Outer Borated Poly Filler (cm)***	***Steel Container Thickness (cm)***
GNS	5	35	40	5.822	48
GNS	10	30	40	5.822	48
GNS	6	36	42	3.822	48
GNS	5	38	43	2.822	48
GNS	6	37	43	2.822	48
GNS	7	36	43	2.822	48
GNS	5	40	45	0.822	48
GNS	6	39	45	0.822	48
GNS	7	38	45	0.822	48
GNS	8	37	45	0.822	48
GNS	10	35	45	0.822	48
FUELSOLUTIONS	5	45	50	6.912	13.6
FUELSOLUTIONS	10	40	50	6.912	13.6
FUELSOLUTIONS	5	48	53	3.912	13.6
FUELSOLUTIONS	5	50	55	1.912	13.6
FUELSOLUTIONS	10	45	55	1.912	13.6



Figure 32. (left) A commercially available transport cask by GNS. (right) A 3-D rendering of imager concept in a cask-like container that would fit in a fuel encapsulation facility [59] [34].

3.5.1. Procedure

In order to converge on the ideal detector geometry, a comprehensive set of simulations were conducted investigating the imager parameters described in the previous section. The best design minimizes the time to resolve individual fuel pins. The simulation, measurement, and data evaluation procedure needs to identify the best compromise between efficiency, resolution, and gamma exposure management in a package of acceptable size. Computationally, this is split into two – gamma exposure evaluation, and neutron response simulations. The simulations, measurements, and analysis methodology is outlined below.

- Gamma Exposures
    - Using the "worst case scenario" spent fuel source, compute exposures for a survey of parameter space using MCNP for all 512 geometries. The fuel source used in all the gamma simulations was a standard 17 × 17 fuel assembly with a

homogeneous distribution of gammas throughout the pins. A burnup of 40GWd/MTU was used after 1-year cooling time. This is the minimum time before a fuel assembly can be moved and would have the highest exposures.

- Understand how exposures at the detectors scale with imager parameter changes and, develop a way to relate the required exposure to required imager geometry. The gamma exposures and various close and open fractions will be used to develop an equation to predict the ideal geometry to limit the gamma-ray exposures to a specific value.
- Identify limits of ability of a single module of neutron detector to reject gamma-rays using measurements. This will help identify operational requirements (threshold) for real in-field measurements. The measurements will be described in a following chapter.
- Identify configurations that are acceptable based on the measurement data and simulations predicting the largest exposures seen at the detectors using the worst-case source.

- Neutron Response
  - The collimator creates a complicated neutron response that is hard to predict. First, simulations using a ^{244}Cm line source will be used to understand what the expected point spread function looks like for the various imager geometries being considered.
  - Ideally it would be nice to know the detector response to every point within the fuel cavity. However, this is not feasible since it would require running ~100,000 simulations for each of the 512 configurations. The number of simulations was estimated at 100,000 because the fuel annulus has an area roughly around 350 mm × 350mm, and to get the resolution down to the mm scale, ~100,000 simulations would be required. A smaller set of simulations using a ^{244}Cm line source will be conducted in order to feed into understanding how the neutron counts scale and be extrapolated to a full response. This will include estimating and calculating how the direct signal component, the slit edge component, and

the noise or collimator penetration scales for each configuration. This will all feed into the reconstruction code in order to correct for errors.

- A signal to noise ratio (SNR) code developed for this data will be used to identify the "good" or acceptable data that agrees with the findings from the gamma exposure analyses. The set of configurations where the SNR starts to deteriorate will also be identified.
- A final detector geometry will be selected. The final geometry will be used to simulate a setup of five line sources in order to test that reconstruction is possible. A follow-up simulation of a full up PWR fuel assembly will be conducted and a sonogram of the data will be calculated. This will be the input data for the reconstruction code.

3.6. Neutron Detectors

The detectors selected for this application and project are commercially available boron straw detectors. The rationale for selecting this particular detector was that it was the easiest way to maximize neutron efficiency while minimizing the gamma-ray sensitivity in an affordable manner. All neutron detectors are sensitive to gamma-rays to some extent because most nuclear material emits 10 or more times as many gamma rays as neutrons [60]. For spent fuel applications gamma exposures over 2000 R/hr are common, making the gamma-ray sensitivity of the detectors a high priority. The gammas transfer energy to electrons in the detector fill gas via Compton scattering interactions. The resulting high energy electron produces a column of ionization along its path, and the electronic pulses produced may be comparable to neutron pulses, or if many small pulses are registered close together within the resolving time of the detector electronics, they can pileup resulting in potential false counts. Detector materials can be designed to favor neutron absorption. Thermal neutrons can be absorbed with a higher probability than gamma-rays, but when it comes to fast-neutrons, the gamma-ray interaction probabilities are comparable to the neutron interaction probabilities as shown in Table 4 [60].

From the data presented in in the table, it can be seen that the thermal neutron detectors have the best combination of neutron sensitivity and gamma-blindness. The two top choices for

thermal neutron detectors are boron-lined proportional counters and ^{3}He detectors. Boron-10 lined cylindrical proportional counters are one of the oldest developed neutron detection technologies but once ^{3}He became more widely available, it became the most common approach for neutron detection. The high cost of ^{3}He then made alternatives like boron lined detectors more attractive for applications [61]. The advantages of boron-lined straws are:

- Gas detectors are fairly stable and can be easily deployed
- The detectors have high neutron interaction probabilities while maintaining low gamma interaction probabilities, making it useful in spent fuel applications where the detectors need to be placed close to the spent fuel (~50-60 cm away).
- The neutron capture process can be modeled and simulated using existing transport codes.
- Although these are small detectors, the straws can be scaled up and instrumented in larger arrays to make larger detectors that is a requirement for neutron imaging to increase the efficiency due to the modest neutron source.

Table 4. Neutron and gamma-ray interaction probability for common neutron detectors [60].

	Interaction Probability	
Thermal Detectors	***Thermal Neutron***	***1-MeV Gamma-ray***
^{3}He (2.5 cm diam., 4 atm)	0.77	0.0001
Ar (2.5 cm diam., 2 atm)	0.0	0.0005
BF_3 (5 cm diam., .66 atm)	0.29	0.0006
Al tube wall (0.8 mm)	0.0	0.014
	Interaction Probability	
Fast Detectors	***1-MeV Neutron***	***1-MeV Gamma-ray***
^{4}He (5 cm diam., 18 atm)	0.01	0.001
Al tube wall (0.8 mm)	0.0	0.014
Scintillator (5.0 cm)	0.78	0.26

3.6.1. Boron Coated Straw Detector Configuration

The boron coated straws selected for this application are commercially available and are manufactured by Proportional Technologies, Inc. (PTI). The design concept is to embed the boron straws in a matrix of high density polyethylene (HDPE) to moderate the fast neutrons from spent fuel down to thermal energies to be detected by the straws. A single straw consists of a long copper tube that has a thin layer of ^{10}B-enriched boron carbide ($^{10}B_4C$). The fast neutrons that are thermalized are captured by the ^{10}B in the B_4C layer and are converted into secondary particles via the $^{10}B + n \rightarrow {}^{7}Li + \alpha$ reaction. The ^{7}Li particle has 0.84 MeV of energy and the α particle has an energy of 1.47 MeV and when either of these two particles escape the boron carbide layer, they enter the detector fill gas and ionizes it as they traverse through it. The straw detector acts as a proportional counter, where the tube wall acts as the cathode, and the thin anode wire passes down the center of the straw. The electrons that are created in the gas drift towards the anode wire and a signal is generated when the detector threshold is exceeded. A cross section diagram of a single straw is shown in Figure 33.

The thickness of the boron carbide layer can be varied in order to maximize the neutron efficiency. In order to minimize gamma sensitivity, the number of straws instrumented per readout channel should be minimized. A single detector for this system is envisioned as a group of straws arranged in rows embedded in a HDPE matrix. PTI investigated three different straw pitches (1.0, 1.1, and 1.2 cm) for a geometry with 100 detectors and different thicknesses of B_4C to calculate the expected efficiency. A figure of the three detector geometries evaluated is shown in Figure 34. The results from the evaluation of the three straw pitches is shown in Figure 35.

The simulation results below show that the efficiency peaks at different thicknesses for the three different pitches investigated. For this particular system, one way to minimize gamma sensitivity to a detector, is to reduce the active volume of the detector, or choose the geometry with the least number of straws. The largest pitch case has a maximum efficiency at 1.4 μm thick B_4C which is ~2.5% less than the most efficient configuration. This proves to be the most favorable design since the large pitch size means that this geometry requires the least number of straws per detector, making it more economical and least gamma sensitive. The chosen design for most of the simulations presented here consists of 23 straws per detector

(pitch size of 1.2 cm), with 100 detectors in total and a 100 slits pointing down to the center of each detector. For the simulations to follow for the 100-detector geometry, 1mm of Cd was inserted as a layer on the inner radius of the detectors, and 3mm of Cd was modeled on the outer radius of the detectors. The main components in the straw along with their dimensions are shown in Table 5. These detector component dimensions are also used in the simulations. Although the final geometry of the detectors changed in the end (as will be described in a later chapter), the straw components in the table below remained the same. Figure 36 shows a cross sectional view of an MCNP model of a single straw.

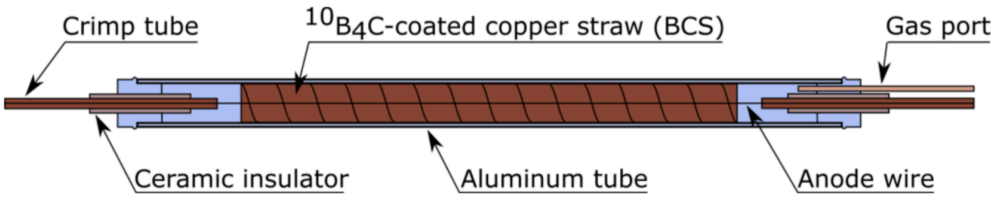


Figure 33. Cross sectional image of a single boron carbide straw [62].

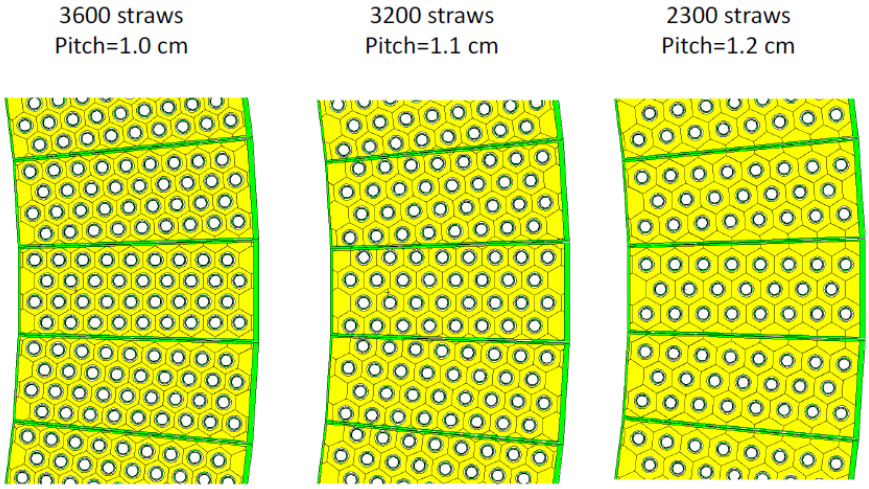


Figure 34. Illustration of three different detector straw geometries simulated by PTI [34].

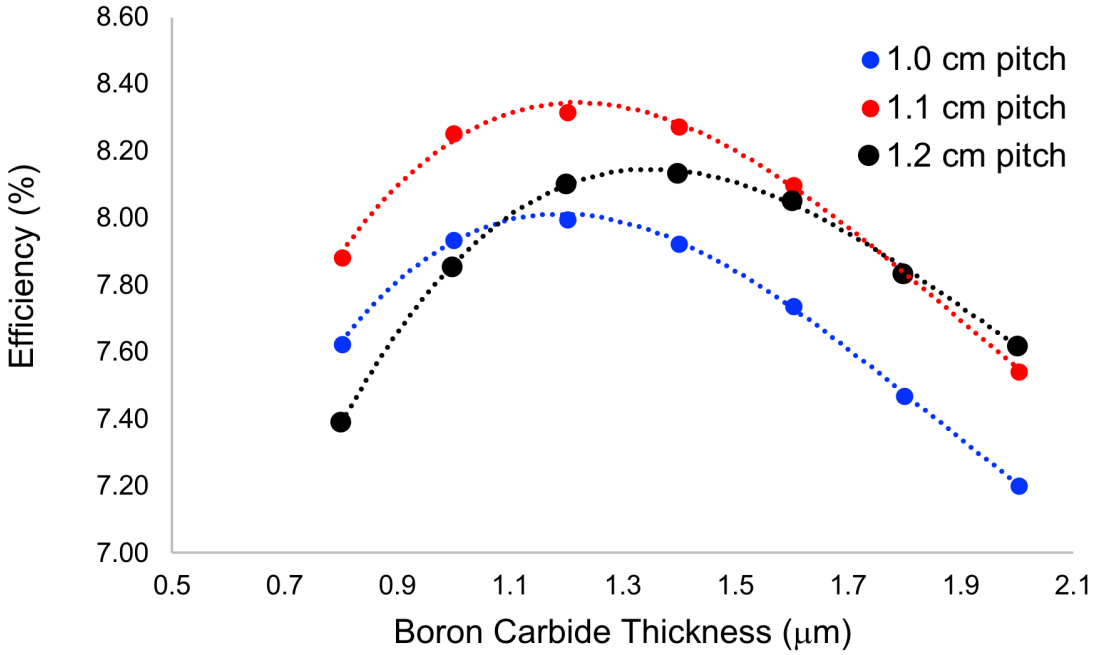


Figure 35. Detector efficiency as a function of boron carbide thickness for the three different pitch sizes simulated [34].

Table 5. Main components of a boron carbide straw and respective dimensions and material parameters [61].

Component	***Material***	***Radius (cm)***	***Thickness (cm)***	***Density (g/cm^3)***
Fill gas	90% Ar, 10% CO_2	0.22150	-	$1.20\text{x}10^{-3}$
Boron Carbide	B_4C with ^{10}B enriched to 96%	0.22164	$1.4\text{x}10^{-4}$	2.38
Coating tube	Copper	0.22434	$2.7\text{x}10^{-3}$	8.96
Detector wall	Aluminum	0.27666	$5.2\text{x}10^{-2}$	2.70

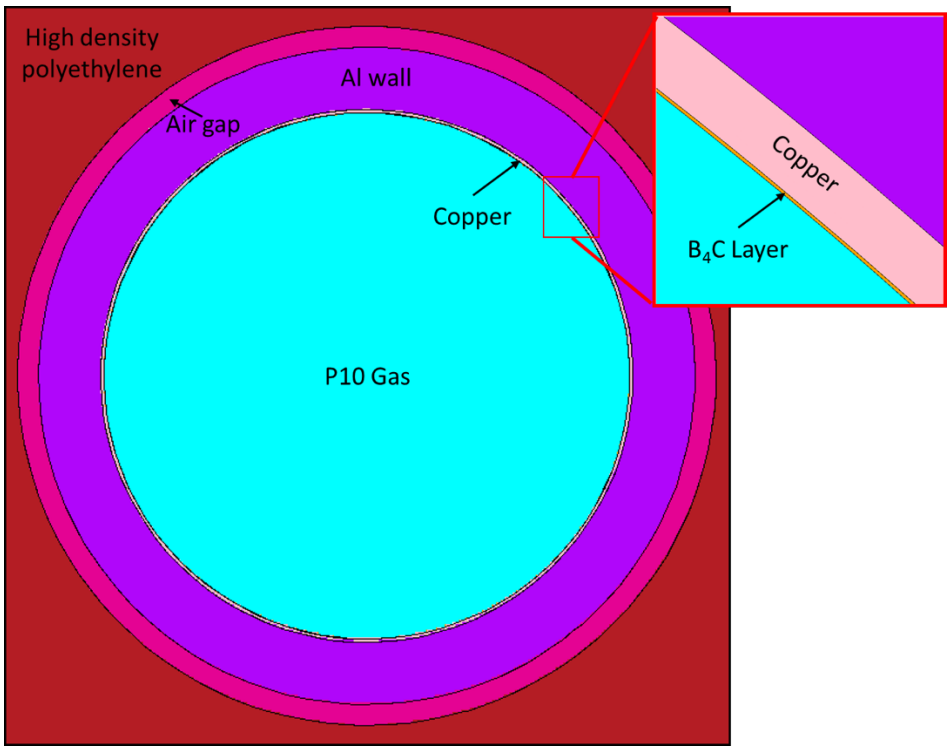


Figure 36. MCNP model of a single straw and its various components located in a high density polyethylene matrix.

3.7. Simulated Geometry

To build a complete imager geometry, over 300 plane surfaces were used in just building the collimator slits and had to be generated at different positions for each of the 512 geometries. The detectors were constructed using a repeated hexagonal lattice structure to alternate the number of straws 8-7-8. Each lattice consisted of universes corresponding to either an empty polyethylene hexagon cell or a hexagon filled with a straw detector surrounded by polyethylene. A box constructed with four surfaces enclosed the lattice of 23 detectors, and this box was translated and repeated 100 times going around 360˚. A close-up of the lattice is shown in Figure 37. The translations for the detector boxes and the 49 planes that bound the 100 detector wedges were calculated for each of the different geometries using a MATLAB script. A Python script was then used to generate the 512 MCNP input decks by combining the collimator surface cards and cells with the detector surface cards and cells.

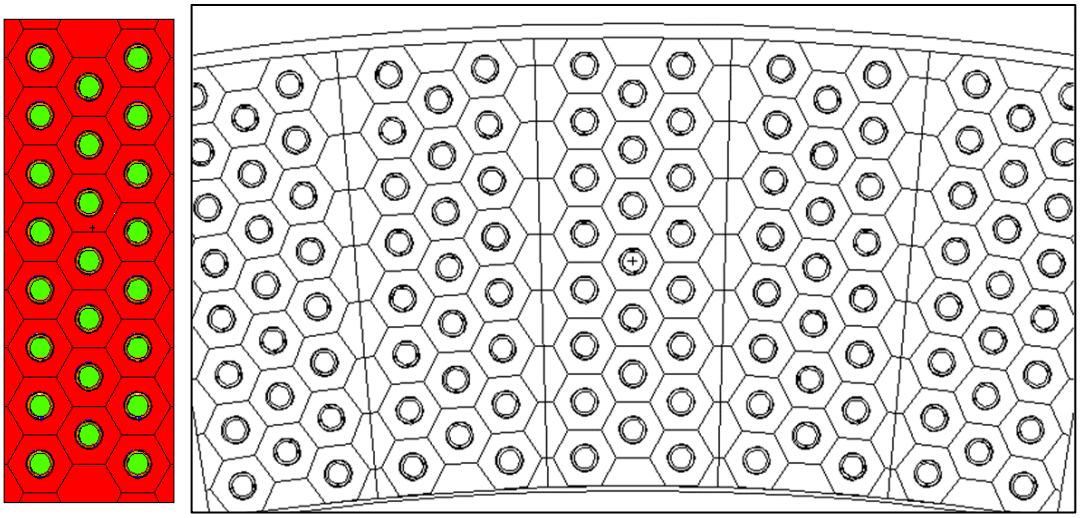


Figure 37. (Left) The detector box with a repeated hexagonal lattice filled with 23 straws in an 8-7-8 pattern. (Right) A close-up of what the 100 repeated detector cells look like when the box on the left is translated.

4. GAMMA EXPOSURE SENSITIVITY

When it comes to evaluating neutron detectors for use in high gamma-ray exposure environments, pulse pileup can be of concern and may cause false count rates in the detector. This chapter will focus on the experiments conducted with a detector module provided by PTI at ORNL. The experiments were used to evaluate the detector electronics' capability to reject gamma counts and identify the operational limits of the system. The experiments were followed by a series of simulations evaluating all 512 geometries identified in the previous chapter to calculate the maximum gamma-ray exposures seen at the detectors when exposed to a full fuel assembly.

4.1. Experiments

To experimentally determine the sensitivity of the boron straw detectors to high exposures, a series of measurements were performed at the ORNL RaSCaL cesium-137 irradiator facility with a prototype neutron detector with 23 straws. At the time of these experiments, the activity was 1012 Ci. A picture of the detector mounted on the irradiator table is shown in Figure 38 and a view of the straws as seen from the detector end is shown in Figure 39.

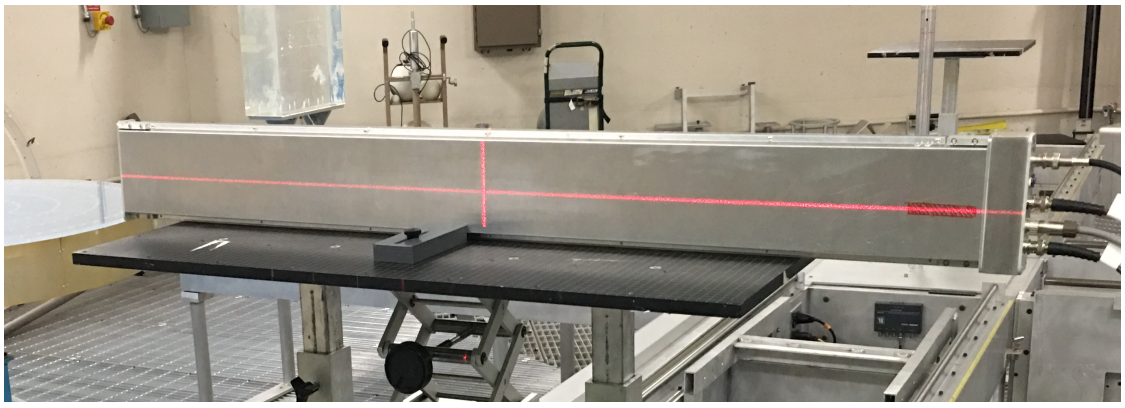


Figure 38. The prototype detector during irradiation experiments at the RaSCaL facility. The gamma radiation from the ^{137}Cs source was centered on the crosshairs of the red laser,

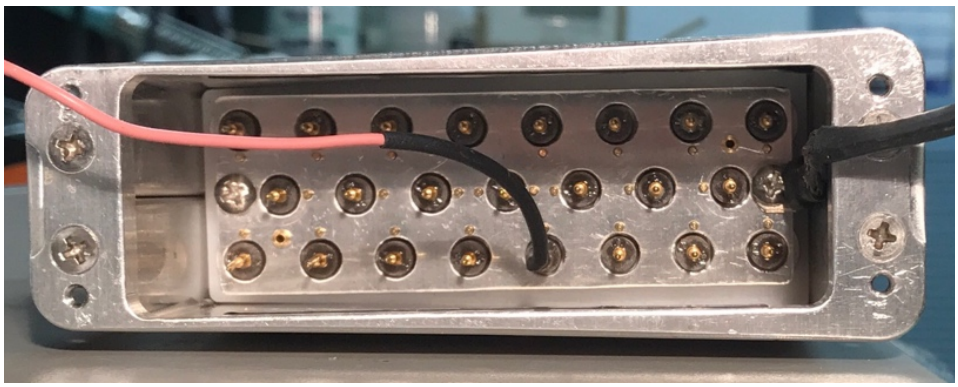


Figure 39. View from end of detector showing all 23 straws.

To emulate exposure to comparable exposures to those originating from spent fuel, the detector was exposed to the highest possible exposures available from the irradiator. This was done by positioning the irradiator table a distance 78 cm from the irradiator opening. At this distance, the source illuminated approximately 1/3 of the detector with a maximum exposure of 432 R/hr, a configuration equivalent to exposing 8 straws of the 23 in their entirety to 432 R/hr. Table 6 shows the list of exposures the detector was exposed to in the series of measurements conducted.

In total, three different experiments were conducted at the RaSCaL facility in order to test different preamplifier circuit designs and their ability to perform at the higher exposures. The initial circuit that was tested with the detector was designed at ORNL. A diagram of the experimental setup is shown in Figure 40. The detector was setup in the irradiation bay on a platform that could move it further and closer to the ^{137}Cs irradiator. Long BNC cables were connected from the detector, out the shielded doors, into the neighboring measurement room where the computer controlling the irradiator was. The electronics were also placed in the measurement room as shown in the diagram below. For the first two experiments, the signal out of the detector feeding into the quad single channel analyzer (SCA) was a low voltage TTL, but for the final set of experiments the signal was a linear analog output, which is why the setup varied slightly between the first two and the last measurement campaign.

The difference was in how the threshold was set. In the first two experiments, the threshold was set by using an external low-noise, high-precision voltage source and in the last

experiment the threshold was set directly at the SCA as shown in Figure 40 using the same source in its auxiliary lower threshold input. The goal of the measurements was to evaluate the detector's ability to reject gamma-ray counts for various exposures in order to converge on the final operating threshold that makes the detector sensitive primarily to neutrons. The terminated signal out of the detector was fed into the Quad SCA which is connected to the threshold setting box. The threshold box allows for varying the threshold without having to adjust it on the detector itself. The terminated output from the Quad SCA is then fed into a counter. The counts registered by the counter were then divided by the measurement time to calculate a count rate. Depending on the threshold value, the measurement time was varied from 1 minute to 5 minutes to get statistically accurate count rates.

Table 6. Gamma source information for Cs-137 irradiator facility (RaSCaL) at ORNL. The exposure at three different source-detector distances is shown along with the attenuation factors.

Source Type	Cs-137	
Half-life	30.17 years	
Exposure (on Feb 1, 2018) (R/hr)	***Source-Detector Distance (cm)***	***Attenuation Factor***
430	77.9	*none*
105	156.9	× 4
22	240.2	× 20

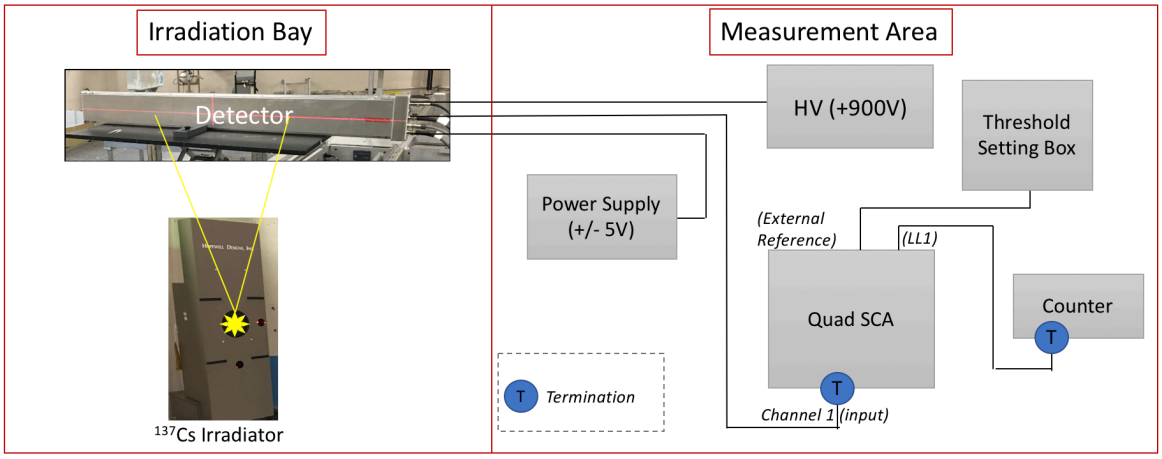


Figure 40. Experimental setup for the final measurement campaign conducted at the RaSCaL facility.

4.1.1. Measurement Campaign #1

The first set of measurements were performed on October 4, 2017. For this set of measurements, a ^{252}Cf source was placed in a polyethylene block on the back side of the detector (opposite side exposed to the irradiator). The placement of the block with the ^{252}Cf source is shown in Figure 41. The count rate data from exposing the detector to the three different exposures as a function of varying detector threshold is shown in Figure 42. The reason the exposures is slightly different from those listed in Table 6 is because of the source calibration data listed was acquired after the first campaign. This circuit had a 250 ns peaking time bipolar signal. The tail on the left side of the curve is due to the count rates increasing significantly as the threshold is reduced because the detector is accidentally triggering on gamma pulse pileup events. The data set shown in grey (0R/hr) shows count rate data taken with just the ^{252}Cf source present. Ideally, once the threshold is set high enough, the count rates seen should only be reflective of the detector counting neutrons, and the blue, red, and pink curves should align with the 0R/hr curve. However, it was observed that the count rates dipped lower than the 0R/hr curve as the threshold was increased. It was observed that this data was gathered without termination on the signal cables. A second set of measurements was conducted with 50 Ω terminators on the signal cables. The data from the second set of

measurements is shown in Figure 43. The curves align slightly better with the 0R/hr data as expected at higher threshold values, but still drift slightly below the 0R/hr line. Also, the counts only drop down to match the 0R/hr data around 110 mV. The goal is to get the threshold at which the gamma pileup dies down to be as low as possible, so measurement times can be decreased.

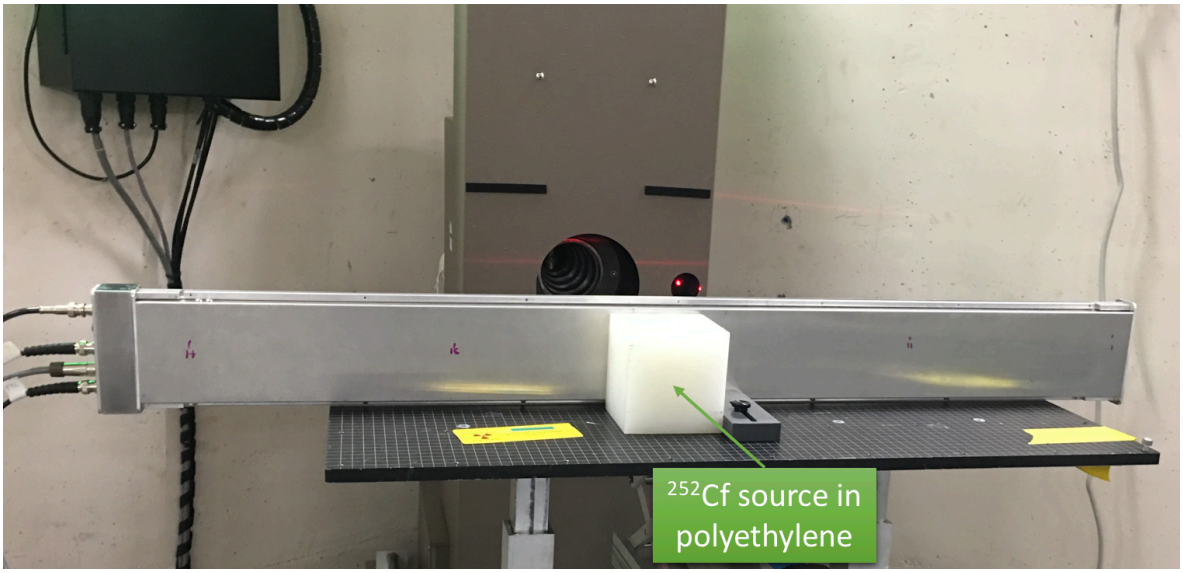


Figure 41. Setup with ^{252}Cf source for the first measurement campaign on October 4, 2017.

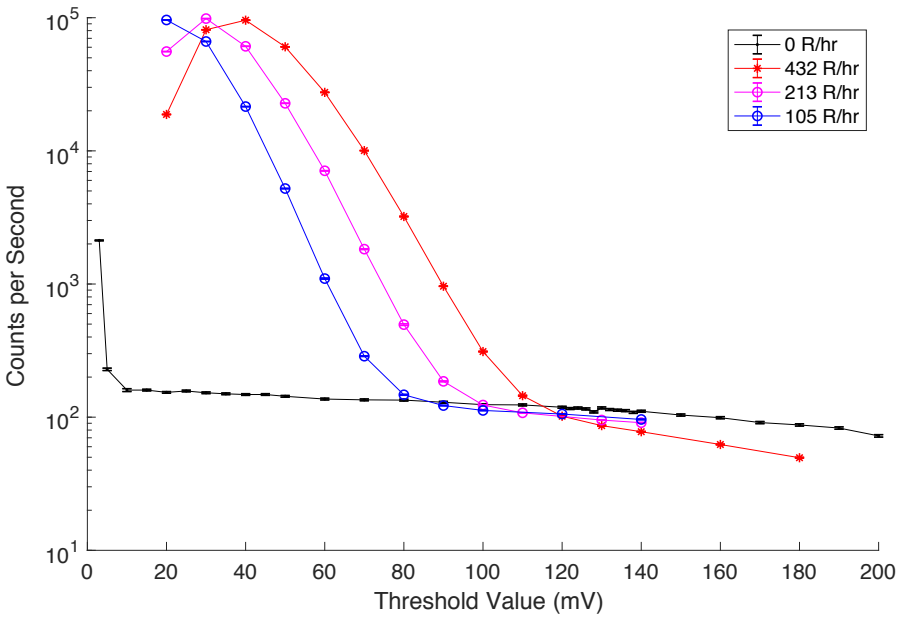


Figure 42. Count rate measured as a function of threshold setting using the first bipolar circuit design for the three different exposures as well as a 0R/hr measurement. This data set was collected without cable termination.

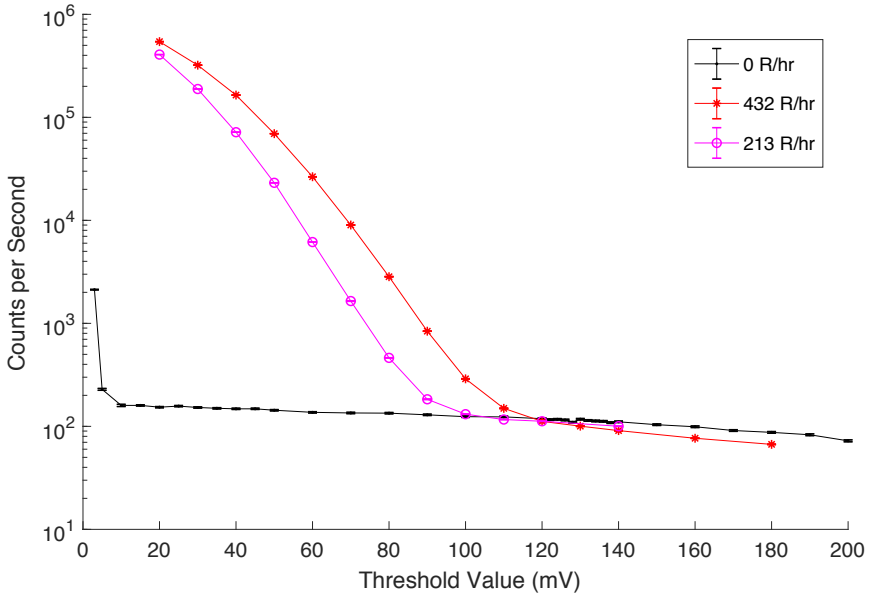


Figure 43. Count rate measured as a function of threshold for different exposures with 50Ω termination on the signal cable.

4.1.2. Measurement Campaign #2

The second measurement campaign was conducted on November 29, 2017 and December 13, 2017 and the ORNL circuit was replaced with a circuit manufactured by PTI and improved by ORNL. This circuit had a short unipolar signal with a 50 ns peaking time. The downside of this choice for the signal shape is that the baseline will not be able to remain at 0 at high count rates, which may result in the count rates seen at the higher exposures drifting below the 0 R/hr line. This was somewhat mitigated by the presence of a Robinson baseline-restorer, but the problem remained at very high exposures. Data from this measurement is shown in Figure 44.

There are two possible reasons as to why the count rates drifted below the 0R/hr line: (1) the detector gas itself can only give off so many electrons, so the ionizations from the intense gamma rays are so overpowering that there aren't enough electrons to make up the gain for the neutrons detected, or (2) the gain in the detector is not constant, and goes down as the count rate in the detector increases because of the high voltage filtering resistor used in the circuit. The reason for the count rates dipping below the 0 R/hr line ended up being due to the gain shift at higher exposures induced by the company-supplied high voltage filter resistor. A simple circuit diagram is shown below in Figure 45. Here, at higher exposures the gamma-ray signals are so frequent that they look like a continuous current to the detector. This current creates an additional voltage drop across the resistor shown in Figure 45, so the high voltage seen by the detector is lower (since it is the difference between the high voltage applied and the voltage drop). Thus, the effective gain applied to the detector goes down, and as a result the pulses generated by the detector may not be high enough in amplitude to hit the set threshold level, thus it appears as if the detector registers less counts, making the count rate at higher exposures fall below the 0 R/hr line. One way to mitigate this is to replace the megaohm resistor used in this circuit with a resistor of a lower value.

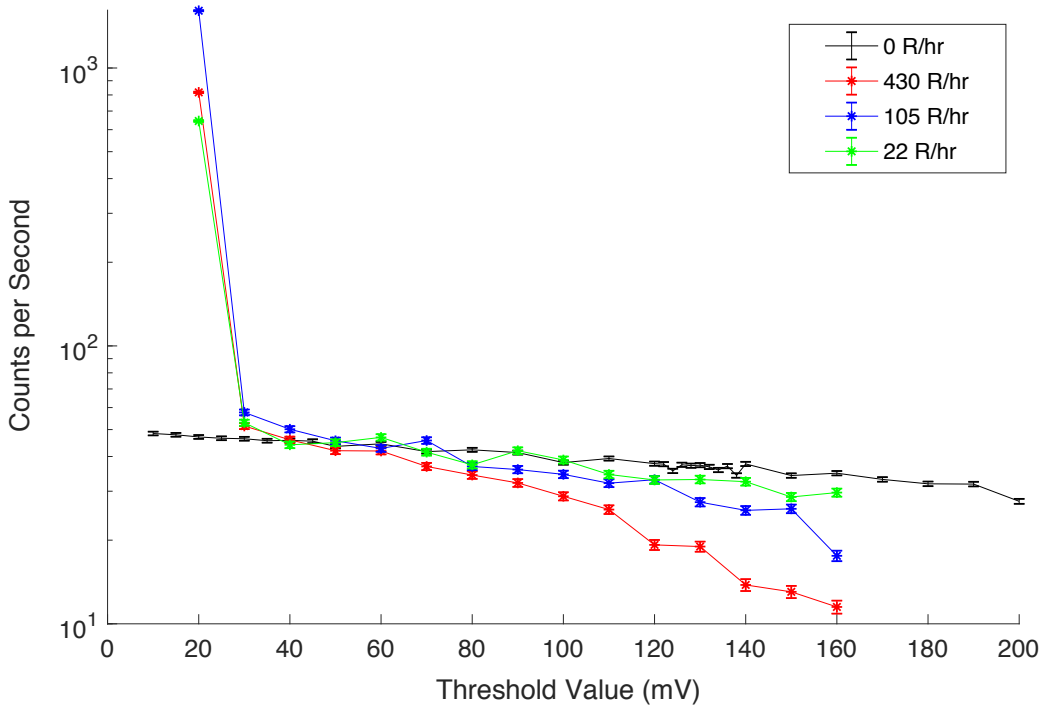


Figure 44. Count rate as a function of threshold for different exposures using the circuit provided by PTI with the ^{252}Cf source present.

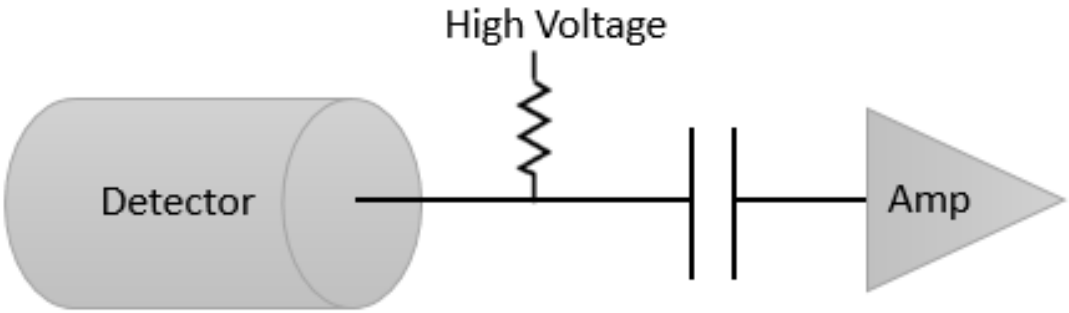


Figure 45. Circuit diagram of PTI's configuration.

4.1.3. Measurement Campaign #3

The third measurement campaign took place on February 1, 2018. For this set of experiments, the same circuit was used as in Figure 45, but the megaohm resistor was replaced with a 10 kilo-ohm resistor in order to reduce the current pull at higher count rates and lessen the effect of the count rates dipping below the 0 R/hr line at higher count rates. The reduced resistor value was chosen to ensure that the high voltage filtering effect was still effective. The data for this set of experiments is shown in Figure 46. The data here is more promising since the count rate at higher exposures does not dip below the 0R/hr line. To get a better idea of whether the detector circuit is limited by large single gamma pulses, the 430R/hr curve was divided by 4. If the electronics are limited by large gamma pulses, the gamma tail (at lower thresholds) for the 430 R/hr data divided by 4 should be identical to and line up with the 105.1 R/hr gamma tail. The same goes for the 105.1 R/hr data divided by 4.77 compared to the 22 R/hr gamma tail. The assumption here is that at 22R/hr the detector is able to measure all pulses. Figure 47 shows the count rate data for all three count rates in addition to the two scaled curves.

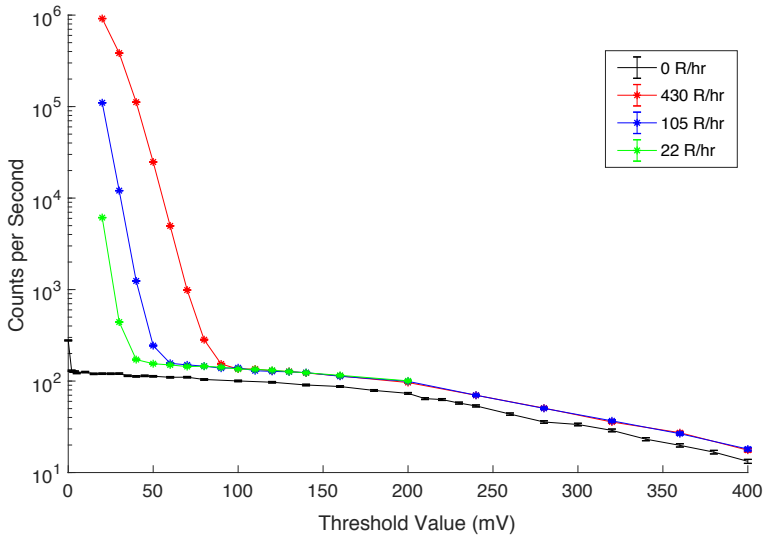


Figure 46. Count rate as a function of threshold for different exposurees using the circuit with resistor replaced.

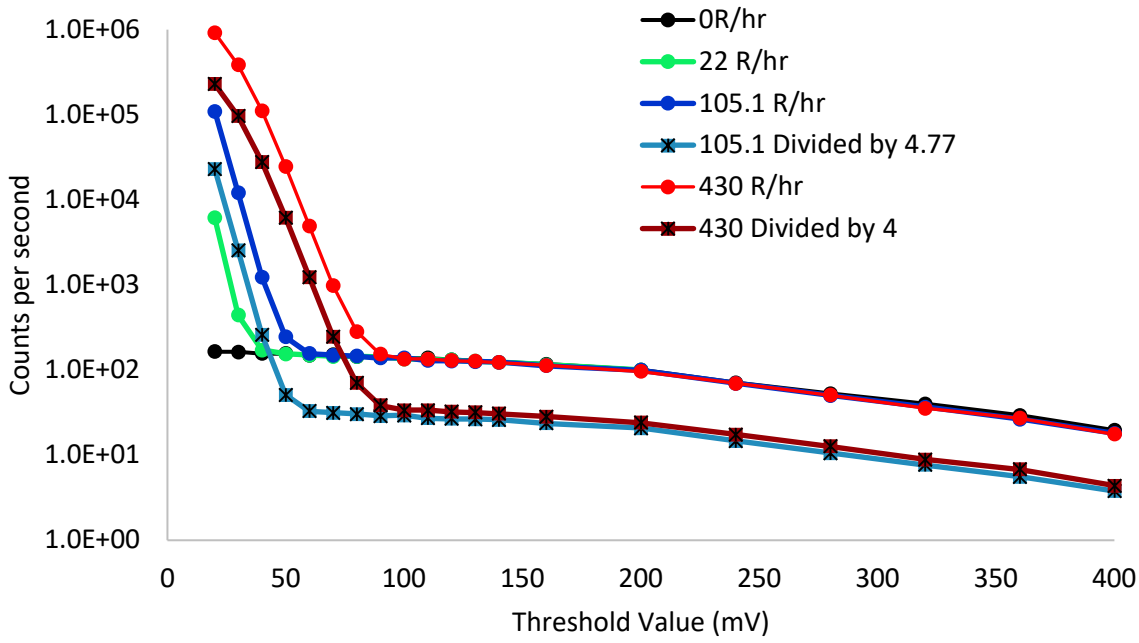


Figure 47. Count rate as a function of threshold for different exposurees using the circuit with resistor replaced. The two additional curves shown are the count rates for 430 R/hr divided by 4 and 105.1 R/hr divided by 4.77.

The gamma tail of the 430 R/hr curve divided by 4 does not line up close to the 105R/hr data, and the gamma tail of the 105 R/hr data divided by 4.77 is not identical to the 22 R/hr but is close. There are two reasons as to why the gamma tails do not line up exactly. The first has to do with the baseline shifting at higher count rates (as mentioned before, the simple baseline-restorer used is not completely effective.) When using unipolar pulses, ideally the baseline stays at 0 which means that between each pulse, sufficient time is allowed to let the signal come down to 0 as shown in Figure 48. Since the circuit does not have a baseline restorer, during high count rate situations, the pulses do not have the ability to get down to 0 between each event, which causes the pulses to overlap, and as a result the baseline to rise above 0 and the pulses cross the threshold shown by the dashed line in Figure 49.

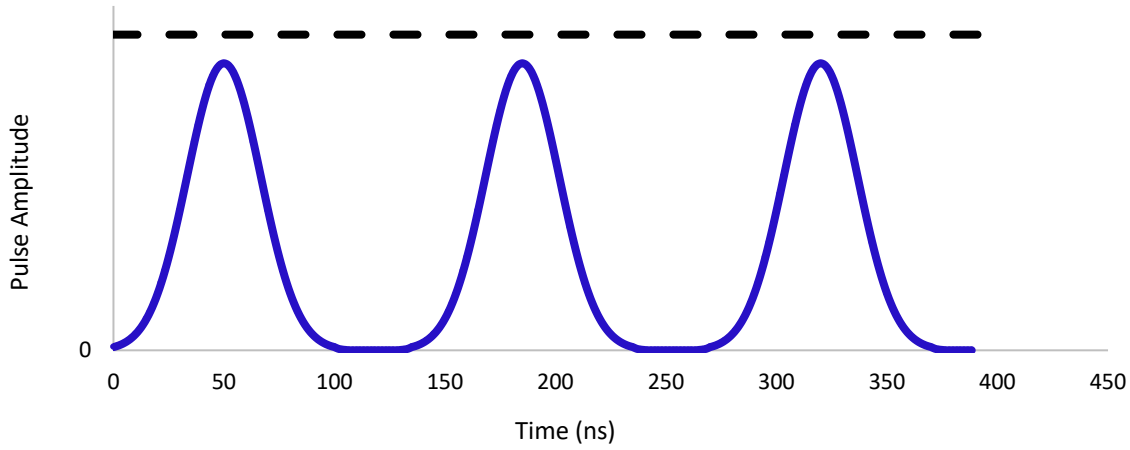


Figure 48. Unipolar pulses with 50 ns peaking time where the signal goes down to 0 between each pulse.

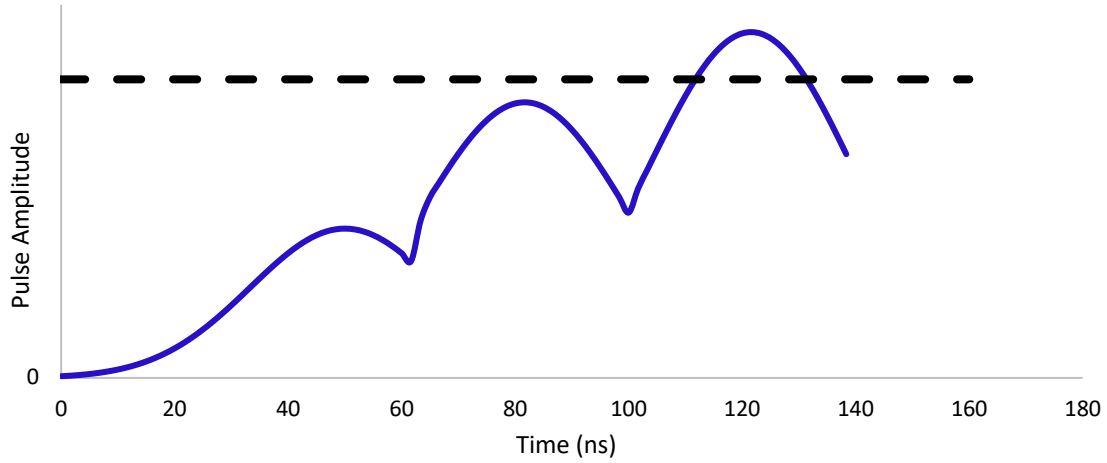


Figure 49. Example of overlapping unipolar pulses in a high-count rate situation where the pulse cannot die down to 0.

When the baseline rises, the effect it has on the pulses is equivalent to lowering the threshold, which means that the circuit is counting more counts than it should. This is why when using the counts from 430 R/hr (C') to scale down to predict 105.1 R/hr (C), when dividing C' by a constant factor (f), it will not equal C exactly at low threshold values. This explains why the two curves (C and C') for both the 22 R/hr and 105.1 R/hr on the gamma tail do not line up. The second feature seen on the 430 R/hr curve that isn't evident on the lower exposure curves is the fact that the count rates roll over at lower thresholds. This is an effect that is evident in the 430 R/hr divided by 4 curve which does not line up at all with the 105.1 R/hr curve and is shaped differently. This has to do with the filtering resistor effect where at high count rates the charge (Q) running through the detector causes the current across the resistor (Figure 45) to increase and the gain to drop. With the lower gain, the count rates are lower, resulting in the curved shape at the higher count rate. This means that the detectors are at their functional limitation at 430 R/hr when all 23 rows are instrumented together. The experiments showed that in order to tolerate these higher exposures, the detector rows may need to be instrumented individually in the final design. Oscilloscope traces of the detector baseline when exposed to different exposures are shown in Figure 50. This set of traces also shows that at the highest exposure of 430 R/hr, there is significant deviation from the baseline. The cause of the baseline deviation could be attributed to either pileup effects or gamma rays from the irradiator depositing large amounts of energy.

Figure 51 shows MCNP simulation results of the pulse height registered in 23 straws as a function of the energy deposited (MeV). The gamma simulations are shown on the left and agree with the scope traces from the measurements in that at high exposures, large amplitude signals become highly probable from ^{137}Cs photons depositing higher energies in the gas, thus increasing the count rates. For the gamma simulations, MCNP5 was used to get results from a high statistics simulation. A total of 7.13×10^{10} histories of 662 keV gammas were simulated. A one second simulation of 432 R/hr exposure is equivalent to 9.55×10^{10} gammas. The neutron spectrum simulation was provided by Dr. Jianwei Hu.

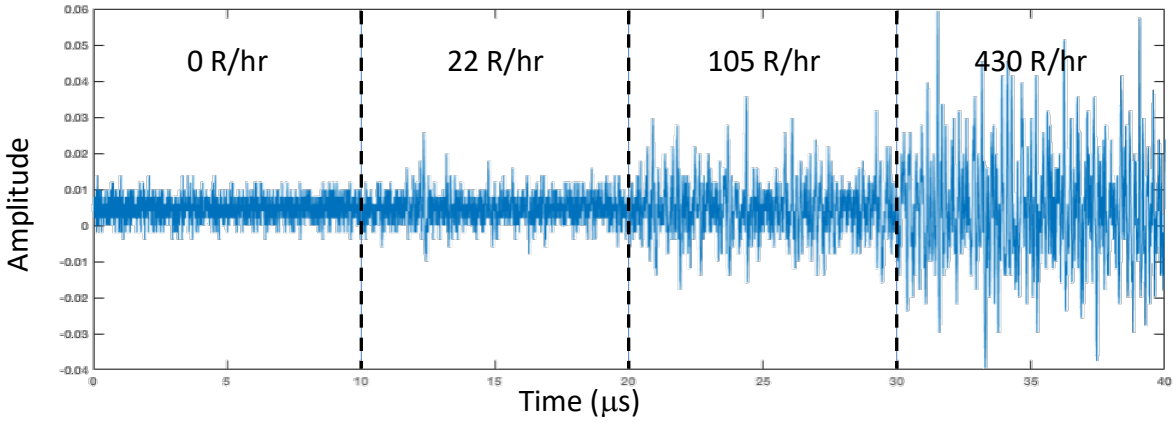


Figure 50. Scope traces from the detector exposed to different gamma exposures [63].

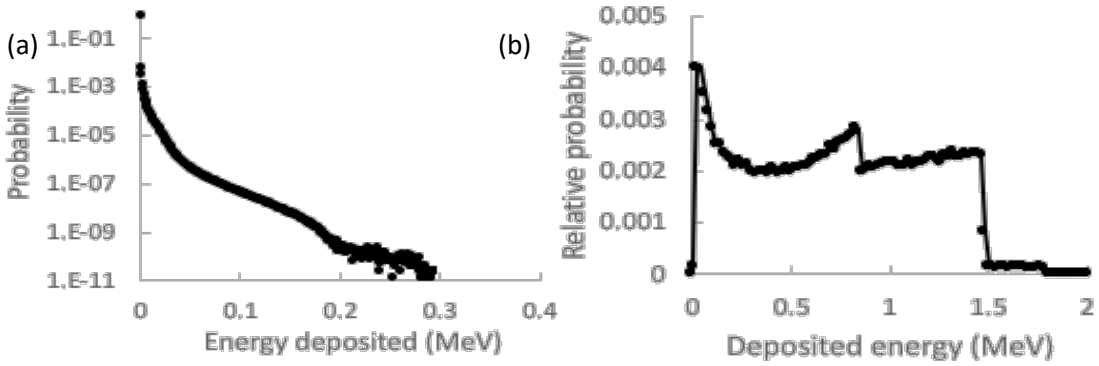


Figure 51. Pulse height spectrum vs. energy (MeV) from a MCNP simulation of a (a) beam of 662-keV photons incident on a single detector and (b) pulse height spectrum for neutrons [63].

Looking at the two curves in Figure 51, it is important to identify the threshold parameter that would ideally exclude all of the gamma contributions [63]. The gamma pulse height spectrum along with the simulated neutron pulse height spectrum was used to calculate the expected count rate as a function of threshold setting (mV) for 430 R/hr and 22 R/hr. A conversion of 300 mV/MeV in the straw detector was used, the simulated curves were plotted along with measured data for exposures of 0 R hr^{-1}, 22 R hr^{-1}, and 430 R hr^{-1}, and are shown in Figure 52 [63]. Here, the calculated count rates track well with the measured count rates at 430 R/hr but over-predict the count rates for lower discriminator thresholds at 22 R/hr. This discrepancy is most likely due to differences in the experimental and modeled spectra from the irradiator. The simulations used a beam of 662 keV gamma-rays as the source, whereas the measurement source includes down-scattered energies from the collimator and attenuators. The simulations show that the detectors are at or close to their fundamental limitation set by low-probability, large amplitude interactions of single gamma rays. As a result, only configurations having a maximum exposure less than 500 R/hr should be considered for this application. To ensure that the amount of detector pileup in imaging measurements is no more than that encountered in the high exposure measurements, the detectors will be instrumented with a preamplifier per row of straws.

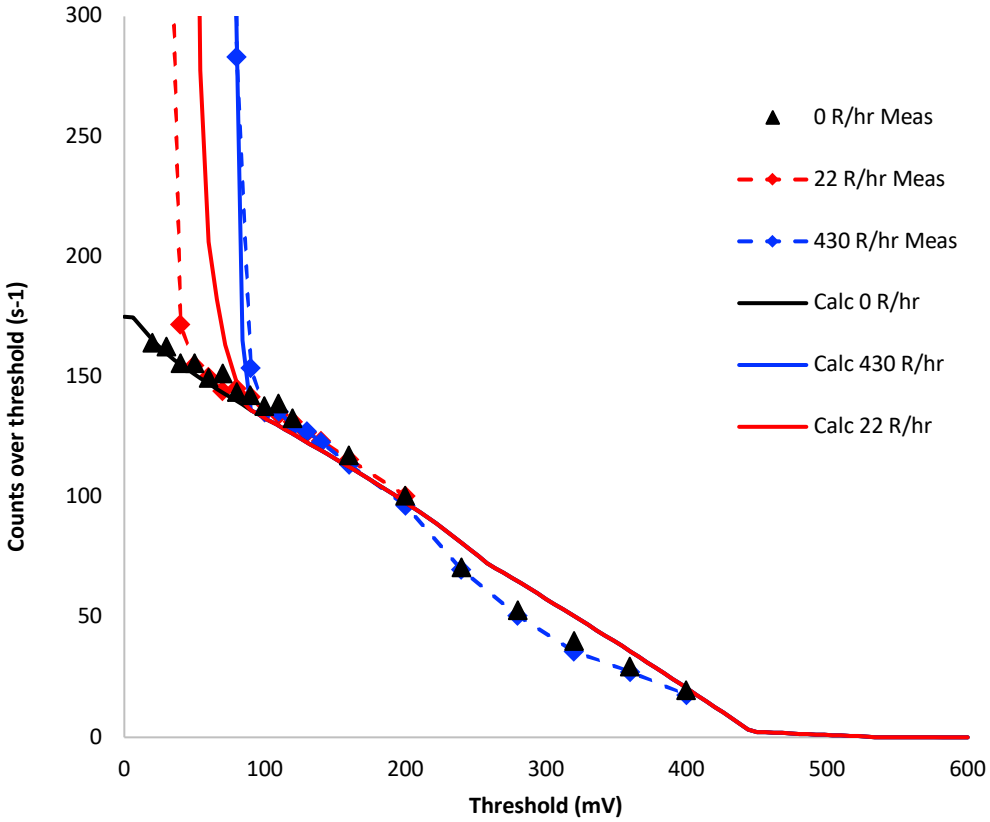


Figure 52. Measured (solid) and simulated (dashed) counts per second in a single detector module as a function of detector threshold for different exposures [63].

5. SIMULATION DESIGN STUDY: GAMMA EXPOSURE

This section will detail the simulations performed to understand how the imager response to gamma-rays from spent fuel changes as a function of the physics design. This data in combination with the neutron response design study (next chapter) will help converge on the optimal imager design. To evaluate the gamma-ray response, exposure rates were calculated for each detector in each configuration and these results were used to understand how the exposures are expected to scale with collimator parameters. The following steps were implemented and will be detailed in this chapter:

- Maximum and average exposures were calculated for a survey of parameter space using MCNP5 for all 512 geometries.
- Understand how exposures at the detectors scale with imager parameter changes and, develop a way to relate the required exposure to required imager geometry. The gamma exposures and various close and open fractions will be used to develop an equation to predict the ideal geometry to limit the gamma-ray exposures to a specific value.
- Identify configurations that are acceptable based on the measurement data and simulations predicting the largest exposures seen at the detectors using the worst-case source.

5.1. Gamma Source Term

The gamma source term used was a standard 17 × 17 fuel assembly with a homogeneous distribution of gammas throughout the pins. The source term was provided by the Reactor and Nuclear Systems Division (RNSD) at ORNL. The software SCALE/TRITON was used to generate the ORIGEN libraries for the source term and ORIGAMI was used with those libraries and power histories to generate the final isotopic compositions for the source term. In the MCNP deck, the source definition specified the gamma emission probabilities for 20 different energy bins, and the material card for the fuel pellets contained the isotopic information output by ORIGAMI for a fuel assembly with a burnup of 40GWd/MTU and a 1-year cooling time. To evaluate the gamma exposures, a 1-year cooling time was used since

that is the absolute earliest a fuel assembly can be moved in the pool. This is the worst-case scenario for gamma exposure that the imager needs to be able to tolerate since gamma sensitivity is the main limitation of such a system. Monte Carlo simulations for all 512 cases were run, and the interactions within the P-10 fill gas in the detectors were tallied using the F6 tally. The F6 tally in MCNP when used with photons, calculates the track length estimate of energy deposition by photons in the material of interest (P-10 gas) and is given by Equation (2) below

$$WT_l\sigma_t(E)H(E)\frac{\rho_a}{m} \quad (2)$$

Where W is the particle weight, T_l is the track length in centimeters which is equal to even transit time × particle velocity, $\sigma_t(E)$ is the microscopic total cross section in barns as a function of particle energy, and $H(E)$ is the heating number $\left[\frac{MeV}{Collision}\right]$ which is the difference between incident gamma energy and the sum of the product between probability of reaction (for incoherent or Compton scattering, pair production, and photoelectric absorption) and average exiting gamma energy for the specific reaction type. Finally, ρ_a is the atom density $\left[\frac{atoms}{barn\ cm}\right]$, and m is the cell mass in grams. The F6 Tally results from the simulations were gathered for each detector cell (every row of 3) and is in units of $\frac{MeV}{gram * photon}$. A sample F6 tally specification for a single detector is shown below:

F6:p (11 < 902 < 21 < 201)

The geometry is built with repeated universes and lattices of straws (cell 11 is the single straw cell corresponding to the P-10 gas, and cell 902 is the repeated hex lattice), so the tally specification above means that the total F6 response is recorded for all 23 occurrences of cell 11 in each detector wedge. This is then converted to R per hour [R/hr] using the following conversion shown in Equation (3). MCNP in the F6 tally, divides the response by the (volume × mass density) of a single straw, and since a detector wedge contains a total of 23 straws, the output tally results need to be divided by 23 again to get the correct wedge averaged result.

$$\frac{R}{hour} = \frac{F6\left[\frac{MeV}{g * photon}\right] * \ 4.02507 \times 10^{16}\left[\frac{photons}{second}\right] * 3600\ \left[\frac{seconds}{hour}\right]}{6.24 \times 10^{7}\left[\frac{MeV}{Rad * gram}\right] * 0.876\ \left[\frac{Rad}{R}\right]}$$

(3)

where the photon intensity of $4.02507 \times 10^{16}\left[\frac{photons}{second}\right]$ was derived from the conversion shown in Equation (4). This assumes that there is 450 kg (0.45 metric tons) of uranium in a typical PWR fuel assembly.

$$8.9446 \text{ x } 10^{15}\ \frac{photons}{second * 0.1\ MTU} * 0.45\ \frac{MTU}{fuel\ assembly} = 4.02507 \times 10^{16}\left[\frac{photons}{second}\right]$$

(4)

5.2. Exposure Simulation Results

Each of the 512 configurations discussed in Chapter 3 were simulated, and for each simulation, 100 tallies were recorded corresponding to each detector. One simulation was conducted recording the exposures at each individual straw for 3 mm wide parallel slits and a collimator with 10 cm of stainless steel and 30 cm of borated polyethylene. The straw-to-straw variations in exposure were useful to understand to see what fidelity simulations were necessary. Figure 53 and Figure 54 show the plan and side views of the MCNP geometry modeled respectively for the gamma exposure simulations. The MCNP simulations were run with 1.0 x 10^9 photon histories.

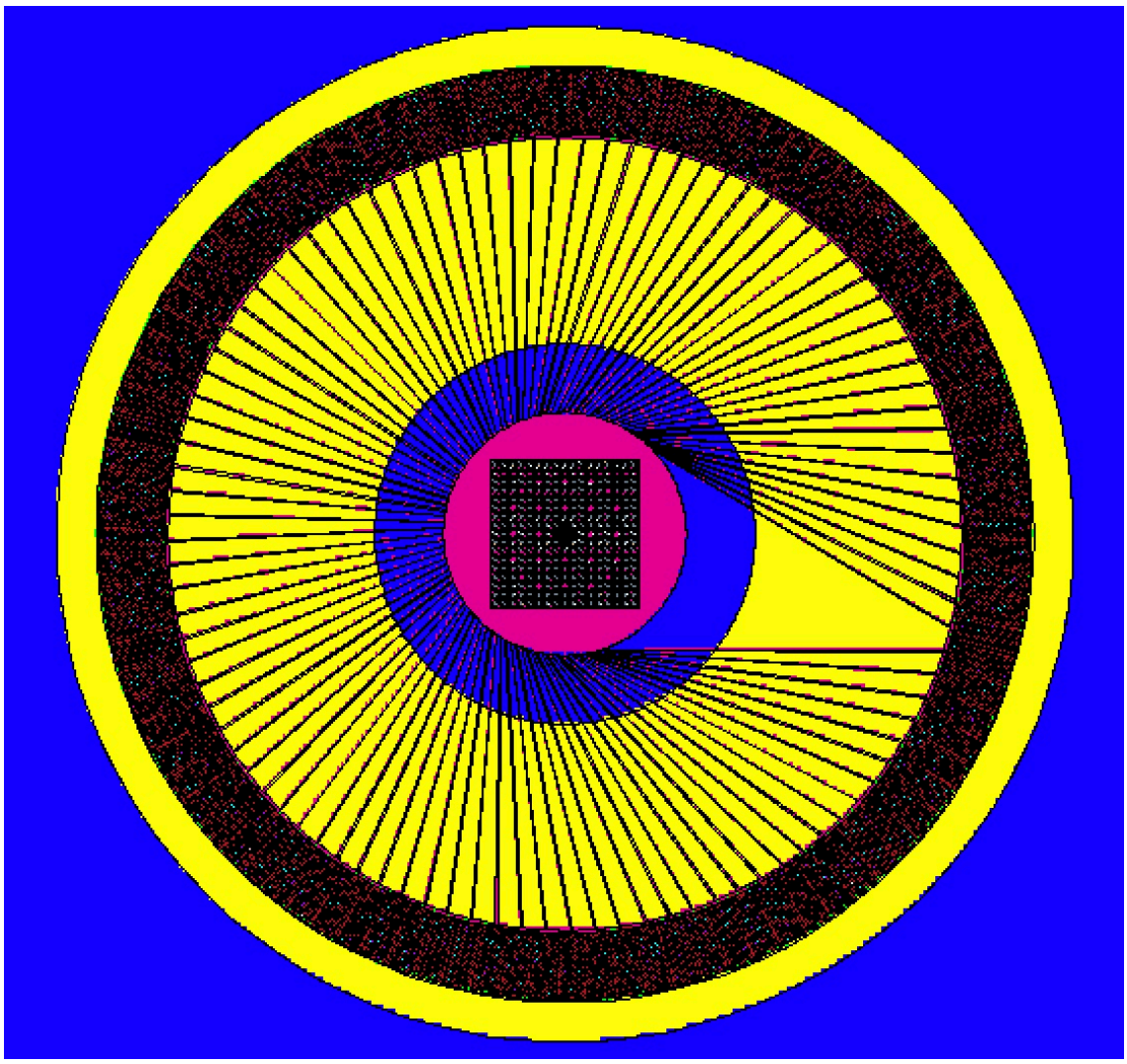


Figure 53. Plan view of the imager with 3 mm parallel slits in the collimator with 10 cm steel and 30 cm borated polyethylene.

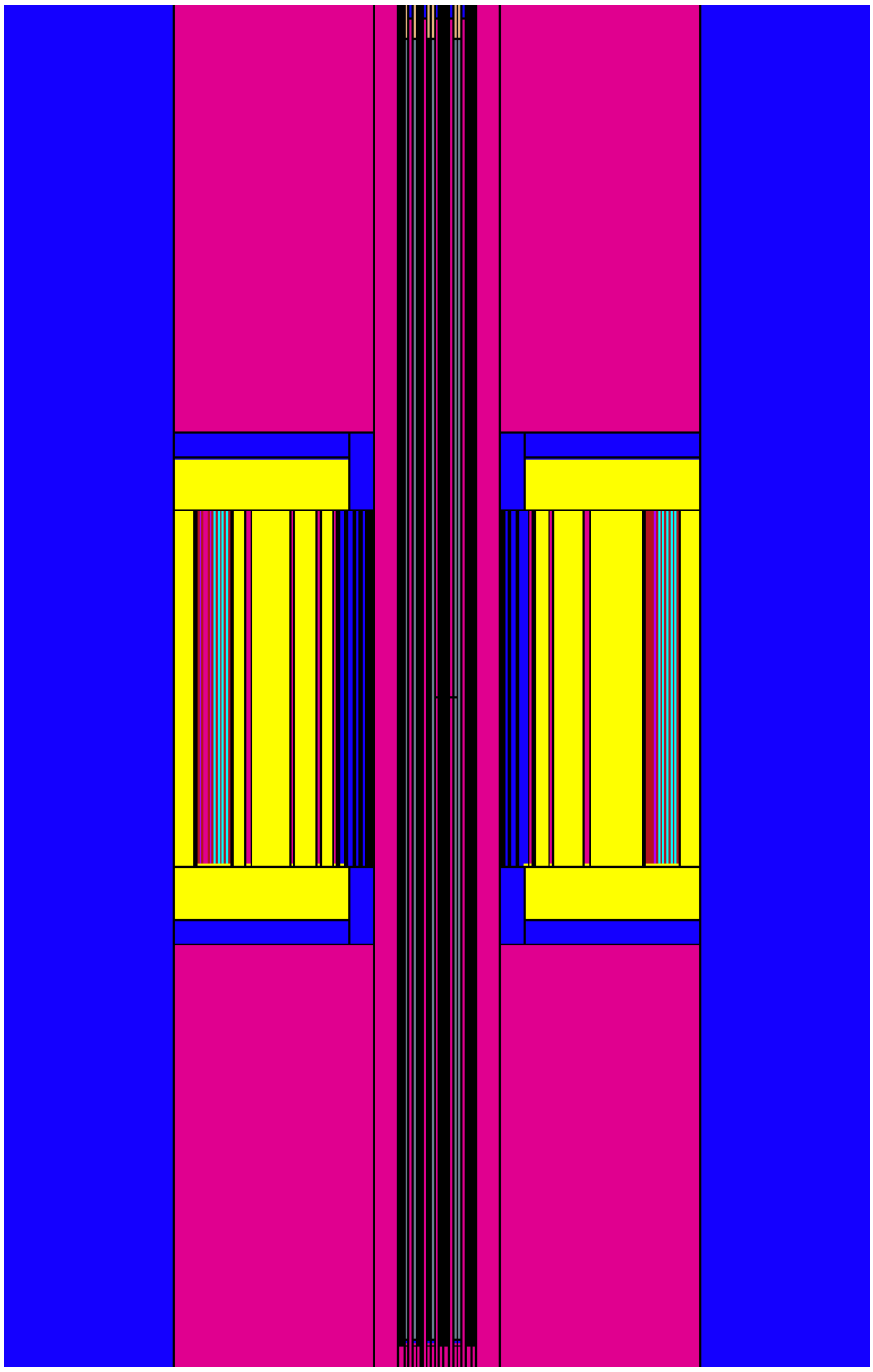


Figure 54. Side view of the MCNP geometry of the fuel assembly, imager, and container.

The simulations were conducted with shielding on the top and bottom (7 cm of stainless steel and 15 cm of borated polyethylene) of the imager to shield the straws from the fuel assembly shine on either side. Figure 55 shows a visual representation of the exposures seen by each of the 2,300 straws in R/hr. The maximum exposures seen at the individual straw level do not exceed 500 R/hr, proving that the imager geometry can successfully bring down the maximum exposure seen by the straws to manageable levels.

The exposures at the detectors are not uniform because of the varying amount of stainless steel between the source and the detectors as you go around. The effective thickness seen by each detector varies as a function of detector position. Figure 56 shows the exposure seen at each of the 100 detectors going around starting at detector 1 (corresponding to the first slit that lies almost horizontal and tangential to the fuel assembly cavity) and ending with detector 100. There are two peaks in the plot corresponding to the parts of the collimator that has the lowest stainless-steel effective density due to the high number of slits that cut in at those positions. As a result, detector number 20 sees the highest average exposure of ~295 R/hr.

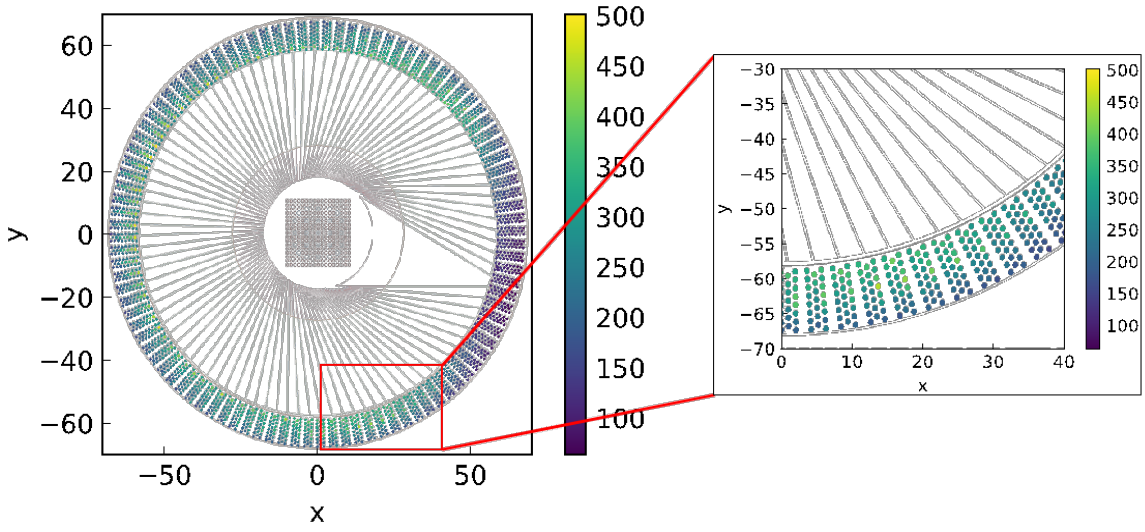


Figure 55. Map of gamma exposures [R/hr] seen at all the detector straws for a collimator with 10 cm stainless steel, 30 cm borated polyethylene, and 3 mm parallel slits with a 40 GWd/MTU burnup fuel with 1-year cooling time as the source term [34].

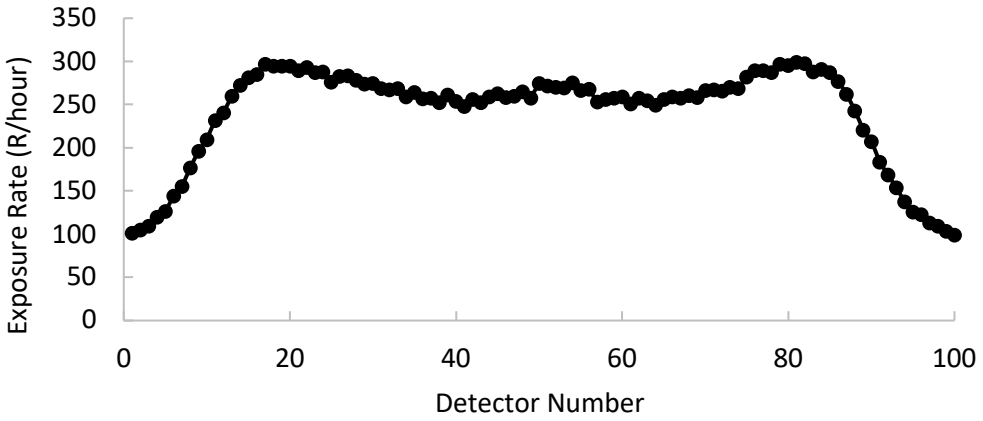


Figure 56. Exposure rate [R/hr] at each detector for an imager with 10 cm stainless steel, 30 cm of borated polyethylene, and 3 mm parallel slits [34].

The exposures seen at detector 20 for the same collimator thickness as before and varying only the slit widths (both parallel and tapered) are shown in Figure 57. Parallel slits going from 0.5 mm to 5 mm in increments of 0.5 mm, and tapered slit cases with inner slit widths from 2 mm to 4.5 mm increasing in increments of 0.5 mm with an outer slit width of 5 mm. With the parallel slits, the exposure increases significantly faster than it otherwise would with tapering the slits because increasing slit width means more radiation can stream down the slits, lowering the average collimator density.

According to PTI's initial findings, the detectors (a set of 23) should be able to perform in radiation fields up to 1000 R/hr. In order to narrow down the geometries being considered, the collimator geometries with maximum exposures higher than 1000 R/hr can be eliminated. However, due to the reasons presented in Chapter 4 about the gamma ray sensitivity measurements of the detector prototype, the maximum exposure tolerable by any of the detectors should be 500 R/hr. Figure 58 shows the maximum exposures for all the cases simulated as a function of stainless steel open fraction. By setting a limit at 500 R/hr (red line), 134 geometries can be eliminated from consideration due to unmanageable exposures. This means that the neutron response will have to be used to calculate the signal to noise ratio for 366 cases.

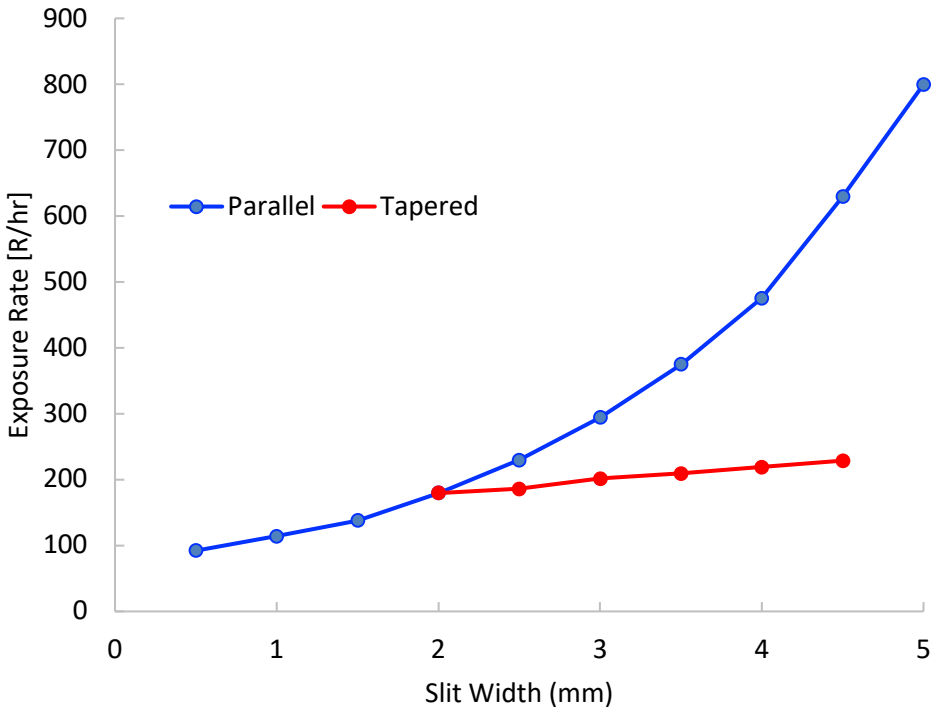


Figure 57. The exposure [R/hr] at Detector #20 which had the maximum exposure as a function of slit width for 10 cm stainless steel and 30 cm borated polyethylene [34].

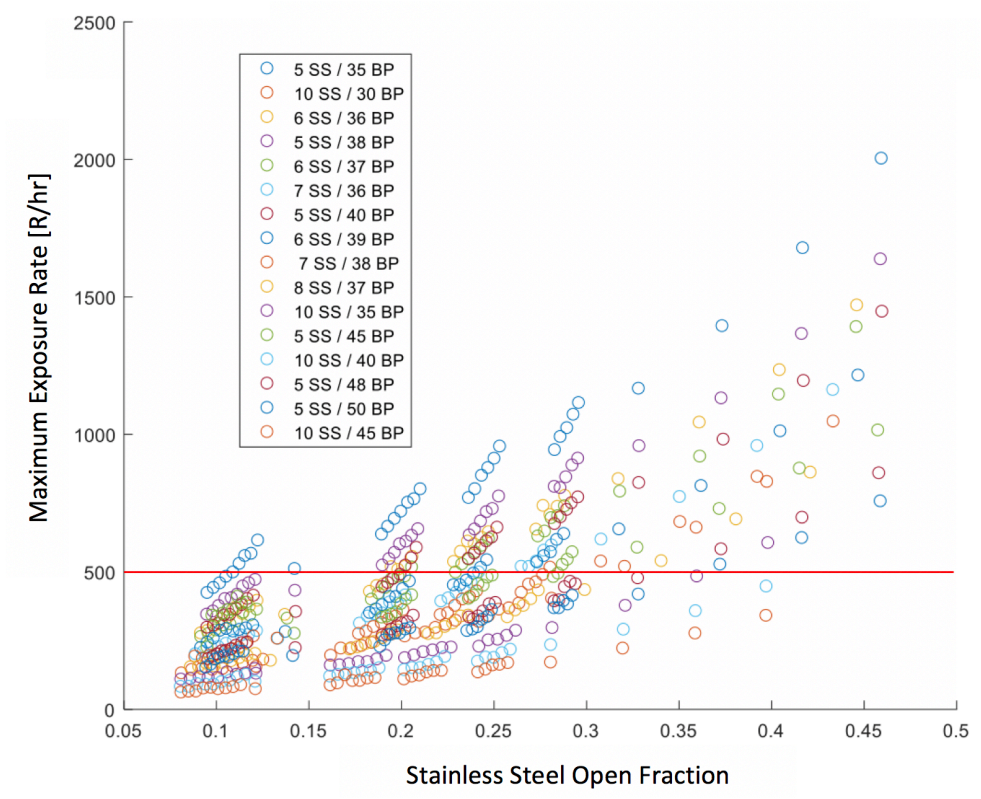


Figure 58. Maximum exposure rates for all 512 geometries modeled as a function of the stainless-steel open fraction. The red line shows the geometries that fall above and below the 500 R/hr limit for maximum exposure tolerable by the detectors.

Figure 59 shows the maximum exposure for all geometries plotted against the corresponding borated polyethylene or stainless-steel open fraction. This shows that the exposure is affected by the borated polyethylene but is more affected by the open fraction in the stainless steel (blue) as opposed to the borated polyethylene and is split into clear bands for each thickness. The role of the borated polyethylene is to modulate the neutrons but as can be seen doesn't do too much to reduce the exposure. The wider the slits, the more gamma-rays the detectors are exposed to, but as will be discussed in the following sections, wider slits and smaller collimators increase efficiency. For this reason, the best design will be dependent on the maximum exposures seen at the detectors, rather than just on the efficiency maximization. From the gamma simulations performed, the tapered slits for all the 16 cases investigated are successful at limiting the exposures, without hurting the neutron efficiency.

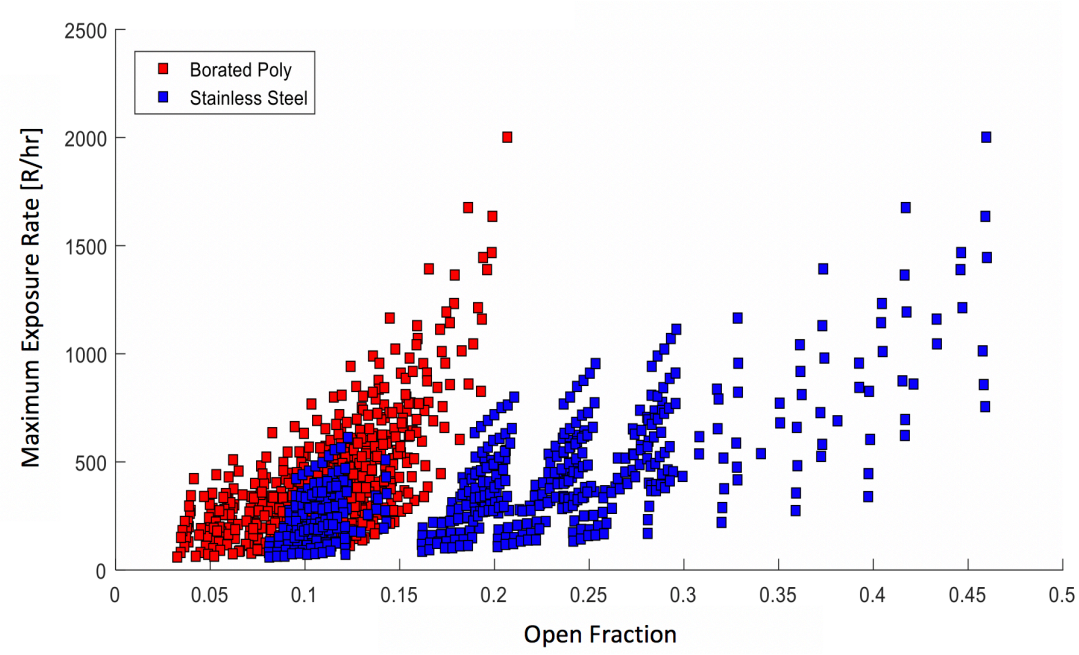


Figure 59. Maximum exposure rate for all 512 geometries being considered plotted as a function of the open fractions of the collimator components. The data in the red is the maximum exposure plotted as a function of the borated polyethylene open fraction, and in blue against the stainless-steel open fraction.

5.3. Constant Exposure Contour

The ideal imager physics design is bound to vary depending on the type of fuel being measured and the cooling time. The second goal of the gamma-ray based simulations was to understand how exposures at the detectors are expected to scale with imager parameter changes and to develop a way to relate a prescribed maximum exposure to required imager geometry. In order to do this, a stainless-steel close fraction and borated polyethylene close fraction was calculated using MCNP for each of the 512 geometries. Since the collimator geometry is not made up of symmetric cells, MCNP was not able to calculate the cell volume as it usually does. 1,024 simulations were conducted in MCNP to calculate the closed fraction of each geometry. Two sets of 512 simulations were conducted, both tallying the surface current using the F1 tally on the top collimator surface using a disk source pointing downwards in the negative Z direction. For one set of simulations, only the neutrons going through the borated polyethylene were tallied, and for the second set, only the neutrons going

through the stainless-steel portion were tallied. The gamma exposures and the calculated close fractions will be used to develop an equation to predict what combinations of geometry parameters result in a desired gamma exposure at the detectors. The areal density for both steel and borated poly is given by Equation (5).

$$\rho_{areal_SS} = \rho_{steel} T_{steel} CF_{steel}$$
$$\rho_{areal_BP} = \rho_{BP} T_{BP} CF_{BP}$$
$$\rho_{areal_tot} = \rho_{areal_SS} + \rho_{areal_BP}$$

(5)

In the equations shown above, ρ_{steel} is 8 g/cm^3 and ρ_{BP} is 1.05 g/cm^3, T_{steel} and T_{BP} are the thicknesses of the stainless-steel and borated polyethylene components of the collimator respectively in centimeters, and CF_{steel} and CF_{BP} are the closed fractions of the stainless-steel and borated polyethylene respectively. The simulated mean gamma-ray exposure per centimeter of stainless steel was plotted against the collimator areal density for all configurations and is shown in Figure 60.

Referring to Figure 60, the relationship given by the equation in red was used to formulate an equation that would help find an acceptable set of configurations given a desired mean exposure. In order to develop this relationship, the set of configurations with a total collimator thickness of 45 cm and parallel slits was used for simplicity since that was the thickness with the most data (45 of the 512 cases). The data for all the parallel slit cases with total collimator thickness of 45 cm is in Table 7.

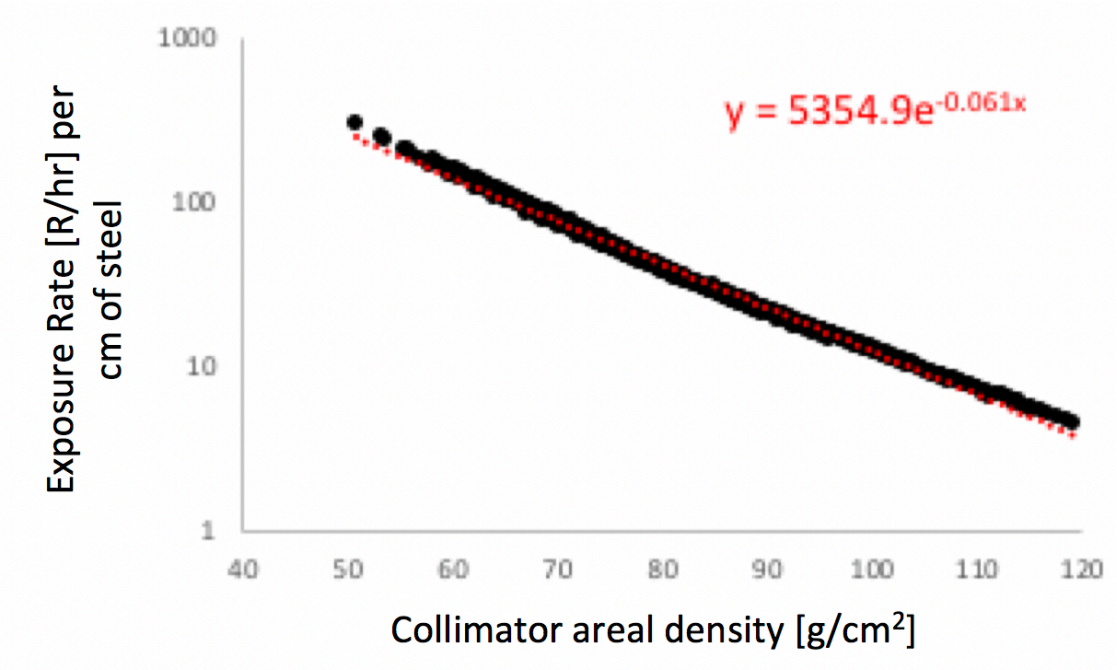


Figure 60. The mean gamma-ray exposure per centimeter as a function of the total collimator areal density [63].

Table 7. MCNP calculated closed fractions and mean exposures for all 45 of the parallel slit cases with total collimator thickness of 45 cm.

Inner Slit Width (mm)	*Outer Slit Width (mm)*	*Steel Thickness (cm)*	*Borated Poly Thickness (cm)*	*SS Closed Fraction*	*BP Closed Fraction*	*Total Areal Density (g/cm^2)*	*Exposure [R/hr]*
1	1	5	40	0.905	0.961	76.564	257.311
1.5	1.5	5	40	0.857	0.942	73.830	303.862
2	2	5	40	0.810	0.922	71.146	363.265
2.5	2.5	5	40	0.764	0.903	68.467	435.623
3	3	5	40	0.717	0.884	65.790	519.299
3.5	3.5	5	40	0.671	0.864	63.154	618.693
4	4	5	40	0.626	0.845	60.516	735.106
4.5	4.5	5	40	0.582	0.825	57.966	869.636
5	5	5	40	0.540	0.806	55.454	1032.495
1	1	6	39	0.908	0.962	82.974	193.845
1.5	1.5	6	39	0.862	0.943	79.994	233.377
2	2	6	39	0.817	0.923	77.026	282.232
2.5	2.5	6	39	0.772	0.904	74.068	341.204
3	3	6	39	0.726	0.885	71.117	413.543
3.5	3.5	6	39	0.682	0.866	68.209	498.659
4	4	6	39	0.638	0.847	65.297	602.456
4.5	4.5	6	39	0.595	0.828	62.463	723.904
5	5	6	39	0.553	0.809	59.660	864.177
1	1	7	38	0.911	0.962	89.429	148.437
1.5	1.5	7	38	0.867	0.943	86.186	180.692
2	2	7	38	0.823	0.924	82.966	219.128
2.5	2.5	7	38	0.779	0.906	79.742	269.353

Table 7. Continued.

Inner Slit Width (mm)	*Outer Slit Width (mm)*	*Steel Thickness (cm)*	*Borated Poly Thickness (cm)*	*SS Closed Fraction*	*BP Closed Fraction*	*Total Areal Density (g/cm^2)*	*Exposure [R/hr]*
3	3	7	38	0.735	0.887	76.538	330.319
3.5	3.5	7	38	0.692	0.868	73.379	402.728
4	4	7	38	0.649	0.849	70.229	493.209
4.5	4.5	7	38	0.607	0.830	67.139	597.969
5	5	7	38	0.566	0.811	64.089	725.541
1	1	8	37	0.914	0.963	95.882	116.173
1.5	1.5	8	37	0.870	0.944	92.388	140.733
2	2	8	37	0.828	0.925	88.936	173.926
2.5	2.5	8	37	0.785	0.907	85.489	213.550
3	3	8	37	0.743	0.888	82.032	265.121
3.5	3.5	8	37	0.701	0.870	78.630	329.854
4	4	8	37	0.659	0.851	75.257	406.898
4.5	4.5	8	37	0.619	0.832	71.947	497.101
5	5	8	37	0.579	0.814	68.654	607.907
1	1	10	35	0.919	0.964	108.926	77.841
1.5	1.5	10	35	0.878	0.945	105.010	94.217
2	2	10	35	0.838	0.927	101.126	116.302
2.5	2.5	10	35	0.798	0.909	97.246	144.014
3	3	10	35	0.758	0.891	93.371	179.713
3.5	3.5	10	35	0.718	0.873	89.538	225.759
4	4	10	35	0.679	0.855	85.708	281.395
4.5	4.5	10	35	0.640	0.836	81.950	346.976
5	5	10	35	0.602	0.818	78.209	429.481

Looking at the equation relating exposure per cm to the total areal density in Figure 60, the equation $y = 5354.9e^{-0.061\,x}$ can be rewritten as $y = Ae^{-\alpha\,x}$. Picking two points along the curve, the respective equations can be written as:

$$y_1 = Ae^{-\alpha\,x_1}$$
$$y_2 = Ae^{-\alpha\,x_2}$$

(6)

Rearranged, the areal density of the two points can be represented by:

$$x_1 = \frac{-1}{\alpha} ln\left[\frac{y_1}{A}\right]$$
$$x_2 = \frac{-1}{\alpha} ln\left[\frac{y_2}{A}\right]$$

(7)

The difference in x moving along the curve is given by:

$$x_2 - x_1 = \frac{-1}{\alpha} ln\left[\frac{y_2}{A}\right] + \frac{1}{\alpha} ln\left[\frac{y_1}{A}\right]$$

$$x_2 - x_1 = \frac{ln\left[\frac{y_1}{y_2}\right]}{\alpha}$$

(8)

The closed fraction (CF) can be re-written in terms of the open fraction (OF) as:

$$CF = 1 - OF$$

(9)

The total areal density for point (x_1, y_1) can be rewritten as:

$$\rho_{areal_tot_1} = \rho_{steel} T_{steel_1}\left(1 - OF_{steel_1}\right) + \rho_{BP} T_{BP_1}(1 - OF_{BP_1})$$

(10)

To find the total areal density at the second point along the curve corresponding to (x_2, y_2), the difference between the two x terms shown in (8) needs to be added to Equation (10). Doing so, gives Equation (11) below.

$$\rho_{areal_tot_1} + \frac{ln\left[\frac{T_{1_Steel}}{T_{2_Steel}}\right]}{\alpha} = \rho_{steel}T_{steel_1}\left(1 - OF_{steel_1}\right) + \rho_{BP}T_{BP_1}(1 - OF_{BP_1})$$

(11)

The equation is not entirely accurate in its current form, because the open fraction needs to be scaled going from one thickness of stainless steel to another by a constant value to account for the change in collimator slit width required to maintain the mean exposure at a particular value. A value 'm' can be calculated to represent the factor by which the slit width needs to change. The constant m incorporating it into Equation (11) gives:

$$\rho_{areal_tot_1} + \frac{ln\left[\frac{T_{1_Steel}}{T_{2_Steel}}\right]}{\alpha} = \rho_{steel}T_{steel_1}\left(1 - m\ OF_{steel_1}\right) + \rho_{BP}T_{BP_1}(1 - m\ OF_{BP_1})$$

$$\rho_{areal_tot_1} + \frac{ln\left[\frac{T_{1_Steel}}{T_{2_Steel}}\right]}{\alpha} = \rho_{steel}T_{steel_2} + \rho_{BP}T_{BP_2} - m\left(\rho_{steel}T_{steel_2}\ OF_{steel_1} + \rho_{BP}T_{BP_2}OF_{BP_1}\right)$$

(12)

Solving for m gives Equation (13):

$$m = \frac{\rho_{areal_tot_1} + \frac{ln\left[\frac{T_{1_Steel}}{T_{2_Steel}}\right]}{\alpha} - \rho_{steel}T_{steel_2} + \rho_{BP}T_{BP_2}}{-\rho_{steel}T_{steel_2}\ OF_{steel_1} - \rho_{BP}T_{BP_2}OF_{BP_1}}$$

(13)

Using the data from Table 7 and the first case of 1 mm parallel slits, 5 cm stainless steel and 40 cm of borated polyethylene as the reference, it is possible to demonstrate the ability to predict the total required areal density, and the slit width change for a given change in stainless steel thickness to maintain the exposure at 257.311 R/hr. The goal here is to show how much the slit width would need to be changed if the amount of stainless steel were to increase from T_{1_Steel} equal to 5 cm to T_{2_Steel} equal to 6, 7, 8, and 10 cm to maintain the

mean exposure at 257.311 R/hr. Corresponding m values for increasing the stainless-steel thickness from 5 cm to the various values using Equation (13) were calculated and are shown in Table 8. Since the base case used 1 mm parallel slits and the m value calculated for 5 cm of stainless steel is 1 means that the m value for larger thicknesses can be interpreted to mean the amount by which a 1 mm slit width needs to be scaled by for each of the larger thicknesses to maintain the same exposure.

Assuming the m values are equivalent to scaling a 1 mm slit width, the above table can be interpreted as meaning that in order to maintain the exposure at 257.311 R/hr, increasing the amount of stainless steel from 5 cm to 6 cm means that the slit width can be increased from 1 mm to 1.53 cm. The MCNP calculated total areal densities for the corresponding slit values can be read from Table 7. Note that the slit values simulated go up from 1 mm in increments of 0.5 mm, so exact areal values pertaining to slit widths of 1.53 mm, 2.01 mm, 2.45 mm, or 3.19 mm will have to be interpolated or can be assumed to be comparable to the areal density values to the closest 0.5mm increment in slit width (i.e. m = 1.53 is comparable to a slit width of 1.5 mm, m = 2.01 to 2 mm, and m =2.45 to 2.5 mm.) For m = 3.19, the total areal density was estimated by plotting the areal density data from Table 7 for 10 cm stainless-steel and 35 cm borated polyethylene and fitting a line to it as shown in Figure 61. The fit equation was then used to calculate the MCNP-estimated total areal density at a slit width of 3.19 mm. Table 9 shows the areal density values from MCNP (calculated and interpolated) and the total areal density values calculated using Equation (12).

The calculated values do not line up completely with the MCNP areal density values and are increasingly underpredicted as the steel thickness increases. This is because although the m value accounts for the amount by which the slit width needs to be increased, it does not account for the change in the open fraction as the radius of the stainless-steel increases and the radius of the borated polyethylene decreases. Hence, the steel open fraction and the borated polyethylene open fractions need to be scaled by two different scaling factors as a function of the different radii shown in Figure 63.

Table 8. Calculated m values using Equation 13 for a starting thickness of 5 cm stainless steel and increasing.

Stainless-steel Thickness (cm)	***m***
5	1.00
6	1.53
7	2.01
8	2.45
10	3.19

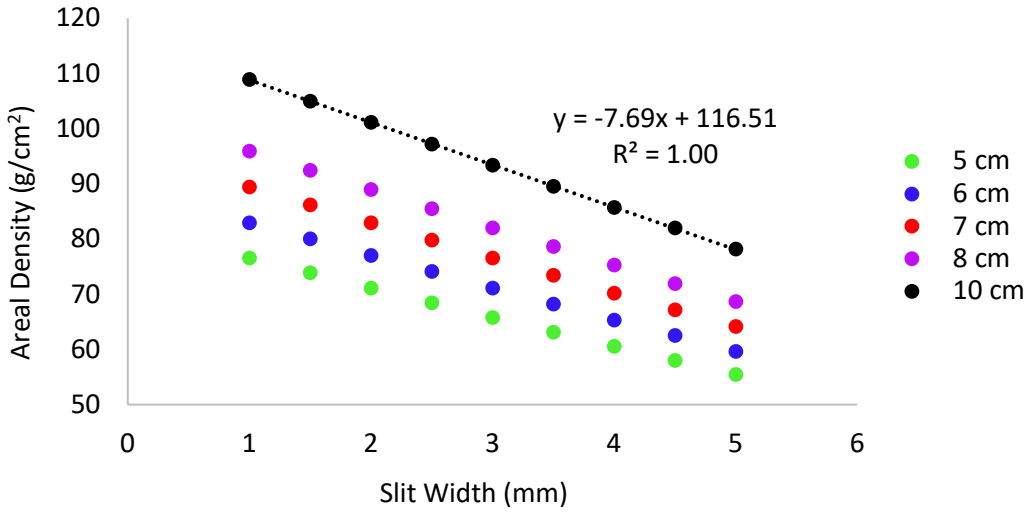


Figure 61. Total areal densities for various stainless-steel thicknesses as a function of slit width while maintaining a total collimator thickness of 45 cm.

Table 9. MCNP predicted and calculated total areal densities for various stainless steel and borated polyethylene combinations to maintain a given exposure.

Stainless-steel Thickness (cm)	***Borated Poly Thickness (cm)***	***m***	***MCNP total Areal Density [g/cm²]***	***Areal Density calculated using m [g/cm²]***
5	40	1.00	76.56	-
6	39	1.53	79.99	79.55
7	38	2.01	82.97	82.08
8	37	2.45	85.91	84.27
10	35	3.19	92.00	87.93

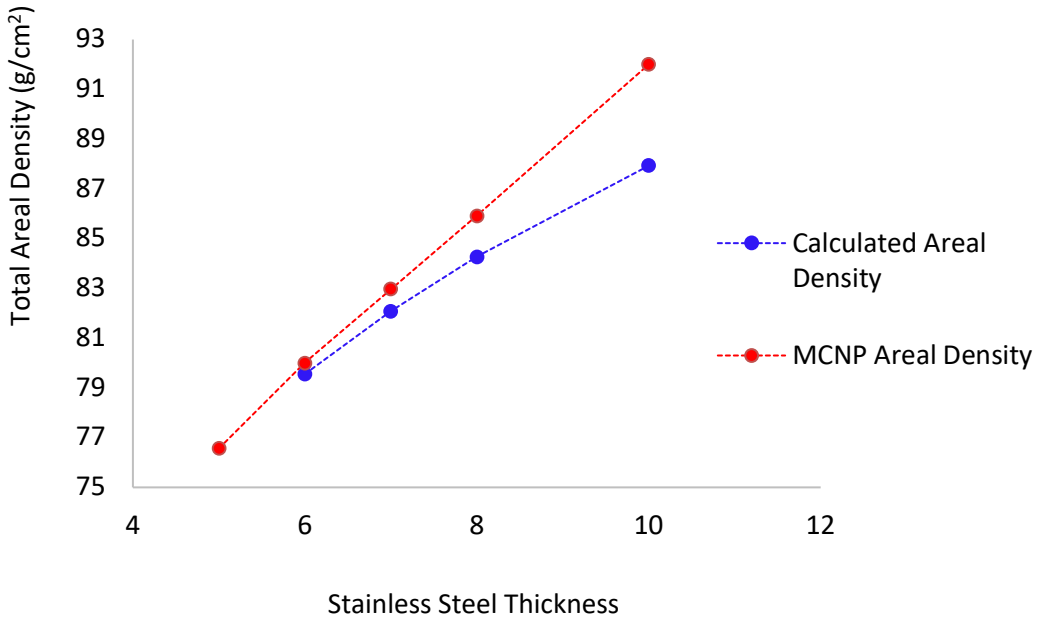


Figure 62. Total collimator areal density as a function of steel thickness to maintain the same exposure. The red curve shows what the MCNP calculated areal density values should be, and the blue curve shows the areal density values calculated using the equation derived and the m value.

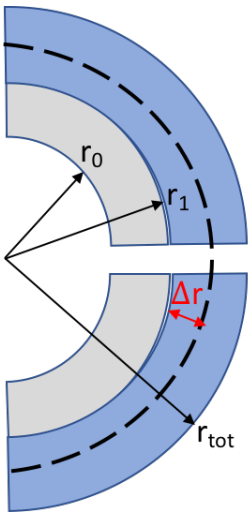


Figure 63. Diagram showing the radius values used to correct for the change in open fraction as the stainless steel (grey) and borated polyethylene (blue) radii change.

In the diagram, r_0 stays constant at 17.6777 cm, r_1 is the original stainless-steel thickness (using the example above, $r_0 + r_1$ = 5 cm + 17.6777 cm = 22.6777 cm), Δr is the change in radius of the stainless-steel component as the steel thickness is increased, and r_{tot} is the total collimator thickness, which is 45 cm in this example. The open fraction needs to be corrected for the change in radius by:

$$OF_{steel_2} = \frac{Old\ configuration\ slit\ area\ \times m \times steel\ scaling\ factor}{Old\ configuration\ total\ area\ \times \frac{new\ total\ area}{old\ total\ area}}$$

$$OF_{steel_2} = OF_{steel_1}\, m\, S_{SS} = OF_{steel_1}\, m\, \frac{(r_1 - r_0 + \Delta r)/(r_1 - r_0)}{\frac{\pi[(r_1 + \Delta r)^2 - r_0^2]}{\pi[r_1^2 - r_0^2]}}$$

$$S_{SS} = \frac{(r_1 - r_0 + \Delta r)(r_1^2 - r_0^2)}{[(r_1 + \Delta r)^2 - r_0^2](r_1 - r_0)}$$

(14)

Likewise, to scale the borated polyethylene open fraction to account for the change in radius, the final borated polyethylene open fraction is scaled by m and a ratio of the areas similar to Equation (14) and can be written as:

$$OF_{BP_2} = OF_{BP_1}\, m\, S_{BP} = OF_{BP_1}\, m\, \frac{(r_{tot} - r_1 - \Delta r)/(r_{tot} - r_1)}{\frac{\pi[r_{tot}^2 - (r_1 + \Delta r)^2]}{\pi[r_{tot}^2 - r_1^2]}}$$

$$S_{BP} = \frac{(r_{tot} - r_1 - \Delta r)(r_{tot}^2 - r_1^2)}{(r_{tot} - r_1)[r_{tot}^2 - (r_1 + \Delta r)^2}$$

(15)

The final equation to calculate the areal density using all three correction factors and knowing the initial can be written as:

$$Calculated\ Areal\ Density = \rho_{SS} T_{SS}\left(1 - OF_{steel_1} m S_{SS}\right) + \rho_{BP} T_{BP}\left(1 - OF_{BP_1} m S_{BP}\right)$$

(16)

The calculated areal densities are shown below in Table 10 and Figure 64. Compared to Figure 62 the calculation predicted areal density values are closer to the MCNP calculated values. This proves that Equation (16) can be used to successfully predict the required areal

densities for a given thickness of stainless-steel to maintain a given mean exposure. The mean exposure is affected by both the stainless-steel and borated polyethylene open fractions as well as the slit width. Using the various parameters, a method to identify configurations that are acceptable and can satisfy a mean exposure was identified and demonstrated in this chapter. If a facility with a known fuel type and cooling time needs to optimize the imager design, this method can be used to identify the set of acceptable configurations.

Looking at the m value, and how it scales as a function of the steel thickness gives a good idea of how the slit width changes for a given increase in steel thickness to maintain a constant exposure. Figure 65 shows the calculated m values plotted against the steel thickness to maintain the exposure at 257.311 R/hr. As the steel thickness in the collimator increases, the slit width can also be increased. To increase the slit width by about 1 mm, 2 cm more of steel need to be added to the collimator configuration to maintain the exposure. This type of analysis can be applied to other configurations if a different exposure contour is to be calculated.

Table 10. MCNP predicted and calculated total areal densities using all corrections for various stainless steel and borated polyethylene combinations to maintain a given exposure.

Stainless-steel Thickness (cm)	***Borated Poly Thickness (cm)***	m	***MCNP total Areal Density [g/cm^2]***	***Areal Density calculated using all correction factors [g/cm^2]***
5	40	1.00	76.56	-
6	39	1.53	79.99	79.75
7	38	2.01	82.97	82.66
8	37	2.45	85.91	85.42
10	35	3.19	92.00	90.84

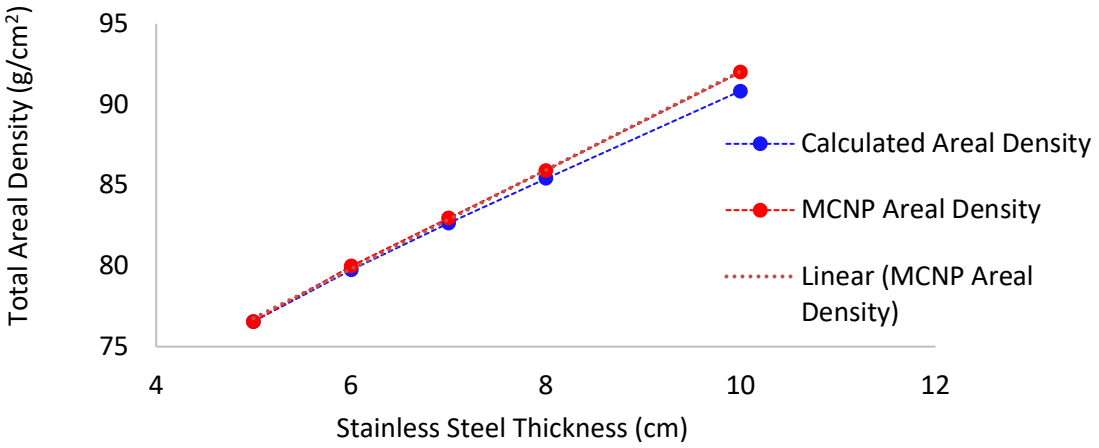


Figure 64. The total collimator areal density calculated using all correction factors as a function of steel thickness to maintain the exposure at 257.31 R/hr. The MCNP areal density values are in red, and the blue curve shows the areal density values calculated using all correction factors.

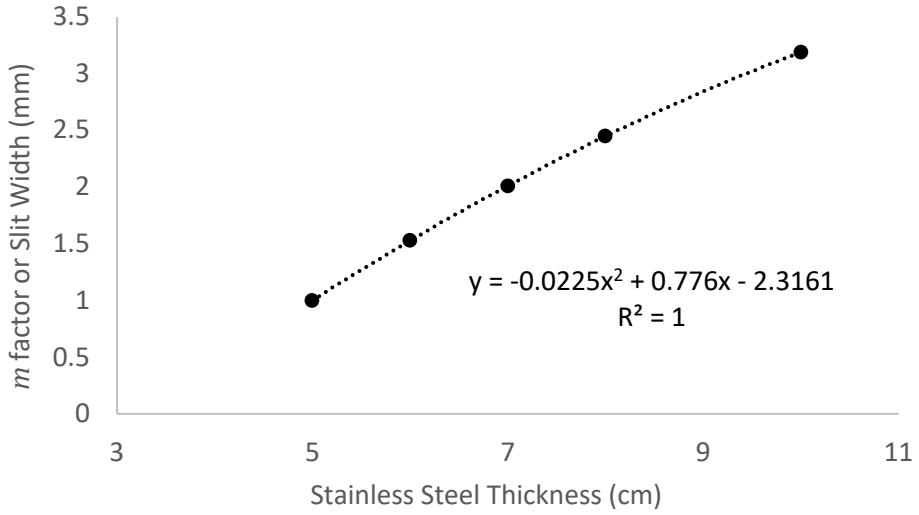


Figure 65. Calculated m values for the various steel thicknesses that maintain the exposure at 257.311 R/hr. The m is reflective of the required collimator slit width at a given steel thickness.

6. SIMULATION DESIGN STUDY: NEUTRON RESPONSE

To identify the best compromise between efficiency, resolution, and gamma exposure management to build a practically sized imager, neutron response simulations in addition to the gamma exposure simulations were conducted. Since the collimator creates a complicated neutron response that is hard to predict, the first set of simulations used a single ^{244}Cm line source to understand what the expected point spread function looks like and how it would change for the various imager geometries being considered. This chapter will focus on the various simulations conducted with neutron sources in order to understand the various factors and responses that need to be accounted for in the image reconstruction software. In addition, the "ideal" final geometry will be identified using an SNR calculation. The various components impacting the resolution of the imager are the collimator slit widths, the slit bore scattering, collimator penetration, and the scattering between detectors. These effects can be seen in the point spread function in the spread of the signal peak, which in an ideal situation would be a delta function. The detector response to each of these effects are discussed in this chapter.

6.1. Neutron Response

The neutron response simulations were conducted to calculate the expected response and performance of the imager components and the ability of the imager to detect a single missing fuel pin within a fuel assembly. Ideally, a full tomography simulation would be conducted for each of the 512 geometries considered, and an SNR would have to be calculated for each image that has been reconstructed. However, this would involve computation and time resources that are not feasible or practical. As a result, an SNR was defined using an approximate imager response using fewer simulations that consisted of simulations looking at individual response components. These components included the inter-detector scattering, the direct (centerline) response to a source, response when the source is located close to the slit edge, and collimator penetration response. The goal in this section is to gather the necessary neutron responses that would be able to generate the ideal correction factors to be incorporated into the reconstruction code. The neutron response of concern in this project is only the absorption reaction of neutrons in the boron carbide layer within each straw. The

idea is that the fast neutrons from the source (^{244}Cm) would traverse down the collimator slits. The borated polyethylene portion of the collimator will help modulate the neutron response so the lower energy neutrons do not reach the detectors, and primarily fast neutrons traversing down each slit will reach the detectors. The fast neutrons then will be thermalized within the high-density polyethylene matrix that the 23 straws are embedded in, after which they will be detected by the thermal neutron detectors via neutron absorption reaction. Figure 66 shows a plot of the neutron cross sections in the detector's boron carbide layer enriched to 96% in ^{10}B. The blue curve shows the total cross section, and the red shows the absorption cross section for neutrons. At thermal neutron energies (2.5E-8 MeV), the absorption cross section is about 2969 barns (b), which is significantly higher than the neutron absorption cross section of the other detector materials.

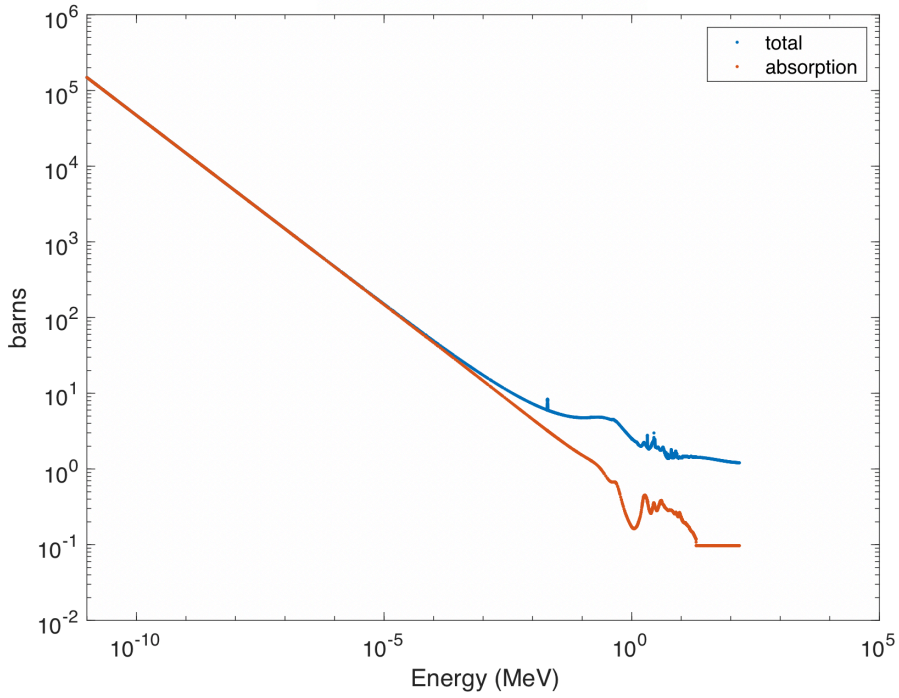


Figure 66. Total neutron cross section and the absorption cross section for neutrons in boron carbide [64].

The approximated neutron response from the tallied absorption reactions will form the basis of the SNR calculation and the optimal design's response will be used as the forward projection data in the iterative reconstruction code to generate the final image map. All of the neutron response simulations were conducted using MCNP6. In order to tally the neutron absorption in the straws, the F4 tally function was used. The F4 neutron tally by itself is a track-length estimate of the average cell flux. If a particle of weight W makes a track of length T (cm) within a specified cell of volume V (cm^3), the contribution to the flux in the cell is given by Equation (17) below [64].

$$W\frac{T}{V} \quad (17)$$

The sum of these contributions is reported as the F4 tally in the MCNP output. The units of the F4 tally outputs are in particles per centimeter squared. Since the quantity of interest is the reaction rate of neutrons captured on boron carbide, a tally multiplier was used to convert the F4 tally to a reaction rate as shown below.

F14:n 12(12<902<21<201)

Fm14 -1 6 -2

The first line of the two in the tally example above specifies which detector cell and within which lattice universe to tally the neutrons in. The second line is the tally multiplier for F14. The '-1' instructs MCNP to use the atomic density of the material number specified by the next term, which is '6' (corresponds to the definition for boron carbide), and the '-2' tells MCNP to tally using the corresponding neutron capture cross section [64]. The final units of the tallied quantity is the reaction rate per number of source particles (nps), and is shown in Equation (18).

$$\text{neutron capture reactions per nps} = F4\,N\sigma_{abs}V \quad (18)$$

where N is the number density of boron carbide $\left[\frac{atoms}{barn\ cm^3}\right]$, σ_{abs} is the absorption cross section of the boron carbide in barns, and V is the volume of boron carbide a single detector straw in cubic centimeters.

6.2. Point Spread Function

As introduced in Chapter 3, the point spread function (PSF) is used to characterize an imaging system and, more importantly, determines its spatial resolution. The PSF of an imaging system is the response of the system to a single point source, and the degree of spreading in the PSF is a measure of the resolution limitation of the imager. The PSF can be thought of as being made up of two portions, a "true" response in the center and a "scatter" response elsewhere and underlying the true response in the center. For the imager design being investigated, PSFs for all 512 geometries being considered were generated using a ^{244}Cm line source centered on detector 51 as shown in Figure 67. The detectors are numbered starting from 1 to 100 starting at the bottom collimator slit that sits tangential to the fuel assembly cavity and going around clockwise.

To generate the PSF, the reaction rate for each neutron detector was tallied, as described earlier in this chapter, and plotted against the detector number. Since it is not computationally feasible to conduct 100,000 simulations for each of the 512 configurations to understand the detector response at the mm scale, a smaller set of simulations using a ^{244}Cm line source were conducted in order to feed into understanding how the neutron counts scale and be extrapolated to a full response. To understand how the direct (peak) and collimator penetration (noise) scale as a function of the various parameters, simulations with a ^{244}Cm line source at two locations along the centerline of slit 51 were conducted. Detector 51 was selected as the template because the slit pointing at this detector had the most direct view compared to the other slits that have the slits pointing at a different angle with respect to the detector. A response for how the neutron signal peaks as it passes down each slit will be applied and correct for the detector response for neutrons passing down each of the slits. Figure 68 is a diagram of the two source positions used in the two sets of simulations, both aligned to slit 51. The first source position selected along the slit 51 centerline is 14.30 cm from the slit opening (shown in red.)

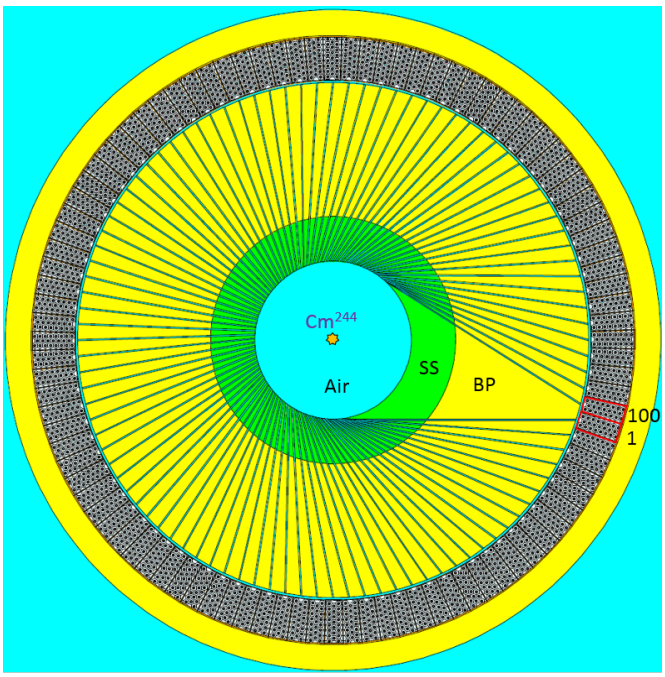


Figure 67. Simulation set up showing location of the 244Cm line source aligned to the centerline of the slit opening to detector number 50. The detectors are numbered 1 to 100 starting at the bottom tangent slit (#1) going around clockwise to detector 100 [34]..

This position closer to the origin was chosen to assess how the collimator penetration changes as a function of geometry since the PSF here has a clean baseline. A second source position (blue) was chosen to be closer to the slit opening (7.40 cm from the opening) so it would be 1cm outside of the area overlapped by slits 50 and 51. This second source position is not in the direct line of sight of slit 50. This allows the source at this position to provide an estimate of the direct 'down-slit' component of the signal. The point spread function curves for the two source positions are shown in Figure 69 below. The reason for the two peaks around detectors 23 and 79 on the blue curve is because at that particular source position, those detectors have a field of view that overlaps with detector 51.

To illustrate how different slits, have different views of the line source as it changes position, a single ^{244}Cm line source was moved and simulated at 114 different equally spaced out positions along the slit 51 centerline from the slit opening all the way across the field of view. The detector response was calculated for the source at each of the positions, and an intensity

map was generated. To show clearly how the counts at each detector compare to the central detector 51, a ratio of the counts at detector 51 to each of the detectors was calculated and the resulting image is shown below in Figure 70. When the source is close to the slit opening along the centerline, three peaks as seen in the blue curve in Figure 69 appear, and as the source moves further down the centerline the detectors that have a field of view of the source change, and eventually the field of view converges to a single peak close to 14.30 cm from the slit opening.

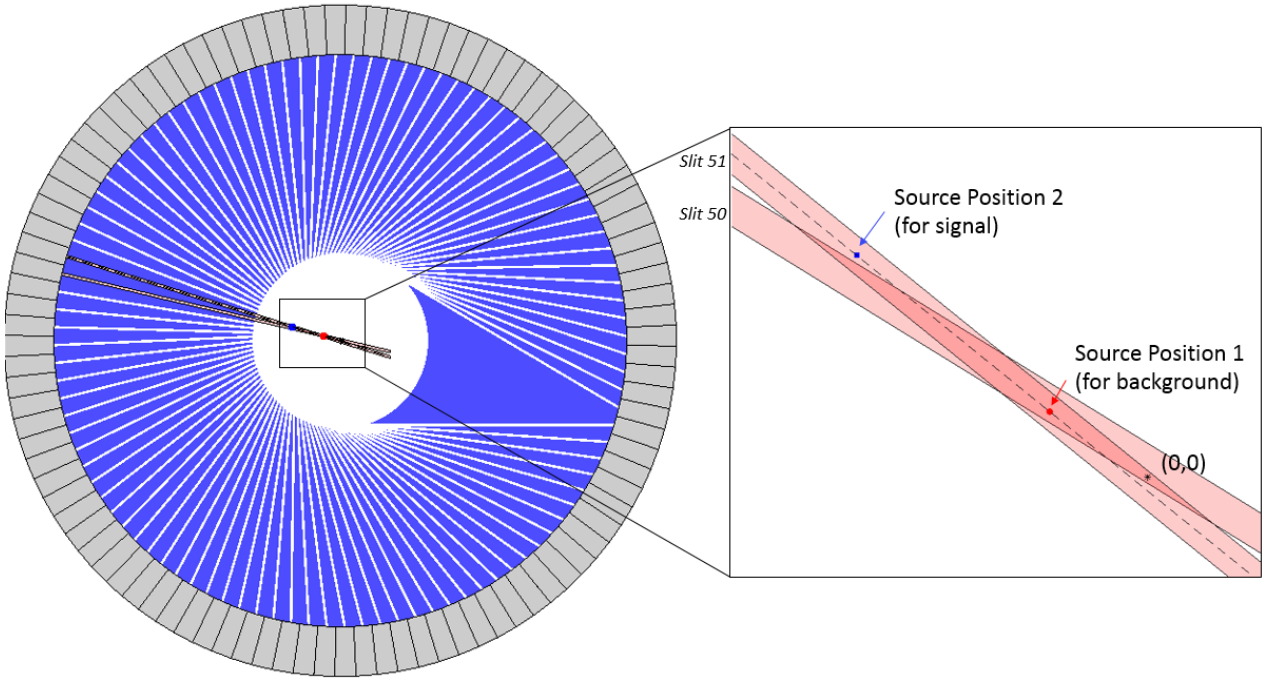


Figure 68. Diagram showing the areas overlapped by the fields of view of slits corresponding to detectors 50 and 51. The two source positions along slit 51's centerline used to generate the PSFs are also shown here relative to the origin (0,0), which is the center of the fuel cavity. The ^{244}Cm was first placed in the position marked by the red dot to generate PSFs for background quantification and was placed in the position marked by the blue dot outside of the overlap region of the two slits for a second set of simulations to accurately quantify the signal [65].

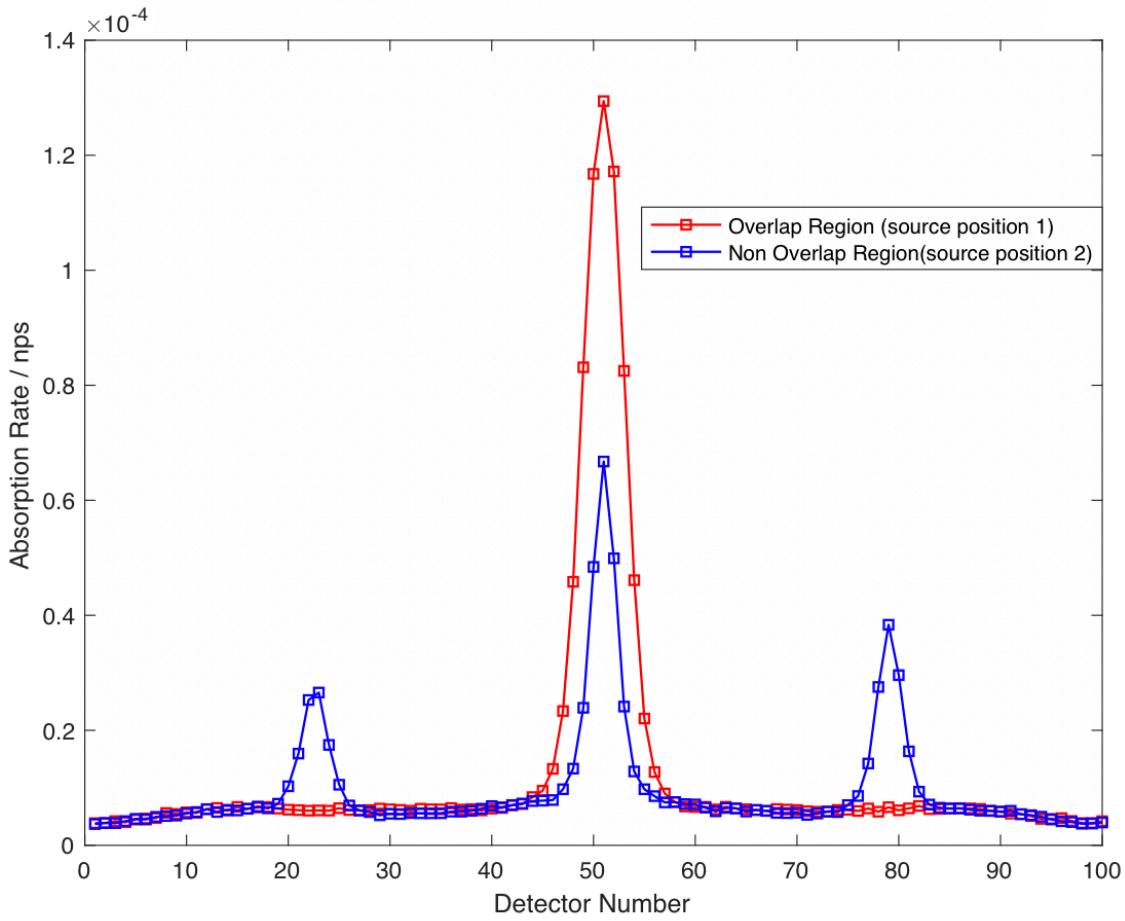


Figure 69. Point spread functions for a ^{244}Cm line source at two different distances from the slit 51 opening using a collimator with 10 cm stainless steel and 30 cm borated poly and 3 mm wide parallel slits [65].

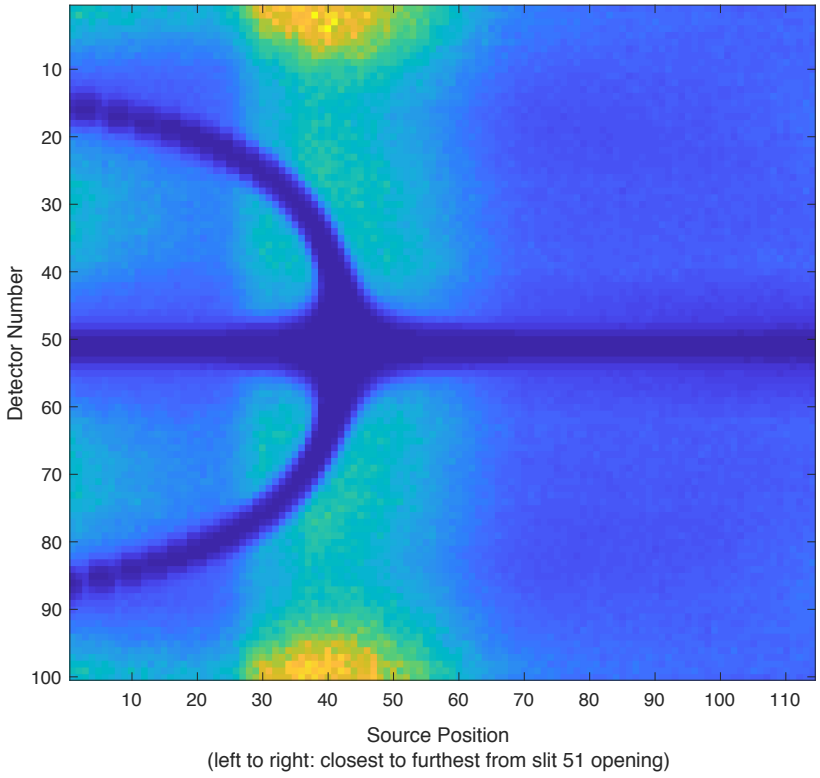


Figure 70. Ratio of counts seen at detector 51 to all the other detectors for a line source moving down the centerline of slit 51 across the field of view.

Using the point spread functions for the source placed in the non-overlap region (closer to the slit), the peak counts (only at detector 51) were extracted and plotted and are shown in Figure 71 and Figure 72 below. The peak counts do not increase in a constant manner as the slit width increases. This makes it harder to use this data set to predict how the direct component scales. To understand how the peak height or signal changes as a function of the slit width, the slit 51 count data was plotted against the open fraction of the borated polyethylene component of the collimator for all 512 cases. Since the borated polyethylene component of the collimator contributes most to the neutron moderation, the neutron count rates seen at the detectors are expected to change primarily as a function of the open fraction of borated polyethylene. Figure 72 shows the absorption rate at detector 51 when the source is placed in location 2 (the non-overlap region) as a function of the borated poly open

fraction. The signal component has a mostly quadratic relationship with respect to the borated poly open fraction. It was later found that the source position used to conduct this was not far enough away from the neighboring slits as the slit width increased, thus the amount of leakage into the neighboring slits was an issue, contributing to the non-constant count rate increase. To fix this, a set of simulations with a single slit were conducted in order to better understand the direct contribution.

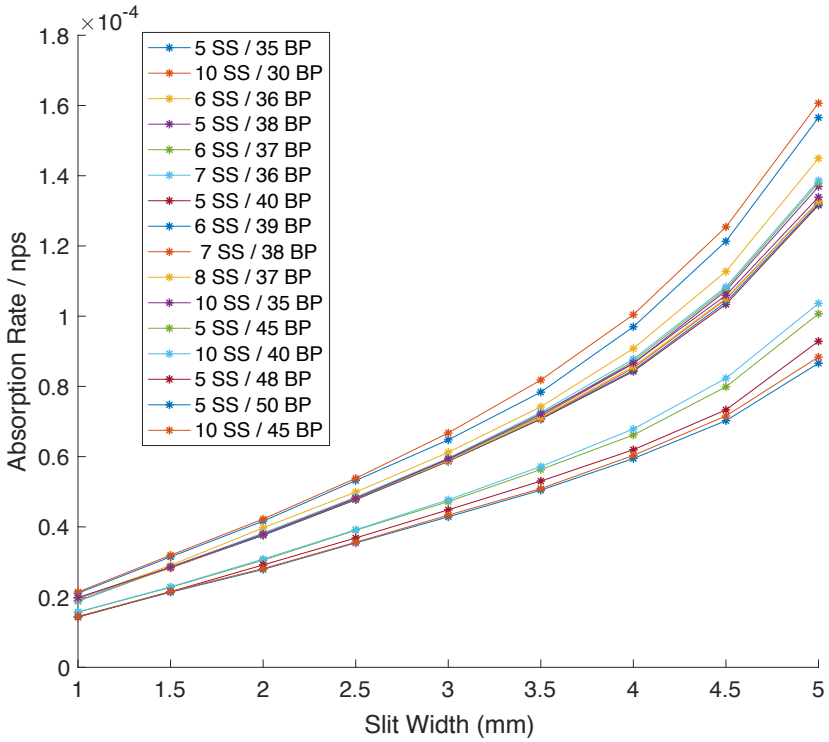


Figure 71. Detector 51 response to a ^{244}Cm line source placed in the non-overlap region (source position 2).

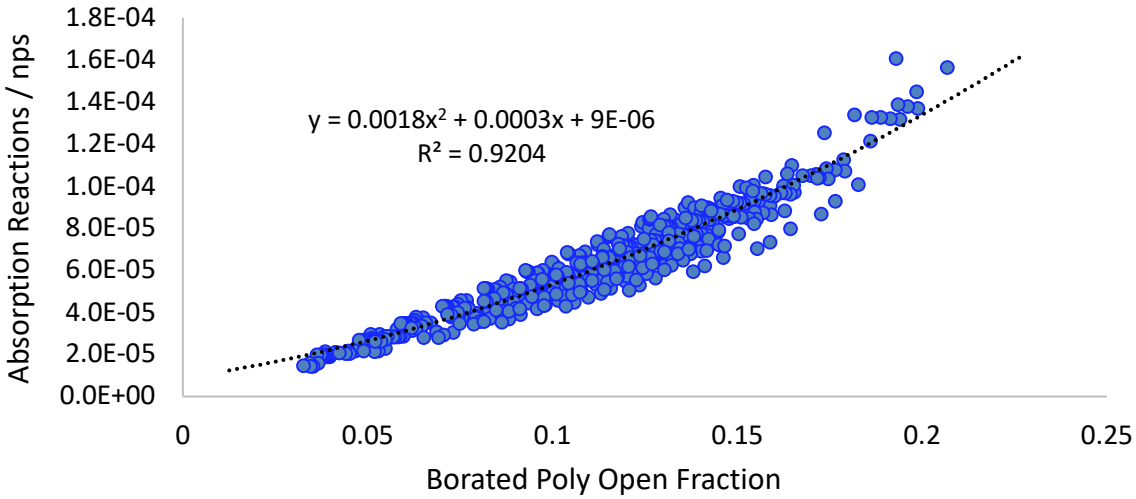


Figure 72. Signal at detector 51 for all 512 cases as a function of the borated polyethylene open fraction.

6.3. Inter-Detector Scatter

One of the biggest factors limiting the resolution of the imager is the inter-detector scatter of neutrons traveling down a particular slit. Inter-detector scattering occurs when neutrons go down one slit and then scatter from the intended detector at the end of the slit into another neighboring detector before being detected. This results in the imager having lower spatial resolution because a fraction of detected neutrons associated with a particular collimated path are wrongly attributed to a nearby path. To understand the amount of inter-detector scattering to expect in the system, a simulation with a simple geometry consisting of 11 detectors for simplicity sake with a single slit pointing to the center detector was performed by pointing a ^{244}Cm beam into the center detector as shown in Figure 73. In this figure, all of the neutron interactions (collision and absorption) with the collimator/detector materials are shown in order to show how far the neutrons aimed at the central detector traverse. This proved that no more than 11 detectors need to be simulated in order to identify the full width half maximum of the inter-detector scatter spread.

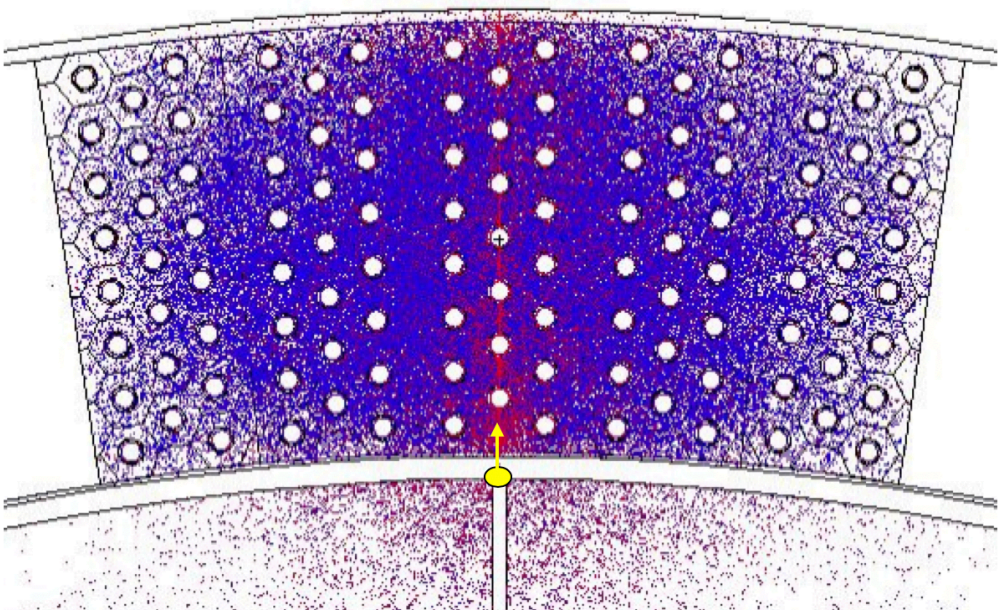


Figure 73. All interactions (collision and absorption) of neutrons in the imaging system originating from a beam of ^{244}Cm neutrons shot at the central detector. The red points show where the maximum probability of interaction is, and the blue shows areas with lower interaction probabilities [34].

Figure 74 shows a visual representation of only the neutrons absorbed by the boron carbide in each of the detector straws. This fraction represents those that will be detected by the proposed detector system. The image below and above both show a significant amount of the neutrons entering the center detector are scattered into the adjacent detectors and are subsequently absorbed. The detectors immediately next to the center detector see ~66% of the counts the center detector sees, and the counts seen at the detectors one removed from the center goes down to ~23%. The spread across detectors observed will directly affect the spatial resolution. The desired spatial resolution should be on the order of 1 cm to be able to identify individual pins. The resolution achieved with this simulation is also on the order of 1 cm assuming the spatial spread is equal to the FWHM of the spread multiplied by the slit spacing. The FWHM is about 3 detectors, and the slit spacing is 0.3cm. Geometries that can achieve this level of resolution will be good enough to identify the gaps between individual pins. The amount of expected inter-detector will limit the SNR and will be accounted for in the reconstruction code.

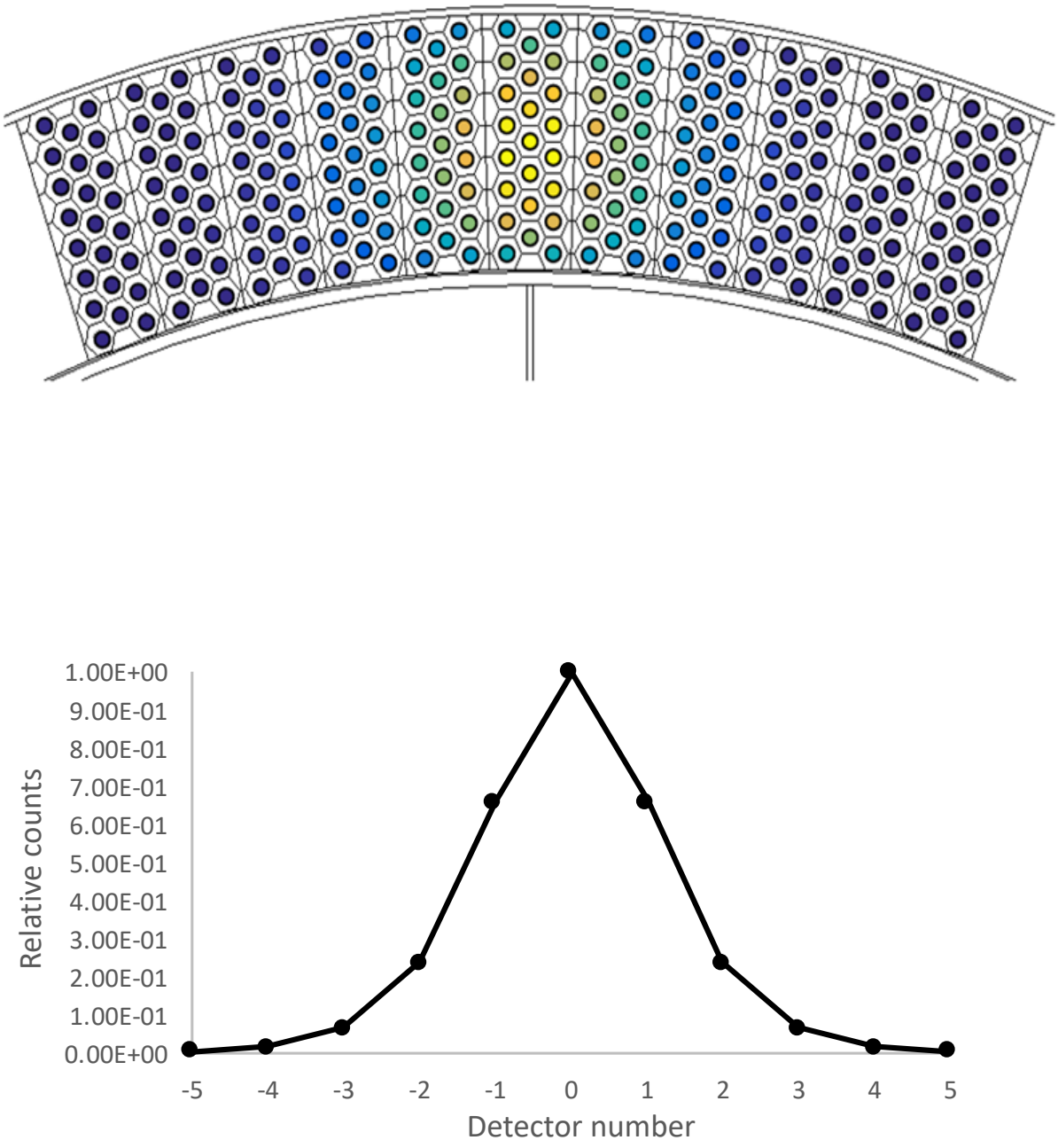


Figure 74. Visual representation of neutron absorption reactions seen in each straw (in the boron carbide layer) when a beam of ^{244}Cm neutrons is shot to the center detector only. The bottom plot shows the average relative counts of boron captures (per 10^6 source particles) [34] [63].

Ideally, a given detector in the imager would be sensitive only to neutrons along the path that the corresponding collimator slit sees. However, when accounting for the inter-detector scatter from neighboring detectors, a given detector is sensitive to neutrons along the neighboring detectors' paths to some degree as specified by Figure 74. An example image showing what the detector response actually looks like when accounting for inter-detector scatter is shown in Figure 75. The image shows what the detector 50 response looks like when accounting for inter-detector scatter to each point in the inspection area (counts/source neutron) for an imager with 3 mm slits.

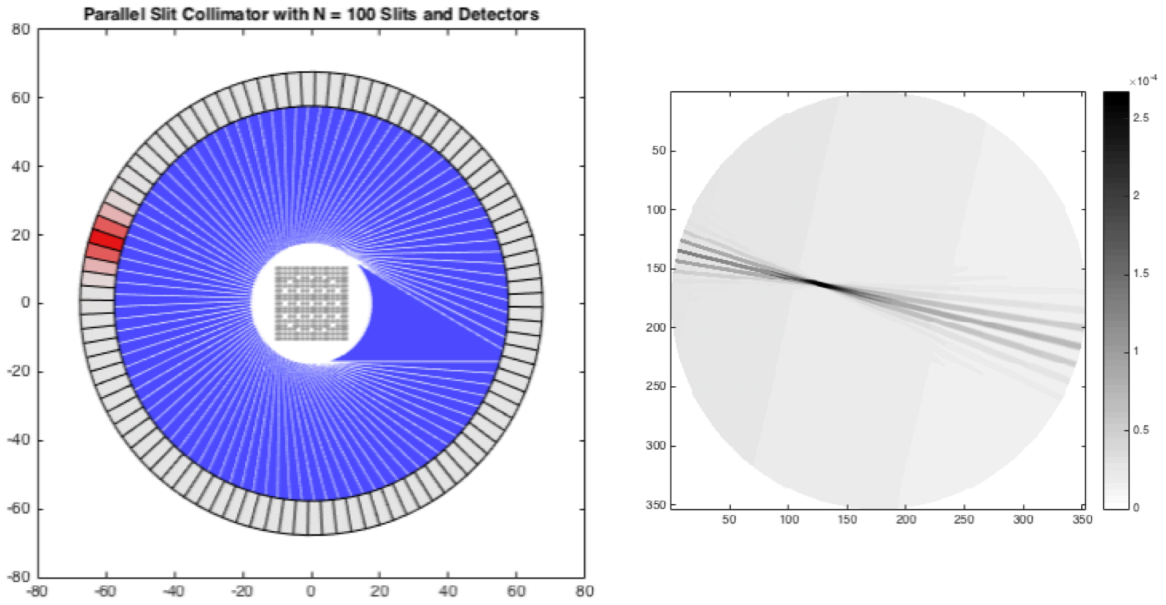


Figure 75. Detector 50 response in counts per source particle to each point in inspection area for an imager with 3 mm slits [65].

6.4.“Direct” and “Edge” Effects on Neutron Counts

Since the collimator geometry is more complicated than a standard parallel slit collimator, to understand the individual contributions to the neutron response such as the response at the edge of a slit, the signal peak, and collimator penetration over the field of view, a simplified geometry was used. The entire imager geometry was assumed to have a single slit (pointing at detector 51). To see how the response changes across the field of view, a single ^{244}Cm line source was moved perpendicular to the slit 51 centerline at three different distances from the slit opening (5.04 cm, 10.08 cm, and 20.16 cm). The collimator thickness used for this set of simulations was 5 cm of steel and 45 cm of borated polyethylene. The response with various parallel slit widths was investigated for only the source-slit distance of 10.08 cm. The goal from this simulation study was to understand the single slit response and apply it to multiple slits in the reconstruction code as a sum of responses to individual slits.

Figure 76 shows a diagram of the single slit geometry and the various source positions simulated are shown as points (red, black, and blue) in the center annulus. The line in black corresponds to the chord 10.08 cm away from the slit 51 opening and the positions when the line source was moved along the chord. The source was placed in 118 different positions going from -150 mm to +155 mm with respect to the distance from the slit 51 centerline. From distances going from -35 mm to +35 mm, the source was moved in 1 mm increments, beyond which the source was moved in 5mm increments along the chord. For the 118 source positions along the 10.08 cm away chord, the response to various slit widths was simulated as well. These included 0, 1, 1.5, 2, 2.5, 3, 3.5, 4, 4.5, and 5 mm. The red line in the Figure 76 corresponds to the perpendicular chord 5.04 cm away. A total of 240 source positions extending from -118 mm to +120 mm from centerline were simulated at this distance with the source being moved in 0.5 mm increments between -40 mm and +40 mm, beyond which the source was moved in 2 mm increments. Each of the 240 source positions along this chord were simulated with slit widths of 0 mm and 5 mm. Finally, the blue line shows the source moving along the perpendicular chord that is 20.16 cm away from the slit opening. At this distance 285 source positions were simulated. Similar to the 5.04 cm chord, the source was moved in 0.5 mm increments between -40 mm and +40 mm relative to the slit 51 centerline,

and was then moved in 2 mm increments extending to -162 mm and +166 mm. Each of the source positions along this line were also simulated with 0 mm and 5 mm slit widths.

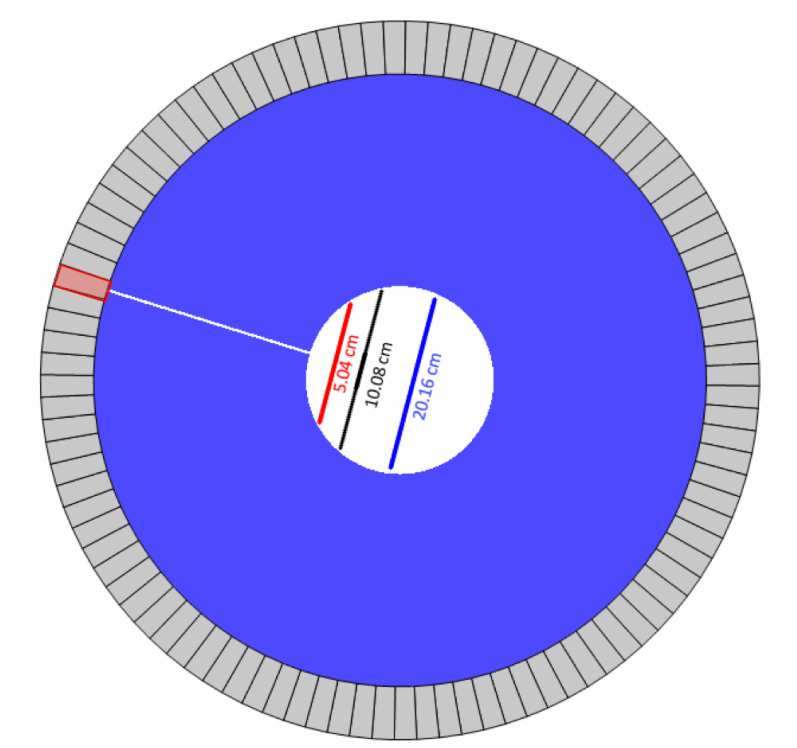


Figure 76. Single slit geometry pointing at Detector 51 (highlighted in pink) used to simulate a line source at 3 different distances moving perpendicular to the slit 51 centerline [65].

Figure 77 shows the detector response for the different source positions along the 10.08 cm chord for the 9 different slit widths. As the slit width increases, so does the intensity of the detector response. The "peak" signal at distance from centerline equal to 0 can be plotted from this data set to show how the signal component in a point spread function would actually change as a function of the slit width. To understand how the central peak counts behave as a function of slit width, the net central counts – the difference between the peak counts (source at centerline) and "noise" (source location furthest from centerline) – was plotted as a function of slit width. The response is pretty linear for the peak signal. Figure 78 shows the net peak counts as a function of slit width when the source is located directly on the centerline of detector 51. Unlike the trend seen in Figure 71, here the peak counts scale linearly as the slit width increases. This is the correct predicted response since this geometry had only one slit and the probability of leakage into the neighboring slits was eliminated. The fact that the counts scale linearly at the center mean that the direct peak component is proportional to the solid angle of the detector for a given slit width.

The collimator penetration is the second aspect that needs to be understood. This part is everything beyond either side of the peaks seen in Figure 77. The collimator penetration plotted against the source position relative to the slit centerline is shown in Figure 79. The collimator penetration has an overall quadratic relationship, and the fits are shown in the plot below as well. In addition to understanding how the direct component changes as a function of the slit width, these simulations with the single slit were used to understand the amount of "leakage" into the neighboring detectors to expect for a source at various positions in the sample cavity when the source is close to the edge of a slit and the probability of neutrons leaking into a neighboring slit need to be quantified in order to be able to account for it in the reconstruction. In order to illustrate the data from the three distances on the same scale, a projected width (W_p) was calculated. The projected width is illustrated in the image below and is the edge of the slit seen by the opposite end of the detector at a given distance. As the source gets further away from the detector, the projected width gets larger. The calculated W_p values for each of the chords and slit widths are shown in Table 11.

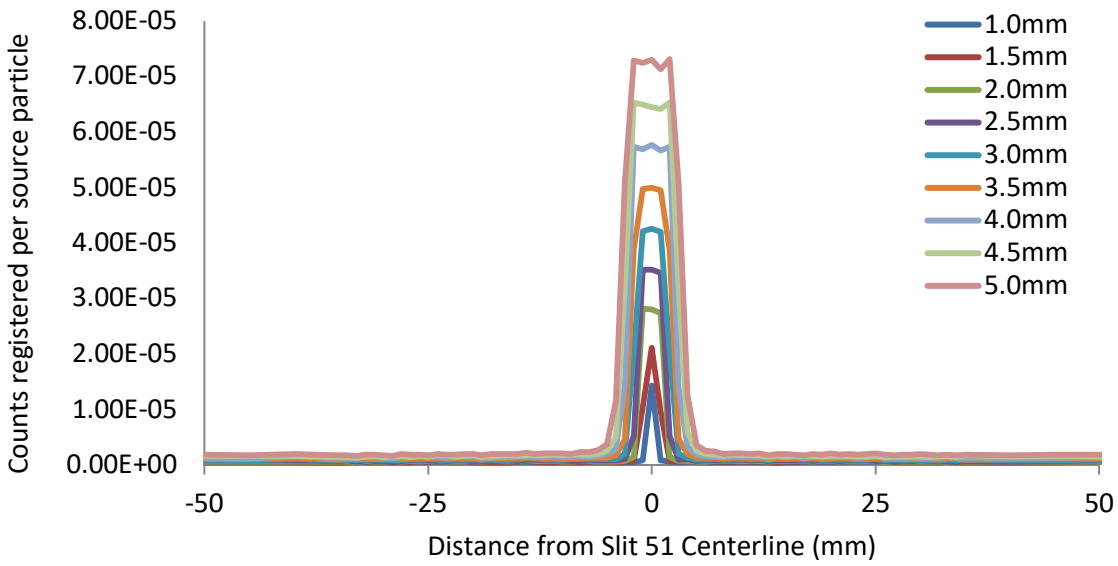


Figure 77. Detector 51 response for various source positions along the 10.08 cm away chord for the different slit widths investigated.

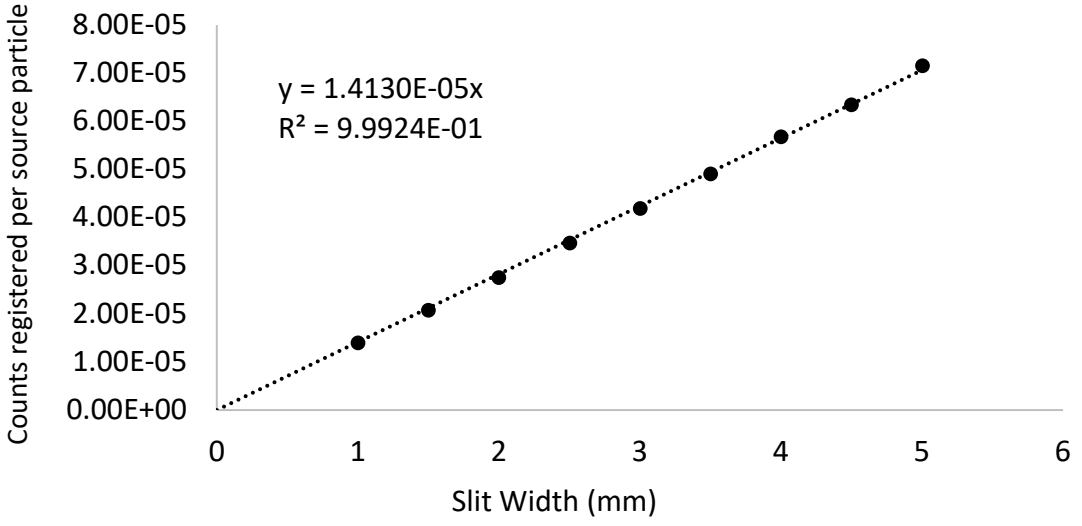


Figure 78. Plot of the peak counts registered at Detector 51 with the single slit geometry when the source is located on the slit 51 centerline 10.08 cm away for various parallel slit widths.

Table 11. Calculated W_p values for the different distances and slit widths simulated

Chord Perpendicular Distance from Slit 51 Opening (mm)	***Slit Width (mm)***	***Collimator Thickness (mm)***	W_p ***(mm)***
100.8	1	500	0.2016
100.8	1.5	500	0.3024
100.8	2	500	0.4032
100.8	2.5	500	0.504
100.8	3	500	0.6048
100.8	3.5	500	0.7056
100.8	4	500	0.8064
100.8	4.5	500	0.9072
100.8	5	500	1.008
50.4	5	500	0.504
201.6	5	500	2.016

A scaled intensity of counts seen at Detector 51 was calculated for each source position for each of the three chord distances by subtracting a calculated collimator penetration value at each source position using the respective polynomial fit constants corresponding to Figure 79 from the MCNP registered tally counts. The scaled intensity for each of the three chords were then normalized to their respective maximum values so that the source positions with direct line of sight to the detector had scaled intensities of 1. The scaled intensity for each of the chords is plotted against the source distance from the slit edge in units of W_p, as shown in Figure 80. This way $x = 0$ corresponds to the slit edge position for all three curves. This scaled relative intensity data as a function of the distance from slit edge in terms of W_p is shown in Figure 81. For the 10.08 cm curve data for all 9 slit widths is also included and they all fall very close together as shown in black.

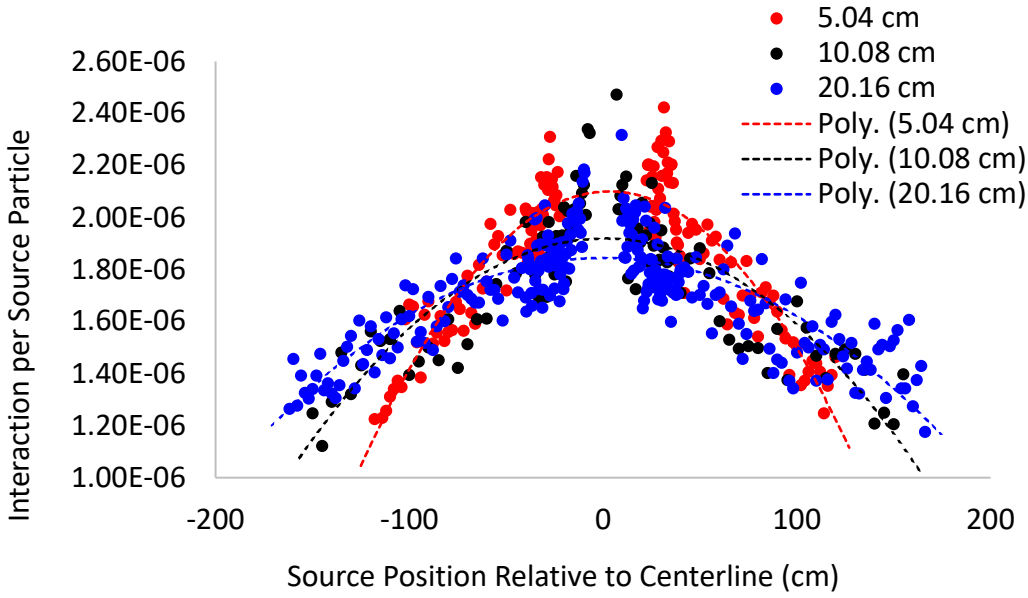


Figure 79. Collimator penetration components of the detector response for the 3 distances as a function of the source position relative to the slit centerline.

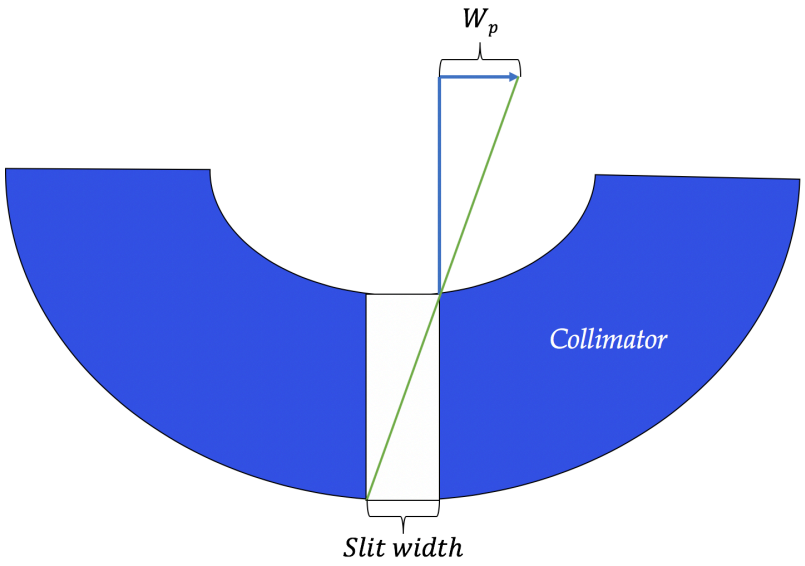


Figure 80. Projected width (W_p) in the single slit geometry [65].

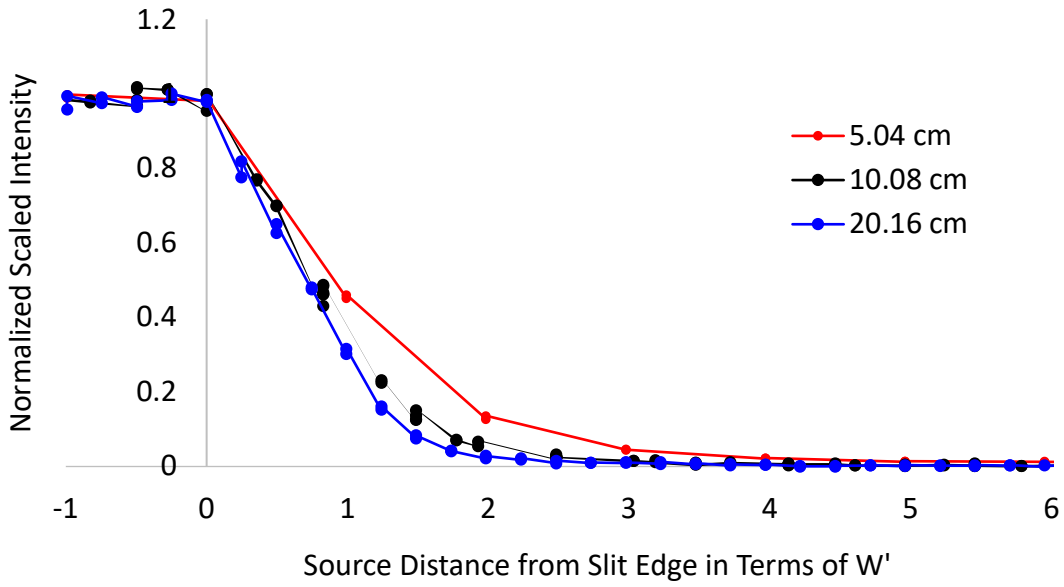


Figure 81. Scaled intensity calculated for all source positions at the three distances and plotted as a function of the source distance from the slit edge in terms of W_p [63] [65].

From the figure above, it can be seen that the response for all three curves is similar because when scaling the x to be in terms of W_p, the detector's view of the source for each of the three lines is similar. However, the lines do not completely overlap and the difference in source distance from slit opening has more of an effect than the slit width itself on the scaled intensity. This can be attributed to the fact that at the three different distances, the neutrons have varying amounts of collimator thickness to traverse due to the circular geometry, and at the shorter distance (5.04 cm), the neutron's path length is shorter, which elevates the scaled intensity. The neutron leakage can be estimated using this plot. The source can be assumed to be completely out of sight of a neighboring slit once it is beyond $3W_p$ from the respective slit's edge. Between 0 and $3W_p$ there is a non-negligible probability that the source is in the field of view of the slit. This intensity scaling once applied in the reconstruction code should be able to scale the response seen by each detector based on the source position and the relative distance to the corresponding slit edge.

6.5. Collimator Penetration

The collimator penetration are the components of the point spread function on either side of the peak as shown by the red curve in Figure 69. It is important to understand and be able to predict how the collimator penetration at every point and for every detector since the collimator is not homogenous dues to the slits cutting in at different angles and the collimator open and closed fractions do not stay constant as you go around the imager, thus the number of neutrons that pass through the collimator or down the slits varies around all 360°. The collimator penetration is a component of the noise, and it needs to be well characterized and understood so that it can be subtracted from the signal component accurately in order to improve the SNR and be able to reconstruct individual pins accurately. An additional source of noise in addition to the collimator penetration is the neutrons that scatter back into the detector from the surrounding borated polyethylene and stainless steel. The amount of backscatter into the detectors will differ for each of the seven different geometry radii because the neutrons reaching the detectors scale as $1/r$, and there are two different fuel cask configurations considered to house the imager which had different thicknesses of borated polyethylene and stainless steel on the outside.

The goal of this section is to predict the collimator penetration for the various geometries and parameters using the simulated dataset. The backscatter neutrons were found to be an issue after simulations looking at the detector response with no collimator at the seven different detector radii (40 cm, 42 cm, 43 cm, 45 cm, 50 cm, 53 cm, and 55 cm.) The point spread functions for a source located 14.30 cm from the slit 51 opening (same as source position 1) were computed using a single line source for the seven radii and are shown in Figure 82. The no collimator response is to be used in scaling the registered response with the collimator in place in order to correct for the $1/r$ drop off. The point spread function for the 45 cm case does not lie between 43 and 50 as would be ideally expected with the $1/r$ relationship.

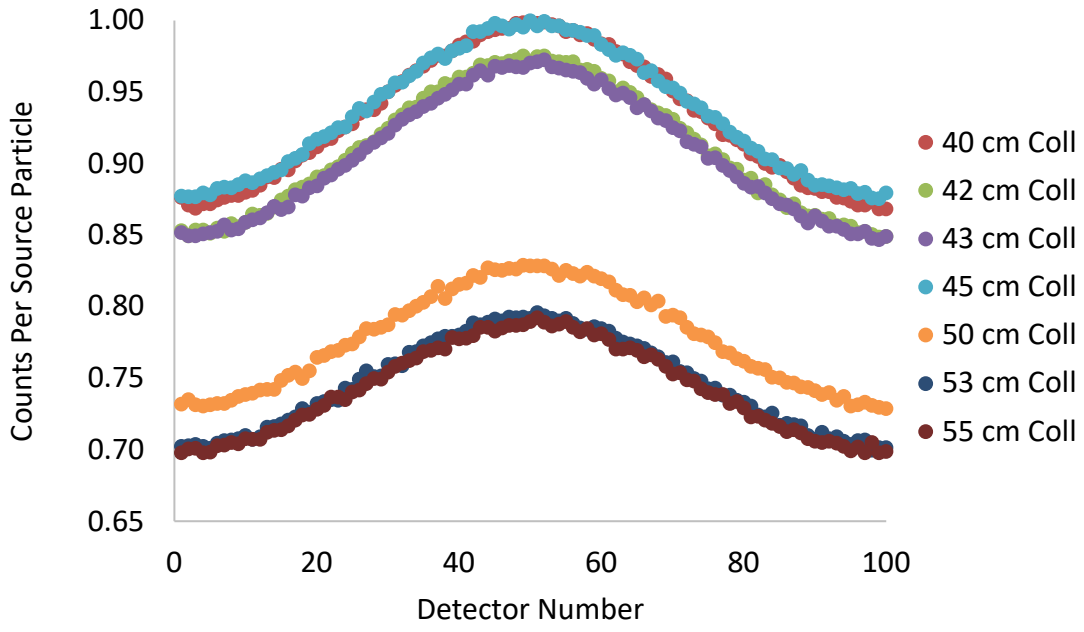


Figure 82. Normalized point spread functions for the seven different detector radii with no collimator in place.

The predicted $1/r$ dropoff was calculated using the change in total radius (fuel assembly cavity + collimator thickness + air gap thickness + inner Cd layer) to the detector. The calculated $1/r$ points are shown in black in Figure 83, and the MCNP calculated response at Detector 51 normalized is shown in red. The normalized data plotted against each of the seven collimator thicknesses confirms that the detector response for the 45 cm thick collimator is indeed higher than would be predicted, and unlike the other data points, does not sit on the $1/r$ curve. As a result of this, a set of simulations looking at the direction of neutrons passing each surface was tallied to verify what effect was causing this.

To verify that this was caused by the backscattered neutrons, seven more simulations were conducted with the source in the same position, but the F1 MCNP tally was used instead of the F4 to give the particle current through the surface. To be able to identify backscatter neutrons from neutrons escaping the imager, a cosine bin was used to separate the neutrons exiting the surface (moving away from the center) and entering the surface (moving towards

the center of the geometry). The F1 cosine bin tally was implemented on the outer Cd layer to see what fraction of neutrons entered back into the detector versus what fraction traveled out. Figure 84 shows the diagram of the imager geometry used to conduct the no collimator simulation and the F1 backscatter simulations. The issue with the back scattered neutrons is that they elevate the count rate but can also increase inter-detector scatter. This, it would be good to limit geometries to those with limited backscatter. Table 12 lists the outer borated polyethylene thicknesses simulated for each of the collimator thicknesses.

Using the MCNP simulation F1 tally data and taking the ratio of the neutrons backscattered into the detectors to the neutrons leaving the detector and representing it as a function of the outer borated polyethylene layer thickness is shown in Figure 85.

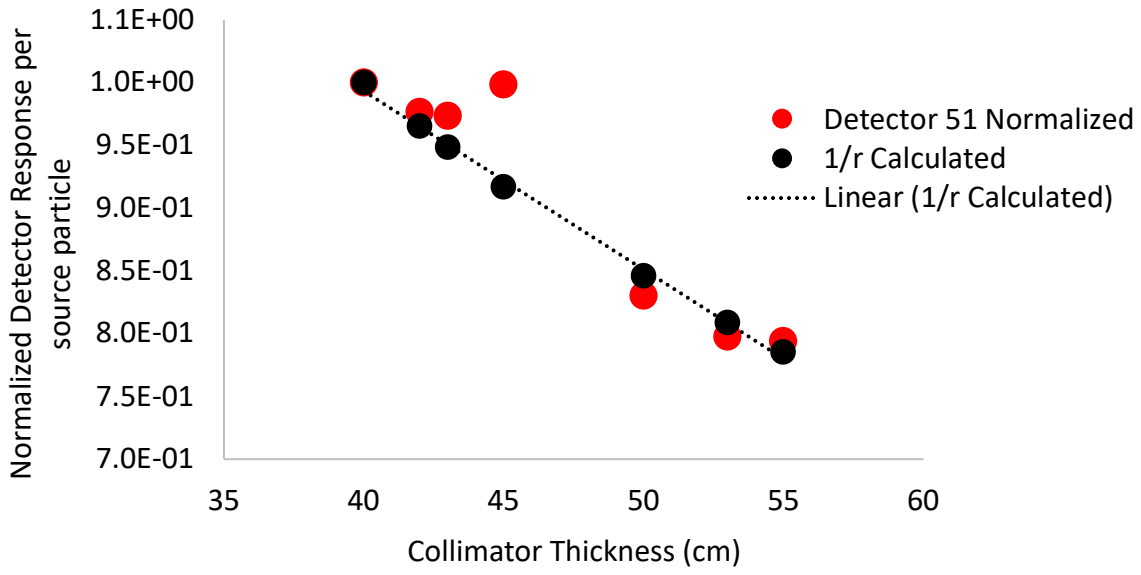


Figure 83. Normalized Detector 51 F4 response per source particle for each of the 7 collimator radii (corresponding to different collimator thicknesses). The black dots are calculated $1/r$ and the red dots show the actual drop-off seen with the MCNP simulations.

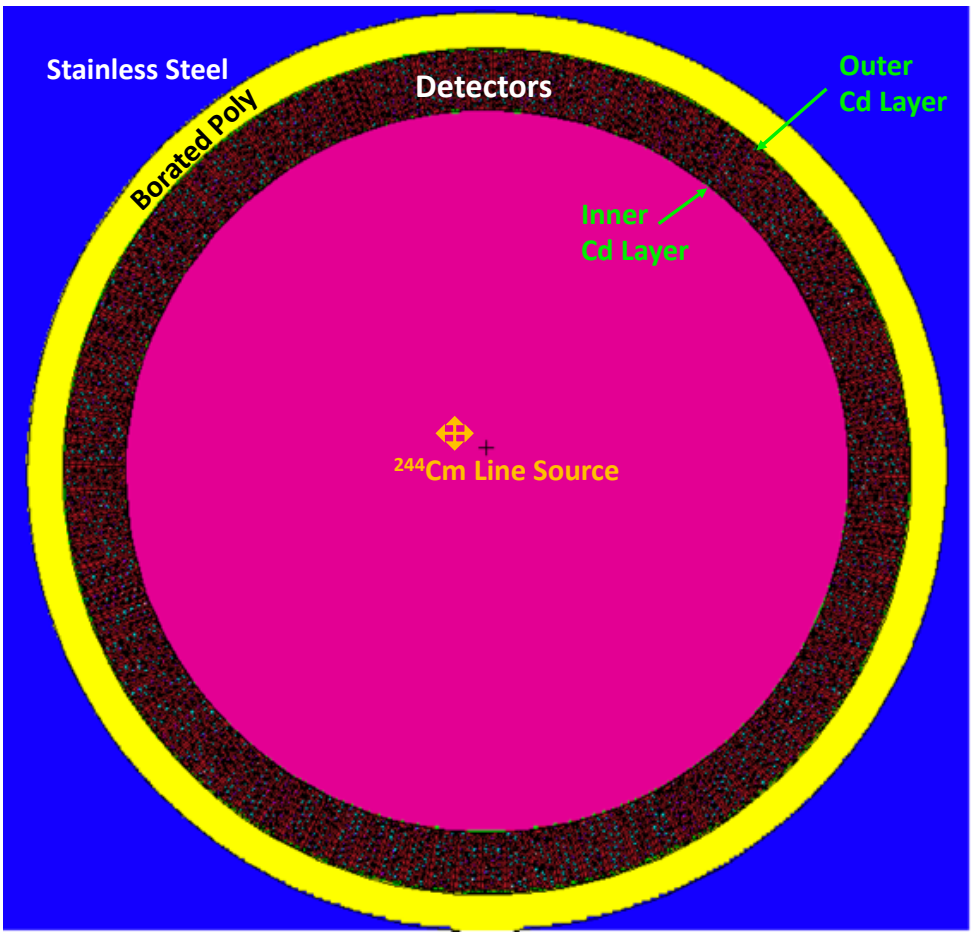


Figure 84. Diagram of imager geometry without collimator used to conduct the backscatter and 1/r simulations.

Table 12. List of the total collimator thicknesses and outer borated polyethylene thicknesses.

Collimator Thickness (cm)	*Outer Borated Poly Layer Thickness (cm)*
40	5.822
42	3.822
43	2.822
45	0.822
50	6.912
53	3.912
55	1.912

Small thicknesses of borated polyethylene result in a larger amount of backscatter, and the relationship tapers off at a non-uniform rate as the thickness is increased. The normalized surface flux (going into the detector) is shown in Figure 86. The highest number of particles being reflected back into the detector correspond to the collimator thickness of 45 cm, which has the thinnest amount of borated polyethylene on the outside of the detectors (0.822 cm). The amount of backscatter can be reduced by 50% by increasing the amount of borated polyethylene on the outside to 5.822 cm.

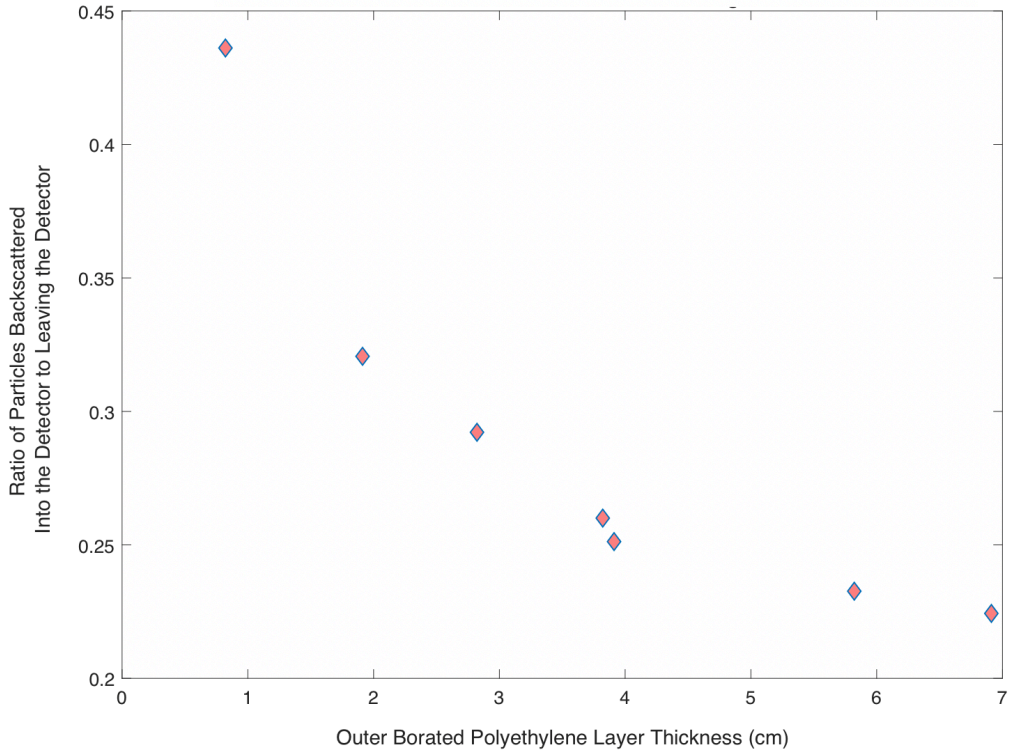


Figure 85. Ratio of the neutrons backscattered into the detector to the ones leaving the detector as a function of the thickness of the outer borated polyethylene.

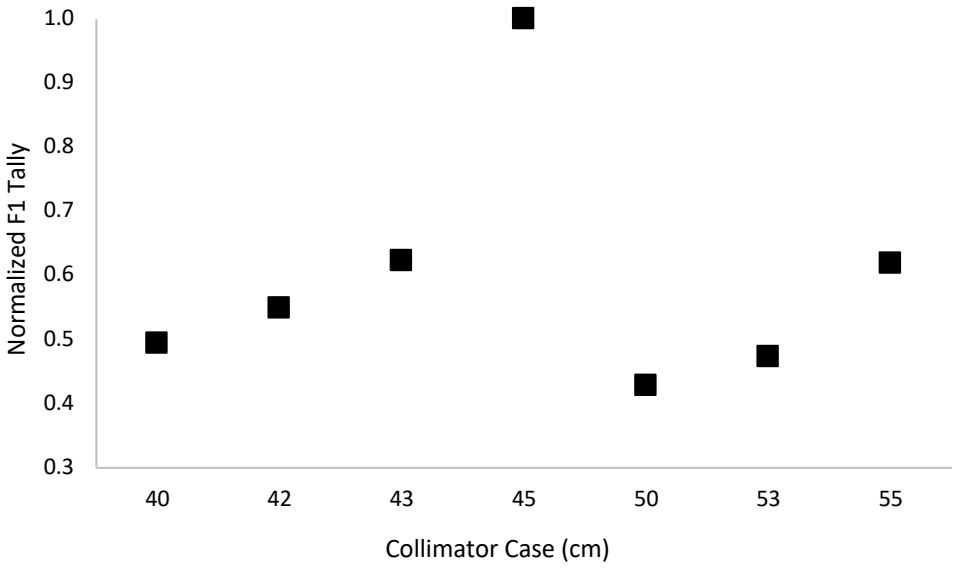


Figure 86. Plot of the normalized particle flux on the surface showing the fraction of particles backscattered into the detectors for each of the seven different radii.

6.5.1. Predicting Collimator Penetration

The next step is to take the no collimator data, the no slit data, the open and closed fractions of the borated polyethylene, and the open and closed fractions of the stainless steel to try to predict the collimator penetration for a given configuration. In order to do this, the 512 point spread functions generated with the ^{244}Cm line source located at the first source position (14.30 cm from the slit 51 opening) were used. The collimator penetration from the MCNP simulations was calculated for each configuration by assuming it was equivalent to the average count rate between detector 25 to 30 and 70 to 75 since the detector response in the PSF was the flattest in this range of detectors. Assuming for a given collimator total thickness T_{tot}, R_1 is the inner radius of the collimator, R_2 is the outer radius of the collimator, and T_{SS} is the stainless-steel thickness. The respective dimensions are shown in Figure 87 below.

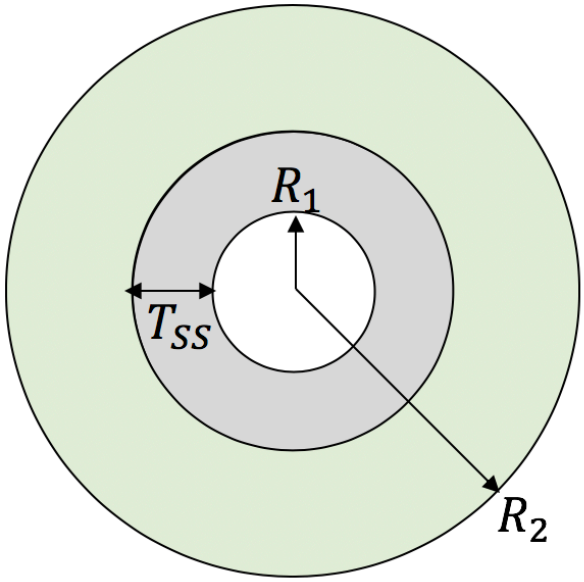


Figure 87. Dimensions of the collimator components labeled. Steel is shown in grey and borated polyethylene is shown in green.

For a solid shield (no slits), the transmission through the material scales as

$$N = N_0 e^{-\mu T}$$

where μ is the material attenuation coefficient, and T is the material thickness. A first order prediction of how the collimator penetration, or transmission, scales through a collimator consisting of two materials with slits cut into it can be presented as:

$$\text{Transmission} = \frac{1}{R_2} e^{-\mu_{BP}\frac{\rho_{\text{actual BP}}}{\rho_{\text{donut BP}}}(R_2 - R)} e^{-\mu_{SS}\frac{\rho_{\text{actual SS}}}{\rho_{\text{donut SS}}}(T_{SS})}$$

(19)

where $\rho_{\text{actual BP}}$ is the density of the borated polyethylene component of the collimator with the slits cut in, $\rho_{\text{donut BP}}$ is the density of the borated polyethylene component of the collimator assuming no slits were cut into the collimator and was a completely solid donut. Similarly, $\rho_{\text{actual SS}}$ is the density of the stainless-steel component of the collimator with slits cut into it, and $\rho_{\text{donut SS}}$ is the density of the stainless-steel portion of the collimator with no slits cut into it. Finally, μ_{BP} and μ_{SS} are the attenuation coefficients of borated polyethylene and stainless-steel respectively. The value for the borated polyethylene attenuation

coefficient was assumed to be 0.2 cm^{-1}, and 0.02 cm^{-1} for stainless steel. The density ratios are proportional to the close fractions (F_C) of the collimator components calculated using MCNP. Equation (19) can be re-written as an expression of the mean free paths

$$\frac{\rho_{\text{actual BP}}}{\rho_{\text{donut BP}}} = F_{C\,BP}$$

$$\frac{\rho_{\text{actual SS}}}{\rho_{\text{donut SS}}} = F_{C\,SS}$$

$$-\log(R_2 * \text{Transmission}) = \mu_{BP} F_{C\,BP} T_{BP} + \mu_{SS} F_{C\,SS} T_{SS}$$

(20)

The right side of the equation directly above gives the estimated mean free path, which can be compared to the MCNP-calculated mean free path. The MCNP-calculated mean free path is the *actual* thickness and can be calculated using the MCNP generated simulations by using the neutron response from the no collimator cases ($N_{\text{no collimator}}$) for each case and the neutron response or transmission (N) for each geometry. The actual thickness, or transmission through the collimator is given by

$$\text{MCNP Calculated Transmission} = \log\left(\frac{N_{\text{no collimator}}}{N}\right) = \log(N_{\text{Ratio}})$$

(21)

If the predicted mean free path equation shown on the right side of Equation (20) is an accurate prediction, the calculated transmission should be equivalent to the actual MCNP modeled transmission in Equation (21). The difference between the calculated value and the actual MCNP transmission is the error in mean free paths (Δ) where

$$\Delta = \text{Calculated Thickness} - \text{Actual Thickness}$$

(22)

The error if the predicted equation is correct, should be constant and centered around 0 for all measured transmission values. Using Equation (20) and Equation (21), the error was calculated for all 512 geometries, and it is plotted against the actual transmission in Figure 88. The 16 different data sets plotted are the different stainless-steel and borated polyethylene combinations. As the actual transmission increases, the error goes down. Additionally, the

error is not close to 0. This indicates that Equation (20) is missing some correction factors. The curves are also staggered, and the error seems to get higher (curves are displaced higher) the thicker the layer of borated polyethylene is. The orange curve has the lowest error values and corresponds to the 10 cm steel and 30 cm borated polyethylene case, and the curve that has the highest error values is the case with the largest amount of borated polyethylene with 5 cm steel and 50 cm of borated polyethylene. The borated polyethylene content primarily influences the neutron transmission as a result, it would be expected that for all the cases, the ones with similar borated polyethylene open fractions would have similar transmission values. To visualize how the error changes relative to the polyethylene content it plotted against the borated polyethylene open fraction for each of the 512 cases shown in Figure 89. The lines are clustered closer together, but the error goes up as the open fraction goes up. This effect is due to the fact that the calculated thickness value does not account for streaming paths that are created in the slit or the effect of the stainless steel in attenuating the neutrons. The first step in trying to get closer in estimating the calculated transmission as accurately as possible to the actual transmission is to eliminate the dependence on the stainless-steel component of the collimator. If the stainless-steel had a negligible effect on the collimator, then the slopes of all the lines in Figure 89 would be approximately the same regardless of the steel thickness; however, that is not the case. Also, the lines with same borated polyethylene thickness and different steel thicknesses cross each other as the borated polyethylene open fraction increases. This can be seen in the 5 cm steel / 40 cm borated polyethylene and 10 cm steel / 40 cm borated polyethylene cases. This shows that the steel has an effect that needs to be accounted for in the calculated estimate of the effective thickness. A correction factor for the stainless-steel component needs to be calculated in order to develop a more accurate estimate of the calculated transmission. Each of the 16 data sets has a linear slope, and the slope for each of the cases is listed in Table 13.

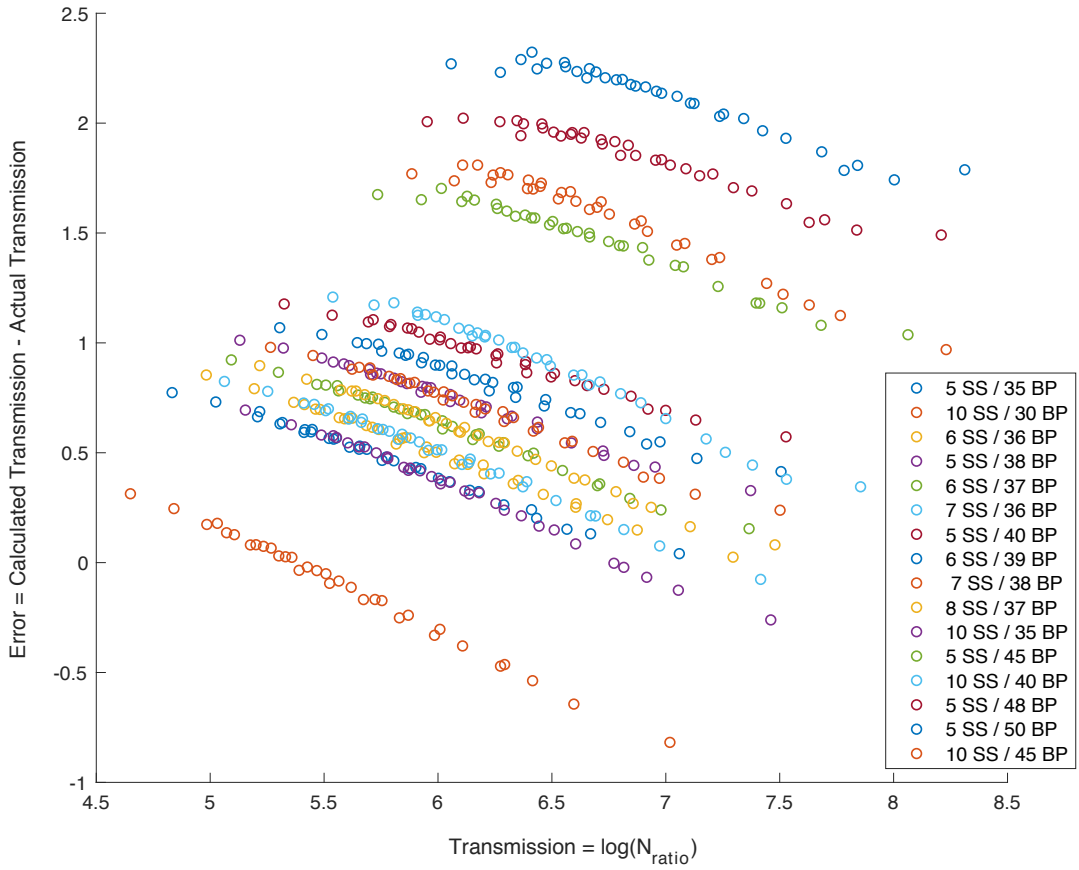


Figure 88. The error or the difference in mean free paths between the calculated transmission and the actual tranmission plotted against the actual transmission for all 512 geometries.



Figure 89. Error, or difference between the calculated and actual transmission plotted as a function of the borated polyethylene open fraction.

Table 13. To extract the stainless-steel correction factor, the slope of each line from the previous figure was extracted. The slopes of the lines with the same steel thicknesses are similar and are listed here.

Case	***Stainless Steel Thickness (cm)***	***Borated Polyethylene Thickness (cm)***	***Slope***
1	5	35	4.044
2	10	30	6.2451
3	6	36	4.5048
4	5	38	3.9039
5	6	37	4.3692
6	7	36	5.0243
7	5	40	3.5386
8	6	39	4.0312
9	7	38	4.5164
10	8	37	4.9246
11	10	35	5.8792
12	5	45	4.4985
13	10	40	6.328
14	5	48	3.9565
15	5	50	4.2101
16	10	45	5.9438

The slopes from Table 13 were plotted as a function of the stainless-steel thickness and the data was fit to a line to understand the effect of adding stainless steel. The data is shown in Figure 90, and the points with same steel thickness should have similar slope values, but will not be the same because each of the cases with the same steel thickness have different thicknesses of borated polyethylene on the outer layer, which would prevent the transmission responses from being the same. The data, however, does appear to lie along a line, and the slope from the fit equation could be used to develop a correction term to incorporate into the equation to calculate the transmission.

The correction term to incorporate into the calculated thickness equation was estimated to be a function of the steel thickness, steel close fraction, and the corresponding open fraction of the borated polyethylene ($F_{O\,BP}$). The borated polyethylene open fraction is incorporated in this correction factor because it has to be scaled for two reasons– once for the steel component since the open fraction changes for each of the steel thicknesses, and once for streaming paths. Using the slope of the data in Figure 90 as a factor by which to scale these components results in the last term in the following equation

$$\text{Calculated Thickness} = \mu_{BP} F_{C\,BP} T_{BP} + \mu_{SS} F_{C\,SS} T_{SS} - 0.414\, F_{O\,BP}\, T_{SS} F_{C\,SS} \quad (23)$$

Using this to calculate the effective thickness of the collimator and looking at the difference between the calculated values and the MCNP values shows that the different slopes seen in Figure 89 were corrected for the most part, and the lines with different steel thicknesses and same polyethylene thicknesses are close together and do not cross each other as the open fraction increases. This shows that the steel component correction developed in Equation (23) was a decent approximation. The revised error values using Equation (23) is shown below in Figure 91. The values at borated polyethylene open fraction of 0 correspond to the cases with no slits.

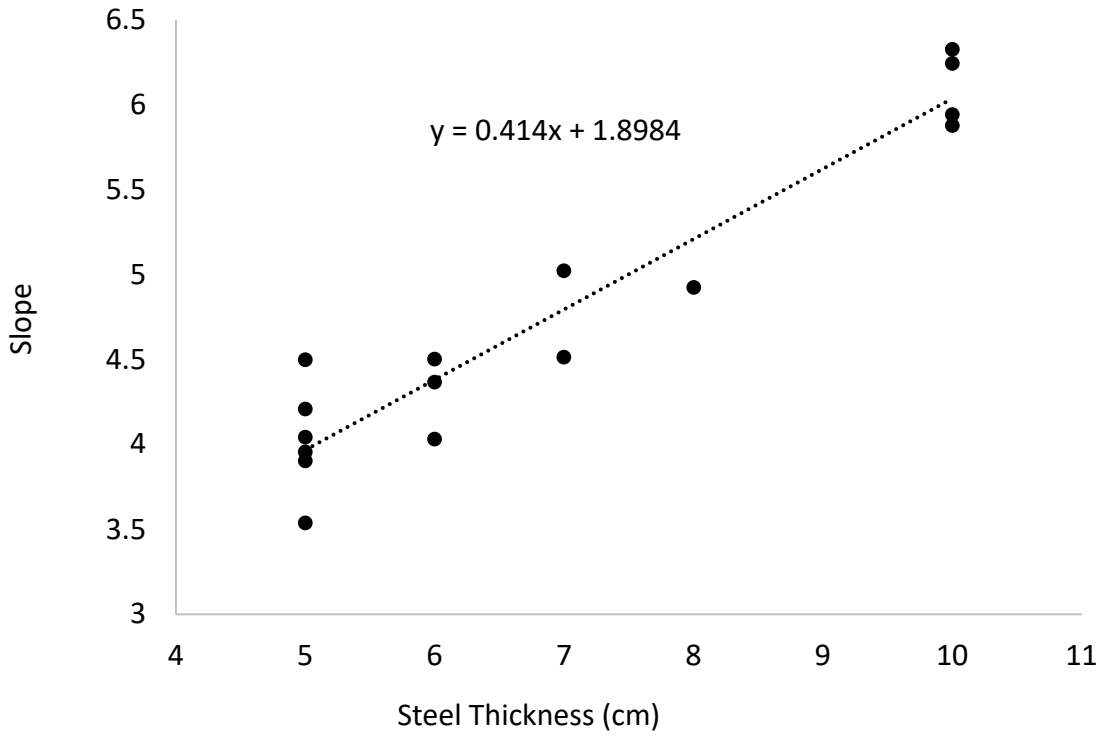


Figure 90. To understand how the stainless-steel affects the neutron transmission through the collimator, the slope values of the lines for each of the 16 cases was extracted and are plotted against the steel thickness.

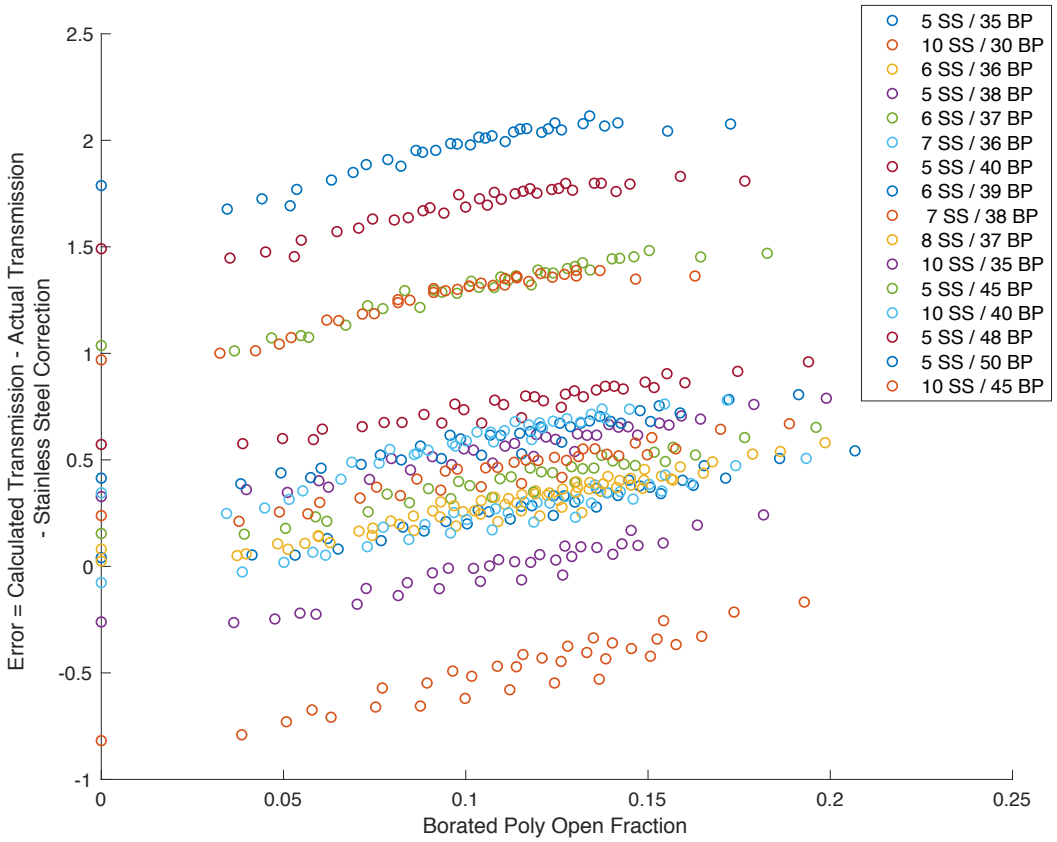


Figure 91. Error, or difference between the calculated and actual transmission corrected for the stainless steel component plotted as a function of the borated polyethylene open fraction

The calculated thickness equation as it stands currently assumes a homogeneous material with the open fraction distributed uniformly throughout the collimator material, but that is not the case. As slits are cut into the collimator, streaming paths for neutrons are created, which means not all the neutrons interact with the same amount of collimator as they traverse through the material. This affects how the effective thickness needs to be calculated to match up better with the MCNP model. The streaming paths created require a correction to the open fraction of the borated polyethylene, after which the slope of the lines in Figure 91 should be eliminated. To eliminate the change in difference between the calculated and actual thicknesses as a function of the borated polyethylene open fraction, the slopes of the lines in Figure 91 were extracted. The respective slopes of each of the data sets were used as the factors to scale the open fraction by. Equation (23) was modified by subtracting the open fraction of borated polyethylene scaled by the respective slope values (m) to yield

$$\text{Calculated Thickness} = \mu_{BP} F_{C\,BP} T_{BP} + \mu_{SS} F_{C\,SS} T_{SS} - 0.414\, F_{O\,BP}\, T_{SS} F_{C\,SS} - m\, F_{O\,BP} \quad (24)$$

Using this revised estimation of the effective thickness results in error values for each of the 16 cases where the slope is altogether eliminated, thus effectively eliminating the streaming path effects. The revised error values using Equation (24) are shown in Figure 92. The estimate of the calculated thickness in Figure 92 has corrected for streaming paths but is not quite right because it is assuming that the behavior of $\log(N)$ versus the effective through the collimator is linear, but that is not the case. Plotting the log of the average noise for all 512 cases in Figure 93 against the initial estimate of the effective thickness in Equation (20) shows that the relationship is not quite linear, and as the thickness increases and the neutrons traverse through more material, the data curves up and a tail appears. This means that the attenuation coefficient does not stay constant as the neutrons penetrate the collimator. If the attenuation coefficients were constant, then the line would be linear. Figure 93 shows that the attenuation coefficients are decreasing at larger effective thicknesses since the logarithm of the counts does not decrease at the same rate at lower thicknesses.

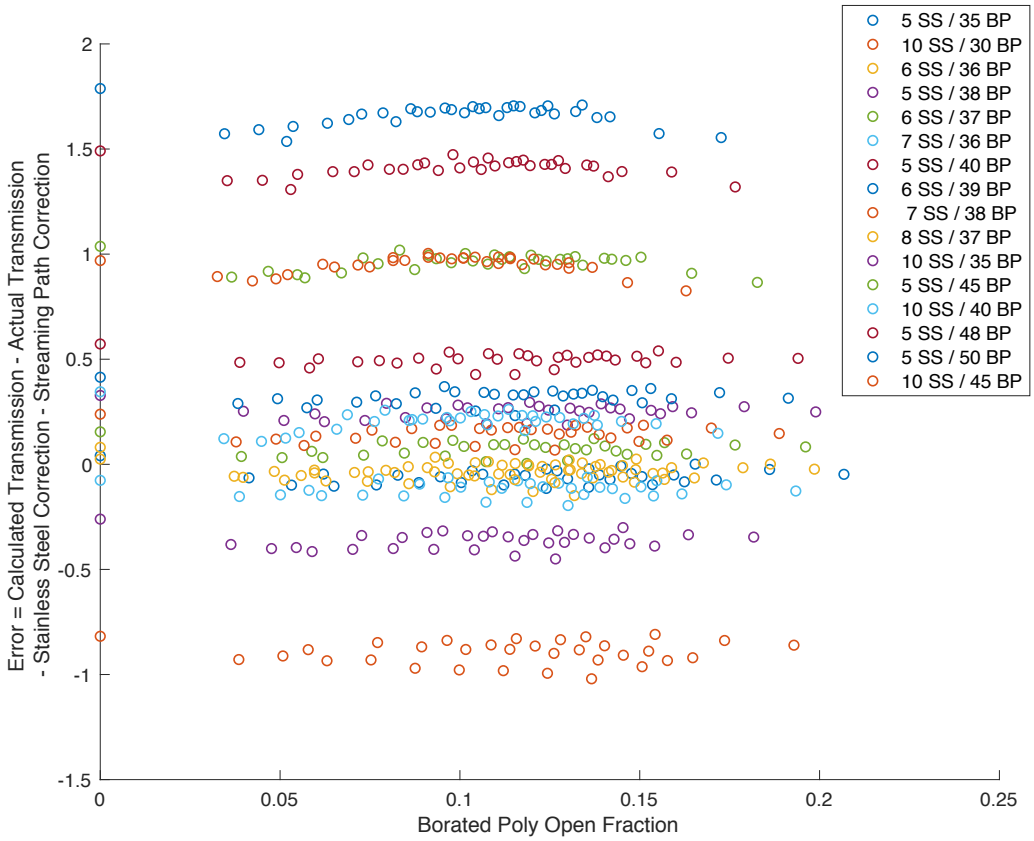


Figure 92. Error values (difference between the calculated and actual transmission) after corrected for steel and streaming paths as a function of the borated polyethylene open fraction.

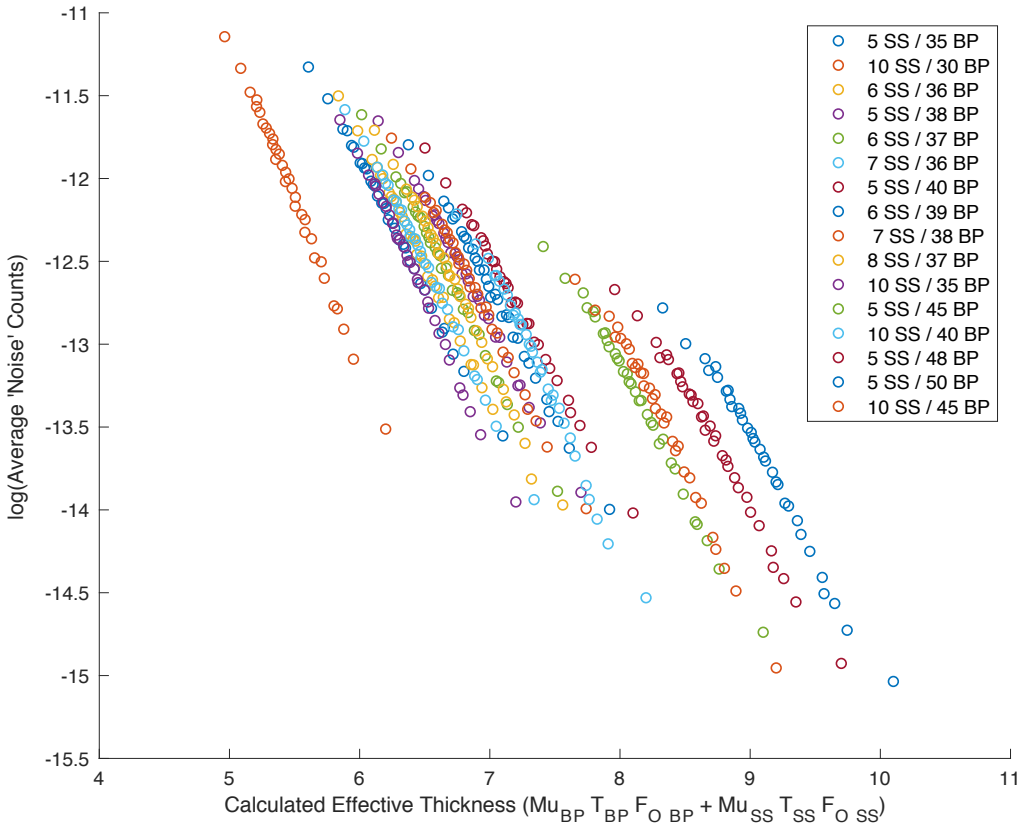


Figure 93. The log(noise) as a function of the effective thickness for each of the different cases simulated.

This effect of changing attenuation coefficients is due to beam hardening, which means the average energy of the neutron spectrum is increasing as it goes through more material since the borated polyethylene absorbs more of the lower energy neutrons as the neutrons pass through the collimator material. This means the relationship between calculated transmission and measured transmission isn't perfect yet. The energy shift in the neutrons increases rapidly in the initial amount of distance traversed and stabilizes after a crossed thickness. Another constant needs to be applied to correct for the borated polyethylene thickness based on each case to correct for the beam hardening effect. Once this is incorporated, the error values should be close to 0 for all cases, and the data sets in Figure 92 should be clustered closer together about $Y = 0$. Since the offset from $Y = 0$ requires a correction factor applied to the borated polyethylene collimator thickness, the Y intercepts of the data in Figure 92 were extracted again. The Y intercepts were then plotted as a function of the polyethylene thickness as shown in Figure 94. The data was then fit to a line. The fit equation shown in the plot was applied to the borated polyethylene thickness, which becomes the beam hardening correction. The final version of the equation to calculate the transmission for a given geometry and predict the average noise in the imager is:

$$\text{Calculated Thickness} = \mu_{BP} F_{C\,BP} T_{BP} + \mu_{SS} F_{C\,SS} T_{SS} - 0.414\, F_{O\,BP}\, T_{SS} F_{C\,SS} - 0.1135 T_{BP} - 4.1983 \quad (25)$$

The error values calculated using this revised equation are plotted in Figure 95. The error values are all centered around 0.00 ± 0.22 mean free paths. Accounting for the steel correction, the effect of the streaming paths on the borated polyethylene open fraction, and the beam hardening effects on the neutrons as they traverse larger thicknesses reduces the error significantly.

Finally, plotting the calculated transmission using all the correction factors in mean free paths against the actual transmission also in mean free paths in Figure 96. The values lie approximately along a straight line. Although it is not a perfect one-to-one relationship due to the complicated collimator geometry, the correction factors developed in this section provides a good approximation of the average noise for each of the different collimator geometries.

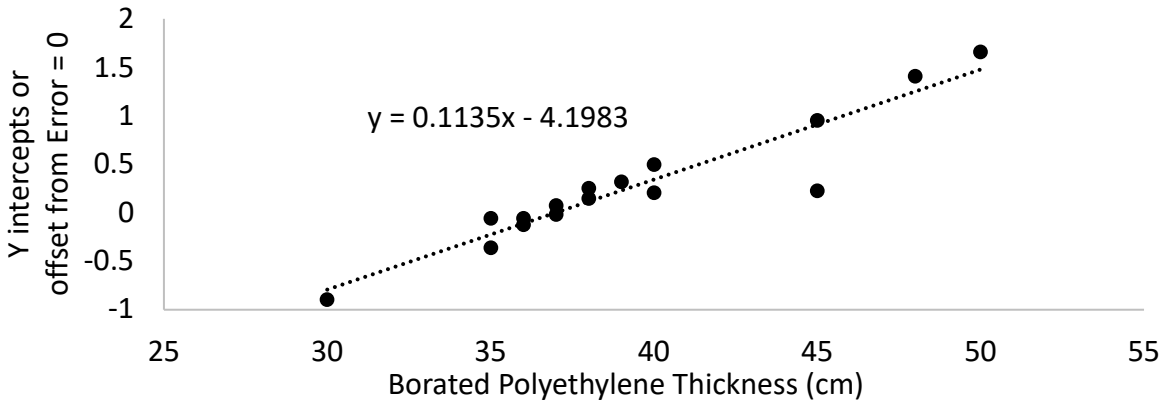


Figure 94. Extracted *Y* intercept values from the open fraction correction applied plot as a function of the borated polyethylene thickness.

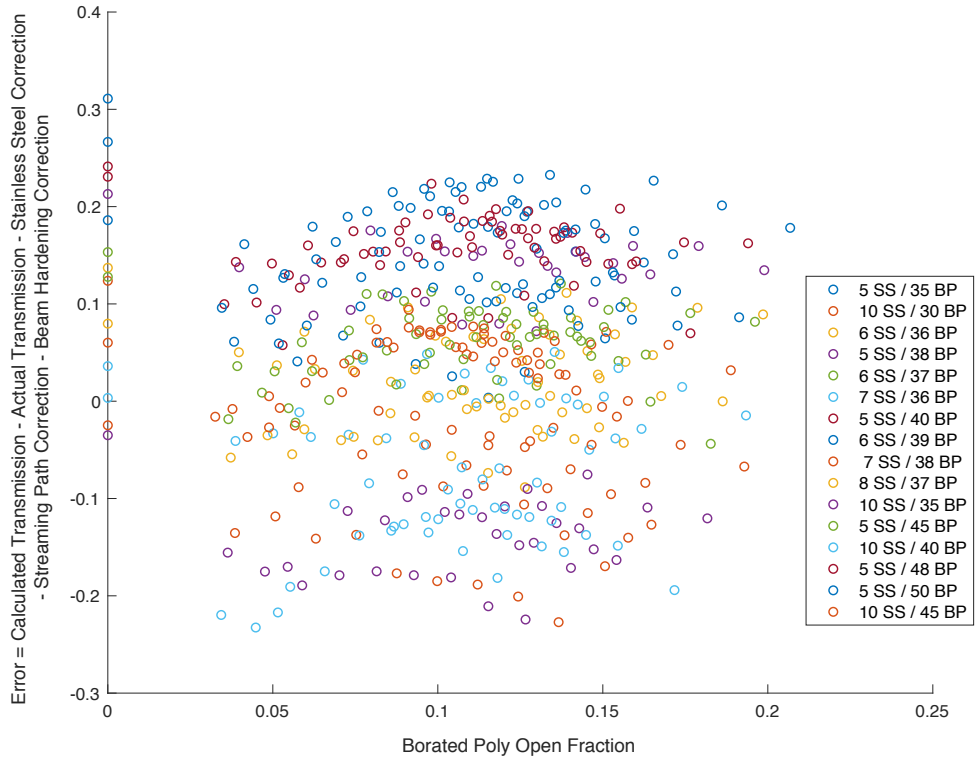


Figure 95. Error between the calculated and actual transmission as a function of the borated polyethylene open fraction. The calculated transmission here accounts for all the correction factors.

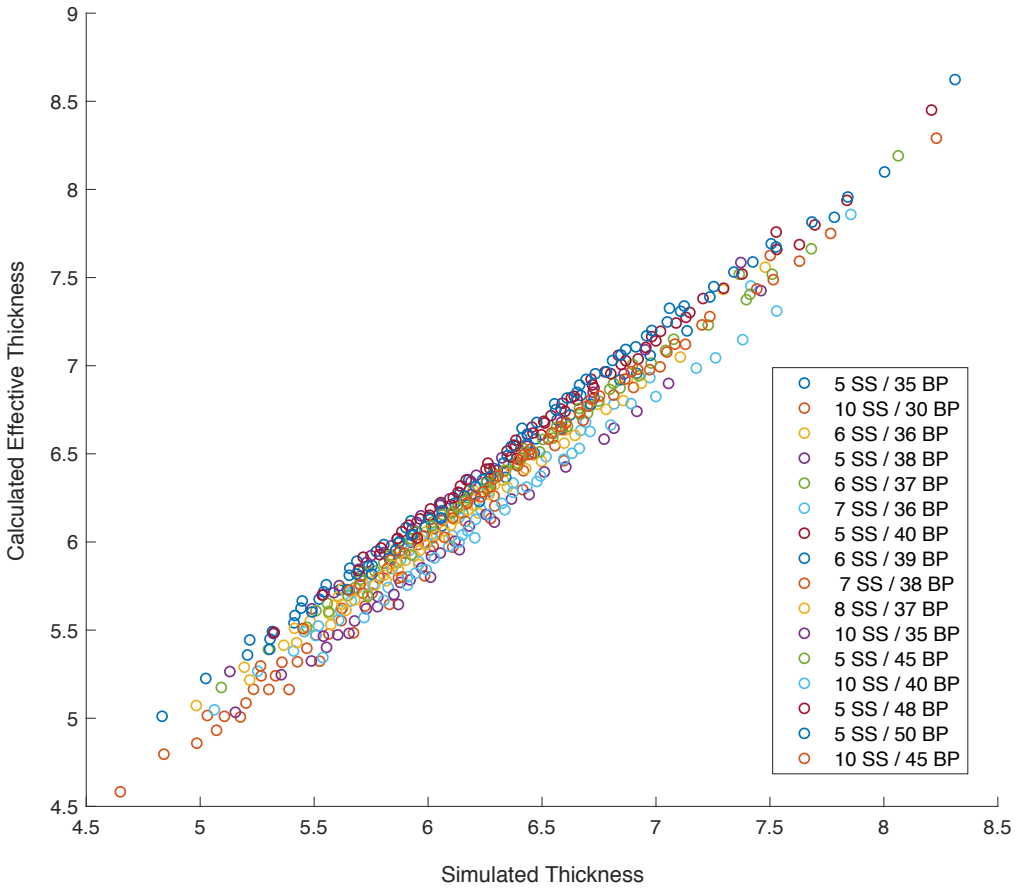


Figure 96. Calculated thickness using all three correction factors in mean free paths versus the simulated actual thickness in mean free paths for all 512 cases.

6.6. Parametric Study and Signal-to-Noise Ratio Results

To evaluate the 512 different configurations and identify the best one suited for spent fuel tomography, an SNR code was developed to process the data. For this work, the SNR was defined as the metric by which the 512 designs would be evaluated in lieu of a full up reconstruction code. The SNR calculation will help identify the most desirable configuration that is compact in size, has good spatial resolution, and can manage the gamma exposures effectively at the detectors. The goal of the SNR is to use the point spread functions from the two sets of 512 simulations with the source placed at the two different locations. From the previous sections, it is evident that the background, or collimator penetration values decrease as the collimator thickness increases or the slit width decreases. The signal increases linearly with the slit width, and also increases with thinner collimators. The inter-detector scatter plays a role in calculating the SNR, and also the signal at a particular detector depends on where relative to the respective slit edge the source is located since the amount of leakage down a neighboring slit depends on the source location. All of these factors affect how the reconstruction will be conducted, and also the ability of the imager to associate the neutron activity with an individual fuel pin versus the space between the fuel pins. The most ideal configuration will have the most drastic difference between the source (fuel pin), and the gap between the pins. The signal is the difference between the calculated response of the imager to each pin and the activity attributed to the gap or the "halo" around each pin. A cartoon highlighting the respective areas is shown in Figure 97.

The SNR is a comparison of the magnitude by which the signal changes to the counts from a complete assembly, so the noise component which is the denominator ends up being the square root of the counts of the complete assembly. The SNR is shown in Equation (26) and is the sum over all 100 projections.

$$SNR = \sum \frac{|\, Response\ to\ single\ pin - Response\ to\ pin\ halo|}{\sqrt{Response\ to\ complete\ assembly}} \quad (26)$$

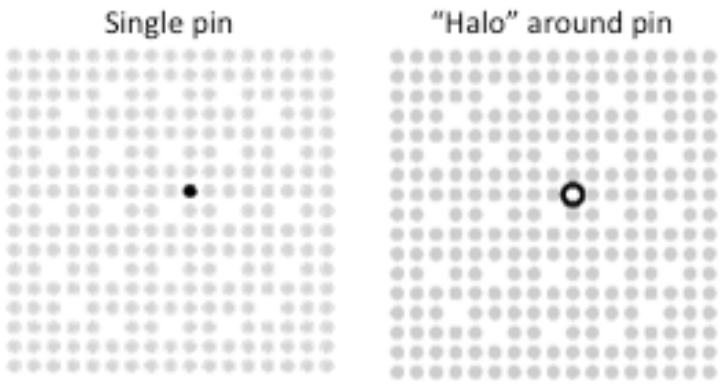


Figure 97. Image of a 17 × 17 fuel assembly with the two components making up the signal highlighted. In the left image, a single pin is shown, and on the right, the area around the pin, the "halo" is highlighted [63].

A pictorial of the SNR equations showing the respective sinograms that contain the data used for a sample projection is shown in Figure 98. To calculate an SNR for a given configuration, the imager response across the entire field of view needs to be estimated on a millimeter scale to be able to identify a fuel pin with a diameter of 0.90 cm, and a pin pitch of 1.2780 cm. This means that the imager needs to be able to identify the gap between the pins, which is 0.378 cm. The approximate imager response was developed using the point spread functions from the simulations of the ^{244}Cm placed at two different positions. The direct component and collimator penetration values from the neutron simulations detailed in this chapter were used and the response was extrapolated to the various points in the field of view. The signal component is the difference between the peak and the collimator penetration in the point spread function. The peak value for each position was scaled based on the distance between the source location and the detector. The estimated response to the source positions that do not lie directly in line with a slit is found by using the projected slit width. The response is scaled using the data shown in Figure 81 since the response from the edge of the slit to 1.8 projected slit widths lies along a line. The numerator and denominator in the SNR equation were scaled by the number of source particles in the MCNP simulations (1×10^6) per pin per projection. The resulting SNR values for all the configurations are shown in Figure 99 as a function of the geometric mean of the slit widths. The geometric mean of the slit widths is the square root of the product of the inner and outer slit widths. The SNR

values for the parallel slit cases with slit widths greater than 2.5mm calculated using Equation (26) needed to be scaled because the source position used to generate the point spread functions resulted in some leakage down the neighboring slits at larger slit widths, thus artificially increasing the peak value. Ideally, the peak at the center needs to rise linearly as a function of slit width, but as shown in Figure 71, this didn't end up being the case. Scaling factors for each of the 16 cases were calculated by plotting the peak heights for the parallel slit widths, and fitting a linear slope to the 1mm, 1.5mm, 2mm, and 2.5mm data. Since the expected peak height for larger slit widths is expected to lie along a line, the fit equation was used to solve for the expected peak values that were then compared to the actual peak values to find the scaling factors.

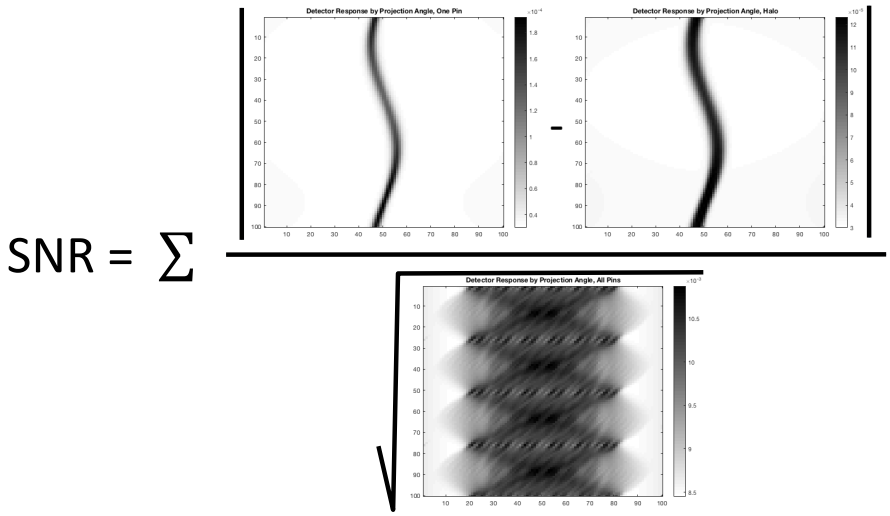


Figure 98. Pictorial of the SNR equation used to evaluate all the geometries with sinograms [65].

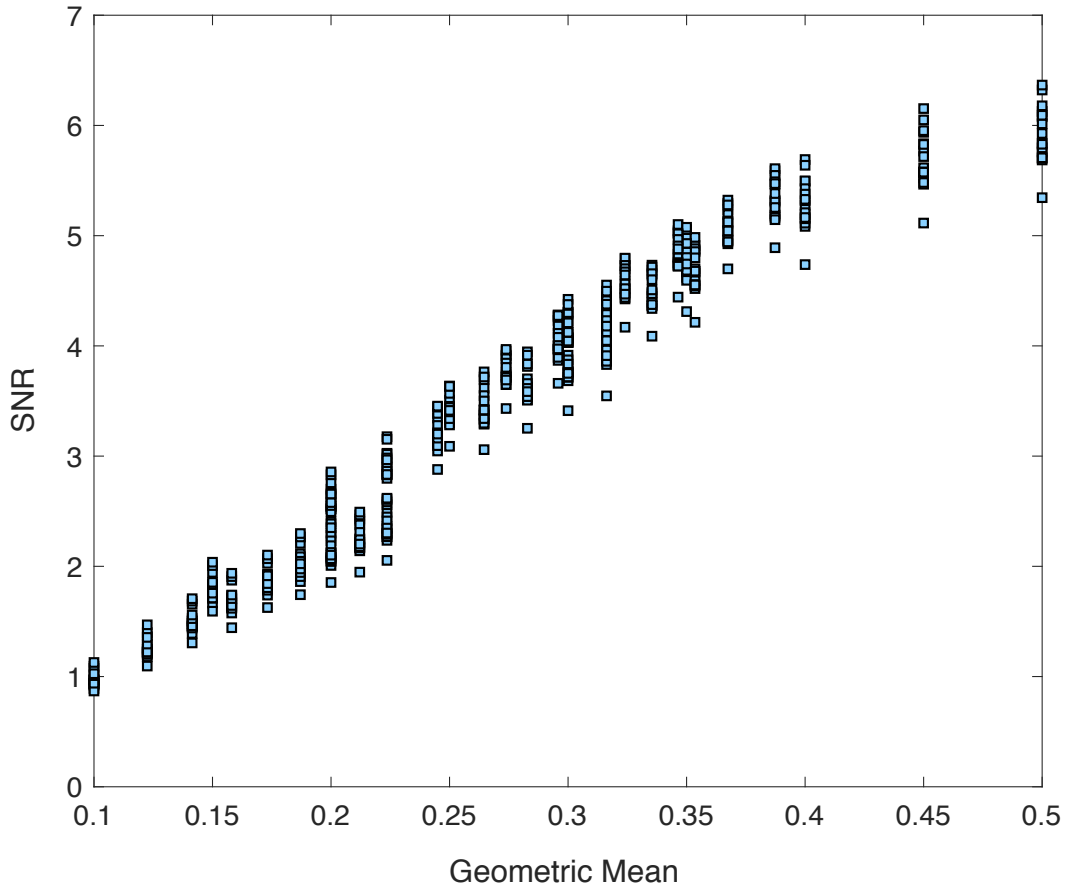


Figure 99. SNR values for all 512 cases plotted against the geometric mean (cm) of the slit widths.

To visualize more clearly how for a given case the SNR varies, the cases with the least (30 cm) and most (50 cm) amounts of borated polyethylene are shown below. The case with the least amount of borated polyethylene has the lowest SNR, and the case with the most borated polyethylene has the highest SNR. The SNR increases as the slit width geometric mean increases, so even if a smaller collimator design was chosen, the desired SNR could be achieved by modifying the slit width. The SNR values do not roll over completely because the slit width that limits the spatial resolution enough to lower the SNR was not simulated.

To narrow down and select the set of geometries that satisfy the most important factor in developing a neutron imager – tolerance of gamma exposures – the scaled SNR is plotted against the maximum gamma exposures for each of the 512 cases. As covered previously, the fundamental limitation for the detectors is that they cannot operate at exposures higher than 500 R/hr. Figure 101 is a plot of all the SNRs for all 512 configurations and the corresponding maximum gamma exposures. A line showing the 500 R/hr limitation is also shown. Each of the 16 configurations lies on its own trajectory with increasing SNR corresponding to increasing maximum exposures since the slit width increases as well. As the steel thickness increases the curves move more to the left, and the points get closer together. The curves show that with more steel and less polyethylene an imager with sufficient SNR can be built in a more compact form factor that meets the gamma exposure limitation.

The SNR values for the two cases with the most compact geometry (40 cm thick collimator) and the two sets of data making up the largest geometry (55 cm thick collimator) were plotted in Figure 102. The amount of steel makes the most difference in cutting down the gamma exposure. While maintaining the same total thickness of the collimator at 40 cm, comparable SNRs can be achieved by increasing the steel thickness to 10 cm from 5 cm. Increasing the total thickness to 55 cm can also lower the maximum exposure, but the improvement in SNR achievable is not notable. The curves for the 10 cm steel / 30 cm borated polyethylene and the 5 cm steel / 50 cm borated polyethylene overlap for the most part and diverge as the parallel slit widths increase. An SNR of 5 or better is achievable with the 10 cm steel / 30 cm borated polyethylene case if more tapered slit cases were investigated.

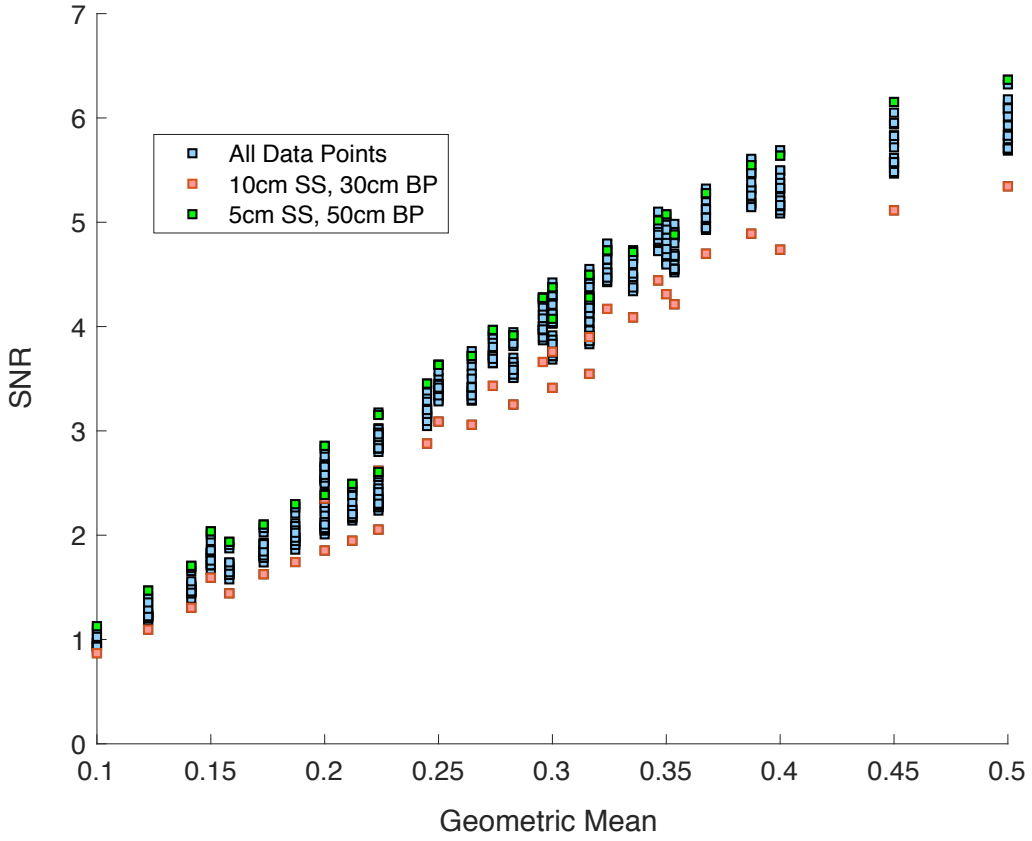


Figure 100. SNR for all 512 cases plotted against the geometric mean (cm) of the slits. The case with the least amount of borated polyethylene (10cm steel and 30 cm borated polyethylene) and the most amount of borated polyethylene (5 cm steel and 50 cm borated polyethylene) are highlighted.

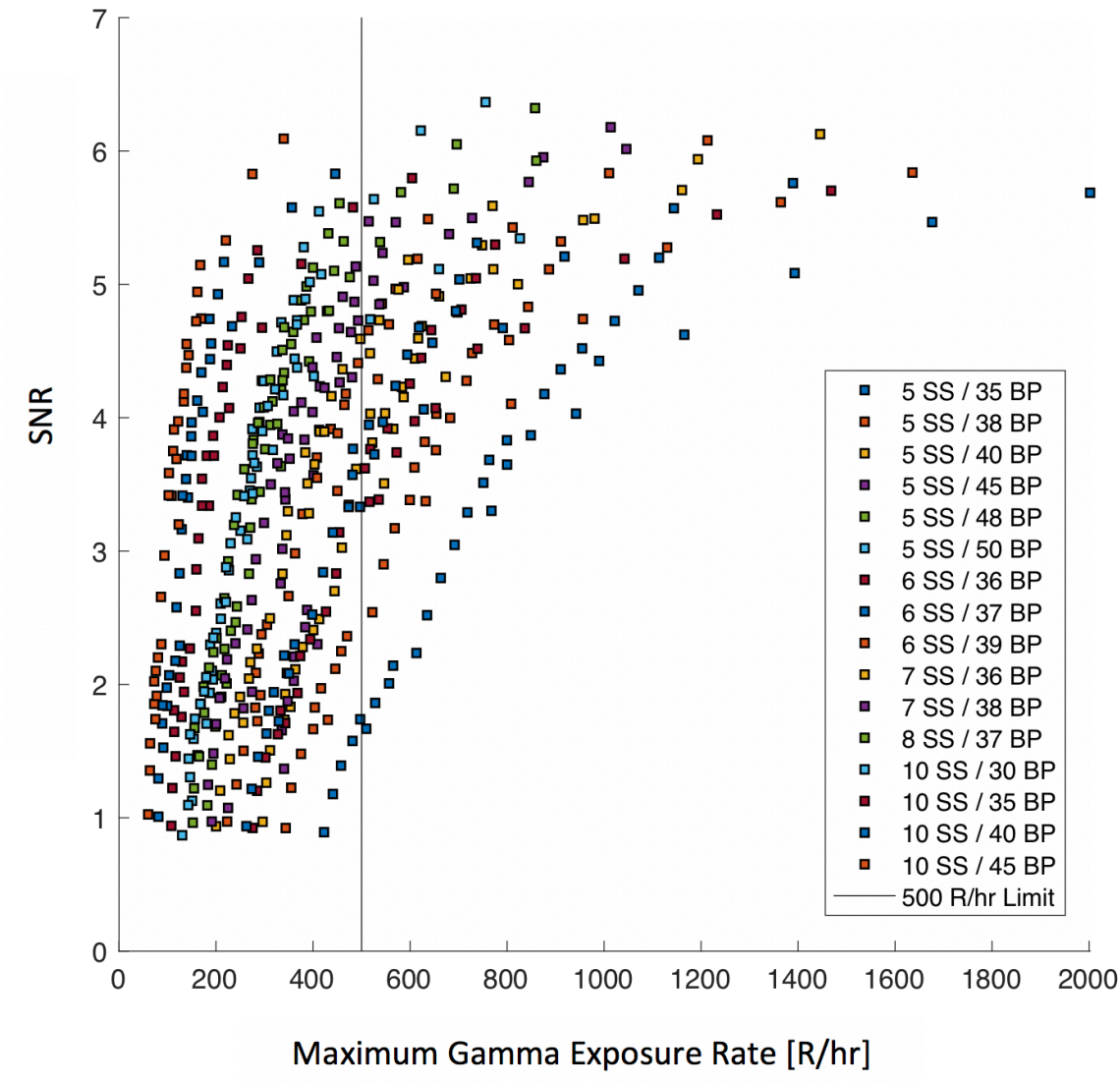


Figure 101. The SNRs for all 512 geometries plotted against the maximum gamma exposures for each configuration. The line defining the 500 R/hr operational limit for the detectors is shown on the plot as well.

If a size constraint did not exist for the imager, the 10 cm steel and 45 cm borated polyethylene case (shown in green in Figure 102) would provide the best SNR value (> 6) if extrapolated out to 500 R/hr. Assuming an SNR of 5 and above is sufficient, an imager with a smaller footprint with 10 cm of steel and 30 cm of borated polyethylene can be built. Figure 103 shows the SNR values for the 10 cm steel and 30 cm borated polyethylene case broken up by slit width case (parallel slit and the four different tapered slit sets). Also shown on the plot is a fit line extrapolating how the SNR for the 3mm inner slit width tapered cases would increase if the outer slit width were increased. Since the gamma exposure mitigation occurs mostly closer to the inner diameter of the collimator, keeping the inner slit width smaller and increasing the outer slit width allows for higher neutron efficiency while keeping the gamma exposure down to manageable levels better than the parallel slit cases would. Thus, the ideal configuration for the imager that has to comply with the resolution requirement and size limitation would be one that has a 10 cm steel and 30 cm borated polyethylene collimator with tapered slits. The tapered slits with 3mm inner slit width and larger that 5mm outer slit width would be able to meet the spatial resolution requirements, cut down the exposures to manageable levels, while increasing the neutron efficiency. For the final imager design, to get to an SNR greater than 5 with this configuration while keeping the maximum gamma exposures below 500 R/hr, a tapered slit was chosen with 3mm on the inside and 8mm on the outside.

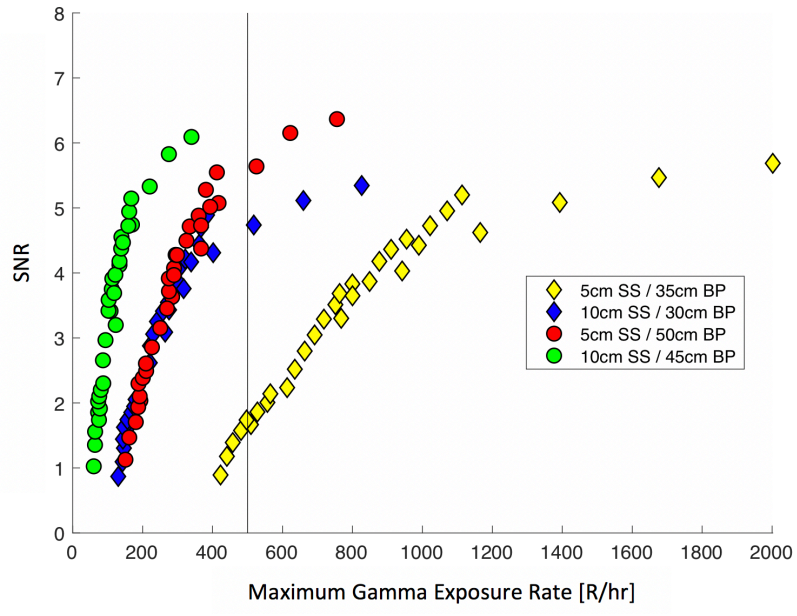


Figure 102. SNR values for the four cases with the thickest (55cm) and thinnest (40cm) collimator configurations as a function of the maximum exposure.

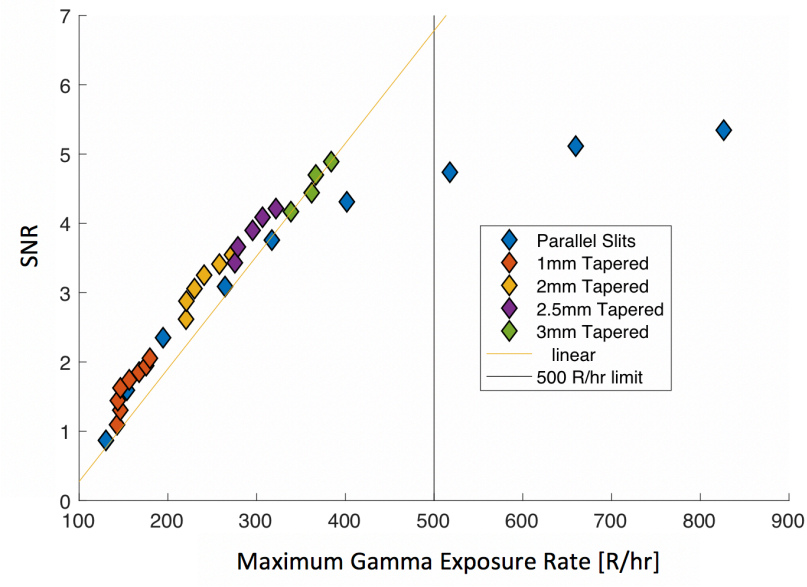


Figure 103. SNR values for the 10 cm steel and 30 cm borated polyethylene case broken up by parallel slits, tapered slits with inner slit widths of 1 mm, 2 mm, 2.5 mm, and 3 mm. A line of fit (yellow) shows what the SNR would scale as if the inner slit width remained at 3 mm and the outer slit width were increased beyond 5 mm.

7. FINAL IMAGER DESIGN

The results of the comprehensive parametric study showed that the ideal imager design to achieve the desired SNR has 10 cm of stainless steel and about 30 cm of borated polyethylene. To achieve the desired SNR with a compact design, tapering the collimator slits is expected to help achieve higher efficiency and maintain the spatial resolution. The final simulated design has 96 slits with 3 mm inner slit width and 8 mm outer slit width. The initial envisioned design had 100 detectors and 100 slits, but because the electronics have 8 channels, the number of detectors has to be a factor of 8. Thus, the number of detectors was reduced to 96. This chapter will detail the final selected geometry, the results of MCNP simulations, SNR calculations using the final geometry, experiments with a prototype detector module, and the outcome of simulating a complete fuel assembly.

7.1. Final Geometry

The detectors in the final geometry are no longer separated by 3 rows. The final imager has 12 separate detector modules, with each module containing 24 rows of 8 detectors. The rows are not parallel to each other, and all have the same origin of geometry as the rest of the imager unlike the previous design where each detector was made up of 3 parallel rows of detectors placed in an 8-7-8 pattern. Each of the 96 slits point to the center of every 3 rows, and each row of 8 straws has a single read out. The signal from every three rows is summed to calculate a final detector response. The final dimensions of the imager are shown in Table 14. The final imager design also has 5 cm of borated polyethylene on the outside of the detector. A picture of the final prototype detector module is shown in Figure 104 and an image of the MCNP model of the module is shown in Figure 105. The module consists of 24 rows of 8 straws.

Table 14. Dimensions of the final collimator design.

Imager Component	***Dimension***
Overall imager height	100.000 cm
Fuel assembly cavity radius	17.677 cm
Stainless steel thickness	10.000 cm
Borated polyethylene thickness	29.523 cm
Air gap between collimator and detector	0.300 cm
Inner slit width	0.300 cm
Outer slit width	0.800 cm
Al wall	0.0635 cm
Cd layer	0.0406 cm
Detector HDPE thickness	9.9187 cm

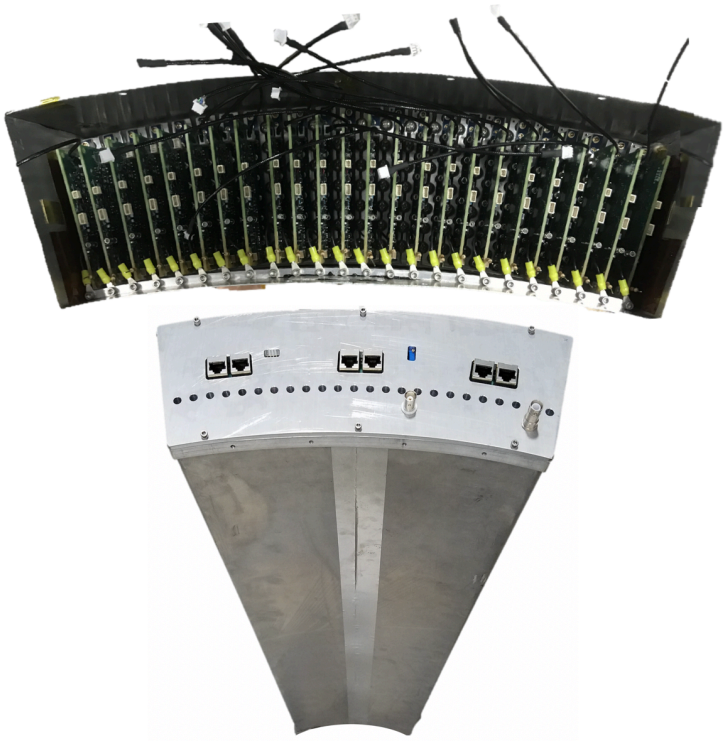


Figure 104. Photos of the final detector module with 24 rows of straws. (Top) the view of the detector circuitry with the top open. (Bottom) The outer view of the detector module aluminum casing and the 6 readout ports [57].

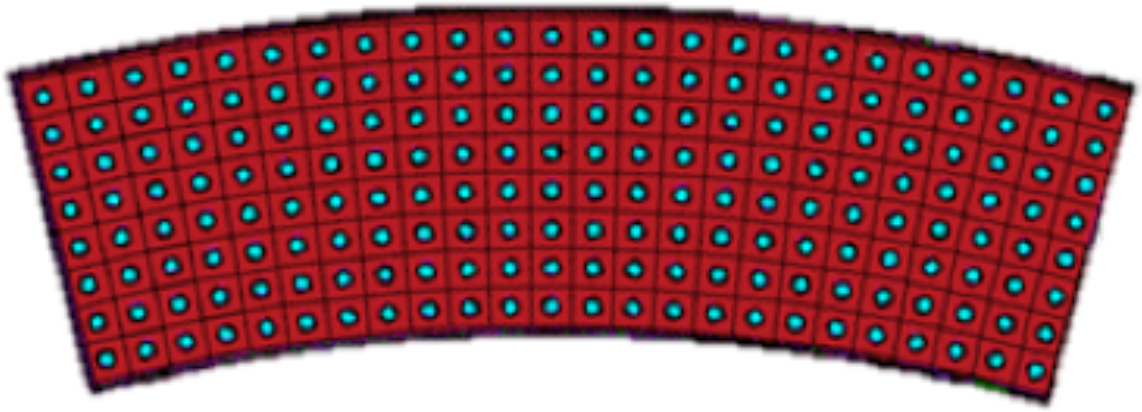


Figure 105. MCNP model of a single detector module in the final geometry. A single module contains 24 rows of 8 straws, and the imager contains 12 modules, or 288 rows of straws [57].

The MCNP model was constructed by creating a single module of 24 rows embedded in a high-density polyethylene (HDPE) matrix. A single row of 8 detectors was translated 24 times in a lattice spacing calculated carefully based on the experimental prototype. The pitch between individual straws is 1.1988 cm, and each row is rotated 1.25° about the origin. A single detector module consisting of the 24 rows of straws in HDPE, the air gap surrounding the HDPE matrix containing the straws, aluminum walls, and Cd layers on the inner and outer radii make up another universe in MCNP that is rotated and repeated 12 times to make up 360° of detectors. Figure 106 shows what the interface between two modules looks like. The purple walls are the Al walls of the detector modules, and the green is the outer Cd layer, and the pink is the air gap within the detector. A close-up of the imager geometry is shown in Figure 107. The first slit points to row number 14 the way the MCNP geometry was constructed. Every single slit points to the center of every 3 rows. The parts in yellow in the image correspond to borated polyethylene. The blue on the outside of the borated polyethylene layer is the stainless steel of the ‘cask-like’ container, and the pink in the slits and between the detector and collimator is the air-gap.

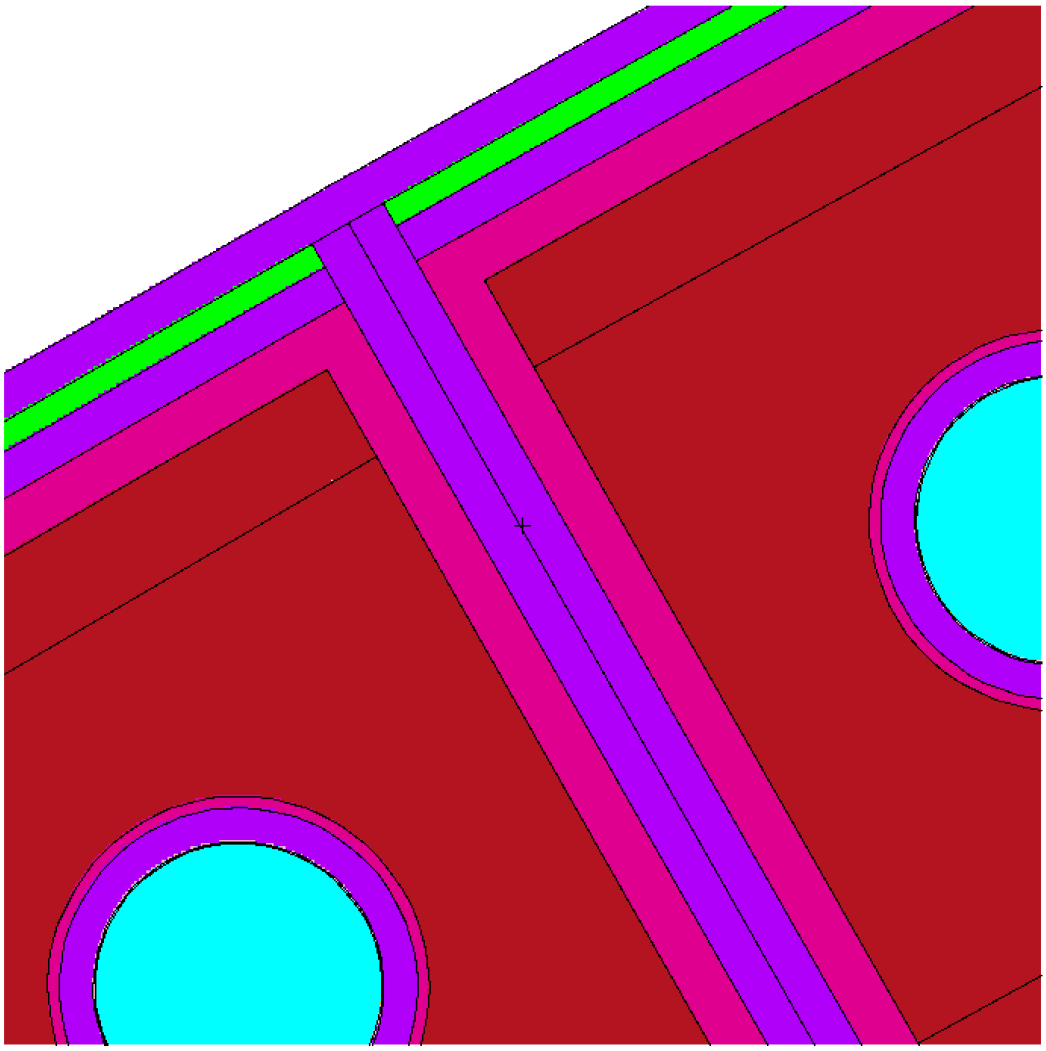


Figure 106. Close-up of two detector modules showing the Al walls (purple), air gap (pink), and the Cd layer (green).

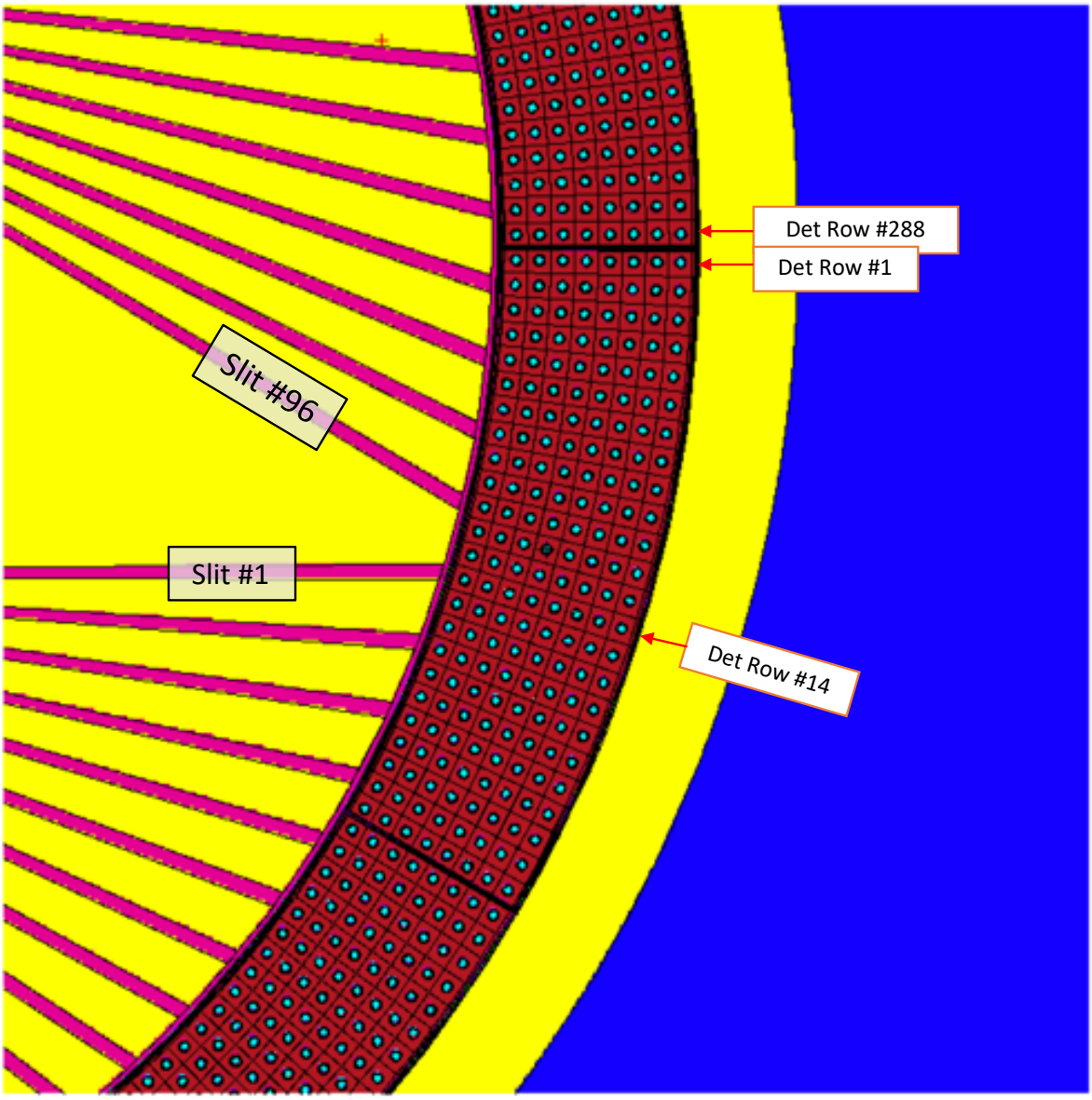


Figure 107. Close-up of the final imager geometry in MCNP. The slits corresponding to the first (1) detector and last (96) are labeled in the picture, as are the first and last rows as constructed in MCNP.

7.2. Edge Effects in the Final Geometry

Similar to the study done in Section 6.4, to accurately account for the edge effects the final geometry was modified in MCNP to just have a single slit at detector 49, and a single ^{244}Cm source was moved perpendicular to the slit at three different distances – 5.04, 10.08, and 20.16 cm from the slit opening. A projected width (W_P) was calculated for the tapered slit case as shown in Figure 108. The projected width is the distance from the centerline of the slit when a line is drawn from the far-side of the detector in the outer slit width and the opposite side of the inner slit width. A scaled intensity of counts seen at Detector 49 was calculated for each source position for each of the three chord distances by subtracting a calculated collimator penetration value at each source position. This was done by subtracting counts calculated using respective polynomial fit constants corresponding to the respective quadratic fits of the collimator penetration for each of the three distances. The normalized data from all the distances is shown in Figure 109. The scaled intensity response is similar to that seen in Figure 81 for the 100-detector parallel slit geometry. There is a linear drop between $0 < W_P < 1.8$, and for the 5.04 cm case the drop off there is more leakage than for the other 2 cases at each projected width, and the leakage for 10.08 cm is slightly but insignificantly more than that for 20.16 cm. The reason for this is because at closer distances like 5.04 cm the amount of collimator that the neutrons have to traverse isn't significant enough to shield them, so the counts are higher than they are for the two other distances.

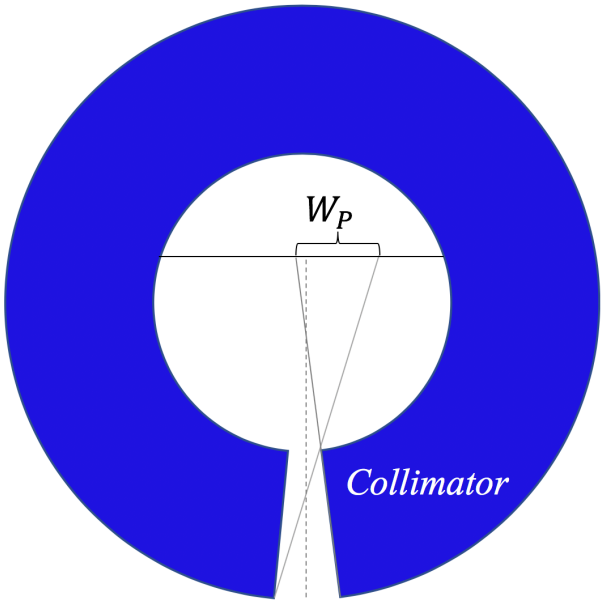


Figure 108. Diagram showing how the projected width for a tapered slit is calculated for a source at a specific perpendicular distance from the slit.

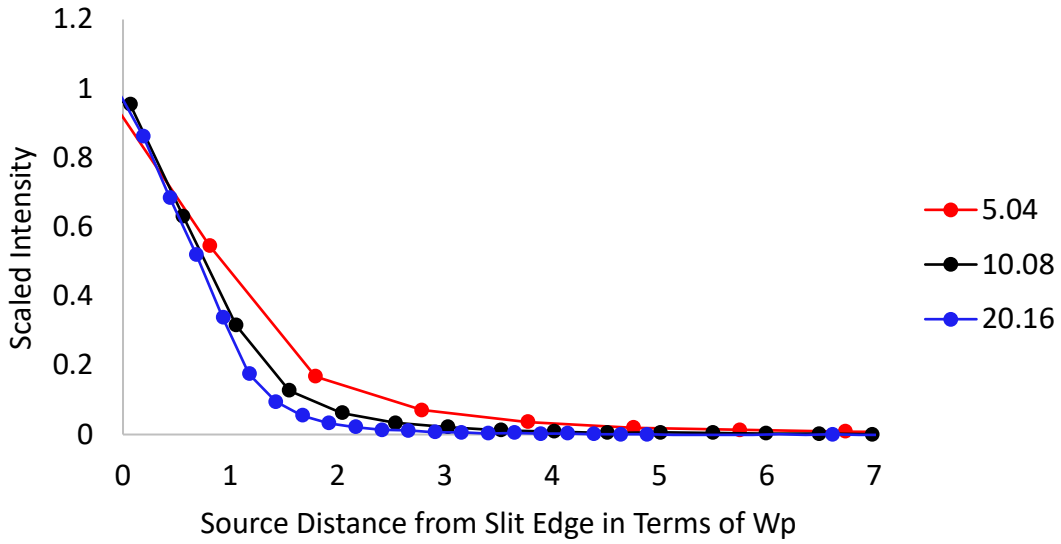


Figure 109. Scaled intensity at Detector 49 for a source moved perpendicular to a single slit at three different distances (5.08, 10.08, and 20.16 cm).

To develop an estimate of how to predict the scaled intensity as a function of the collimator thickness, an average pathlength through the collimator was calculated for each of the 45 source positions along each of the three chords. The average pathlength for a given position was found by calculating the amount of collimator the neutrons would traverse to get to 9 equidistant points along the outer slit width. To calculate the average pathlength for each of the 45 source positions, the following formula was used:

$$\frac{1}{9}\sum_{i=1}^{9} e^{-\frac{Pathlength_i}{mean\ free\ path}}$$

(27)

The mean free path was estimated to be 7 cm. The average pathlength plotted alongside the scaled intensity values are shown in Figure 110 to Figure 112 for each of the three distances. The results from these simulations show that the average pathlength calculated using Equation (27) is a close enough approximation to the scaled intensity at a detector for a single slit when looking at the edge effects. The path length estimate can therefore be used in the reconstruction code for a given source position to estimate the leakage.

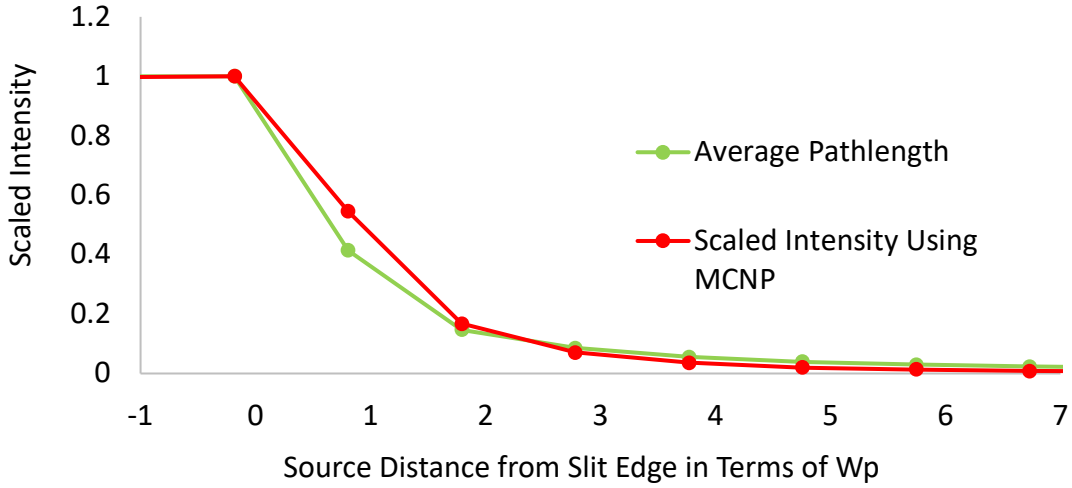


Figure 110. Scaled intensity calculated using the MCNP results plotted against the calculated average path length for a ^{244}Cm line source moved perpendicular to a single slit 5.04 cm away from the slit opening.

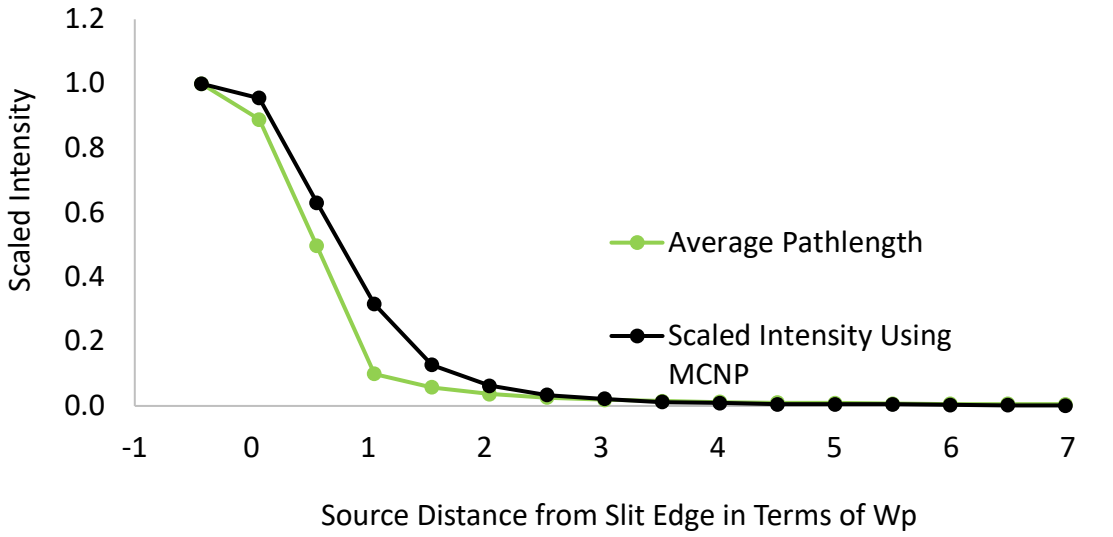


Figure 111. Scaled intensity calculated using the MCNP results plotted against the calculated average path length for a ^{244}Cm line source moved perpendicular to a single slit 10.08 cm away from the slit opening.

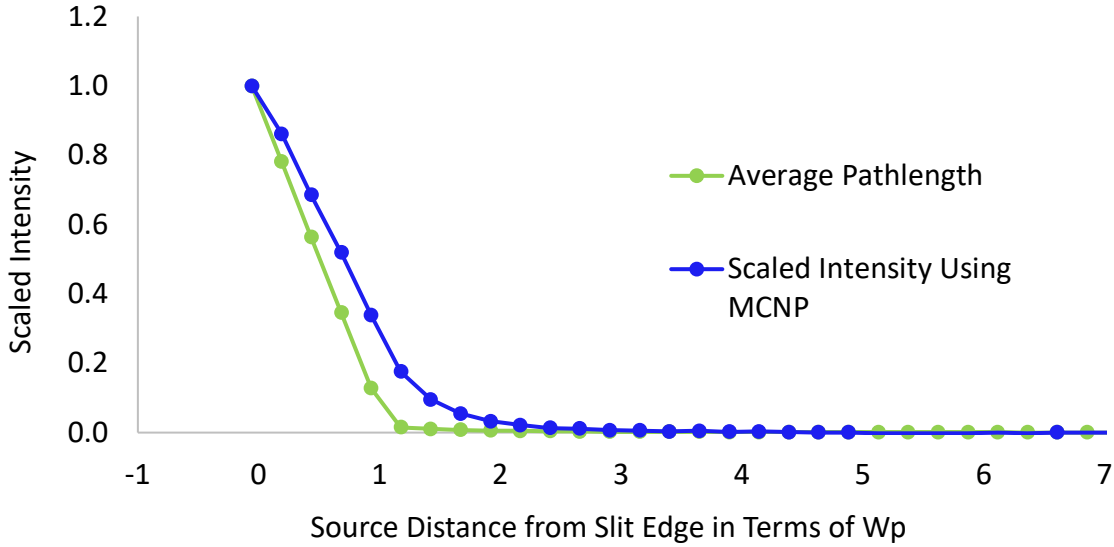


Figure 112. Scaled intensity calculated using the MCNP results plotted against the calculated average path length for a ^{244}Cm line source moved perpendicular to a single slit 20.16 cm away from the slit opening.

7.3. Correction Factor for Direction of Slit

The imager's collimator geometry is complicated in that although it acts as a functional equivalent to a parallel slit collimator, the slits are not parallel to one another. Additionally, the slits do not open up perpendicularly to the corresponding detector, thus the signal in some cases will peak at the neighboring detector or detector row. To be able to correct for the different rows the signal peaks at for a given slit, a series of 96 simulations were conducted where a beam of ^{244}Cm neutrons were shot down each slit. The detector response at all 288 rows was tallied, and the 96 curves were fit individually to find the centroid and peak widths. The response from the detector rows next to the Al walls of the module (rows 1 and 24) were found to have lower efficiencies, so for each of the 12 modules, the response in the respective 1st and 24th rows was multiplied by 1.0688 to get rid of the reduced efficiency on either side of the Al.

The results of the 96 simulations showing the detector response of neutrons being shot down each of the 96 slits is shown below in Figure 113. The detector row numbers were adjusted so that the row the respective slit the source was shot down was row 0, and this way all the detector row responses could be plotted together to see the deviation in centroid and full-width half max (FWHM). The figure also shows that the signal for some of the cases as predicted does not peak at the row of interest (row 0), instead peaks at the row next to the row at which the slit points directly at (row -1 or +1). This can create some level of uncertainty in the reconstruction, as a result the centroid correction and FWHM need to be well understood for this imager geometry.

A double Gaussian fit was found to be a closer approximation to fit each of the peaks. The basic equation for a double Gaussian is shown below:

$$A_1 e^{\frac{-(x-b_1)^2}{2\sigma_1^2}} + A_2 e^{\frac{-(x-b_2)^2}{2\sigma_2^2}}$$

(28)

Here, A_1 and A_2 are the respective amplitudes of the two Gaussian curves, $b_1$and b_2 are the centroids of the two curves, and σ_1 and σ_2 are the standard deviations of the two curves. To simplify the equation, the second term was written in terms of the first Gaussian. The two centroids are assumed to be the same, so $b_1 = b_2$. To get σ_2 in terms of σ_1, the ratio between

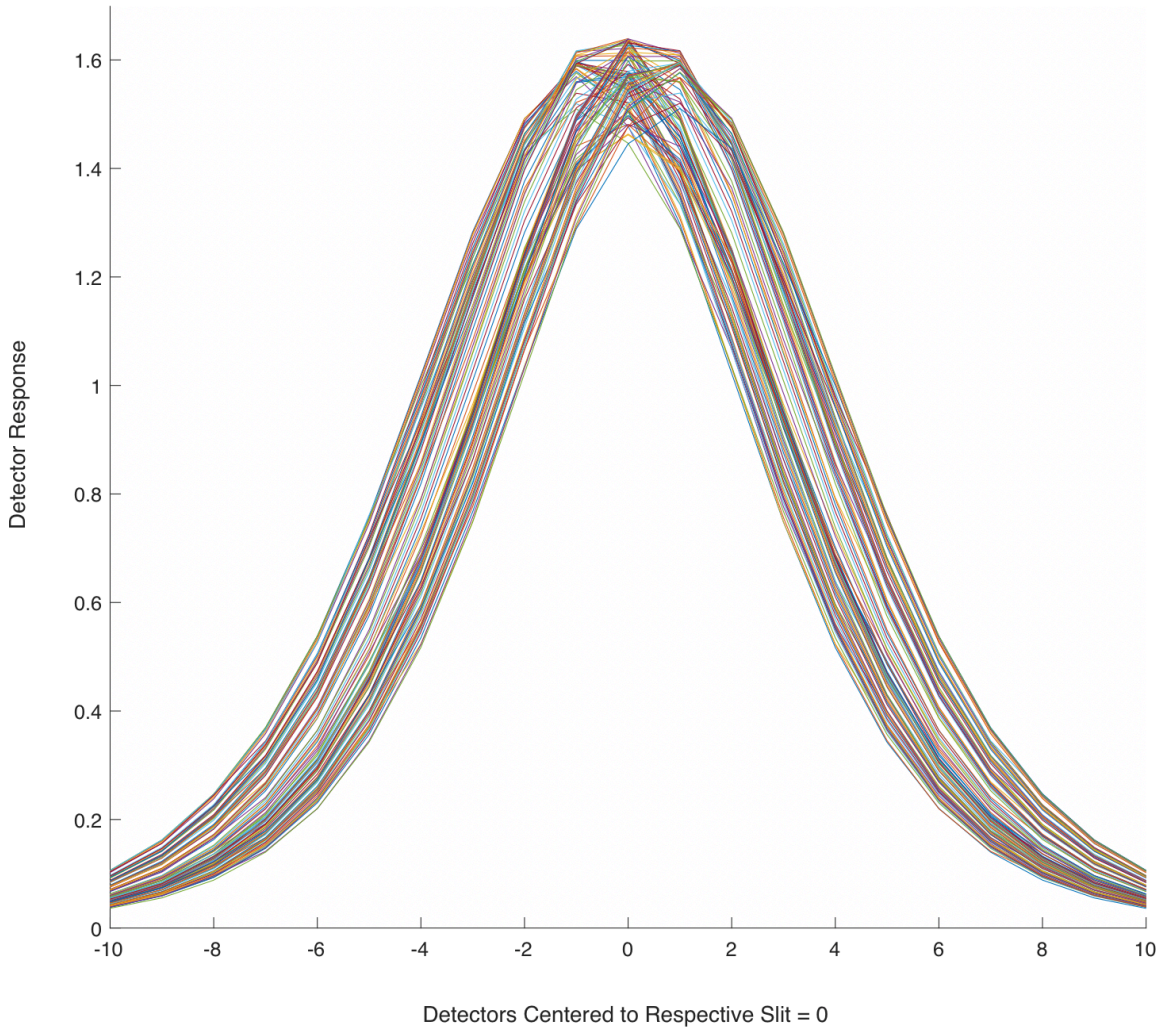


Figure 113. Response of all detector rows for 96 simulations where a ^{244}Cm source was shot down each of the 96 slits in turn. The row numbers were adjusted so that for a given slit the source was being shot down, the row was renumbered as 0 to make it easier to visualize the detectors at which the signals peak and show that not all slits point directly perpendicular into the row of interest so the signal peaks at the neighboring row.

the mean FWHM of the second curve and the first curve was taken to be the scaling term since the FWHM is given by

$$FWHM = 2.35482\sigma$$

(29)

A standard double Gaussian fit was used to solve for FWHM and centroid of all the 96 curves. To find the scaling factor by which to scale σ_2 in terms of σ_1, all of the FWHM values for the two curves were plotted against one another to see how they scaled. Figure 114 shows the two FWHM terms plotted against one another for all 96 cases. There are two regions where the FWHM of the curves cluster – one on the top left part of the plot, and one on the bottom right part. To further investigate which of the two clusters of points can be used to scale the second FWHM in terms of the first, the centroid values $b_1$and b_2 for all 96 curves calculated from the fit were plotted as a function of the slit number to see how they aligned. Figure 115 shows the calculated centroid values for the first and second Gaussian term. Centroid values between +1 and -1 for the two Gaussians overlap the closest.

To accurately find the term by which to scale one of the FWHM terms, the curves that had similar centroid values between +1 and -1 were selected, and the corresponding FWHM values for the double gaussian term when plotted similarly to Figure 114. The FWHM terms of the first and second Gaussian curves which have similar centroid values between the two curves are shown in Figure 116. The data in Figure 116 shows that the FWHM values of interest are the FWHM values that lie in a line in the top left part of Figure 114. The scaling factor by which to scale the second FWHM term by to be in terms of the first gaussian was found by taking the ratio of the mean FWHM values. The ratio of the average FWHM values of the second Gaussian to the average FWHM values of the first gaussian using the select points in Figure 116 is 1.745. Thus, assuming and forcing $b_2 = b_1$, the standard deviation values of the two curves can be related by

$$\sigma_2 = 1.745\,\sigma_1$$

(30)

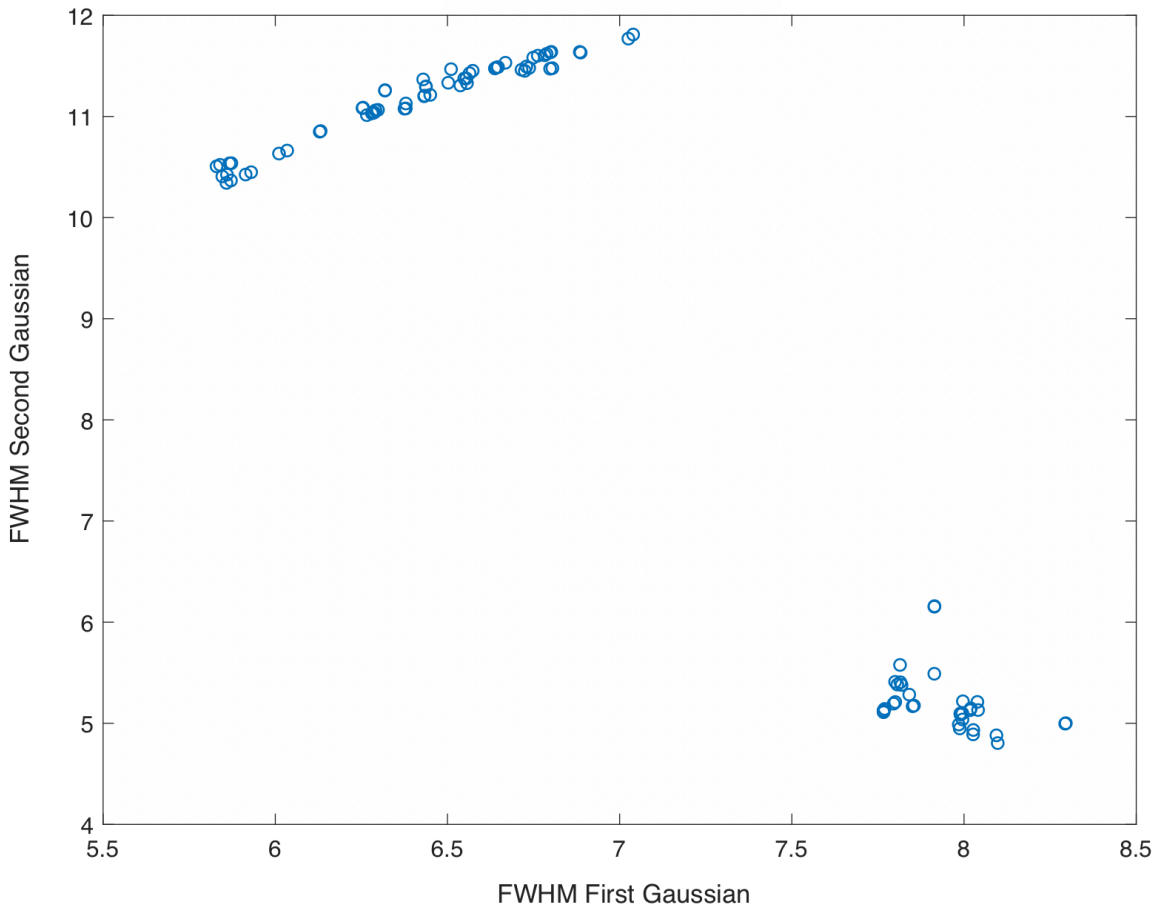


Figure 114. Plot of the FWHM (in unites of detector rows) of the two Gaussian curves against one another for each of the 96 curves.

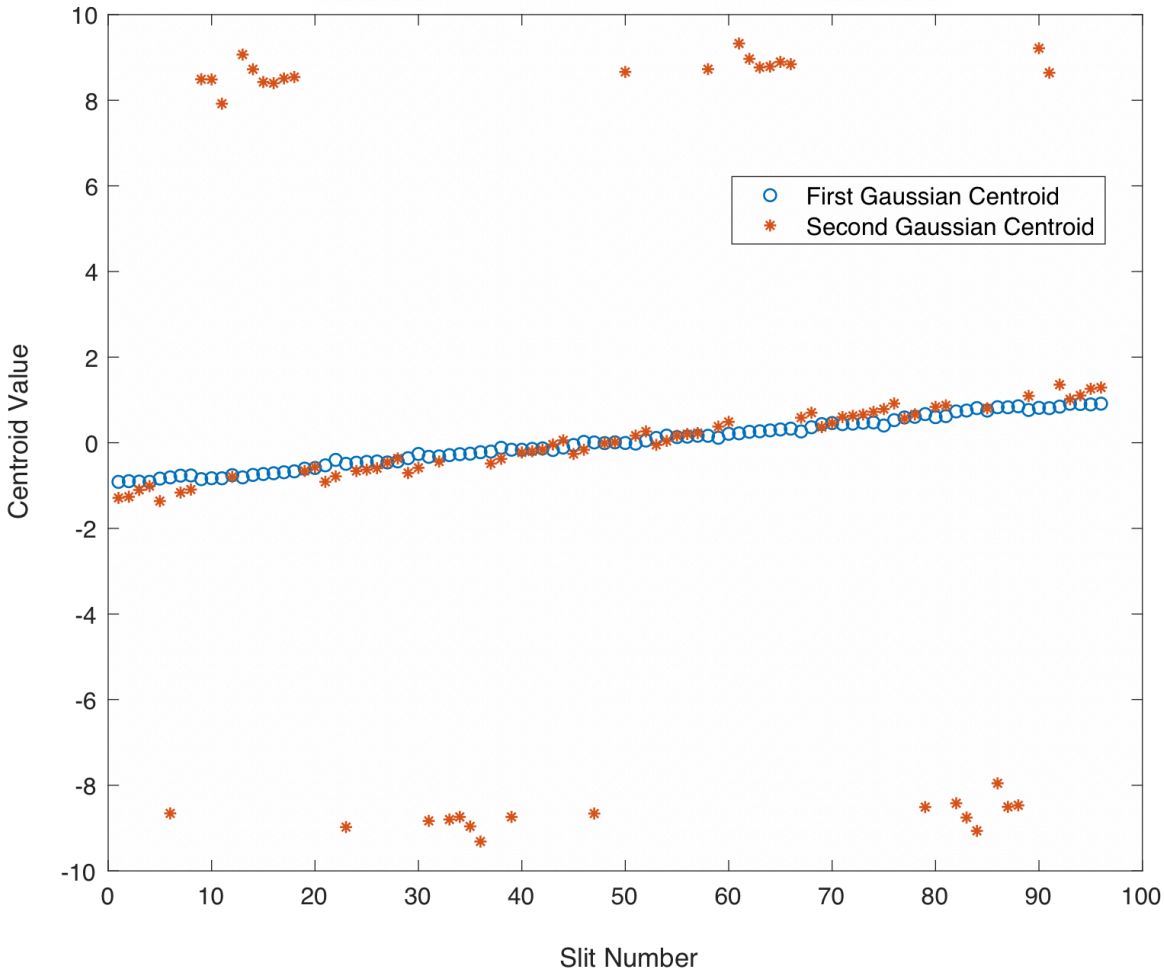


Figure 115. Centroid values for the first and second Gaussian terms calculated for all 96 slits.

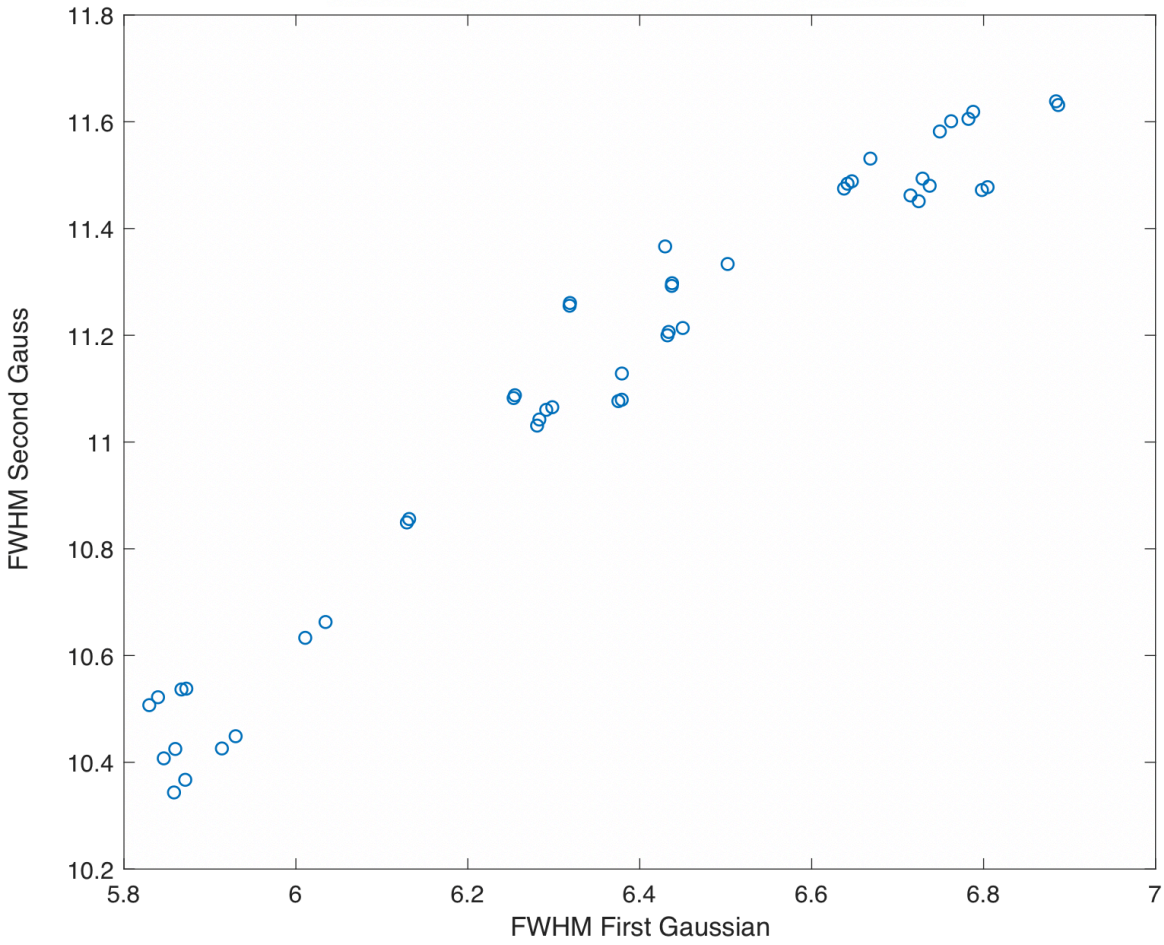


Figure 116. FWHM values of the first and second Gaussian curves making up the data that has centroid values b_1 and b_2 between +1 and -1.

Employing the relationship above, a revised equation for the double Gaussian fit was used where the standard deviation of the second gaussian term was written in terms of the first, and the two centroids were assumed to be equal. The final equation used to generate fit coefficients for all 96 curves is

$$A_1 e^{\frac{-(x-b_1)^2}{2\sigma_1^2}} + A_2 e^{\frac{-(x-b_1)^2}{2(1.745\sigma_1)^2}}$$

(31)

A MATLAB function was used to generate and solve for the best coefficients to fit each of the 96 curves. A [96 ×4] matrix of coefficients was generated by the code, and all the coefficients are listed in the Appendix. The four constants solved for were: A_1, A_2, b_1, and σ_1. The FWHM as a function of the simulation or slit down which the source was pointed is shown below in Figure 117. The FWHM outliers that go up and down the most correspond to the rows that are closer to the Al walls in the detector. There seems to be an outlier for slit number 5, where the FWHM is the lowest. A closer look at the slit 5 data with the custom fit superimposed in Figure 118 shows that visually the fit is actually pretty consistent with the data, so the fact that the FWHM is lower than the others should not be an issue when it comes to fitting the data and incorporating it into the reconstruction algorithm.

The centroid values b_1 for all 96 curves that was output from the custom fit plotted as a function of the slit number is shown in Figure 119. The centroid shifts from peaking to the left side of the intended row, to 0, and eventually to the right side of the intended row as the slit number being considered goes from 1 to 96. This is expected based on the geometry of the slits and the relative direction in which they open up to the detector rows on the outer radius.

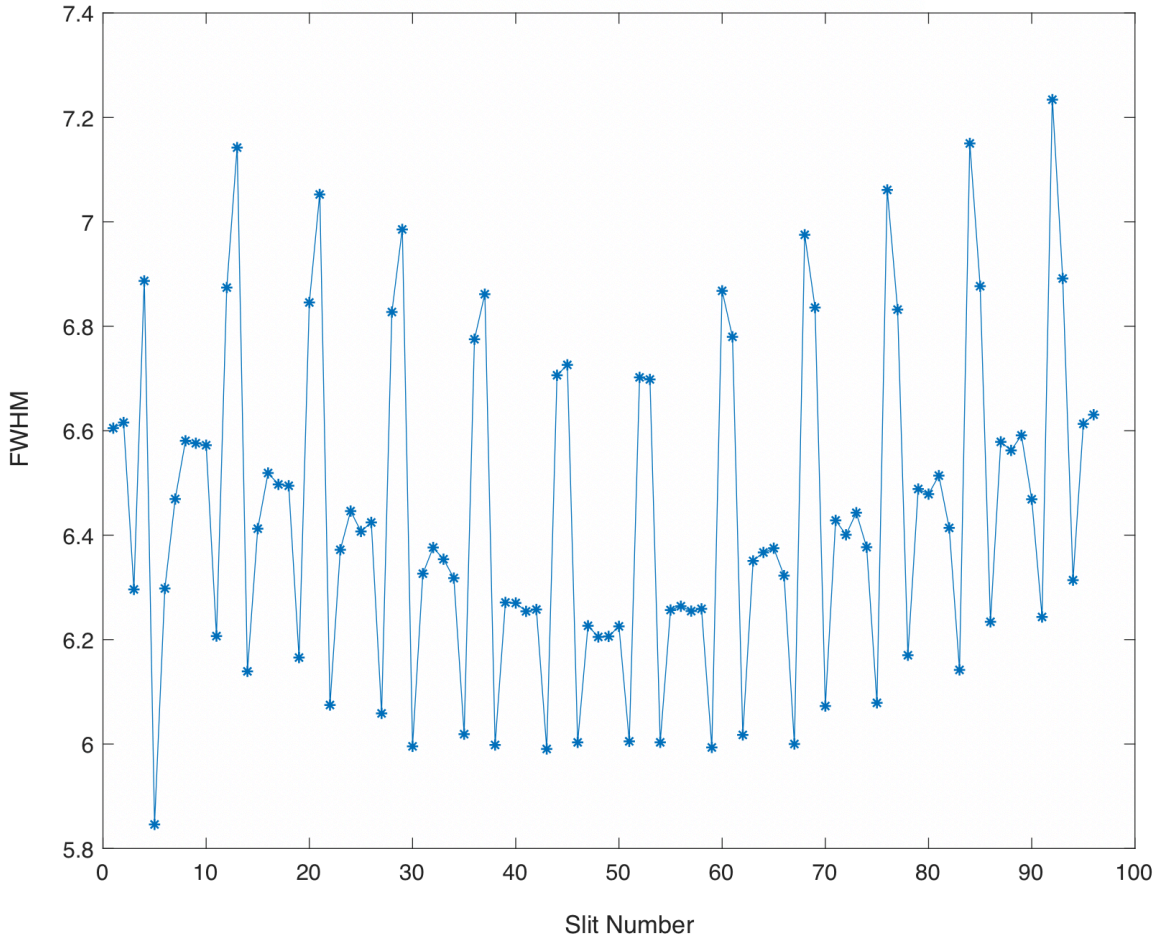


Figure 117. Calculated FWHM using the custom double Gaussian equation for all 96 simulations.

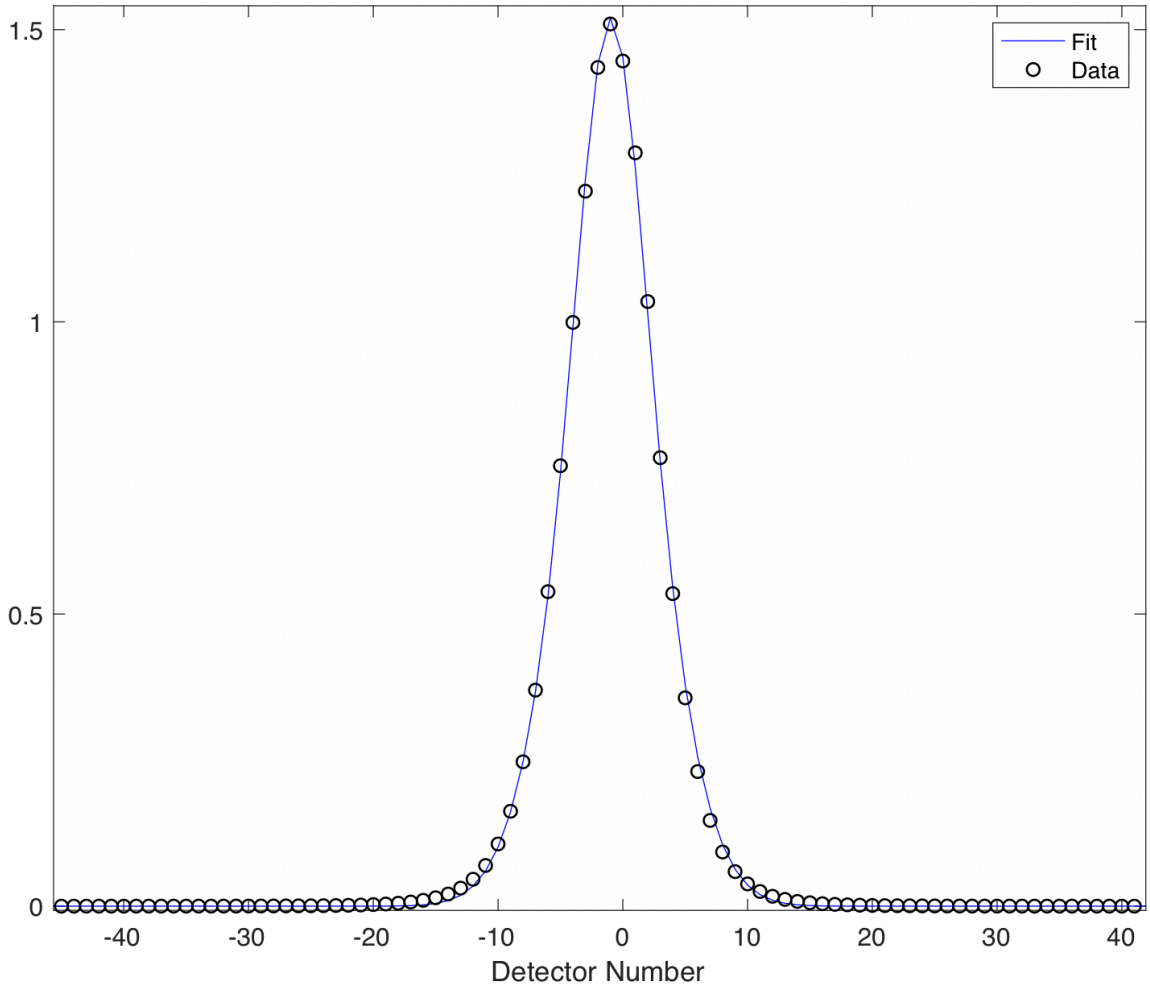


Figure 118. Data for source pointing down slit 5 (black points) along with the custom double Gaussian fit (blue).

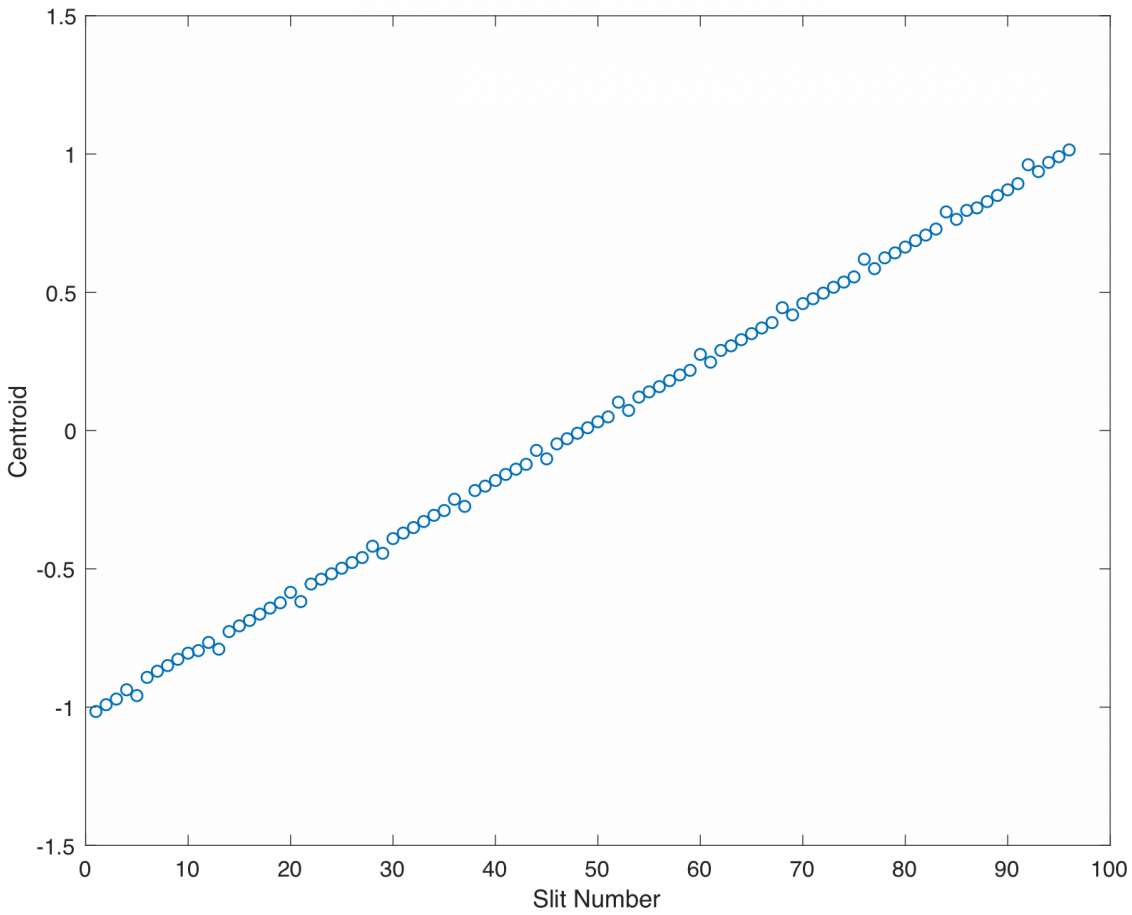


Figure 119. Centroid values for curves generated for source pointing down each of the 96 slits. The centroid values increase from -1 to +1 as the slit numbers increase.

7.4. Predicting Collimator Penetration

For a given point spread function, the areas on either side of the peak are due to the collimator penetration of neutrons being transmitted through the collimator. The distribution is not flat on either side of the peak and varies based on the amount of open fraction of collimator each detector sees. To get a more accurate estimate of the collimator penetration and the offset from 0 of the peak to feed into the reconstruction, this distribution needs to be able to be predicted. As covered in the previous chapter, the collimator penetration depends on two factors – the change in effective thickness for different collimator dimensions, and the other is the change in effective thickness due to different collimator slit widths. The effect of the change in effective thickness due to different collimator dimensions is beam hardening, the effect of the effective thickness changing due to the different slit widths is the change in streaming paths. A more simplified equation that calculates an initial guess of the effective thickness ($T_{eff,calc}$) for a completely solid collimator assuming the primary component acting in changing the collimator penetration is the borated polyethylene is given by the product of the thickness of borated polyethylene (T_{BP}), and the attenuation coefficient (μ). For a collimator with slits cut into it, the thickness needs to be scaled using the closed fraction of borated polyethylene ($F_{C\ BP}$), so the calculated thickness can be written as $\mu T_{BP} F_{C\ BP}$. The beam hardening effect of the neutron energy spectrum shifting as they pass through the collimator needs to be accounted for since this means that the attenuation coefficient changes as a function of the polyethylene thickness. The attenuation coefficient accounting for the beam hardening effect can be expressed as a quadratic: $\mu \approx \mu_0(1 - \Delta\mu T_{BP})$ [63]. Incorporating this into the calculated thickness equation gives

$$T_{eff,calc} = \mu_0 T_{BP} F_{C\ BP}(1 - \Delta\mu T_{BP} F_{C\ BP}).$$

(32)

The effect of the streaming paths needs to be accounted for in the collimator geometry and is represented as a linear function of the open fraction of the borated polyethylene [63]. The calculated thickness assuming only the borated polyethylene component affects the collimator penetration becomes

$$T_{eff,calc} = \mu_0 T_{BP} F_{C\,BP}(1 - \Delta\mu T_{BP} F_{C\,BP}) - C_{sli} T_{BP}(1 - F_{C\,BP}).$$

(33)

This estimate of the calculated thickness works well for the 5 cm steel thickness collimator cases, but not well for the 10cm steel thicknesses. The estimate of the calculated thickness presented in Chapter 6 is more accurate since it accounts for the steel components as much as possible. However, the estimate in Equation (33) is good enough to accurately calculate the close fraction seen by each detector along the point spread function. The reason for trying to better estimate the close fraction for each of the detector rows is that the collimator penetration in a given point spread function is not constant on either side of the peak and dips low towards the ends (close to the large borated polyethylene wedge). This changing collimator penetration as a function is evident in the point spread function on either side of the peak shown in Figure 120.

To more accurately reconstruct an image, a better estimate of the close fraction that each of the detector rows sees would be useful. The approach to be able to predict the collimator penetration as a function of detector number chosen was to use the existing suite of simulations from the 10 cm steel and 30 cm borated polyethylene case to find the values of μ_0, $\Delta\mu$, and C_{slit} that make the close fractions as estimated in Equation (33) equal to the MCNP calculated closed fractions. To start with, Equation (33) was programmed and initial guesses for the three constants were iterated upon to find the calculated thicknesses for the corresponding 32 simulations conducted for the 10 cm steel and 30 cm borated polyethylene case with 32 different slit widths. The closed fractions used in Equation (33) to obtain the calculated thicknesses were the values calculated previously for the 32 different geometries using MCNP. The results were then plotted against the actual thickness in mean free paths for each of the 32 geometries, which was calculated using the logarithm of the ratio of the mean counts without a collimator present and with the collimator present. The constants were manipulated by looking at a visual output of how close the MCNP vs. calculated thickness in mean free paths data for the 32 points were to a 1-to-1 line. The best fit is shown below in Figure 121 where the blue data points are the thicknesses in mean free paths and the red line is a reference 1-to-1 line. The goal was to find the set of 3 constants that would result in the blue dots lying along the red line. Even the best combination of 3 numbers did not result in

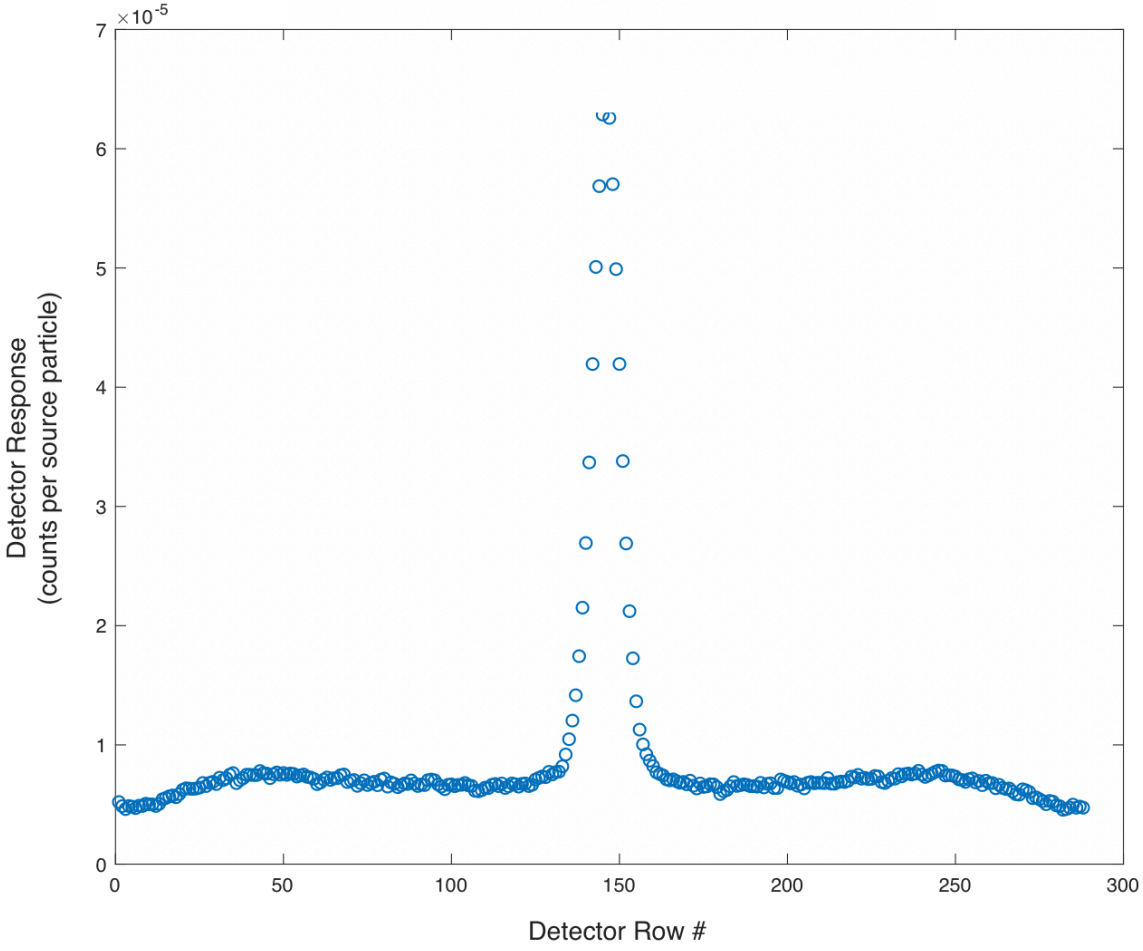


Figure 120. Point spread function for a ^{244}Cm line source placed close to the origin (17.5cm from the slit 49 opening).

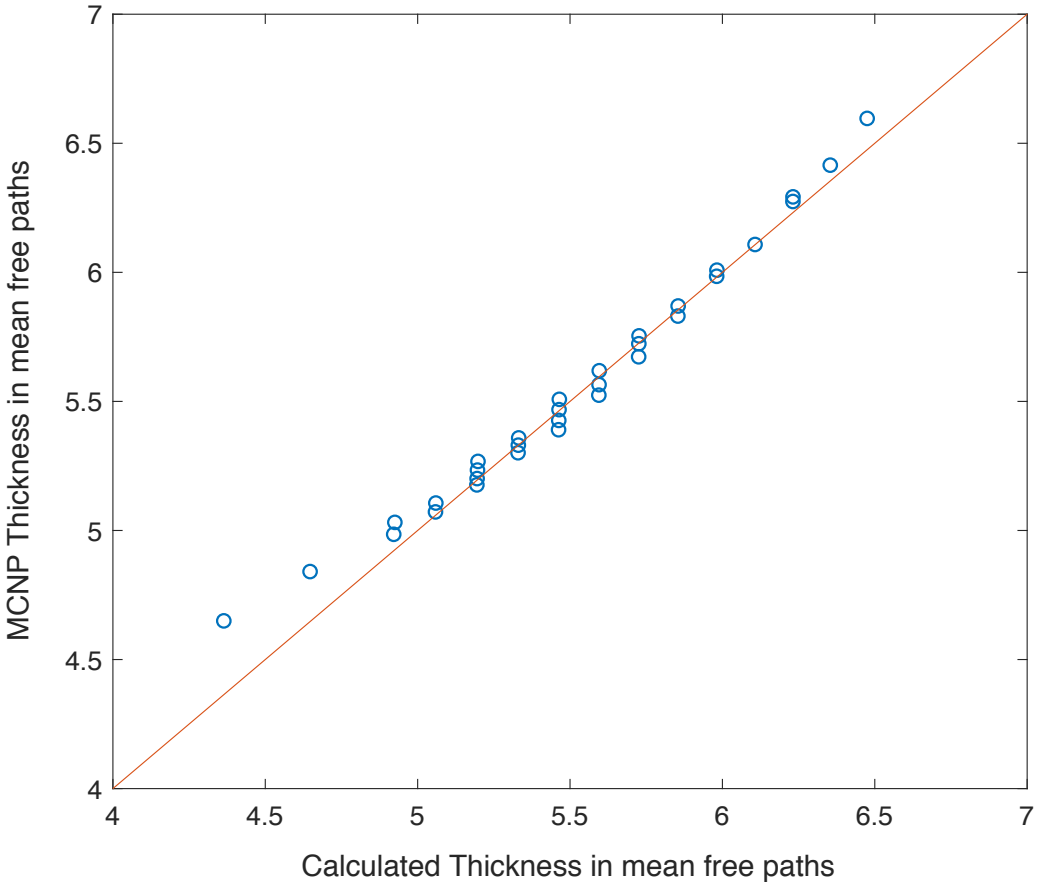


Figure 121. The MCNP effective thickness in mean free paths plotted against the calculated effective thickness using Equation (33) for 10 cm steel and 30 cm borated polyethylene. Each of the 32 points corresponds to a different slit width case simulated.

all the 32 data points falling along the red line. This is probably due to the fact that Equation (33) was formulated using only the data from 5 cm steel cases, and at 10 cm steel, the relationship is too simple and doesn't account for the effect the steel may have on altering the collimator penetration. The final set of constants that best aligned the 32 points along the slope of 1 line are shown in Table 15.

The next step was to fix the values for μ_0, $\Delta\mu$, and C_{slit} in Equation (33), and to infer a closed fraction value for each of the 288 detector rows for the final geometry, which will then be used to calculate the effective thickness seen by each of the 288 rows, and the collimator penetration (CP) seen at each of the 288 rows. To use this equation to calculate the closed fractions seen by each of the detector rows and compare it to an MCNP calculation, two sets of MCNP simulations were used with the final geometry. Two simulations of the final geometry with and without the collimator with a ^{244}Cm source placed close to the origin (17.5 cm from the slit 49 opening) were conducted. The effective thickness of the collimator in terms of mean free paths is equivalent to the logarithm of the ratio of mean counts from either side of the peak between a case with no collimator present and a case with the collimator present. For a given detector row *i*, the effective thickness (T_{eff}) is given by

$$T_{eff,\ i} = \log \frac{Counts_{No\ Coll}}{Counts_{Coll}} \quad (34)$$

Table 15. Values for the three constants (μ_0, $\Delta\mu$, and C_{slit}) in Equation (33) that result in the calculated effective thickness in mfp plotted against the MCNP calculated effective thickness in mfp lying along a slope of approximately 1.

Constant	***Value***
μ_0	0.44
$\Delta\mu$	0.0158
C_{slit}	0.3148

Looking at the simulation data for the final geometry with the collimator present in Figure 120, the detector response for the rows corresponding to the peak, which are rows 122 to 170, were set to 0 in order to ignore the points during the fit of the CP. To get the effective thickness in terms of mean free paths for each of the 288 rows, the MCNP data from the two simulations was substituted into Equation (34) to get the effective thicknesses for each detector row. The resulting matrix of 288 T_{eff} values were then set equal to Equation (33) along with the constants from Table 15, and with T_{BP}=29.523 cm. The equation was then solved symbolically and evaluated for all 288 detectors for $F_{C\,BP}$. The closed fractions from solving this reflect the closed fractions each of the detector rows sees and were saved in a matrix. These closed fractions were then plotted against the detector number and a 6th degree polynomial was fit to the data. The data along with the line of fit and corresponding equation are shown in Figure 122. The equation coefficients from the line of fit in in Figure 122 were extracted to form the basis for a 'predicted closed fraction'.

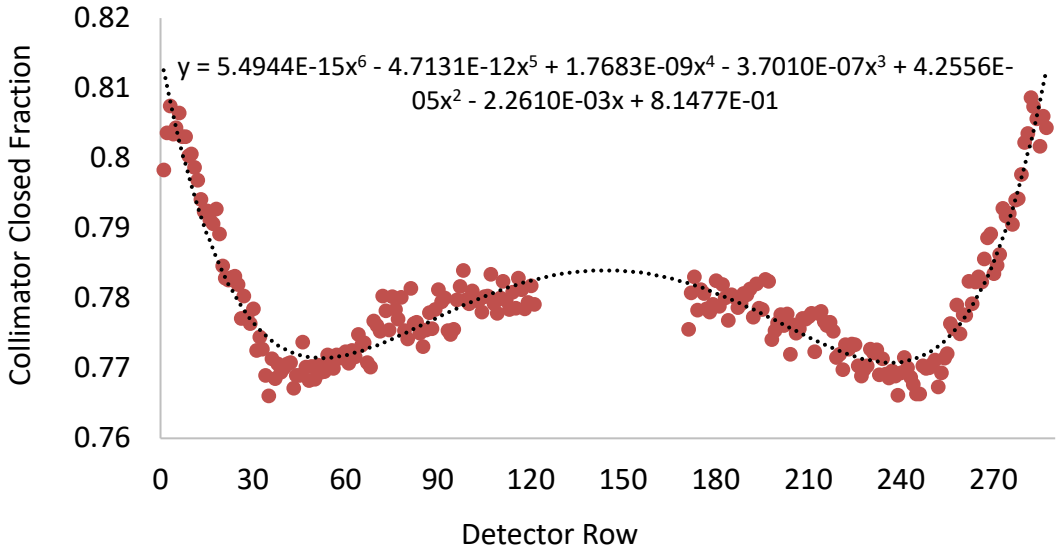


Figure 122. Closed fraction of the collimator seen by each of the 288 detector rows as calculated using Equation (33), the constants from Table 15, and the borated polyethylene thickness of 29.523 cm.

The line of fit was used to calculate the collimator closed fractions for each of the 288 detector rows. To show that using these closed fractions provide a decent estimate of the CP on either side of the peak, the values were used in Equation (33) to find the calculated effective thickness in mean free paths ($T_{eff,calc}$). The effective thickness in terms of mean free paths is shown below in Figure 123 using both the MCNP model (blue points) and the calculated data (red points). Using the effective thickness values, a calculated collimator penetration ($CP_{calculated}$) for each detector i was solved for using Equation (35). The calculated collimator penetration was overlaid on top of the MCNP point spread function in Figure 124. This shows that the calculation provides a very good estimate of the detector response at each of the rows by accounting for the closed fraction each of the detector rows sees.

$$CP_{calculated,\ i} = \frac{\frac{1}{288}\sum_{i=1}^{288} Counts_{No\ Coll}}{e^{T_{eff,calc,\ i}}}$$

(35)

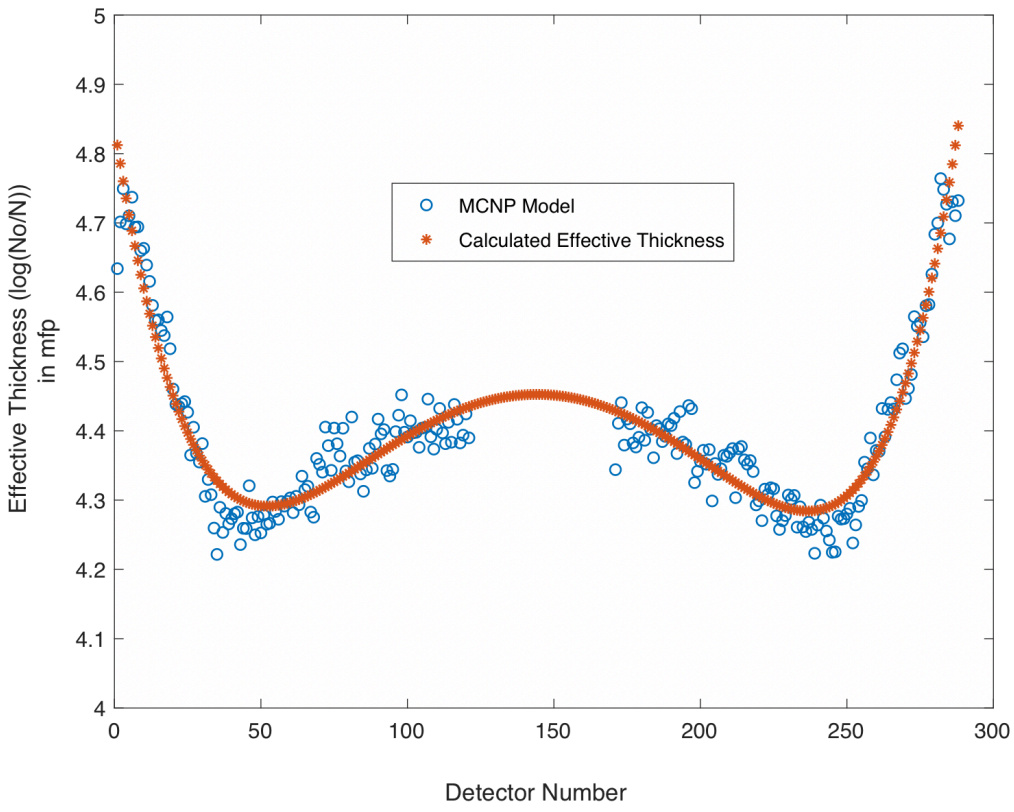


Figure 123. Calculated effective thickness and the MCNP effective thickness in mean free paths seen for each of the detector rows.

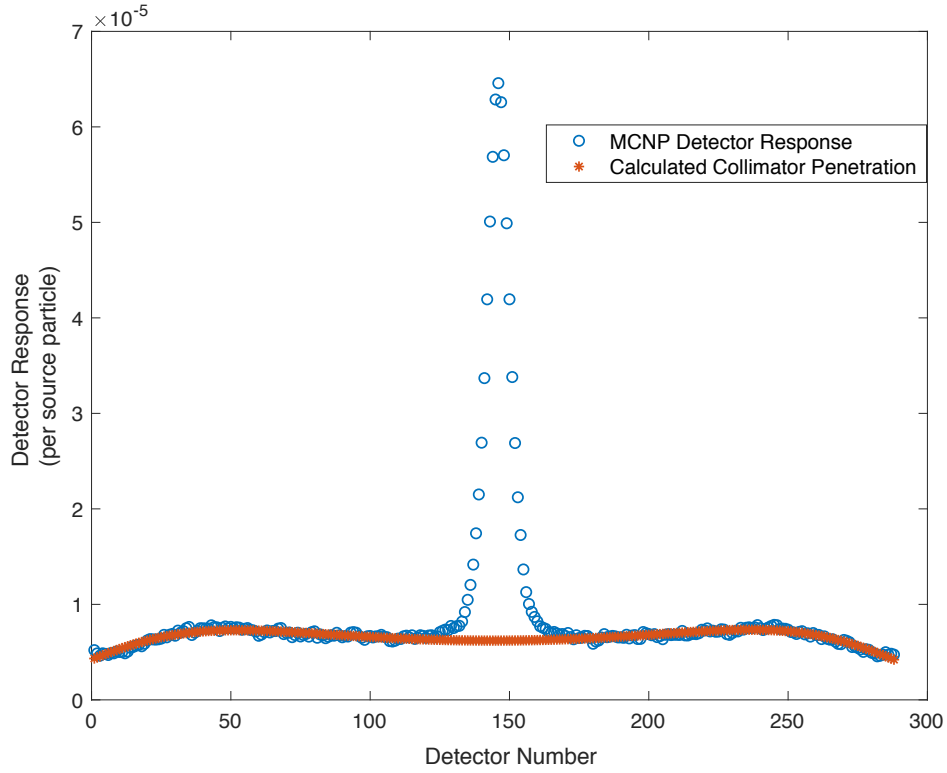


Figure 124. Detector response per source particle from the MCNP simulation (blue), and the calculated collimator penetration (red).

The detector response predicted by the collimator penetration provides a good estimate to be incorporated into the reconstruction code. The varied closed fractions seen by each of the detector rows will be used to scale the response in each detector in combination with adjusting the $1/r$ scaling of the response for each of the detectors according to a given source position within the fuel assay area with respect to the data generated in this study at a source position close to the origin.

7.5. Expected Signal-to-Noise of Final System

In order to understand how the SNR of the final geometry scales for various slit widths, a series of simulations with parallel slits and a ^{244}Cm line source placed at two different positions – one placed 5 cm from the slit opening, and one 17.5 cm from the slit opening –

were conducted. The position close to the slit opening was selected to be 5 cm from the slit 49 opening along the centerline since this would keep the source 3 W_P away from the edge of the neighboring slits for the largest parallel slit width configuration simulated (1.1 cm) using the definition of projected width shown in Figure 80, thus minimizing leakage down the neighboring slits. Although this source position was geometrically 3.11 W_P away from the neighboring slit, the slits for this collimator at the larger slit widths cut into each other, causing more collimator material to be removed to accommodate the slit size. Figure 125 shows a comparison of how going to larger slit widths like 1.1 cm (left) in this modified radial collimator geometry would result in more collimator material being removed compared to narrower slit widths (Right). The image on the right is a collimator with 3mm inner slit width and 8mm outer slit width.

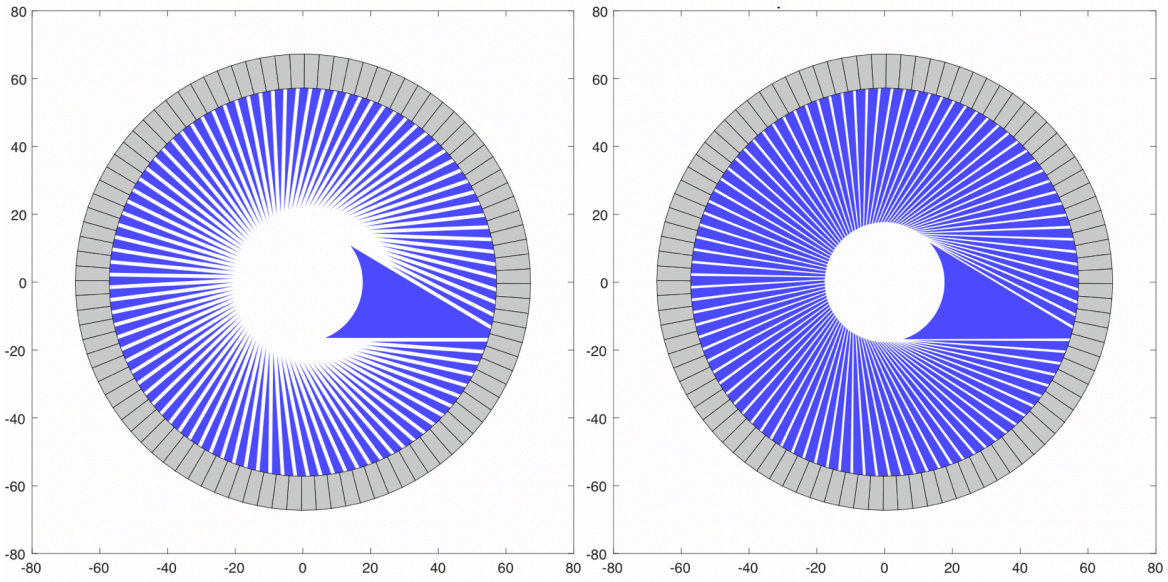


Figure 125. (Left) diagram of the collimator with 96 slits with a slit width of 1.1 cm. This shows how extending the slit width to larger sizes requires that more of the collimator be removed. (Right) Diagram showing what the collimator with 96 tapered slits looks like with 3 mm inner slit width and 8 mm outer slit width.

Looking at the peak values as the parallel slit width increases, the detector response values of the detector row centered on slit 96 (row 158), does not increase linearly as should be expected because of the fact that more of the collimator is being cut into at larger slit widths. The detector response registered at the detector (row 158) pointing at slit 49 for a ^{244}Cm source on the centerline 5 cm away for a variety of parallel slit widths ranging from 0.1 cm to 1.1 cm is shown in Figure 126. The signal increases in a linear fashion up until 0.4 cm slit width, after which the signal increases as a third order polynomial. As a result, similar to how the SNR values for the 512 cases simulated were scaled, the SNRs for the final geometry were scaled as well by fitting the detector response data below from a slit width of 0.1 cm to 0.4 cm to a line. The values of the detector response beyond 0.4 cm were then scaled according to what the expected values would be along a trendline to find the scaling factor. A list of the scaling factors is shown in Table 16.

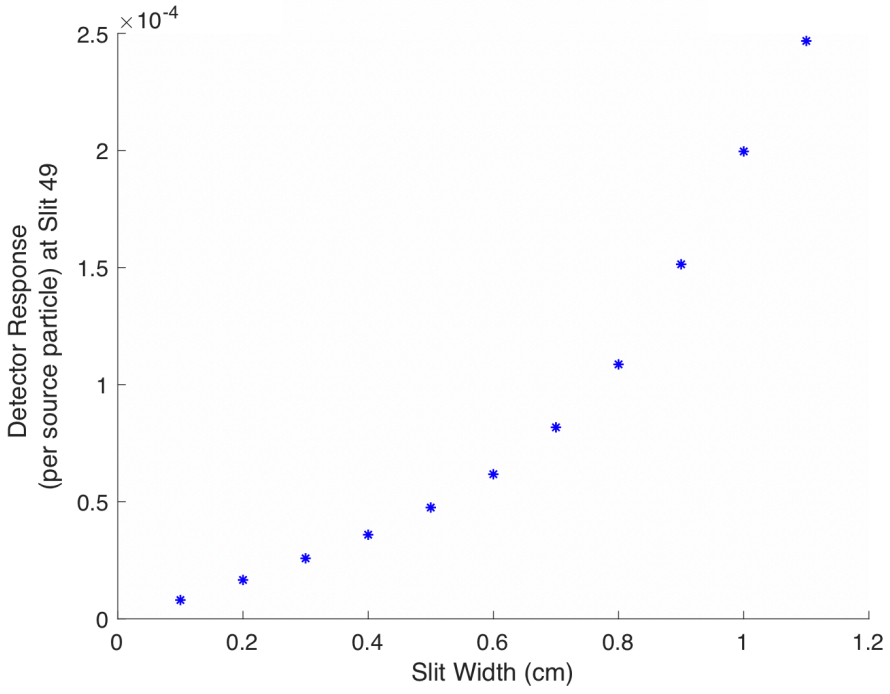


Figure 126. Detector response registered at the detector (row 158) pointing at slit 49 for a ^{244}Cm source on the centerline 5 cm away for a variety of parallel slit widths ranging from 0.1 cm to 1.1 cm.

Table 16. List of slit widths and corresponding scaling factors.

Slit Width (cm)	*Detector Response*	*Scaling Factor*
0.1	8.04E-06	9.19E-01
0.2	1.66E-05	9.49E-01
0.3	2.58E-05	9.85E-01
0.4	3.59E-05	1.03E+00
0.5	4.75E-05	1.09E+00
0.6	6.18E-05	1.18E+00
0.7	8.18E-05	1.34E+00
0.8	1.09E-04	1.55E+00
0.9	1.51E-04	1.92E+00
1	2.00E-04	2.28E+00
1.1	2.47E-04	2.56E+00

The scaling factors were used to scale the respective SNR values. In addition to the 11 slit width cases ranging from 0.1 to 1.1 cm, an SNR calculation was completed for the tapered slit case the final geometry was based on: 3mm inner slit width and 8mm outer slit width. The SNR for the tapered slit case was scaled using the 0.3 cm parallel slit scaling factor found from fitting the data points in in Figure 126. This is because for the tapered slit case, the primary shielding effects and the leakage is calculated based on the inner slit width. The scaled SNR values for all 11 tapered slit cases and the final tapered slit design are shown below as a function of the geometric mean of the slit width in Figure 127. The SNR of the tapered slit case (red point) was calculated to be 5.809, which is very close in SNR to the parallel slit case with 0.5 cm slit width. This shows the advantage of tapering the slits – the tapered slits will shield the detectors from the gamma exposures better than the 0.5 cm parallel slit case would.

From Figure 103 it can be seen that the 0.5 cm parallel slit case results in a maximum gamma exposure above 800 R/hr, which would mean the exposure would be well above the operation limit of 500 R/hr. But the 0.3 cm tapered slits keep the maximum exposure under the 500 R/hr limit while achieving an SNR similar to the 0.5 cm parallel slits. Additionally, the slit width geometric mean to achieve the highest SNR was identified. An imager geometry with a geometric mean slit width of 0.6 cm achieves the highest SNR of 6.234, beyond which the

SNR starts dipping low. This is expected since as the slit width is increased, the spatial resolution deteriorates since the imager is trying to resolve pins on the 1 cm scale, and resolve the gap between pins which is on the order of 0.378 cm. Having a 0.3 cm inner slit width and 0.8 cm outer slit width allows for the imager to resolve the gap or "halo" around each of the 1 cm diameter fuel pins with sufficient spatial resolution according to the SNR calculations.

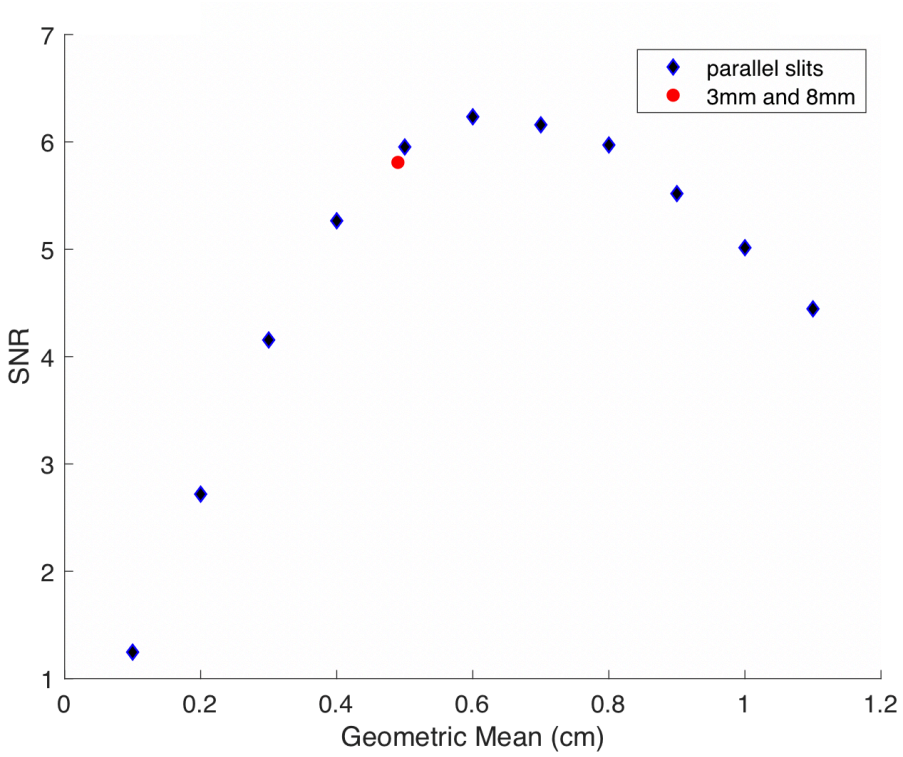


Figure 127. SNR for all 11 parallel slit cases and the final tapered slit design with 3mm inner slit width and 8mm outer slit width.

7.6. Tomography Simulations

With the selection of the final imager design completed, two sets of tomography simulations were conducted using MCNP. The tomography simulations were done by generating collimator and surface cards in 96 different positions or geometries corresponding to the 96 rotation positions the collimator would have to acquire data in to gather detector response from 360° around the sample cavity. A python script was used to combine the different collimator geometries along with the existing static detector surface and cell card definitions and the source definitions, and finally submit the files to run on the cluster. The first set of tomography simulations that were conducted were with only five ^{244}Cm line sources spaced according to the fuel pin pitch. The line sources were placed in positions that would give insight into whether or not the imager to could resolve lines next to each other, diagonal from each other, or one removed. A diagram of the source positions is shown in Figure 128 which is a sample empty fuel pin lattice, and the red points show where the line sources were placed relative to one another. The results of the tomography simulations are shown in the form of sonograms in Figure 129. The sonogram was generated by plotting an intensity map of counts seen at a particular detector per projection angle. From the picture, 5 different threads are visible, indicating that the imager works and has the ability to discern 5 sources in close proximity to one another. Figure 130 shows the reconstructed image using the MCNP data, and five source locations are clearly visible. The reconstruction accounts for the slit response, inter-detector scattering, collimator penetration, and the lowered efficiency at the detector edges. This proves that the imager design does work and can image sources placed close together.

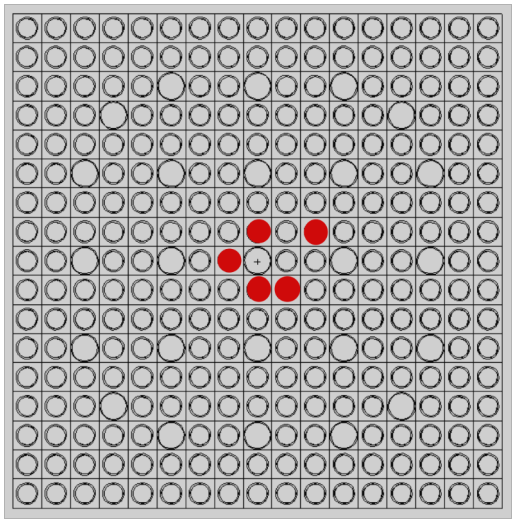


Figure 128. The red points are overlaid on a 17 ×17 fuel assembly lattice to show where the ^{244}Cm line sources were placed for the tomography simulations [57]..

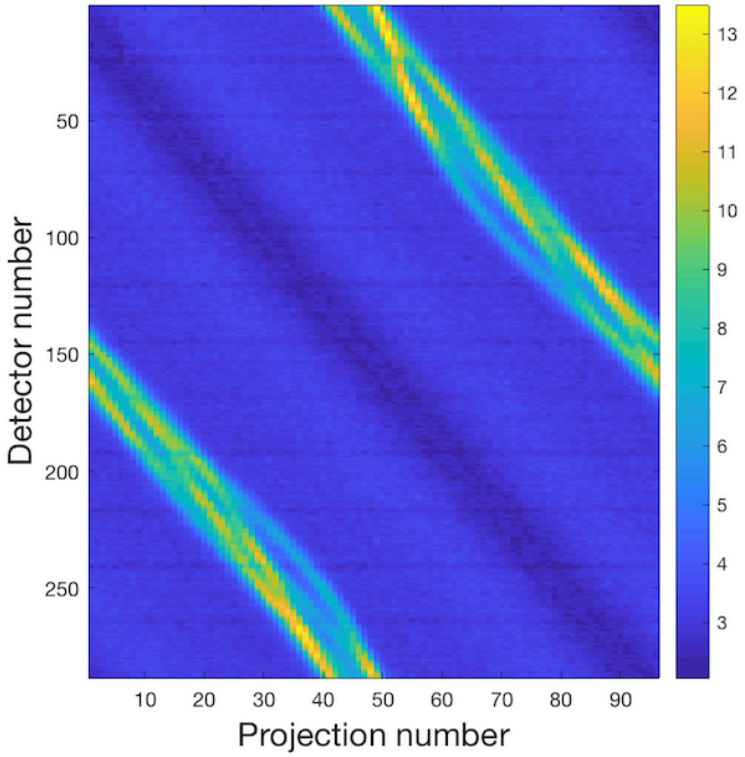


Figure 129. Sinograms from a tomography simulation of five-line sources. The fact that we are able to isolate 5 threads in the sinogram proves that imaging with this geometry could be feasible [57].

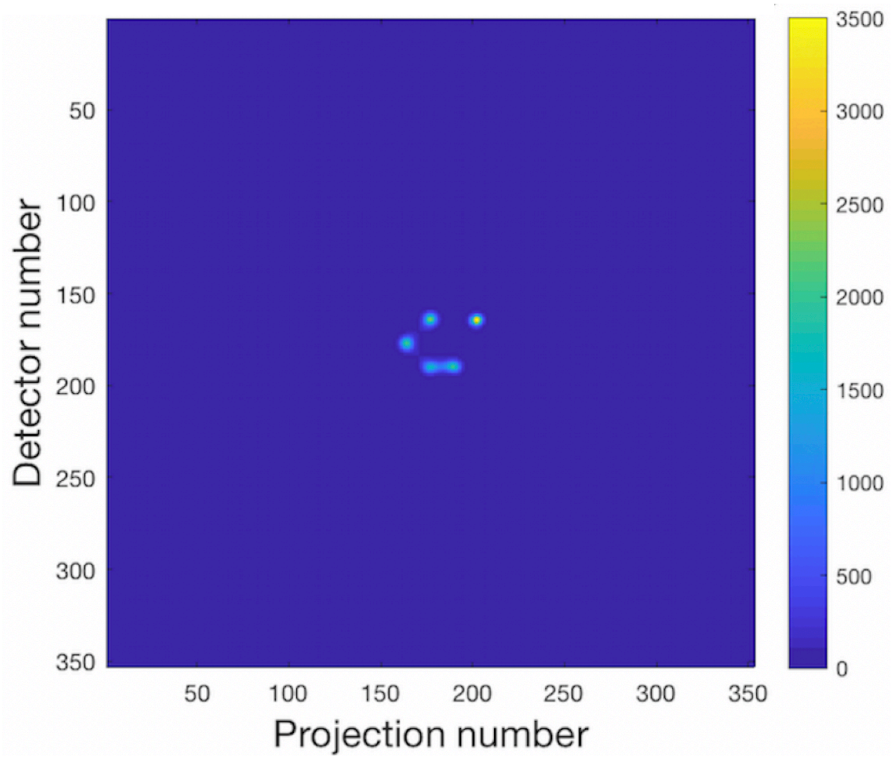


Figure 130. Reconstructed image using the sinogram data from the simulations of five line sources.

The second set of tomography simulations conducted were with a standard PWR 17 ×17 fuel assembly that had homogenous or equal burnup in each pin, but five pins were removed in the assembly. The fuel source definition for this set of 96 simulations had the same characteristics as the assembly source term used for the gamma exposure simulations, but instead of the gamma emissions, the neutron emission probability in each energy bin was provided by another group at ORNL. The source definition, surfaces and cells corresponding to the fuel assembly geometry were deconflicted and integrated into the imager input deck using a python script and were submitted to run on the cluster. Figure 131 shows a diagram of the fuel assembly. The fuel pins are shown in grey, the guide tubes in pink, and the five missing or removed pins are shown in yellow. These five positions were selected to remove fuel pins from because they reflected different scenarios of interest to test the imager's expected capability to detect a pin missing where the:

- Missing pin spot sees highest fuel interference
- Missing pin is surrounded mostly by air
- Missing pin is surrounded by both air and fuel
- Missing pin is hidden between two air cells
- Missing pin is exposed

The sinograms from the tomography simulation are shown in Figure 132. Both in Figure 129 and Figure 132, the sinograms are diagonal along the detector and projection number because of the unique collimator geometry. For a standard design, the sinograms would be upright, but regardless, the data contained in these figures are equivalent to what would be collected using a standard parallel slit collimator. Although visually it is impossible to discern individual fuel pins in the picture below, there are a couple of features worth noting. The horizontal lines seen running across the image are most likely due to the Al walls placed every 24 rows, which lower the efficiency slightly of the corresponding detector rows. As a result, in the reconstruction the response of those rows will have to be scaled accordingly. Additionally, there are patches running across the yellow portions, which most likely correspond to the inter-pin spacing. Although the reconstruction code is currently under development and will eventually be needed to show that the 5 missing pins can be identified, the sinograms from the two simulations are promising.

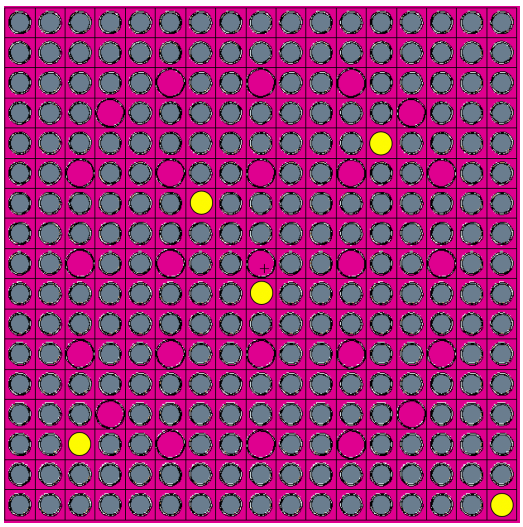


Figure 131. Diagram of a standard 17 ×17 fuel assembly used in the tomography simulations. The grey points correspond to fuel pins, the pink ones are empty guide tubes filled with air, and the yellow points are the positions where fuel pins were removed in the tomography simulations.

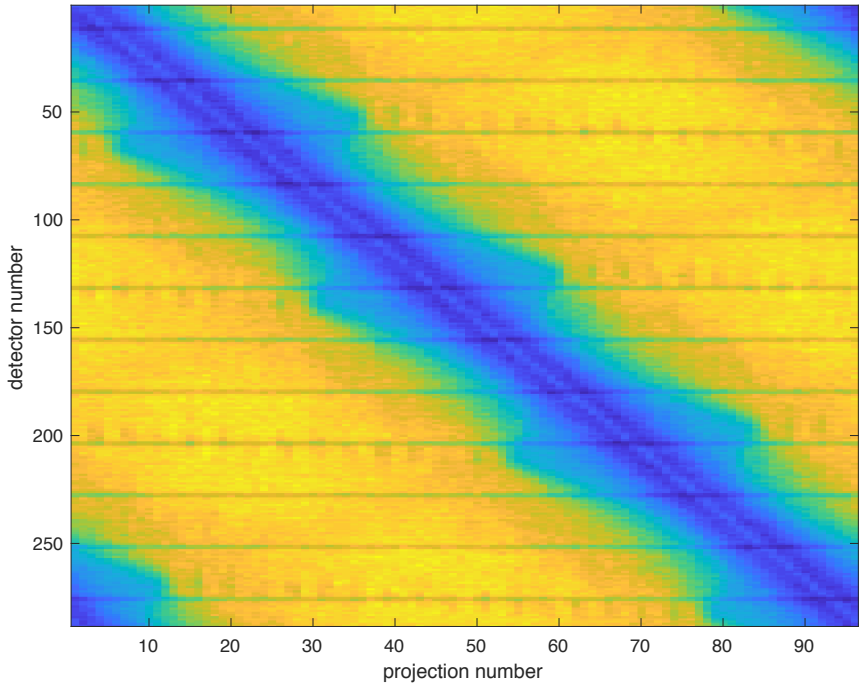


Figure 132. Sinograms from a tomography simulation of a standard 17 ×17 fuel assembly with five pins missing.

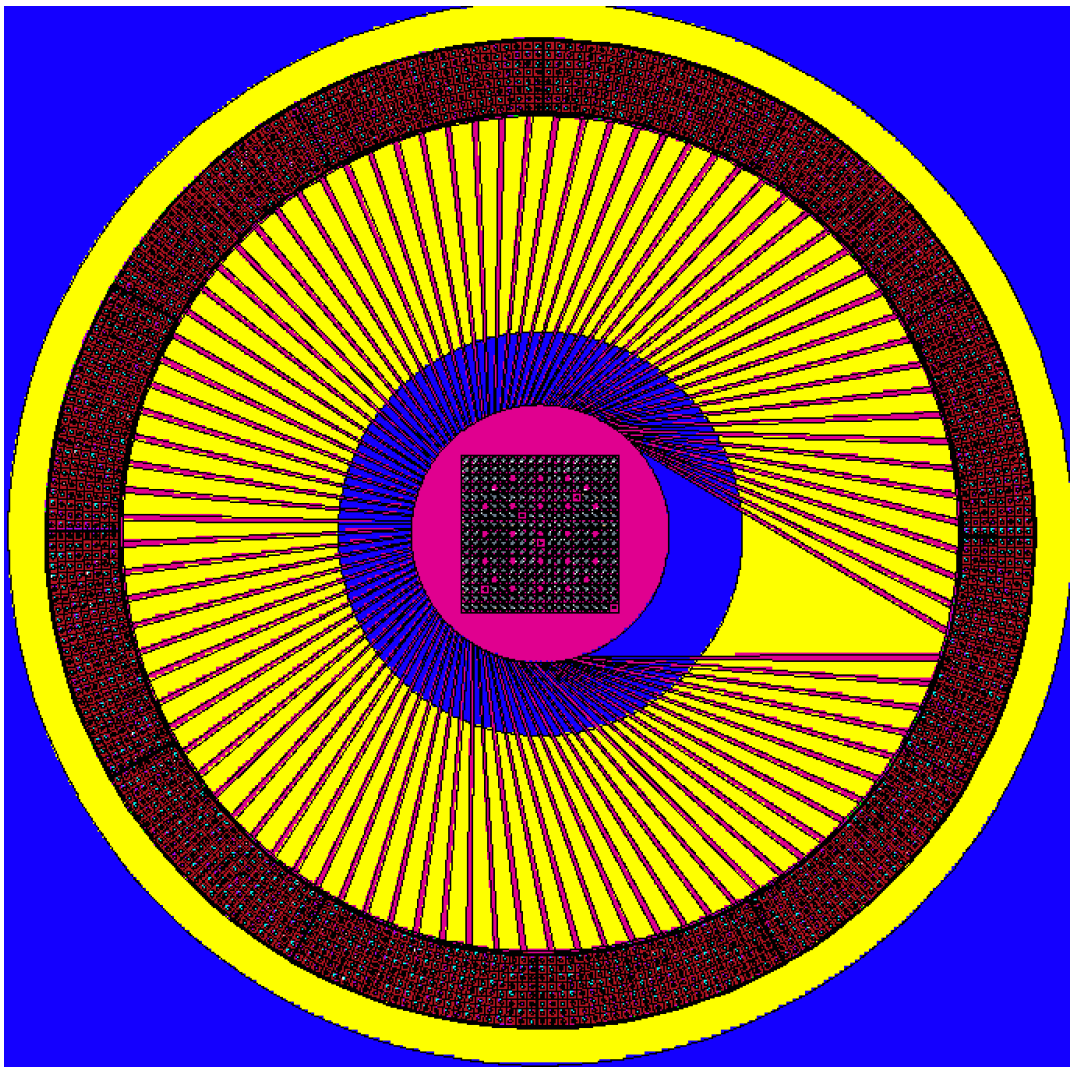


Figure 133. Plan view of the final imager geometry with 96 slits and a fuel assembly in the center with five pins removed.

7.7. Testing of Detector Prototype

A single detector prototype in the final design was shipped to ORNL for testing in October 2018. The goal for the set of measurements presented here was to investigate and show what the inter-detector scatter looks like for the final module and compare it to the simulation results. The single module incorporated a circuit designed by ORNL and had a single readout per row of straws. The low-voltage differential signaling (LVDS) signal for every 4 rows was fed and read out by 6 ethernet cables while still retaining the single row data. A picture of the top of the detector rows and each row's preamplifier without the high voltage board is shown below in Figure 134 on top, and the picture of the high voltage board with the six readout ports is shown in the middle of the same picture, and the top cover with readout ports for the detector is shown at the bottom.

The high voltage supplied was 800 Volts (V), and the DC power was supplied at ±7 V, and the threshold was set at 63 mV. The LVDS signals are read out from the detector and are fed into a 32-channel interface box. The output from the interface box was read out in two ribbon cables and fed into a CAEN Board model V1190 which has four TDC (time to digital conversion) chips with the ability to accept a total of 128 signals or channels, but in this setup only 2 were used. Figure 135 shows a picture of the six ethernet cables containing the signals from all 24 rows feeding into the interface box and the two ribbon cables that feed into the CAEN board.

Another ribbon cable containing the output of a 20 kHz pulser was fed into another chip of the CAEN TDC after being processed through the NIM bin shown in Figure 136 in order to convert the signals to NIM pulses, which after going through the ribbon cables are transformed into ECL pulses, which are accepted by the CAEN board. In addition to the detector signals, a 20 kHz pulser was fed into a Quad CFD and converted from NIM signals to ECL pulses that were directed to the CAEN TDC. The reason for incorporating the 20 kHz pulser was to tell the post processing software that one clock rollover has occurred and keeps track of which cycle the clock is in so that the counts over total time can be accurately registered. A simpler block diagram of the overall setup is shown in Figure 137. Finally, a USB-VME bridge mounted onto the CAEN module was used to convert the output to USB2 which is fed into a computer.

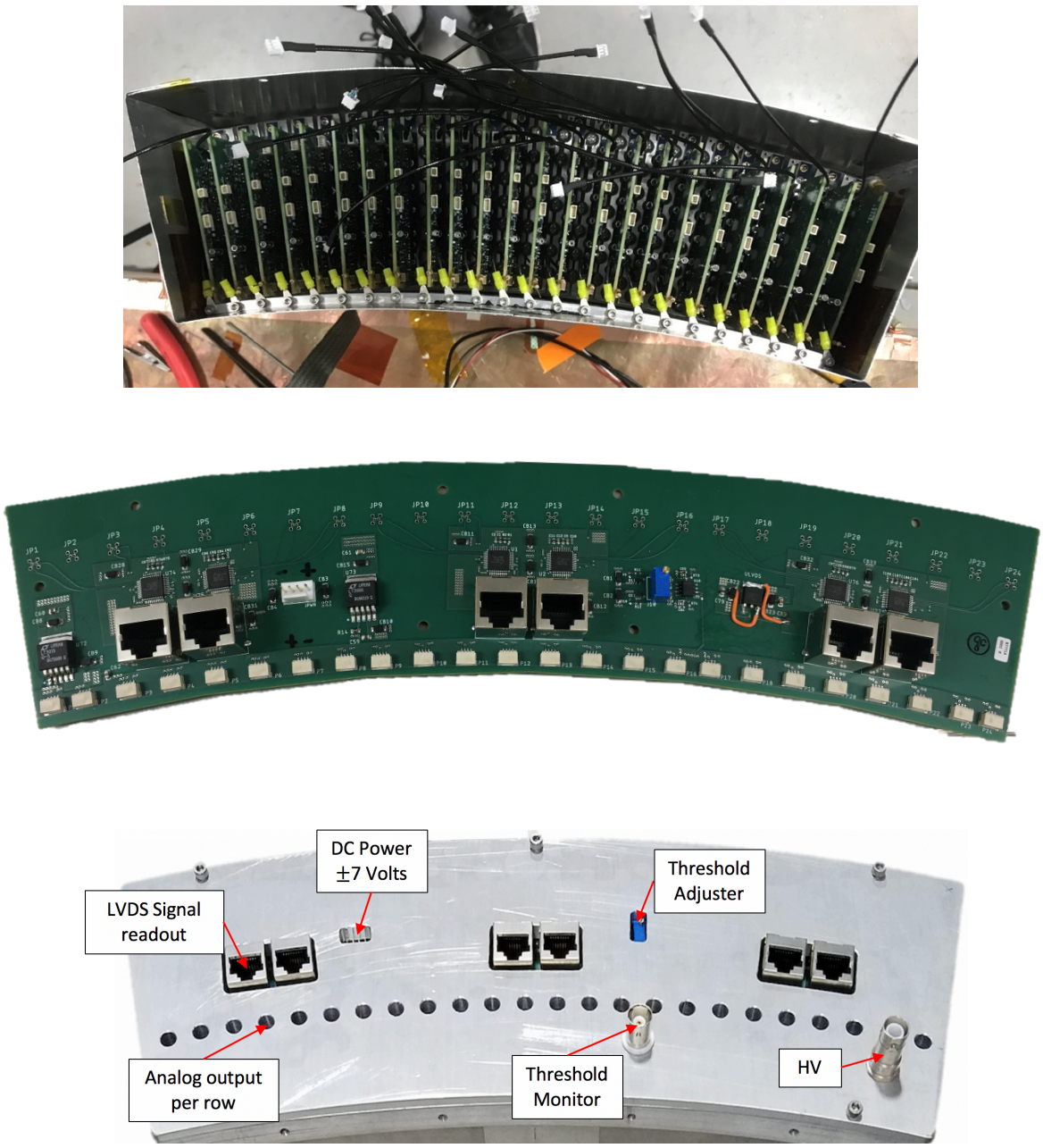


Figure 134. (Top) Final detector module top view without the high voltage board. Here the 24 rows of straws with their corresponding preamplifiers are shown. (Middle) Readout board showing the 6 ethernet cable ports that are used to readout the signals from each straw. (Bottom) Top layer of the detector with various readouts and ports labeled.

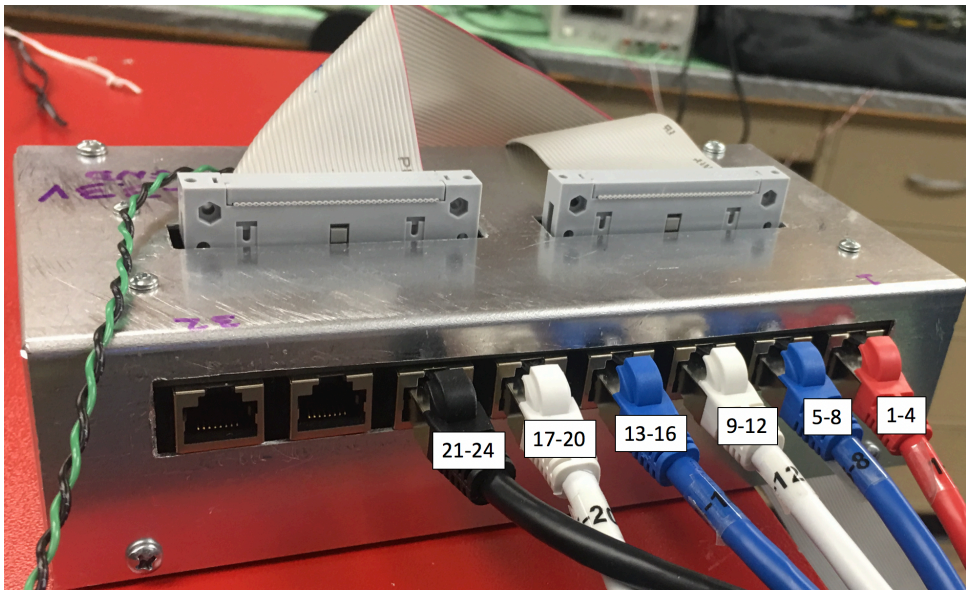


Figure 135. Interface box that takes in the 24 LVDS signals from the 6 ethernet cables reading the 24 rows and sends the signals out in 2 ribbon cables that feed into a CAEN TDC.



Figure 136. Ribbon cables from the interface box feeding into the CAEN boards. (Not Shown) a 20KHz pulser was used for timing synchronization because of the way the post processing software was written.

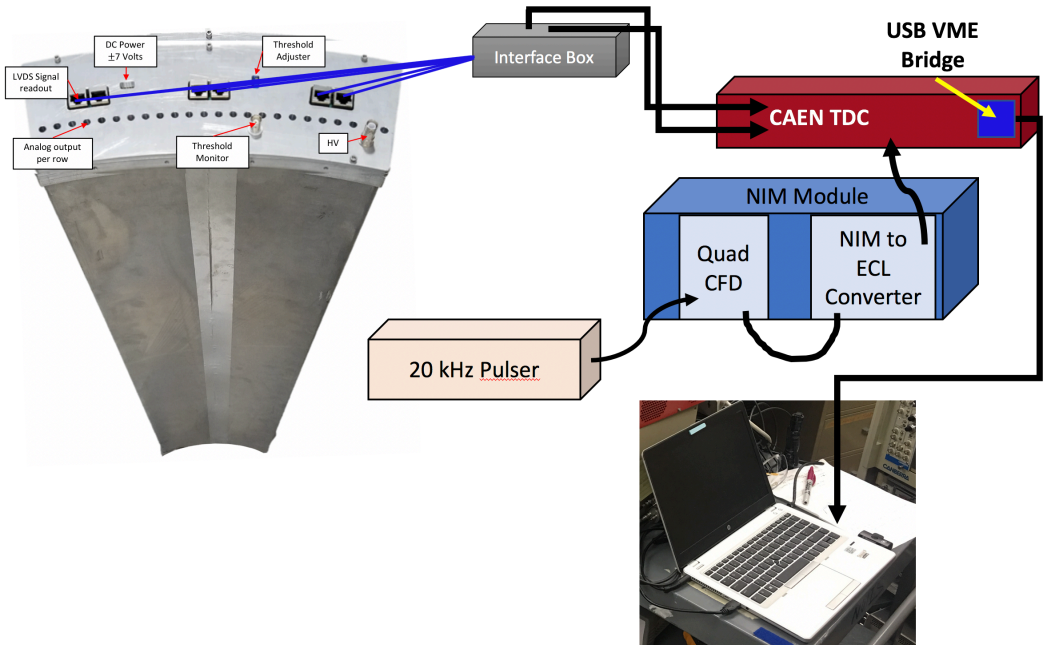


Figure 137. Block diagram of the readout electronics from a single detector.

The post processing software was developed at ORNL for a prior project and was modified to acquire the data for the experiments with this final detector module. To test the final detector module, a single slit collimator wedge made of 30 cm of borated polyethylene was built at ORNL. The collimator was built with eight 1" slabs of borated polyethylene. The collimator slit was formed by bolting 4 slabs on either side spaced by 1mm thick spacers on either end of the slit. A tapered slit with 3mm on one side and 8mm on the other side was used in the measurements. The source used in the set of experiments was a tube filled with six ^{252}Cf pellets that were fabricated at the same time and have the same initial activity. The source information is given in Table 17.

The six pellet sources were placed inside a piece of tubing and taped to the slit opening. To shield the sides of the source and the detectors, blocks of polyethylene were placed behind and to the sides of the source to prevent the neutrons being emitted from the ^{252}Cf sources from bouncing off the surroundings in the lab and being detected in the detector module. In addition to the polyethylene blocks, sheets of borated aluminum were placed along the detector sides and behind the blocks on the backside of the source to absorb any other neutrons that would escape the polyethylene blocks. The data acquisition software was initiated using the command prompt on the laptop by running a script developed by others at ORNL. The input parameters included a command to specify the measurement count time, but when the measurement was initiated, the actual count time was 10 to 15% more than specified. A picture of the measurement setup with the detector, collimator, the polyethylene blocks and borated aluminum sheets are shown in Figure 138. The ^{252}Cf pellets aligned to the center slit cannot be seen in the picture because it is hidden behind the shielding blocks.

For the single slit experiments, the single slit collimator was pointed at row number 13, and the source was taped to the center of the slit opening and halfway along the length of the collimator. Figure 139 shows a picture of the center-slit positioning of the tubing with the source pellets in them. A series of measurements were conducted with the sources placed in different positions as shown in Figure 140. The three measurements with the source present were all about 15 minutes long, and the background measurement was 10 minutes long.

Table 17. Source information for the six ^{252}Cf pellets used in the experiment along with the initial activity and date created.

Source ID	***Activity (Ci)***	***Date Created***
Cf252-4863	5×10^{-4}	2/15/1996
Cf252-4864	5×10^{-4}	2/15/1996
Cf252-4865	5×10^{-4}	2/15/1996
Cf252-4866	5×10^{-4}	2/15/1996
Cf252-4867	5×10^{-4}	2/15/1996
Cf252-4868	5×10^{-4}	2/15/1996

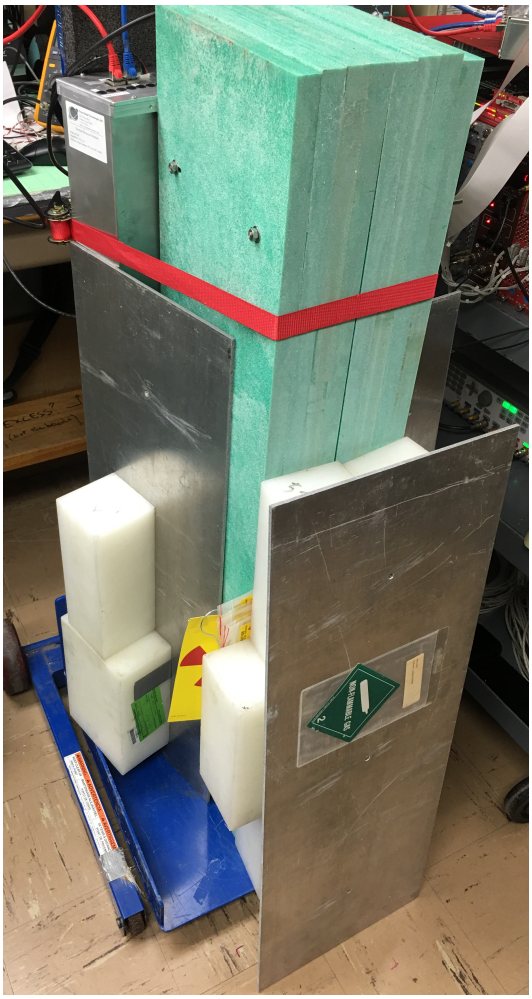


Figure 138. Measurement setup for the single slit experiment showing the single module, borated polyethylene collimator, the polyethylene shielding blocks, and the borated aluminum sheets. The six ^{252}Cf pellets are present and aligned to the slit but are hidden in this setup.



Figure 139. The tubing with six 252Cf pellets taped to the center of the slit opening, and aligned to the middle of the collimator length-wise. The tubing was surrounded by polyethylene blocks to shield from neutrons escaping the source.

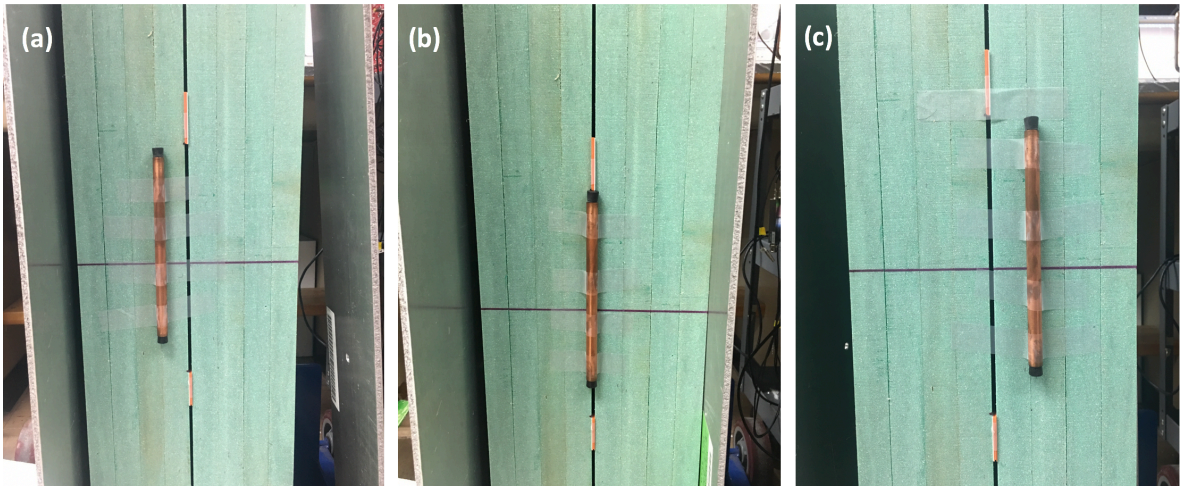


Figure 140. The three source positions used to acquire data for the single slit measurements.

In addition to aligning the source to the center, the two other experiments with the source present were conducted by moving the source 1” to the right of the slit and 1” to the left of the slit while maintaining the same height off the floor. The reason for doing so was to be able to quantify the amount of collimator penetration through the collimator on either side of the slit. The background count rate data is shown below in Figure 141 for a 10-minute measurement along with the corresponding error bars. The count rate is fairly constant across detector rows except there seems to be an outlier at row 5. This probably has to do with the high voltage boards being manufactured defectively due to components being placed too close together, and for a future iteration of the detector module, the design will be revised according to specifications provided by ORNL. To mitigate the effect of additional counts being registered falsely, SF_6 gas was flushed through the detector module since as an insulating gas, thus preventing the electronics from firing falsely.

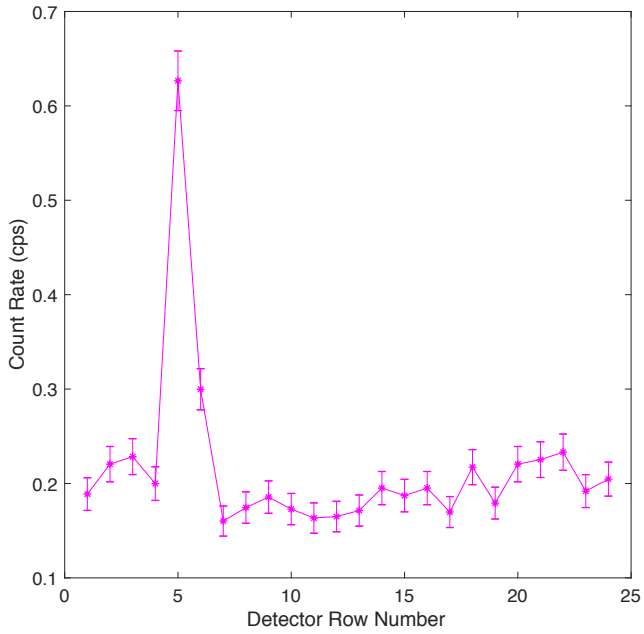


Figure 141. Count rates with corresponding error bars for the background measurement. Count rates for each of the 24 rows are presented.

The background subtracted count rate data and corresponding error bars for the source placed at the three positions is shown in Figure 142 for each of the 24 rows. The data shown in black is for the source placed down the center at the slit opening centered on row #13. As expected, the count rate peaks at row 13. The center slit data is not only background subtracted but the average of the count rates from the source placed 1" to the left and right is subtracted too. This was done in order to account for the collimator penetration on each side and see if the data is comparable to the single slit inter-detector scatter simulation conducted with the older design. The count rates on the sides (rows 1-3 and 21-24) fall below 0 for the center position because the collimator penetration subtraction is an approximate contribution. Looking only at the center data in black, the counts for every 3 rows (assuming row 13 was the center of a detector) were summed since in the final prototype this is how the detector count rates will be analyzed. The count rates were summed in rows of three and then divided by the respective measurement times, background subtracted, corrected for collimator penetration, and then normalized. The normalized measurement data along with the normalized simulation data is shown in Figure 143. The simulation data is what was presented in Figure 74 and shows the average relative counts of boron captures (per 10^6 source particles) for a beam of ^{244}Cm neutrons being thrown into the central detector. The relative spread of counts from the measurements is comparable to what was found via the simulations when corrected for the collimator penetration and background, thus validating the MCNP models.

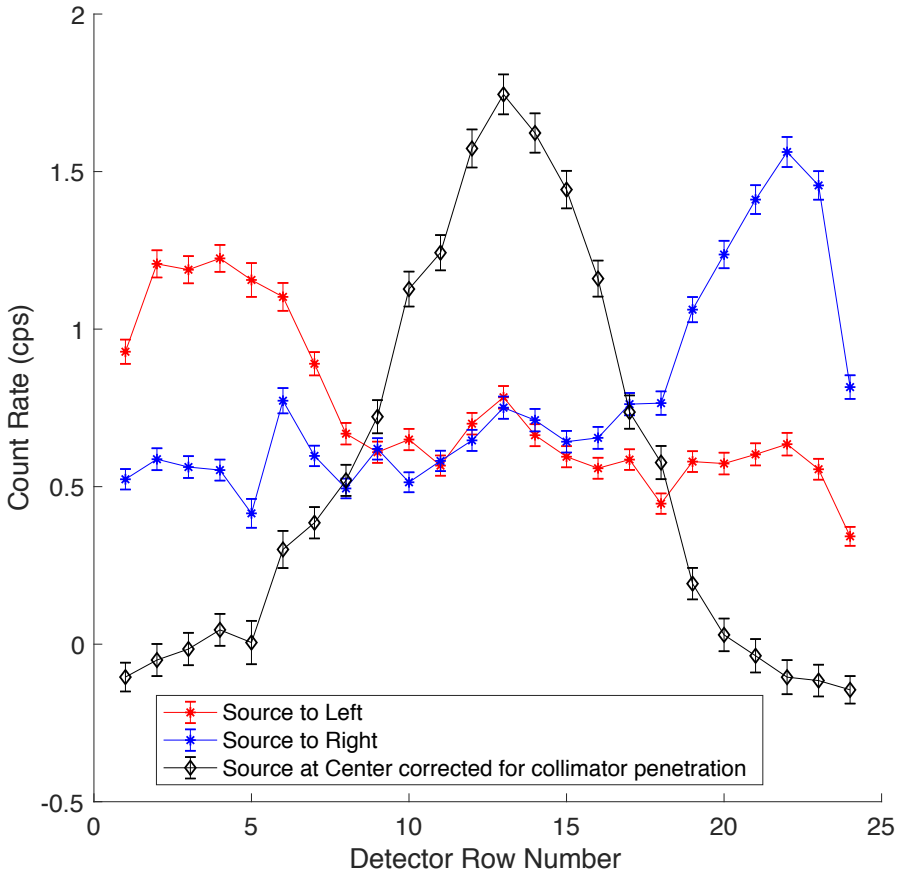


Figure 142. Count rate data for the source placed at the three different positions after subtracting the background contribution.

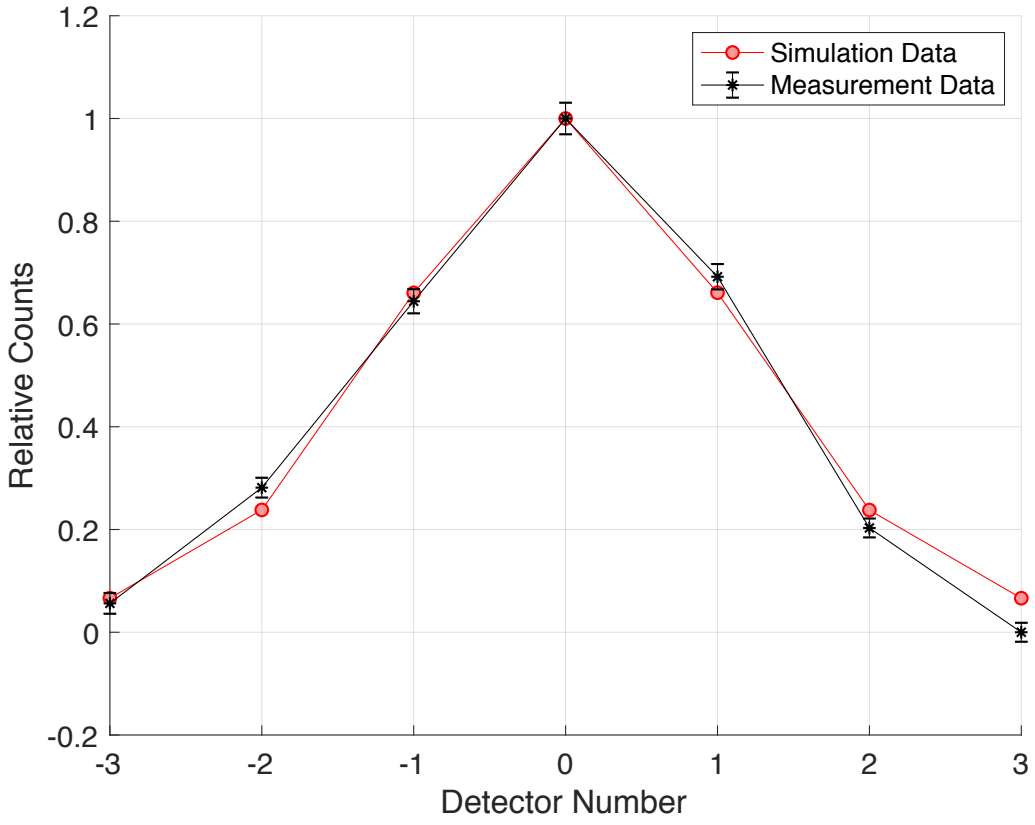


Figure 143. Normalized count rates for the source centered on the single slit corrected for background and collimator penetration from the measurements (blue), and the simulation data showing the spread of inter-detector scatter (red).

8. CONCLUSIONS AND FUTURE WORK

This dissertation describes a set of simulation and measurement work completed in order to investigate and converge on a final design of a fast neutron emission tomography system for imaging a spent nuclear fuel assembly to be used in order to check for its completeness in safeguards applications. If a full-scale system is constructed, this would be a first-of-its-kind system since no feasible neutron-based emission tomography system exists for safeguards applications. The novelty of this imager is in its compact size and its equivalency to a parallel-slit collimator. The neutron-based system offers the advantage that it is possible to be sensitive to the center of larger fuel assemblies since neutrons travel further than gamma-rays do, given that their mean free paths are larger when traversing through dense materials like nuclear fuel and associated structural components.

In order to conduct a constrained optimization for the design, a range of imager design parameters were identified to be varied, and MCNP was used to build the hundreds of geometries to investigate. The analysis was split in two components – a gamma analysis part and a neutron analysis part. The gamma simulations were conducted with a complete 17 × 17 fuel assembly (modeled at 1-year cooling time and 45 GWd/MTU burnup) placed in the assay area, and the exposures at each of the 100 detectors were tallied. Measurements using a single detector module were conducted at the ORNL RaSCaL facility to investigate the detector's ability to operate at high gamma exposure fields. The detector's operational limit was identified to be at 500 R/hr, and the need to instrument each row of straws individually was identified as well. These measurements were used in conjunction with MCNP simulations to identify the subset of design geometries that satisfied this operation limit. The geometry of the collimator (slit width, steel thickness, and borated poly thickness) is determined by the fuel burnup and cooling time. For the optimal geometry identified in this project, a fuel with burnup up to 45 GWd/MTU and cooling time of 1 year can be measured. As a part of this analysis, a method and relationship were also developed to be able to identify a constant exposure contour, or the range of collimator geometries that would satisfy a given exposure limit. This is useful for identifying different collimator geometries that may be

better suited for various fuel types and cooling times that may have different gamma exposure limitations.

In addition to the gamma simulations, all 512 geometries were simulated using a ^{244}Cm line source placed at two positions along a slit centerline to investigate how the point spread function is expected to vary between each case (including analysis of both signal and collimator penetration). The inter-detector scatter was also analyzed by shooting a beam of neutrons down a single slit to observe the expected spread in the signal, which would affect the spatial resolution. The spatial resolution achievable according to the simulations is about 1 cm FWHM. Over 300 simulations were conducted to understand how the leakage of neutrons is expected to change based on the source position relative to the slit's edge in terms of projected width. The simulated results showed that the leakage is expected to be proportional to the average pathlength the neutrons have to traverse through collimator material to get to the opposite end of the slit. The collimator transmission was also analyzed, and a series of correction factors were identified to compensate for the beam hardening effects and streaming paths within the collimator for the different geometries. This resulted in the ability to calculate the effective thickness of each of the collimators, yielding results close to what the measured effective thicknesses are based on MCNP simulations. An SNR code was used to analyze all 512 cases, using the results of over 1,500 simulations. The expected SNR values were then used in conjunction with the expected maximum exposures seen at the detectors for each of the 512 cases. These results showed that the steel is expected to play a huge part in shielding the detectors from the gamma-rays, and also that to achieve an SNR of 5 or better, it is not expected to be necessary to go for the largest simulated collimator. Tapering the slits helps achieve a higher neutron detection efficiency and higher SNR without exposing the detectors to high exposures that would otherwise cause an issue with parallel slits. The ideal imager configuration amongst the ones investigated was found to be one that contained 10 cm of steel and 30 cm of borated polyethylene with tapered slits of 3 mm on the inside and above 5 mm on the outside. As a result, for the final configuration an imager with 10 cm of steel and 29.5 cm of borated polyethylene with a 3 mm inner slit width and a 8 mm outer slit width was chosen. The final design of the imager also has 96 detectors instead of a 100 due to the electronic channels having to be a multiple of 8. The

final detector module will contain 24 rows of 8 boron straws, and each of the rows will be instrumented separately.

Various simulations to incorporate into the reconstruction code for the final geometry were conducted. The detector response to a source positioned at various projected widths from the slit edge was calculated to verify that the relationship seen in the old geometry still stood. A correction for the relative positioning of the slit opening to the detectors all around the collimator was conducted because the slits do not point directly perpendicular to each of the detector rows, which could result in the signal peaking at a neighboring row of the intended one. A double Gaussian was used to fit the response, and fit constants and centroids were identified for all 96 slits. Since the collimator is not a simple design, an estimate of the calculated collimator penetration ($CP_{calculated}$) for each of the detector rows was found by calculating the closed fraction seen by each of the detector rows. This also will feed into the final reconstruction code. An SNR study of the final detector and collimator with 96 slits was conducted by varying the slit widths. Eleven different parallel slit widths were studied, and the SNR was found to peak at around a geometric mean of 6 mm, beyond which the spatial resolution would not be sufficient to identify a single fuel pin. The final design with the tapered slits with 3 mm inner and 8 mm outer slit width has an expected SNR of 5.809, which is sufficient for imaging down to the single pin level.

To test this selected geometry in simulation space, two sets of tomography simulations were conducted. The first simulated test was with five ^{244}Cm line sources placed close together, and the second simulated test was with a 17 × 17 fuel assembly that had five fuel pins removed from various locations. A quantity of 96 projection simulations were conducted for each of the two cases, and the data was compiled to generate sinograms of the two simulation sets. The sinogram of the five line sources show that five individual lines appear, thus showing that the imager design is expected to be able to resolve sources placed close together. The sinogram with the complete fuel assembly showed that the rows of detectors closest to the Al walls of the detector module are expected to have lower efficiency than the inner rows, thus a scaling factor needs to be incorporated to correct for this. The fuel assembly sinogram is complicated, and individual fuel pin threads cannot be clearly identified as expected. The reconstruction code was developed at ORNL and uses the data

generated by the work presented here to account for the slit response, inter-detector scattering, collimator penetration, and the lowered efficiency at the detector edges. The reconstructed image of the five line sources using the MCNP data proves that the imager design does work and can image sources placed close together.

Finally, a set of measurements with a neutron source were conducted at ORNL to test the inter-detector scatter and compare to MCNP simulations. The measurements showed that the inter-detector scatter spans across three detectors on either side and the relative counts from the measurement are in very close agreement to the simulations, thus validating the MCNP model of the imager. The simulations and analysis presented so far show that the imager design identified is expected to be able to provide sufficient spatial resolution to image individual fuel pins.

With regards to future work, the imager geometry should be simulated with other types of fuel, including VVER-1000 fuel. PGET has not been tested with this type of fuel yet. Also, a fuel assembly with cooling times longer than 1 year and closer to 40 or 50 years needs to be simulated since the PGET only relies on the 662 keV gamma-rays for long-cooled fuel and those gamma rays may be too weak to escape the fuel assembly, and it would be hard to detect any missing pins at that point. Furthermore, fuel assemblies with pins that have varied burnups should be simulated in order to see if one can expect the intensity varying based on the neutron emission rates to be picked up by the imager. Moreover, it would be useful from a safeguards perspective to test the expected ability of the imager to generate a burnup profile of a fuel assembly. Currently inspectors rely only on operator declarations of the burnup, and they use the FDET to verify a gross measurement, not a pin-by-pin measurement.

In summary, a feasible design for an imager based on fast neutron emission tomography has been investigated and identified with spent nuclear fuel verification for international safeguards applications in mind. Simulations and proof-of-concept measurements suggest that it is viable to build a compact equivalent to a parallel slit collimator imager that has sufficient spatial resolution to image spent fuel pins.

REFERENCES

[1] Basics of IAEA Safeguards [Online]. Available: https://www.iaea.org/topics/basics-of-iaea-safeguards
[2] IAEA, "IAEA Safeguards Serving Nuclear Non-Proliferation," IAEA, Ed., ed. Vienna, Austria: IAEA, 2017.
[3] M. A. Humphrey, K. D. Veal, and S. J. Tobin, "The Next Generation Safeguards Initiative's Spent Fuel Nondestructive Assay Project," *Journal of Nuclear Materials Management,* vol. XI, no. 3, pp. 6-11, Spring 2012 2012.
[4] A. Lebrun and S. Zykov, "Status of NDA Techniques in Use for IAEA Verification of Light Water Reactor Spent Fuel," in *Inernational Nuclear Materials Management Annual Meeting*, 2014.
[5] IAEA, "Research and Development Plan: Enhancing Capabilities for Nuclear Verification," January 2018 2018.
[6] IAEA, "Spent Fuel Reprocessing Options," International Atomic Energy Agency, Vienna, Austria2008.
[7] Y. Ham, P. Kerr, S. Sitaraman, R. Swan, and H. Liljenfeldt, "Partial Defect Verification of Spent Fuel Assemblies by PDET: Principle and Field Testing in Interim Spent Fuel Storage Facility (CLAB) in Sweden," presented at the 2015 4th International Conference on Advancements in Nuclear Instrumentation Measurement Methods and their Applications (ANIMMA), Lisbon, Portugal, April 2015, 2015. Available: https://ieeexplore.ieee.org/document/7465608/
[8] V. Pushkarjov and E. Tkharev, "International Safeguards Aspects of Spent-Fuel Storage: Techniques and Approaches are Evolving to Meet Future Challenges," in "Special Reports: Safeguards & Non-Proliferation," International Atomic Energy Agency1986.
[9] W. L. Belew and B. W. Moran, "Safeguards Issues in Spent Fuel Consolidation Facilities," Oak Ridge National LaboratoryDE91 007984, 1991.
[10] IAEA, IAEA, Ed. *Safeguards Techniques and Equipment: 2011 Edition* (International Nuclear Verification Series No. 1 (Rev. 2)). Vienna, Austria: International Atomic Energy Agency, 2011.
[11] B. D. Boyer, "The Rudiments of IAEA Safeguards Showing How Policy Drives Technical Goals," Los Alamos National Laboratory, Los AlamosLA-UR 09-00782, 2010.
[12] S. J. Tobin and P. Jansson, "Nondestructive Assay Options for Spent Fuel Encapsulation," Los Alamos National Laboratory, Los AlamosLA-UR-13-22050, 2014.
[13] S. J. Tobin *et al.*, "Experimental and Analytical Plans for the Non-destructive Assay System of the Swedish Encapsulation and Repository Facilities," presented at the 2014 IAEA Safeguards Symposium, Vienna, 2014.
[14] IAEA, "IAEA Safeguards Glossary," in "International Nuclear Verification Series," IAEA, Austria2001.
[15] J. R. Phillips, "Irradiated Fuel Measurements," in *Passive Nondestructive Assay of Nuclear Materials*, 1991.
[16] S. T. Hsue, T. W. Crane, W. L. T. Jr., and J. C. Lee, "Nondestructive Assay Methods for Irradiated Nuclear Fuels," Los Alamos Scientific Laboratory1978.

[17] C. Willman, "Applications of Gamma Ray Spectroscopy of Spent Nuclear Fuel for Safeguards and Encapsulation," Doctor of Philosophy, Uppsala University, Uppsala, 2006.
[18] J. E. Fast, J. W. Chenault, B. D. Glasgow, D. C. Rodriguez, B. A. VanDevender, and L. S. Wood, "Spent Nuclear Fuel Measurements," Pacific Northwest National Laboratory2014.
[19] O. W. Hermann and C. W. Alexander, "A Review of Spent-Fuel Photon and Neutron Source Spectra," Oak Ridge National Laboratory1986.
[20] N. Ensslin, "Passive Nondestructive Assay of Nuclear Materials," 1991.
[21] S. P. Cerne, O. W. Hermann, and R. M. Westfall, "Reactivity and Isotopic Composition of Spent PWR Fuel as a Function of Initial Enrichment, Burnup, and Cooling Time," Oak Ridge National Laboratory1987.
[22] Nuclear Regulatory Commission. (1993). *CNWRA 96-006, Characteristics of Spent Nuclear Fuel and Cladding Relevant to High-Level Waste Source Term*.
[23] E. Amaral, K. Brockman, and H. G. Forsström, "International Perspectives on Spent Fuel Management," in *Management of Spent Fuel from Nuclear Power Reactors*, Vienna, Austria, 2006, vol. STI/PUB/1295.
[24] The Nuclear Fuel Cycle [Online]. Available: http://www.world-nuclear.org/information-library/nuclear-fuel-cycle/introduction/nuclear-fuel-cycle-overview.aspx
[25] P. M. O'Leary and M. L. Pitts, "Effects of Burnable Absorbers on PWR Spent Nuclear Fuel," presented at the Waste Management, Tuscon, Arizona, 2001.
[26] J. J. Duderstadt and L. J. Hamilton, *Nuclear Reactor Analysis*. New York: Wiley, 1976.
[27] A. C. Kak and M. Slaney, *Principles of Computerized Tomographic Imaging*. New York: IEEE Press, 1988.
[28] D. C. Camp, H. E. Martz, G. P. Roberson, D. J. Decman, and R. T. Bernardi, "Nondestructive waste-drum assay for transuranic content by gamma-ray active and passive computed tomography," *Nuclear Instruments & Methods in Physics Research A,* no. 495, pp. 69-83, 2002.
[29] W. Treimer, "Neutron Tomography," in *Neutron Imaging and Applications*New York: Springer, 2009.
[30] M. Licata and M. J. Joyce, "Combined Fast-neutron/γ-Ray Computed Tomography: a single modality with which to discern both nuclear materials and contrived shielding configurations," presented at the The 2017 International Conference on Applications of Nuclear Techniques, Crete, Grece, 2017.
[31] M. Licata and M. J. Joyce, "Concealed nuclear material identification via combined fast-neutron/γ-ray computed tomography (FNGCT): a Monte Carlo study.," *Journal of Instrumentation,* vol. 13.02, no. P02013, 2018.
[32] M. J. Joyce *et al.*, "Fast Neutron Tomography with Real-Time Pulse-Shape Discrimination in Organic Scintillation Detectors," *Nuclear Instruments & Methods in Physics Research A,* vol. 834, pp. 36-45, 2016.
[33] P. Hausladen, J. Newby, M. Blackston, I. Gauld, and J. Hu, "Detection of Single-Rod Diversion Using Passive Neutron Imaging," 2015.

[34] A. Iyengar *et al.*, "Detection of Fuel Pin Diversion via Fast Neutron Emission Tomography," presented at the European Safeguards Research and Development Association (ESARDA), Dusseldorf, Germany, 2017.
[35] "Managing Spent Fuel from Nuclear Power Reactors Experience and Lessons from Around the World," vol. International Panel on Fissile Materials ed, 2011.
[36] B. Boyer, "The Rudiments of IAEA Safeguards Showing How Policy Drives Technical Goals," in *LLNL Safeguards Summer Lecture Series*, Livermore, 2010, no. LA-UR 09-00782: Los Alamos National Laboratory.
[37] B. Siskind, "Measurement of Spent Fuel Assemblies Overview of the Status of the Technology For Initiating Discussion at NATIONAL RESEARCH CENTRE KURCHATOV INSTITUTE," Brookhaven National Laboratory2013.
[38] K. v. d. Meer, "Use of the FORK Detector in Safeguards Inspections," SCK-CEN, Mol, Belgium2007.
[39] (2017). *LA-UR-17-21223, AEFC for the Verification of Research Reactor Spent Fuel – Field Experience to Date*.
[40] H. O. Menlove and D. Henzlova, "Neutron Detector Technical Requirements for IAEA Safeguards Applications," in *IAEA Neutron Detection Workshop*, Vienna, 2011: Los Alamos National Laboratory.
[41] P. Staples *et al.*, "A Fast Breeder Reactor Spent Fuel Measurements Program for BN-350 Reactor " Los Alamos National LaboratoryLA-UR-99-3513
[42] "Technologies Potentially Useful for Safeguarding Geological Repositories," in "ASTOR Group Report 2011-2016," IAEA, Vienna2017.
[43] S. J. Tobin, P. Peura, C. C. Bélanger-Champagne, M. Moring, P. Dendooven, and T. Honkamaa, "Utility of Including Passive Neutron Albedo Reactivity in an Integrated NDA System for Encapsulation Safeguards," *ESARDA Bulletin,* vol. 56, pp. 12-18, 2018.
[44] S. J. Tobin, P. Peura, C. Bélanger-Champagne, M. Moring, P. Dendooven, and T. Honkamaa, "Measuring spent fuel assembly multiplication in borated water with a passive neutron albedo reactivity instrument," *Nuclear Instruments and Methods in Physics Research Section A: Accelerators, Spectrometers, Detectors and Associated Equipment,* vol. 897, pp. 32-37, 2018.
[45] F. Levai, S. Desi, M. Tarvainen, and R. Arlt, "Use of High Energy Gamma Emission Tomography for Partial Defect Verification of Spent Fuel Assemblies," in "Final report on the Task FIN A98 of the Finnish Support Programme to IAEA Safeguards," Stralsakerhetscentralen Finnish Centre for Radiation and Nuclear Safety1993.
[46] Y.-D. Lee, W. W. Na, Y. G. Lee, W. K. Yoon, and E. H. Kwack, "Sensitivity on the Spatial Assay for Safeguards in the Designed Device," *Applied Radiation and Isotopes,* vol. 48, no. 10-12, pp. 1535-1541, 1997.
[47] S. Jacobsson, A. Bäcklin, A. Hakansson, and P. Jansson, "A Tomographic Method for Experimental Verification of the Integrity of Spent Nuclear Fuel," *Applied Radiation and Isotopes,* vol. 53, no. 4-5, pp. 681-689, 2000.
[48] "Nuclear Verification," in "IAEA Annual Report 2017," International Atomic Energy Agency, Vienna2017.

[49] F. Levai *et al.*, "Feasibility of Gamma Emission Tomography for Partial Defect Verification of Spent LWR Fuel Assemblies," in "Summary report on simulation and experimental studies including design options and cost-benefit analysis," 2002.
[50] T. Honkamaa, F. Levai, A. Turunen, R. Berndt, S. Vaccaro, and P. Schwalbach, "A Prototype for Passive Gamma Emission Tomography," presented at the IAEA Safeguards Symposium, Vienna, 2014.
[51] T. White, "Gamma Emission Tomography for the Inspection of Spent Nuclear Fuel," 2017.
[52] E. Dul, "Monte Carlo Simulation of the Spatial Response Function of a SPECT Measurement Device for Nuclear Fuel Bundles," Bachelor's Thesis, Hospital Physics, Stockholm University, 2017.
[53] E. A. Miller *et al.*, "Hybrid Gamma Emission Tomography (HGET): FY16 Annual Report," PNNL2017.
[54] V. Mozin, "Delayed Gamma-Ray Assay for Nuclear Safeguards," Doctor of Philosophy, Nuclear Engineering, University of California, Berkeley, Berkeley, 2011.
[55] P. A. Hausladen, M. A. Blackston, and J. Newby, "Demonstration of Emitted-Neutron Computed Tomography to Quantify Nuclear Materials," Oak Ridge National Laboratory2011.
[56] P. A. Hausladen, M. A. Blackston, E. Brubaker, D. L. Chichester, P. Marleau, and R. J. Newby, "Demonstration of Emitted-Neutron Computed Tomography to Count Fuel Pins," presented at the Institute of Nuclear Materials Management, Orlando, Florida, 2012.
[57] A. Iyengar, P. A. Hausladen, L. Fabris, J. Yang, and J. Hu, "Use of fast neutron emission tomography for spent fuel verification," presented at the IAEA Symposium on International Safeguards, Vienna, 2018.
[58] S. R. Greene, J. S. Medford, and S. A. Macy, "Storage and Transport Cask Data For Used Commercial Nuclear Fuel – 2013 U.S. Edition –," 2013, Art. no. ATI-TR-13047.
[59] "CASTOR® V/19 Transport and Storage Cask for Spent Fuel (PWR)," G.-G. f. N.-S. mbH, Ed., ed.
[60] T. W. Crane and M. P. Baker, "Neutron Detectors," in *Passive Nondestructive Assay of Nuclear Materials*, 1991.
[61] J. Hu, S. Croft, and R. McElroy, "Boron-Coated Straw Collar for Uranium Neutron Coincidence Collar Replacement," Oak Ridge National LaboratoryORNL/TM-2016/696, 2016.
[62] I. Proportional Technologies. *The 10B(n, alpha) Reaction and Detector Design*. Available: https://proportionaltech.myshopify.com/pages/technology
[63] (2018). *ORNL/SPR-2018/975, A Design Study of the Parallel-Slit Ring Collimator for Fast Neutron Emission Tomography of Spent Fuel*.
[64] J. Goorley, "MCNP6 User's Manual," Los Alamos National Laboratory, LA-CP-13-00634, 2013.
[65] P. A. Hausladen *et al.*, "Modelling Passive Fast-Neutron Emission Tomography of Spent Nuclear Fuel," presented at the International Workshop on Numerical

Modelling of NDA Instrumentation and Methods for Nuclear Safeguards, Luxembourg, 2018.

APPENDIX

Table 18. Coefficients for the double Gaussian fit

Slit Number	A_1	b	σ	A_2
1	1.0545	-1.0158	2.8049	0.5184
2	1.0623	-0.9912	-2.8094	0.5149
3	0.9365	-0.9709	2.6737	0.6453
4	1.1025	-0.9373	2.9246	0.4520
5	0.6366	-0.9583	2.4826	0.8835
6	0.9273	-0.8924	2.6745	0.6565
7	1.0273	-0.8702	-2.7472	0.5669
8	1.0701	-0.8497	2.7946	0.5201
9	1.0695	-0.8269	2.7926	0.5208
10	1.0716	-0.8049	2.7910	0.5208
11	0.9297	-0.7957	2.6358	0.6686
12	1.1190	-0.7660	2.9192	0.4446
13	1.1500	-0.7904	3.0330	0.3706
14	0.8834	-0.7268	2.6071	0.7063
15	1.0238	-0.7061	2.7231	0.5772
16	1.0649	-0.6868	2.7684	0.5341
17	1.0529	-0.6637	2.7591	0.5433
18	1.0530	-0.6419	2.7580	0.5435
19	0.9149	-0.6228	2.6183	0.6839
20	1.1146	-0.5850	2.9071	0.4508
21	1.1607	-0.6184	2.9949	0.3895
22	0.8869	-0.5549	-2.5797	0.7254
23	1.0409	-0.5374	2.7059	0.5826
24	1.0767	-0.5179	2.7374	0.5500
25	1.0701	-0.4977	2.7208	0.5643
26	1.0811	-0.4772	2.7282	0.5568
27	0.9235	-0.4592	2.5729	0.7185
28	1.1565	-0.4181	2.8993	0.4468
29	1.1882	-0.4437	2.9664	0.3982
30	0.8969	-0.3907	2.5461	0.7461
31	1.0535	-0.3705	2.6865	0.5882
32	1.0691	-0.3507	2.7078	0.5681
33	1.0578	-0.3288	2.6983	0.5770
34	1.0480	-0.3063	2.6829	0.5878

Table 18. Continued.

Slit Number	A_1	b	σ	A_2
35	0.9155	-0.2892	2.5560	0.7207
36	1.1402	-0.2484	2.8772	0.4469
37	1.1458	-0.2741	2.9138	0.4227
38	0.8912	-0.2168	2.5472	0.7241
39	1.0238	-0.2010	2.6631	0.5863
40	1.0177	-0.1804	2.6627	0.5826
41	1.0018	-0.1585	2.6559	0.5837
42	0.9952	-0.1395	2.6574	0.5759
43	0.8601	-0.1219	2.5440	0.6886
44	1.0444	-0.0716	2.8479	0.4432
45	1.0352	-0.1021	2.8563	0.4313
46	0.8349	-0.0481	2.5493	0.6590
47	0.9323	-0.0295	2.6441	0.5557
48	0.9215	-0.0097	2.6351	0.5629
49	0.9225	0.0103	2.6355	0.5620
50	0.9321	0.0317	2.6437	0.5563
51	0.8361	0.0495	2.5502	0.6580
52	1.0288	0.1026	2.8462	0.4391
53	1.0412	0.0729	2.8445	0.4461
54	0.8662	0.1211	2.5494	0.6825
55	0.9955	0.1400	2.6570	0.5764
56	1.0064	0.1589	2.6600	0.5796
57	1.0124	0.1806	2.6561	0.5883
58	1.0193	0.2012	2.6579	0.5908
59	0.8886	0.2179	2.5452	0.7266
60	1.1485	0.2753	2.9165	0.4201
61	1.1408	0.2473	2.8791	0.4459
62	0.9134	0.2898	2.5554	0.7226
63	1.0588	0.3065	-2.6969	0.5754
64	1.0641	0.3286	2.7038	0.5711
65	1.0691	0.3505	2.7072	0.5682
66	1.0501	0.3710	2.6849	0.5907
67	0.8978	0.3905	2.5480	0.7444
68	1.1854	0.4444	-2.9621	0.4013
69	1.1600	0.4183	2.9029	0.4438

Table 18. Continued.

Slit Number	A_1	b	σ	A_2
70	0.9297	0.4591	2.5789	0.7122
71	1.0812	0.4767	2.7298	0.5565
72	1.0678	0.4971	2.7181	0.5670
73	1.0768	0.5182	2.7361	0.5506
74	1.0429	0.5369	2.7080	0.5804
75	0.8872	0.5556	2.5815	0.7243
76	1.1629	0.6196	2.9986	0.3873
77	1.1109	0.5855	-2.9013	0.4551
78	0.9163	0.6246	2.6202	0.6819
79	1.0512	0.6425	2.7553	0.5455
80	1.0474	0.6636	2.7512	0.5494
81	1.0622	0.6869	2.7662	0.5364
82	1.0235	0.7070	2.7237	0.5765
83	0.8835	0.7286	2.6082	0.7052
84	1.1517	0.7908	3.0364	0.3684
85	1.1215	0.7638	2.9203	0.4434
86	0.9399	0.7962	2.6474	0.6582
87	1.0739	0.8053	2.7937	0.5175
88	1.0646	0.8280	-2.7867	0.5258
89	1.0740	0.8503	-2.7990	0.5162
90	1.0251	0.8706	2.7470	0.5678
91	0.9044	0.8927	2.6513	0.6795
92	1.1526	0.9612	3.0720	0.3533
93	1.1034	0.9365	2.9266	0.4506
94	0.9422	0.9697	2.6812	0.6389
95	1.0621	0.9905	2.8083	0.5155
96	1.0622	1.0149	2.8158	0.5095

VITA

Anagha Iyengar grew up in the Bay Area and received her Bachelor of Science in Nuclear Engineering from the University of California, Berkeley in 2012. She attended the University of Tennessee, Knoxville from 2012-2013 and received her Master of Science in Nuclear Engineering along with a certificate in Nuclear Security Science and Analysis. Anagha served as a Nonproliferation Graduate Fellow at the Department of Energy National Nuclear Security Administration (DOE/NNSA) in Washington D.C. from 2014 to 2015 where she supported the Office of International Nuclear Safeguards. She then stayed on from 2015 to 2016 as a contractor supporting the same office. Anagha returned to the University of Tennessee, Knoxville as a PhD candidate in the Bredesen Center for Interdisciplinary Research and Graduate Education while appointed as a Post Masters research associate with the Oak Ridge Associated Universities (ORAU) and conducted her research at Oak Ridge National Laboratory. Anagha was also a Nuclear Nonproliferation International Safeguards Fellow from 2016-2019.